

General Disclaimer

One or more of the Following Statements may affect this Document

- This document has been reproduced from the best copy furnished by the organizational source. It is being released in the interest of making available as much information as possible.
- This document may contain data, which exceeds the sheet parameters. It was furnished in this condition by the organizational source and is the best copy available.
- This document may contain tone-on-tone or color graphs, charts and/or pictures, which have been reproduced in black and white.
- This document is paginated as submitted by the original source.
- Portions of this document are not fully legible due to the historical nature of some of the material. However, it is the best reproduction available from the original submission.

NATIONAL AERONAUTICS AND SPACE ADMINISTRATION

The Deep Space Network
Progress Report 42-34

May and June 1976

(NASA-CE-148594) THE DEEP SPACE NETWORK
Progress Report, May - Jun. 1976 (Jet
Propulsion Lab.) 157 p HC \$6.75 CSCL 14B

G3/12

N76-29318
THRU
N76-29338
Uncclas
48419

JET PROPULSION LABORATORY
CALIFORNIA INSTITUTE OF TECHNOLOGY
PASADENA, CALIFORNIA

August 15, 1976



NATIONAL AERONAUTICS AND SPACE ADMINISTRATION

The Deep Space Network
Progress Report 42-34

May and June 1976

JET PROPULSION LABORATORY
CALIFORNIA INSTITUTE OF TECHNOLOGY
PASADENA, CALIFORNIA

August 15, 1976

Preface

Beginning with Volume XX, the Deep Space Network Progress Report changed from the Technical Report 32- series to the Progress Report 42- series. The volume number continues the sequence of the preceding issues. Thus, Progress Report 42-20 is the twentieth volume of the Deep Space Network series, and is an uninterrupted follow-on to Technical Report 32-1526, Volume XIX.

This report presents DSN progress in flight project support, tracking and data acquisition (TDA) research and technology, network engineering, hardware and software implementation, and operations. Each issue presents material in some, but not all, of the following categories in the order indicated.

Description of the DSN

Mission Support

- Ongoing Planetary/Interplanetary Flight Projects
- Advanced Flight Projects

Radio Science

Special Projects

Supporting Research and Technology

- Tracking and Ground-Based Navigation
- Communications—Spacecraft/Ground
- Station Control and Operations Technology
- Network Control and Data Processing

Network and Facility Engineering and Implementation

- Network
- Network Operations Control Center
- Ground Communications
- Deep Space Stations

Operations

- Network Operations
- Network Operations Control Center
- Ground Communications
- Deep Space Stations

Program Planning

- TDA Planning
- Quality Assurance

In each issue, the part entitled "Description of the DSN" describes the functions and facilities of the DSN and may report the current configuration of one of the five DSN systems (Tracking, Telemetry, Command, Monitor & Control, and Test & Training).

The work described in this report series is either performed or managed by the Tracking and Data Acquisition organization of JPL for NASA.

Contents

DESCRIPTION OF THE DSN

Network Functions and Facilities	1
N. A. Renzetti	

MISSION SUPPORT

Ongoing Planetary/Interplanetary Flight Projects

Viking Mission Support	4
D. J. Mudgway and D. W. Johnston	
NASA Code 311-03-21-70	
Helios Mission Support	21
P. S. Goodwin, W. G. Meeks, and R. E. Morris	
NASA Code 311-03-21-50	

SUPPORTING RESEARCH AND TECHNOLOGY

Communications—Spacecraft/Ground

Foldover Effects on Viterbi Decoding	27
J. K. Omura and S. A. Butman	
NASA Code 310-20-67-08	

Computation of Spacecraft Signal Raypath Trajectories Relative to the Sun	33
A. R. Cannon and C. T. Stelzried	
NASA Code 310-20-66-06	

Station Control and Operations Technology

Telecommunications Division Fourth Harmonic Power Analyzer	39
C. Foster	
NASA Code 310-30-68-11	

Decoding with Multipliers	43
L. D. Baumert, R. J. McEliece, and G. Solomon	
NASA Code 310-30-69-10	

Network Control and Data Processing

MODC2 Procedures for Assembly of MODCOMP-II Programs Using the Sigma-5 Assembler	47
J. W. Layland	
NASA Code 310-40-72-02	

Biplex Pipelined FFT	54
R. F. Emerson	
NASA Code 310-40-72-04	

NETWORK AND FACILITY ENGINEERING AND IMPLEMENTATION

Network

Viking Telecommunication Effects of GEOS Satellite Interference Based on Testing at the Madrid Deep Space Station	60
F. V. Stuhr, S. S. Kent, J. L. Galvez, B. G. Luaces,	
G. R. Pasero, and J. M. Urech	
NASA Code 311-03-42-90	

Network Operations Control Center

DSN Standard Interface Adapter and Buffer Assembly Used in the Mark III Data System	75
T. Anderson	
NASA Code 311-03-42-53	

Deep Space Stations

A New Sequential Decoder for the DSN Telemetry Subsystem	84
J. H. Wilcher	
NASA Code 311-03-41-01	
Antenna Pointing Subsystem Conscan Implementation	88
R. Tappan	
NASA Code 311-03-42-54	
High Performance Flat Plate Solar Collector	90
F. L. Lansing and R. Reynolds	
NASA Code 311-03-41-08	

OPERATIONS

Network Operations

An MBASIC Application Program for Relational Inquiries on a Database	100
R. M. Smith	
NASA Code 311-03-14-64	
Maximum Likelihood Convolutional Decoding (MCD) Performance Due to System Losses	108
L. Webster	
NASA Code 311-03-14-20	

DSN Research and Technology Support	119
E. B. Jackson	
NASA Code 311-03-15-30	
Use of "Load and Go" Countdowns by the DSN	
Deep Space Stations	124
J. T. Hatch	
NASA Code 311-03-14-20	

PROGRAM PLANNING

TDA Planning

Aspect of Job Scheduling	129
K. Phillips	
NASA Code 311-03-32-10	
Dynamic Modeling for Evaluation of Solar Collector Performance	141
C. L. Hamilton	
NASA Code 311-03-31-30	
Toward a Mathematical Model of Solar Radiation for	
Engineering Analysis of Solar Energy Systems	147
C. L. Hamilton and M. S. Reid	
NASA Code 311-03-31-30	

N 76-29319

Network Functions and Facilities

N. A. Renzetti
Office of Tracking and Data Acquisition

The objectives, functions, and organization of the Deep Space Network are summarized; deep space station, ground communication, and network operations control capabilities are described.

The Deep Space Network (DSN), established by the National Aeronautics and Space Administration (NASA) Office of Tracking and Data Acquisition under the system management and technical direction of the Jet Propulsion Laboratory (JPL), is designed for two-way communications with unmanned spacecraft traveling approximately 16,000 km (10,000 miles) from Earth to the farthest planets of our solar system. It has provided tracking and data acquisition support for the following NASA deep space exploration projects: Ranger, Surveyor, Mariner Venus 1962, Mariner Mars 1964, Mariner Venus 1967, Mariner Mars 1969, Mariner Mars 1971, and Mariner Venus Mercury 1973, for which JPL has been responsible for the project management, the development of the spacecraft, and the conduct of mission operations; Lunar Orbiter, for which the Langley Research Center carried out the project management, spacecraft development, and conduct of mission operations; Pioneer, for which Ames Research Center carried out the project management, spacecraft development, and conduct of mission operations; and Apollo, for which the Lyndon B. Johnson Space Center was the project center and the Deep Space Network supple-

mented the Manned Space Flight Network (MSFN), which was managed by the Goddard Space Flight Center (GSFC). It is providing tracking and data acquisition support for Helios, a joint U.S./West German project; and Viking, for which Langley Research Center provides the project management, the Lander spacecraft, and conducts mission operations, and for which JPL also provides the Orbiter spacecraft.

The Deep Space Network is one of two NASA networks. The other, the Spaceflight Tracking and Data Network, is under the system management and technical direction of the Goddard Space Flight Center. Its function is to support manned and unmanned Earth-orbiting satellites. The Deep Space Network supports lunar, planetary, and interplanetary flight projects.

From its inception, NASA has had the objective of conducting scientific investigations throughout the solar system. It was recognized that in order to meet this objective, significant supporting research and advanced technology development must be conducted in order to

provide deep space telecommunications for science data return in a cost effective manner. Therefore, the Network is continually evolved to keep pace with the state of the art of telecommunications and data handling. It was also recognized early that close coordination would be needed between the requirements of the flight projects for data return and the capabilities needed in the Network. This close collaboration was effected by the appointment of a Tracking and Data Systems Manager as part of the flight project team from the initiation of the project to the end of the mission. By this process, requirements were identified early enough to provide funding and implementation in time for use by the flight project in its flight phase.

As of July 1972, NASA undertook a change in the interface between the Network and the flight projects. Prior to that time, since 1 January 1964, in addition to consisting of the Deep Space Stations and the Ground Communications Facility, the Network had also included the mission control and computing facilities and provided the equipment in the mission support areas for the conduct of mission operations. The latter facilities were housed in a building at JPL known as the Space Flight Operations Facility (SFOF). The interface change was to accommodate a hardware interface between the support of the network operations control functions and those of the mission control and computing functions. This resulted in the flight projects assuming the cognizance of the large general-purpose digital computers which were used for both network processing and mission data processing. They also assumed cognizance of all of the equipment in the flight operations facility for display and communications necessary for the conduct of mission operations. The Network then undertook the development of hardware and computer software necessary to do its network operations control and monitor functions in separate computers. This activity has been known as the Network Control System Implementation Project. A characteristic of the new interface is that the Network provides direct data flow to and from the stations; namely, metric data, science and engineering telemetry, and such network monitor data as are useful to the flight project. This is done via appropriate ground communication equipment to mission operations centers, wherever they may be.

The principal deliverables to the users of the Network are carried out by data system configurations as follows:

- The DSN Tracking System generates radio metric data; i.e., angles, one- and two-way doppler and range, and transmits raw data to Mission Control.

- The DSN Telemetry System receives, decodes, records, and retransmits engineering and scientific data generated in the spacecraft to Mission Control.
- The DSN Command System accepts coded signals from Mission Control via the Ground Communications Facility and transmits them to the spacecraft in order to initiate spacecraft functions in flight.

The data system configurations supporting testing, training, and network operations control functions are as follows:

- The DSN Monitor and Control System instruments, transmits, records, and displays those parameters of the DSN necessary to verify configuration and validate the Network. It provides operational direction and configuration control of the Network, and provides primary interface with flight project Mission Control personnel.
- The DSN Test and Training System generates and controls simulated data to support development, test, training and fault isolation within the DSN. It participates in mission simulation with flight projects.

The capabilities needed to carry out the above functions have evolved in three technical areas:

- (1) The Deep Space Stations, which are distributed around Earth and which, prior to 1964, formed part of the Deep Space Instrumentation Facility. The technology involved in equipping these stations is strongly related to the state of the art of telecommunications and flight-ground design considerations, and is almost completely multimission in character.
- (2) The Ground Communications Facility provides the capability required for the transmission, reception, and monitoring of Earth-based, point-to-point communications between the stations and the Network Operations Control Center at JPL, Pasadena, and to the mission operations centers, wherever they may be. Four communications disciplines are provided: teletype, voice, high-speed, and wideband. The Ground Communications Facility uses the capabilities provided by common carriers throughout the world, engineered into an integrated system by Goddard Space Flight Center, and controlled from the communications Center located in the Space Flight Operations Facility (Building 230) at JPL.

(3) The Network Operations Control Center is the functional entity for centralized operational control of the Network and interfaces with the users. It has two separable functional elements; namely, Network Operations Control and Network Data Processing. The functions of the Network Operations Control are:

- Control and coordination of Network support to meet commitments to Network users.
- Utilization of the Network data processing computing capability to generate all standards and limits required for Network operations.
- Utilization of Network data processing computing capability to analyze and validate the performance of all Network systems.

The personnel who carry out the above functions are located in the Space Flight Operations Facility, where mission operations functions are carried out by certain flight projects. Network personnel are directed by an Operations Control Chief.

The functions of the Network Data Processing are:

- Processing of data used by Network Operations Control for control and analysis of the Network.
- Display in the Network Operations Control Area of data processed in the Network Data Processing Area.
- Interface with communications circuits for input to and output from the Network Data Processing Area.
- Data logging and production of the intermediate data records.

The personnel who carry out these functions are located approximately 200 meters from the Space Flight Operations Facility. The equipment consists of minicomputers for real-time data system monitoring, two XDS Sigma 5s, display, magnetic tape recorders, and appropriate interface equipment with the ground data communications.

N 76-29320

Viking Mission Support

D. J. Mudgway
DSN Systems Engineering Office

D. W. Johnston
DSN Operations Office

In this article the final operations tests prior to Mars orbit insertion for Viking I are discussed together with the real-time operations support for the two months preceding this event. The report also covers several special operational strategies and procedures designed to optimize the DSN support during the critical planetary phases of the mission. The final phases of Network implementation for Viking and the support afforded to the radio science experiments and Mars radar observations are also included.

I. Implementation

Following the achievement of operational status in the Network Operations Control Center in late April 1976, a number of desirable but not essential features of the system still remained incomplete. In addition, operational usage of the facility soon revealed deficiencies that required attention in order to meet the increasing demands of the Viking mission as orbit insertion activity for Viking I approached. Using the task team that had been established to complete the initial phase of operational readiness, an accelerated work plan was initiated to cover

the "enhancement items" for completion by June 1. The plan encompassed the following major items of software and hardware:

Software

- (1) Modify the data records processor software to allow recall to be restarted just prior to an error received during a recall sequence.
- (2) Install an updated magnetic tape handler program to increase the reliability of the recall merge process and reduce the size of data gaps.

- (3) Correct the Network communications equipment to simultaneously route data to two Network telemetry monitors.
- (4) Provide ability to synchronize on inverted telemetry data.
- (5) Complete the Block III Network Command Subsystem to permit the stations to be configured for "commanding" from the Network Operations Control Center.
- (6) Develop simplified algorithms to reduce the problems created by time regressions during the recall-merge process.

Hardware

- (1) Replace the existing "borrowed" mag-tape assembly with permanent 4-drive units in the Network Data Processing Area.
- (2) Convert four megadata display/keyboard terminals for use in the Network Operations Control Center to provide additional capability.
- (3) Improve air-conditioning facilities for electronic rack cooling and Network data processing terminal.
- (4) Upgrade star switch controllers for overwrite protection.

With the upgrade of the star switch controllers, the time regression problems appeared to be corrected and all work was completed by June 1. The enhanced system now provided much-improved edit, display and format facilities and was considered capable of supporting planetary operations, with adequate margin for failures and anomalies.

II. DSN Planetary Preparation Tests

The DSN planetary preparation test effort continued at an accelerated pace during the months of May and June 1976. The DSN Operations Planning Group conducted 19 Operational Verification Tests (OVT) and Ground Data System (GDS) tests and participated in four additional project tests during the period beginning May 1, 1976, and ending June 18, 1976. The basic objectives of

OVTs and GDS tests are detailed in previous articles of this series. The tests supported were as follows:

A. DSN Tests

1. Operational Verification Test (OVT). One test of this type was conducted with DSS 43 during the first week of May for the primary purpose of increasing station operator proficiency. The other OVTs had been conducted during April. The Code 30 OVT is the standard planetary configuration test and uses the telemetry system to process six telemetry data streams from three Viking spacecraft (two Orbiters and one Lander simultaneously).

2. Automatic Total Recall System Block III (ATRS III) Operational Verification Test.

Three ATRS III OVTs were conducted with DSS 12 at Goldstone and DSS 61 in Spain during May and June. Two tests were conducted with DSS 12, the second being a retest due to equipment problems which caused the failure of the initial test. One test was conducted with DSS 61. This test was designed to test the capabilities of the Automatic Total Recall Subsystem. Test objectives included recall of data from 7-track Digital Original Data Records (DODRs) in the automatic and manual modes, plus the conversion of Analog Original Data Records (AODRs) to DODRs and replay of these DODRs.

3. Configuration Code 61/15 Operational Verification Test.

Five Code 61/15 tests were completed with 64-m DSSs during May and June. One was conducted with DSSs 14 and 43 and three were conducted with DSS 63 in Spain. The two additional tests with DSS 63 were scheduled at that station's request. The Code 61/15 OVTs are designed to simulate the configurations and procedures which will be used by a 64-m station designated as prime for Lander direct S-band link telemetry and command. The code 61 configuration uses two telemetry processing channels for Orbiter data and the remaining four for Lander direct link data. The code 15 configuration is used following the termination of the Lander direct link, using a second telemetry processor as a backup for Orbiter data.

4. Viking Orbiter Telemetry Decommunication Operational Verification Test.

This test was completed with each of the 64-m DSSs. It was requested by the Viking Project, and its primary purpose was to demonstrate the ability of the stations to use the Viking Orbiter 75 Decommunication Program to decommute and display selected engineering data words. The tests were conducted in conjunction with Viking tracking passes. Four engineering measurements were displayed at the stations and values compared in real-time with the values being dis-

played in the Viking Project Operations area. This program operates in the Digital Instrumentation Subsystem (DIS), Telemetry and Command Processor Assembly (TCP), or Simulation Conversion Assembly (SCA) computers at the DSS and would be used in the event of an emergency when the Project has lost the capability to process and display Orbiter engineering data. Key parameters would be selected with the values displayed at the DSSs being relayed to Project Operations by voice.

5. Configuration Code 1 (Modified) Operational Verification Test. This test was conducted with DSS 14 on two occasions. The code 1 (modified) configuration used the telemetry system to route Orbiter science data at data rates of 2 kb/s and lower through two telemetry strings and over a wideband data line and high-speed data line simultaneously. This provided two diversely routed transmission mediums, and in the event of a failure of the prime high-speed data line the data would continue to be transmitted to the Viking Project on the wideband data line. It will be used during Mars Orbit Insertion (MOI) of the first Viking Orbiter. DSS 14 was the prime DSS for this event.

6. Configuration Verification Tests. Configuration Verification Tests were conducted with DSSs 14, 43, and 63 in preparation for Orbit insertion of Orbiter A. These are engineering tests to verify that the configurations defined by the Network Operations Plan can be complied with and functionally checked. Following the successful completion of the CVTs, the DSSs designated as prime for MOI support (DSSs 14 and 63) were placed under configuration freeze. When the configuration freeze is applied, the stations are committed to Viking support only and can track no other spacecraft.

B. Viking Project Tests

1. Training Test Number Three (TT-3). The objective of TT-3 was to verify that the Viking Flight Team could detect and properly respond to selected spacecraft and ground data system failures or anomalous conditions which may occur during the period from separation of Mission A minus 52 hours, through separation. DSSs 43 and 63 supported this test using Configuration Code 15 with both telemetry processors initialized for Orbiter A. The second processor would be used for generating a backup Digital Original Data Record (DODR) and, in the event of a failure on the prime processor, could be redesignated as prime.

2. Ground Data System Test Number 11.0 (GDS 11.0). The primary purpose of GDS 11.0 was to test those capa-

bilities, configurations, software and procedures not previously tested. The test was conducted with DSSs 14, 43, and 63 and included:

- (1) Configuration code 61.
- (2) Configuration code 1.
- (3) Configuration code 15.
- (4) Real-time playback of Analog Original Data Record (AODR) data.
- (5) AODR-to-DODR conversion.
- (6) Use of ATRS III software for automation recall.
- (7) Production of Intermediate Data Records (IDRs).
- (8) Manual command procedures.
- (9) Tracking data for S- and X-band at all Viking-required sample rates and modes.

3. Ground Data System Test Number 11.0 Retest (GDS 11.0R). This test was scheduled due to failures during GDS 11.0 which prevented the successful completion of all test objectives. DSSs 43 and 63 were used during the retest and, for the most part, items tested were those associated with the non-real-time portion of GDS 11.0 such as AODR-to-DODR conversion and use of the ATRS III program for recall of DODR data. This retest was successful, and following its completion the GDS was certified as ready for Planetary Operations.

4. Mission Control Directorate Test (MCD). This test was requested by the Mission Control Director in order to give the Directorate personnel an opportunity to exercise procedures associated with the preseparation checkout and separation phases of the Viking mission. The test was supported by DSSs 14 and 63.

5. Operational Readiness Test Number 3 (ORT-3). The objective of this test was to demonstrate to the Viking Mission Director, the final readiness of all committed elements of the Viking Flight Operations System to support Mars Orbit Insertion of the Viking A mission. Where possible, the same personnel, hardware, software, configurations, etc., used in support of ORT-3 were to be used in support of the actual mission event. The 64-m subnet was used to support this test, with DSS 14 performing the MOI command load update and DSS 63 supporting the simulated MOI.

With the successful completion of ORT-3, the project test effort for Planetary Operations has been completed. The DSN plans to conduct two additional OVTs with DSS 14 just prior to the first direct S-band link from Lander A in order to exercise configuration code 61 and certify DSS 14 for this mission phase.

III. DSN Support of Cruise Operations

A summary of the major cruise support activities is provided in this section.

A. Significant Mission Events

Table 1 lists the significant Viking cruise activities that have been supported by the Network during the period of this report. Many of the spacecraft activities required the transmission of large numbers of commands and/or processing of multiple telemetry streams, including the highest Viking data rate (16.0 kp/s) by the stations. These activities also imposed a workload on the Network Operations Control Center (NOCC) and Ground Communications Facility (GCF) far beyond that which would be expected in a normal "quiet cruise."

B. DSS Support

While Table 1 illustrates the magnitude and complexity of the Viking mission events supported by the DSN, Table 2 depicts the extent of support provided by the Deep Space Stations in terms of the total number of passes, tracking hours, and commands transmitted. No major Network outages occurred during the reporting period.

C. Network Operations Control Center (NOCC) Operations

NOCC implementation for Viking support configuration was concluded on April 26, and all resources were assigned to accomplishment of selected enhancement features of the existing systems. The enhancement effort was completed on May 31, and the NOCC capabilities existent at that time will be under configuration control for the remainder of the Prime Viking Mission. The NOCC existing capabilities are the minimum required to meet the DSN commitment to Viking planetary operations and are considered adequate. System maturity and operator experience are contributing to increased proficiency in the operation of the NOCC on a continuous basis. Training in Intermediate Data Record (IDR) production is considered to be 100 percent complete.

D. DSN Discrepancy Report Status

Table 3 summarizes failures and anomalies in Viking committed Network resources as documented by the Discrepancy Report (DR) System during the period of January 1 through May 30, 1976. The station-dependent number is unusually high due to continued development of new capabilities which are being demonstrated for the first time in support of the Viking Project. The remaining open DRs are under active investigation and are of no immediate impact to operations.

IV. Operations Strategies for Viking I Planetary Phase

A. General

A plan has been devised by the DSN Tracking Analysis Group and coordinated with the Ops Planning Group and Viking Project for three main events of the Viking 1 planetary phase. These events are Mars Orbit Insertion, landing, and daily periapsis passages. The strategies are fully documented in the Network Operations Plan for the Viking Project and are described in lesser detail here.

1. Mars Orbit Insertion tracking strategy. In order to properly align the Viking 1 spacecraft so that its 43-min Mars Orbit Insertion (MOI) motor burn places it into the correct Mars-centered orbit, the spacecraft will go through a sequence of three turns: a roll turn, a yaw turn, and a second roll turn. The combination of the resulting geometric orientation (unfavorable cone and clock angles) and the use of the low-gain antenna will cause the loss of both the uplink and downlink signals from shortly after the start of the yaw turn until the end of the second roll turn and return to the high-gain antenna. Following the burn, the spacecraft will go through the same turns in reverse order to restore it to its original orientation.

The MOI motor burn will nominally have the following characteristics:

(1) Burn start	15:54:01 GMT
(2) Burn stop	16:37:14 GMT
(3) Magnitude (Δ)	1245 m/sec

A profile of the two-way doppler rate of change (DD2) during the burn may be seen in Fig. 1. Additionally, Figs. 2 and 3 illustrate the effect of the burn and subsequent periapsis passage on the exciter frequency (XA) (in DSS transmit time) and the two-way doppler (Earth receive time, ERT).

2. Pre-MOI burn strategy. The pre-MOI motor burn uplink strategy has been designed with the intent of acquiring the spacecraft receiver at the earliest possible time, perhaps before the switch back to the high-gain antenna, with its subsequent return of the downlink signal.

Figure 4 illustrates this tuning strategy along with a nominal time line. The procedure for a nominal burn (start time 15:54:01 GMT) is as follows:

(1) Start tuning	14:40:00 GMT	
(2) Tuning rate	0.0182 Hz/sec	Digital Controlled Oscillator (DCO)
(3) Start frequency	43993800 Hz	(DCO)
(4) Start insurance sweep	15:07:00 GMT	
(5) End insurance sweep	15:09:00 GMT	
(6) Sweep lower limit	43993730 Hz	(DCO)
(7) Sweep upper limit	43993920 Hz	(DCO)
(8) Tuning rate	2 Hz/sec	(DCO)

Because of unfavorable antenna orientation, the downlink signal level will gradually degrade to approximately -186 dBm during the yaw turn and further decrease during the second roll turn. It will be necessary then to quickly acquire the signal after the end of the roll turn in order to have solid telemetry lock throughout the Ground Data System before the start of the burn.

To accomplish this, the station will sweep the prime receiver (Receiver 3, Block IV) at a high rate, using the acquisition (ACQ) mode with the acquisition-to-zero (ATZ) signal enabled. The sweeping will start 5 min before the end of the roll turn in order to ensure receiver lock as early as possible.

3. Post-MOI burn strategy. The post-MOI burn uplink strategy consists of a single sweep at a rate of 2 Hz/sec. This sweep will effectively cover the exciter frequency (XA) plus 80 Hz and minus 50 Hz, to accommodate any trajectory uncertainties as a result of the burn. Start time of the sweep is 1 min after the start of the roll turn unwind and is coincident with the loss of downlink due to the turn.

For the nominal June 19 burn, the post-MOI burn uplink acquisition procedure is as follows:

(1) Start tuning	16:42:00 GMT	
(2) Start frequency (TSF2)	43993920 Hz	(DCO)
(3) Tuning rate	2 Hz/sec	(DCO)
(4) End frequency (TSF2)	43993640 Hz	(DCO)
(5) Sweep duration	2 min 20 sec	

The post-MOI burn tuning is shown in Fig. 2.

To insure quick acquisition whenever the downlink signal level increases to above threshold, the receiver will be swept through a region of frequencies corresponding to one-way doppler (D1) plus and minus 10 kHz at a rate of 2 kHz/sec at S-band.

Nominal time line and frequencies for June 19 were:

(1) Start sweep	17:00:00 GMT	
(2) Upper limit	44677000 Hz	(DCO)
(3) Lower limit	44676000 Hz	(DCO)
(4) Rate	100 Hz/sec	(DCO)

The post-MOI burn uplink reacquisition sweep was designed with the intent of allowing the Flight Path Analysis Group to observe the motor burn in the doppler data unperturbed by changes in the receiver reference frequency. However, if it becomes necessary to reacquire the uplink so that commands may be transmitted at the earliest possible time, the reacquisition sweep may be advanced to occur coincident with the yaw unwind (transmit time) without any change in sweep frequencies. This will, of course, obscure the signature of the burn in the doppler. Additionally, if the reacquisition sweep fails to acquire the spacecraft receiver, a second uplink sweep of plus and minus 50 Hz will be sufficient to insure acquisition.

The current plan calls for a postburn receiver acquisition sweep of frequencies corresponding to one-way doppler plus and minus 10 kHz at a rate of 2 kHz/sec at X-band. However, owing to the low signal level (-161 dBm) expected at that time, this rate will be too high to successfully acquire the downlink.

B. Lander Acquisition Strategy

1. Uplink Acquisition. Approximately 16 hours after the first Viking lander has touched down on the surface of Mars, DSS 14 will commence the initial direct link with the lander. This acquisition as well as subsequent acquisitions has the following characteristics:

- (1) The uplink acquisition will be made in the "blind."
- (2) Two receivers, each connected to a different antenna and with a 15- to 20-dB difference in signal level, are to be acquired.
- (3) There will be, initially at least, large frequency and temperature uncertainties.
- (4) The total acquisition time will be limited.

In order to accommodate these characteristics, very conservative uplink and downlink acquisition strategies have been devised. These strategies are for the initial direct communications system (DCS) link but are, for the most part, applicable to all subsequent lander DCS links. Figures 5 and 6 illustrate time lines for the short and long DCS links.

The starting frequency of the sweep will be chosen such that the start frequency and channel center frequency are in the same direction away from the receiver best lock frequency (XMTREF). Thus, for example, the initial acquisition sweep will start 470 Hz above the channel 13 center frequency (or 22010589 Hz) since the XMTREF is approximately 16 Hz above the center frequency. Upon completion of the sweep, the station will tune to a tracking synthesizer frequency (TSF) chosen to minimize the phase error in the primary command receiver during the remainder of the DCS link. $48 \text{ Hz/sec} < \text{frequency rate} < 219 \text{ Hz/sec}$ will be employed.

2. Downlink acquisition. Because of temperature and power constraints the Viking Lander S-band transmitter will be turned on for at most 92 min (for long DCS links) starting approximately 70 min after the completion of the uplink acquisition sweep. It is therefore necessary to sweep the receivers in such a manner as to quickly acquire the two-way downlink and to allow for the acquisition of a one-way downlink as a contingency.

The sweep should start approximately 5 min before the time that the downlink signal is expected to be seen. Using this high sweep rate, the entire range of frequencies will be swept approximately every 12 sec. The typical receiver sweep frequency range is given in Table 4, which provides a summary of all acquisition parameters.

V. Mars Radar Support

During this reporting period (May, June) the X-band Mars radar facility at Goldstone continued to support an intensified program of observations. The early observations continued previous coverage of the Viking "C-sites," and in June, the view periods began to cover the prime landing "A-sites." Observations were made on the following days with the results tabulated on Table 5.

During the period of these observations, the received signal level decreased significantly due to the increasing Earth-Mars range. Typical C-1 site data taken around April 10, 1976, are compared with typical A-1 site data taken two months later, on June 11 (Figs. 7 and 8).

The quality of the A-1 site observations was enhanced by the additional radar coverage provided by the S-band radar at the Cornell Radio Astronomy Observatory at Arecibo, Puerto Rico. The overlapping areas of coverage for prime A-1 and A-2 landing sites are shown in Figs. 9 and 10.

With these observations, the X-band radar support for the 1976 opportunity totalling 527 hours was concluded. The radar data were intensively analyzed by the Viking Landing Site Selection Group in its landing site selection processes. At the time the radar observations concluded on June 15, the Viking Project decided to await the first of the site certification pictures from Orbiter 1 to correlate with the Goldstone and Arecibo radar data before making the final decision on the actual landing site.

VI. Radio Science

During the months of May and June, three occultation demonstration passes were carried out with DSS 14 and 43. The first two tests on May 12 and 15 produced good data that were processed through the entire system and provided a satisfactory demonstration of end-to-end operation. The third test, on May 31, utilizing both DSS 14 at Goldstone and DSS 43 in Australia simultaneously was a failure due to procedural and predict problems. Corrective action has been taken and further tests are scheduled.

The very long baseline interferometry tests using the Viking spacecraft and a quasar (PO 735+17) had experienced tape recorder problems on five successive passes on April 18, 24, and 28 and May 3 and 7. After several unsuccessful attempts to correct the problem at the stations, it was decided that specialist help was needed, and late in June an engineer was sent to the site to investigate the problems.

Table 1. Viking significant events supported by the DSN

Date, 1976	Spacecraft	Activity
March 26	Lander 2	Inertial reference unit (IRU) No. 2 calibration
27	Orbiter 1	High-gain antenna (HGA) calibration
April 11	Orbiter 1	Software update
12	Orbiter 1	Scan calibration No. 2
14	Orbiter 2	Software update
15	Orbiter 2	Scan calibration No. 2
16	Orbiter 2	Visual Imaging Subsystem (VIS) picture playback and Lander 2 maintenance
17	Orbiter 1	VIS playback
17	Lander 1	Battery charge and tape recorder maintenance
18	Orbiter 2	VLBI with Orbiter 2 and quasar source
20, 21		Demonstration Test No. 4 (DT-4)
23, 24	Lander 1	ICL update
23-26	Lander 1	Battery conditioning sequence
26-29		Training Test Number 5 (TT-5)
May 1, 2	Orbiter 1	Photo calibration and playback sequences
3		TT-3
3	Orbiter 2	Quasar VLBI
5-7	Orbiter 1	ICL update and battery conditioning sequence
8	Orbiter 1	IRTM playback
8, 9, 11	Orbiter 1	Photo calibration 2 playback
12	Orbiter 2	MAWD calibration
13, 14	Lander 1	Battery conditioning sequence
15-18	Lander 2	Battery conditioning sequence
17-20	Orbiter 1	ONS No. 1
19-20	Lander 1	Battery conditioning sequence
21	Lander 1	Battery conditioning
21, 22	Orbiter 2	16 kbs playback
23-26	Lander 2	Battery conditioning
24, 25	Orbiter 2	16 kbs playback
25	Orbiter 1	Gyro and accelerometer calibration

Table 2. DSS support of Viking cruise operations

Month, 1976	DSS	No. of passes	Hours tracked	Commands transmitted
April	11	33	223:39	392
	12	33	236:42	588
	14	1	08:38	20
	42	32	164:03	0
	43	0	0	0
	44	29	194:04	9
	61	33	241:07	45
	62	7	69:43	0
	63	23	208:53	2206
Monthly total:	191		1846:49	3260
May	11	29	217:40	753
	12	25	176:47	490
	14	11	69:37	15
	42	30	214:12	9
	43	24	184:32	574
	44	9	62:27	447
	61	32	281:24	233
	62	4	36:44	28
	63	28	287:55	6274
Monthly total:	192		1531:18	8823
Report total:	383		2878:07	12,083

ORIGINAL PAGE IS
OF POOR QUALITY

ORIGINAL PAGE IS
OF POOR QUALITY

Table 3. Viking DR summary matrix: January 1, 1975–May 30, 1976

	DSS										DSN	GCF	NDPA	NOCA	total	%
	11	12	14	42	43	44	61	62	63	71	5	27	51	45		
Resolution Station- dependent	25	36	118	84	89	22	28	25	86	16	5	27	51	45	607	84.4
Station- independent	4	7	10	7	3	0	2	4	6	1	4	7	13	14	82	11.4
Other or unavoidable	2	2	2	0	1	0	0	1	0	1	14	4	1	2	30	4.2
Total DRs closed	31	45	130	41	93	22	30	30	92	18	23	38	65	61	719	
Total DRs generated	43	47	136	48	100	22	30	30	120	18	27	40	123	70	854	
DRs opened as of May 30, 1976	12	2	6	7	7	0	0	0	28	0	4	2	58	9	185	

Table 4. Receiver sweep frequency range

Uplink acquisition sweep	
TXR on	18:24:00 GMT
TXR power	20 kW
Frequency	44022654.0 Hz
Start tuning (time ϕ)	18:24:36 GMT
Tune to	44020773.0 Hz
Tuning rate (rate ϕ)	-1.0000 Hz/sec
Time (time 1)	18:55:57 GMT
Tune to TSF	44021700.0 Hz
Tuning rate (rate 1)	+1.0000 Hz/sec
Stop tuning (time 2)	19:11:24 GMT
CMD MOD on	19:12:00 GMT
RNG MOD on	20:35:00 GMT
Sweep duration	46 mins 48 sec
Downlink acquisition sweep	
Start sweep	20:24:00 GMT
Sweep upper limit	44752749.0 Hz
Sweep lower limit	44751349.0 Hz
Sweep rate	100 Hz/sec
Ranging parameters	
T_ϕ	21:12:02 GMT
T1	9 sec
T2	9 sec
T3	10 sec
RTLT	36 mins 38 sec
Components	15

Table 5. Goldstone X-band Mars radar observations

Observation date, 1976	Site	Data quality
May 10	Terrain calibration	Partial pass given to Helios
12	Terrain calibration	Good data
14	Terrain calibration	Good data
19	Terrain calibration	Good data
26	Terrain calibration	Good data
29	A-1	Good data
30	A-1	
31	A-1	Good data
June 1	A-1	No pass
2	A-1	No pass due to ORT-3 support
3	A-1	Good data
4	A-1	Good data
5	A-1	Good data
6	A-1	Good data
7	A-1	Good data
8	A-1	Bad data due to transmitter problem
9	A-1	No pass due to midcourse maneuvers
10	A-1	No pass due to optical nonsupport
11	A-1 & A-2	Good data
12	A-2	Good data
13	A-2	Partial pass, good data
14	A-2	Partial pass, good data
15	A-2	No data due to transmitter failure

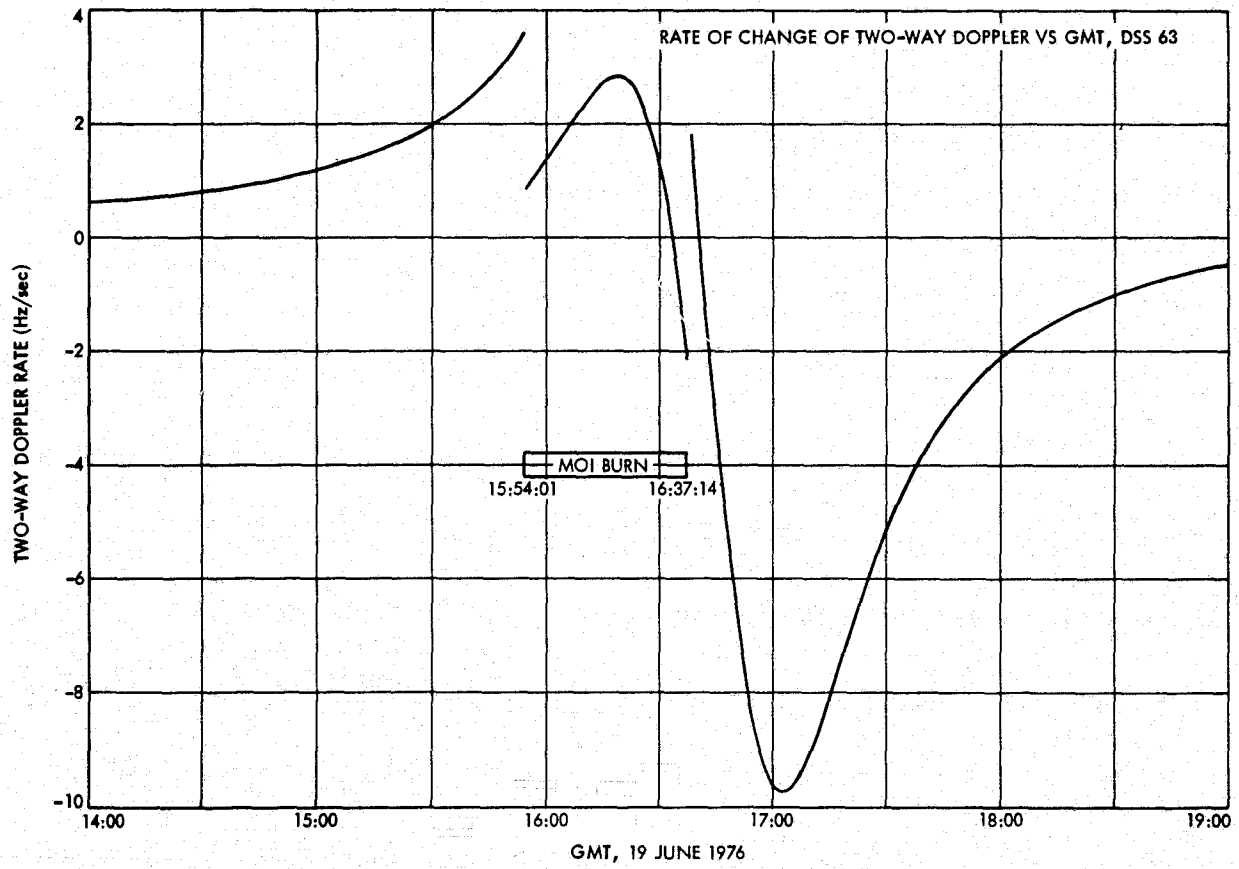


Fig. 1. Rate of change of two-way doppler vs GMT, DSS 63

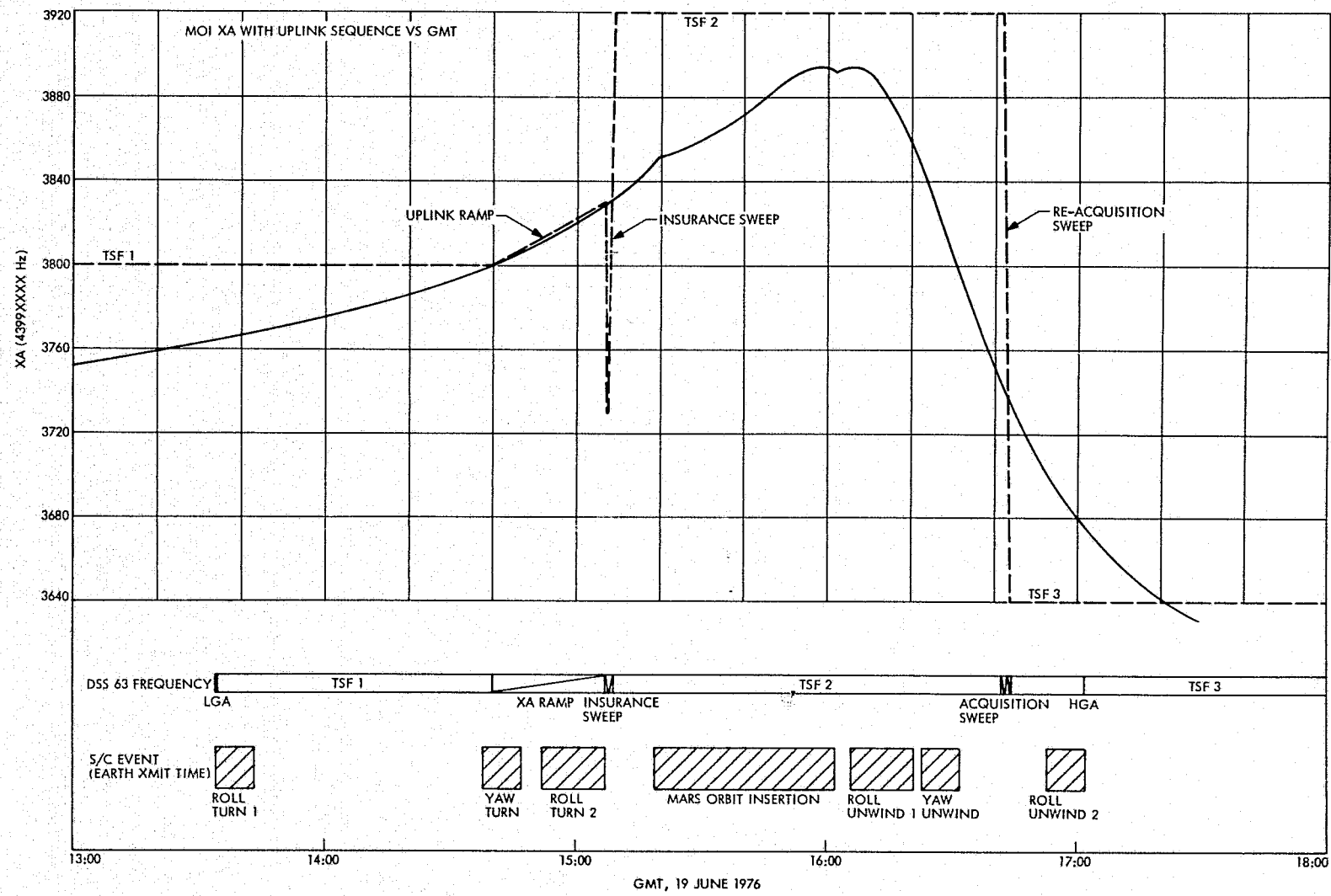


Fig. 2. Mars Orbit Insertion XA with uplink sequence vs GMT

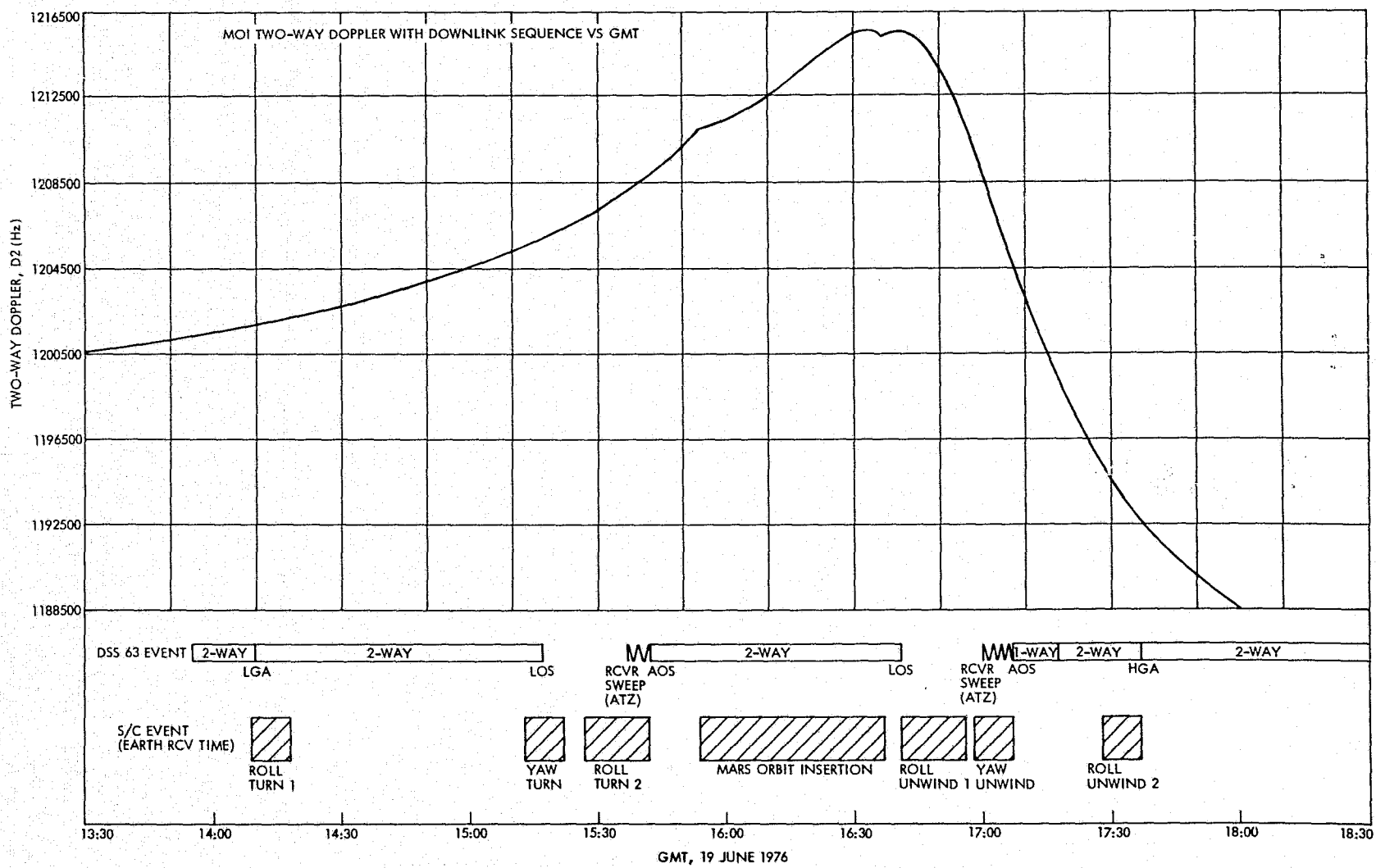


Fig. 3. Mars Orbit Insertion two-way doppler with downlink sequence vs GMT

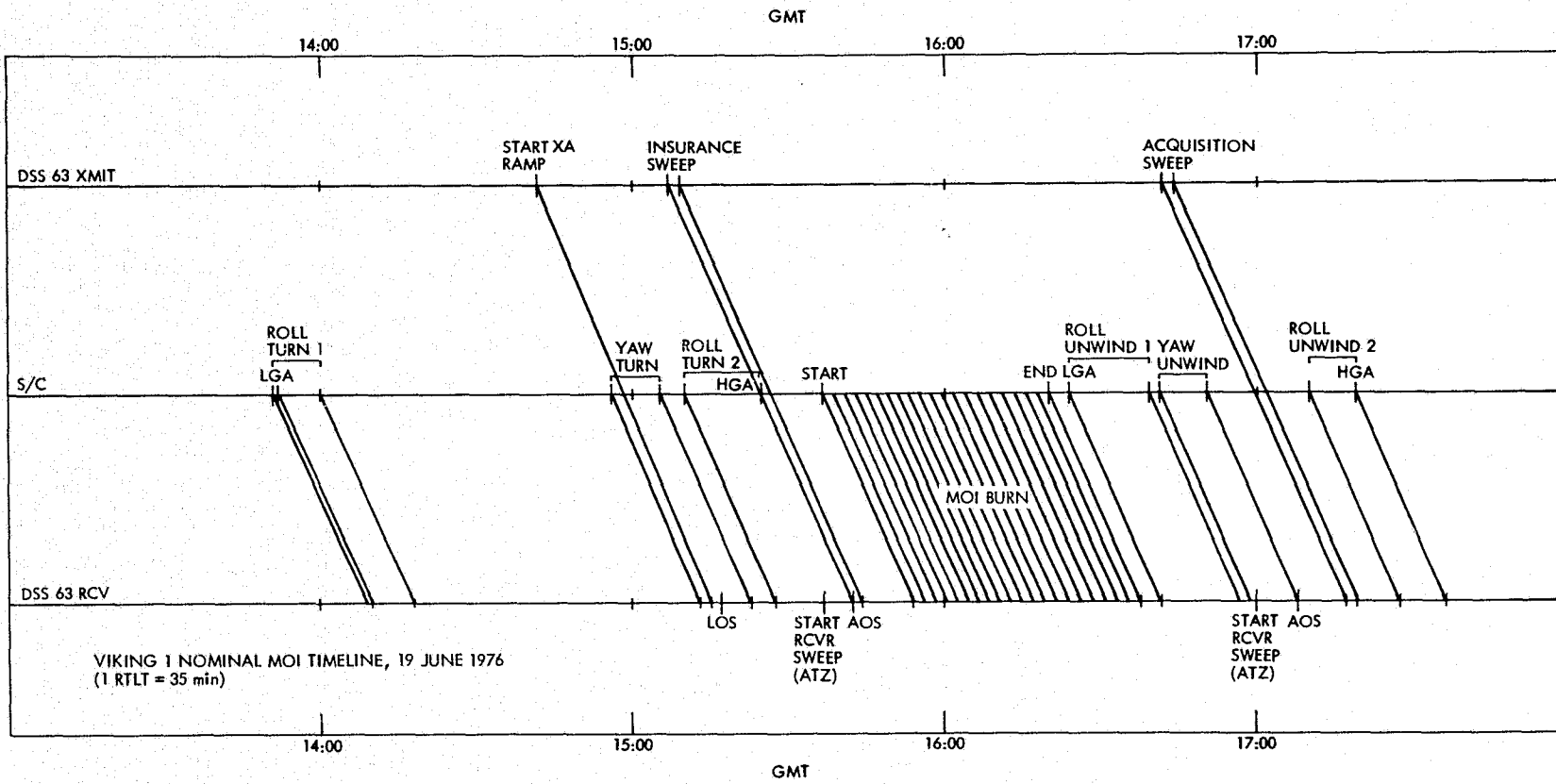


Fig. 4. Viking 1 nominal Mars Orbit Insertion timeline, June 19, 1976

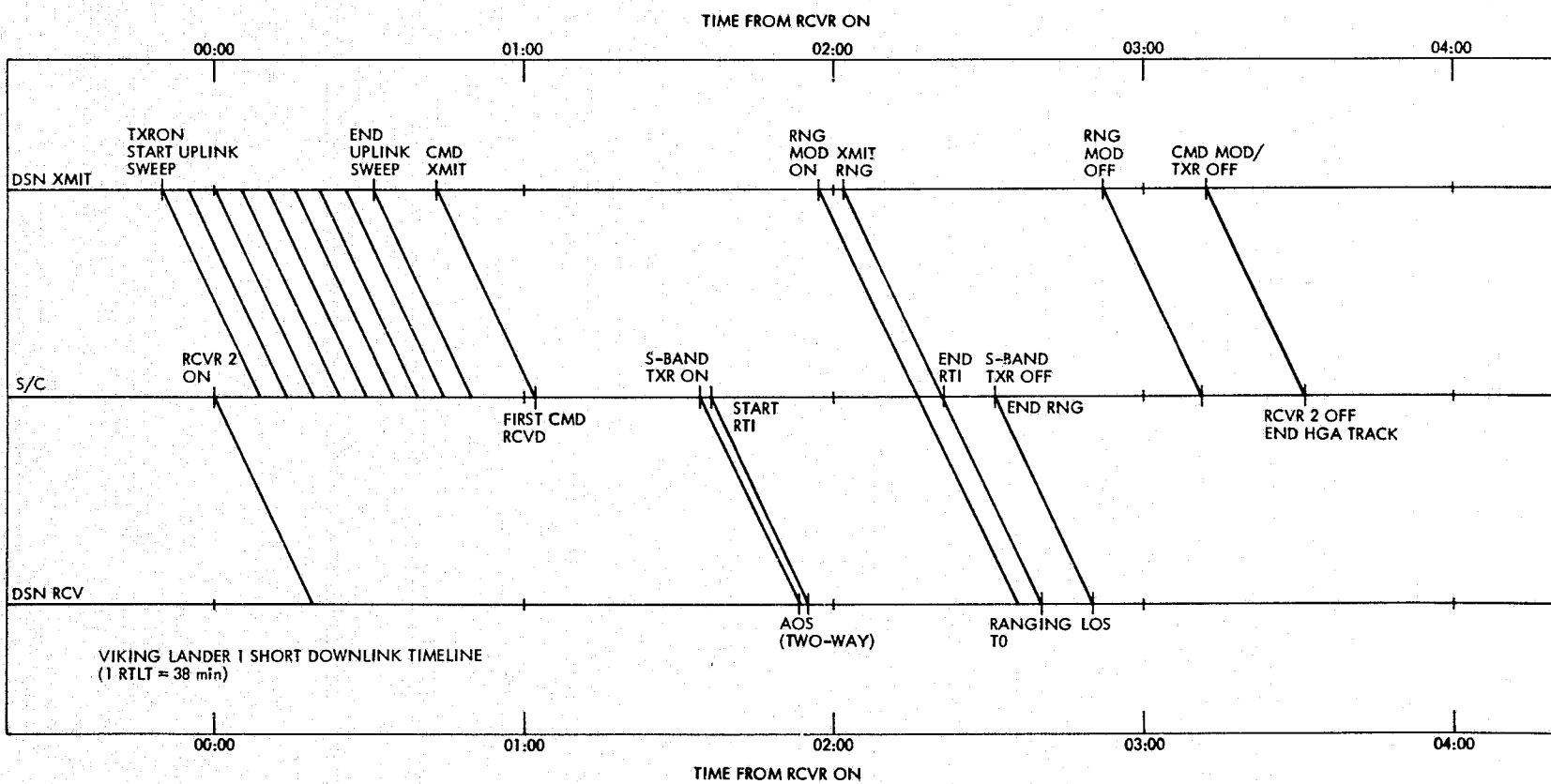


Fig. 5. Viking Lander 1 short downlink timeline

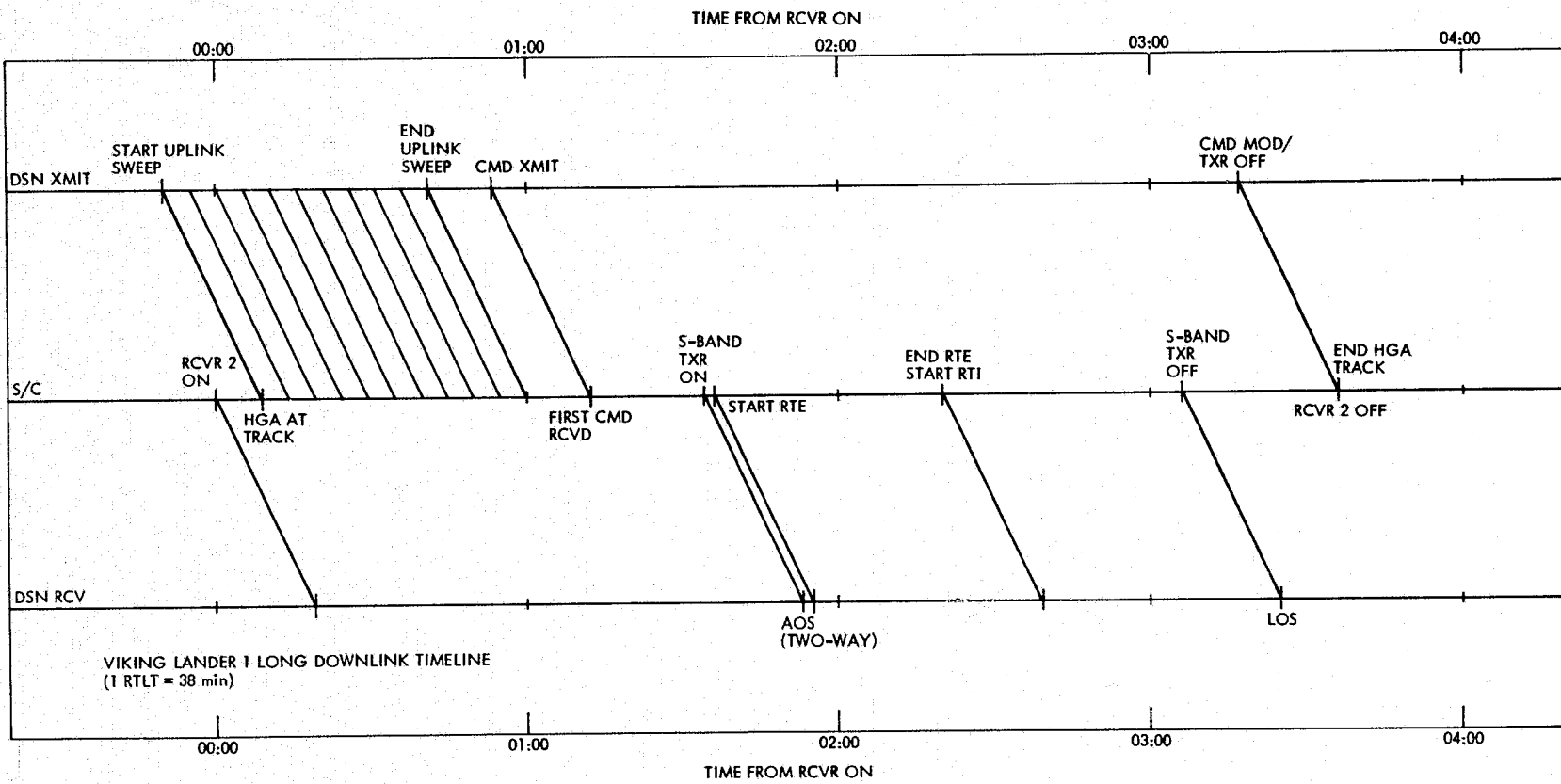


Fig. 6. Viking Lander 1 long downlink timeline

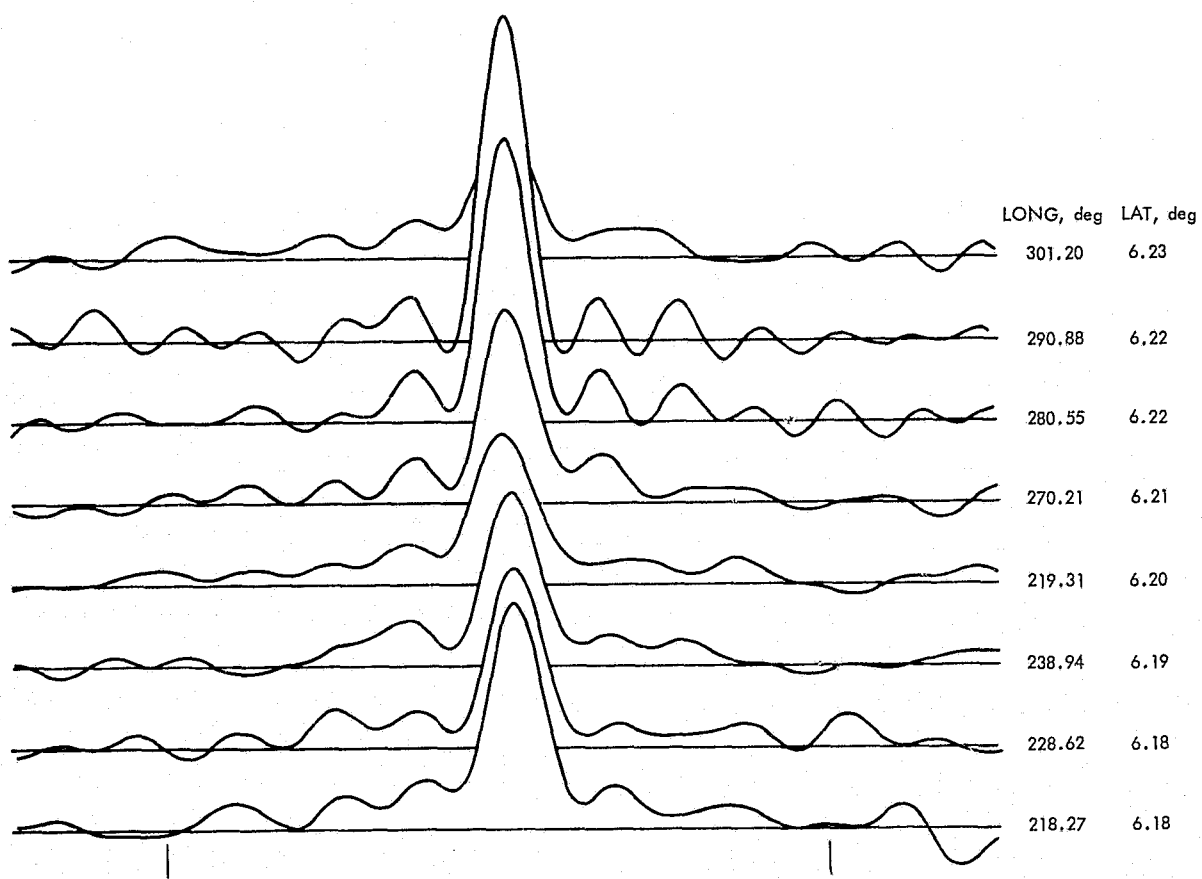


Fig. 7. X-band radar spectra from the Viking C-site observations of April 19, 1976

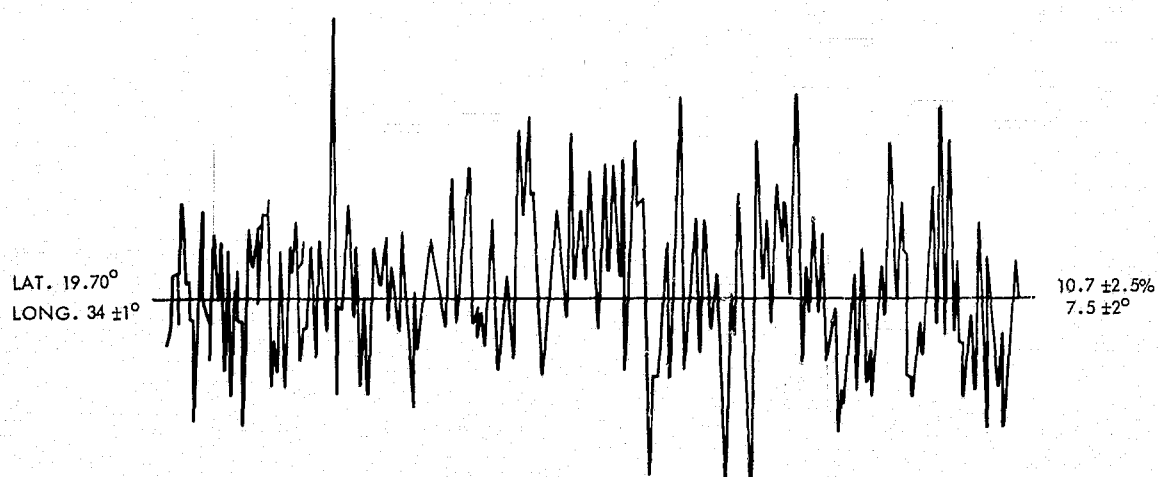


Fig. 8. X-band radar spectra from the Viking A-site on June 11, 1976

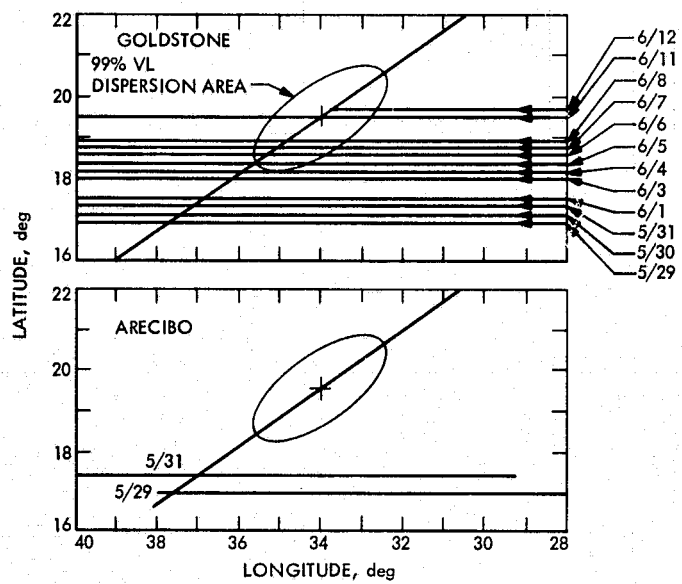


Fig. 9. A-1 radar observations, May–June 1976

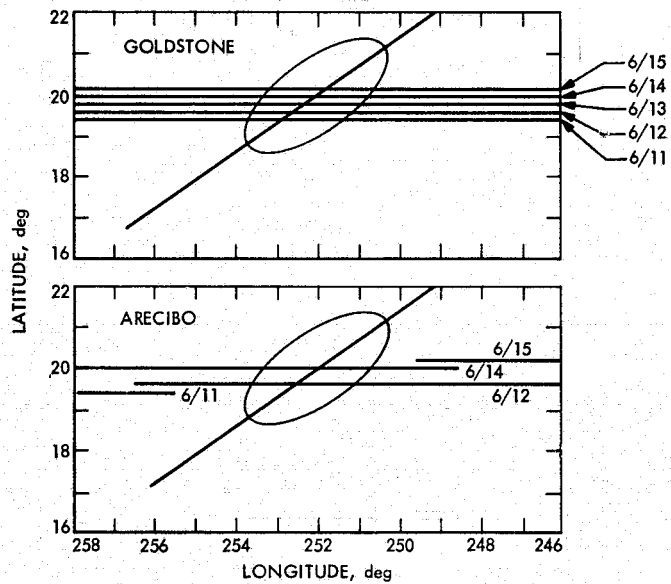


Fig. 10. A-2 radar observations

N 76-29321

Helios Mission Support

P. S. Goodwin

DSN Systems Engineering Office

W. G. Meeks and R. E. Morris

Network Operations Office

The successful flight of the Helios-1 spacecraft continues as it approaches its third aphelion. The Helios-2 spacecraft has entered its first superior conjunction and continues in excellent health. Much valuable scientific information about the solar corona and its effects on electromagnetic waves is expected to be learned from data gathered during this superior conjunction.

I. Introduction

This is the tenth article in a series that discusses Helios-1 and -2 mission support. The previous article (Ref. 1) reported on Helios-1 third perihelion, Helios-2 first perihelion, spacecraft Traveling Wave Tube (TWT) and ranging anomalies, and Helios DSN-Spaceflight Tracking and Data Network (STDN) cross-support activities. This article covers Helios-1 cruise phase, Helios-2 first solar occultation, Helios DSN-STDN cross-support status, DSN-STDN engineering test results, and DSN performance.

II. Mission Operations and Status

A. Helios-1 Operations

Now that Helios-2 has joined Helios-1 in orbit about the sun, data (experiment) comparisons can be made at times

of interest along their respective trajectories. Two points of interest occurred during this reporting period: radial line-up on 3 May 1976 and spiral line-up between 8-13 May 1976.

Radial line-up occurs when the two spacecraft and the sun lie in a straight line. This alignment is important in gathering data about solar winds that emanate from the sun in straight paths (radii) through space. The sun also emits electromagnetic waves that travel spiral paths from the sun. When the two spacecraft happen to be along one of these paths they are said to be in spiral alignment. Correlation can then be made with the magnetic experiments data.

Helios-1 is approaching its third aphelion (2 July 1976) cruise phase. It is radiating data in the high-power mode from the high-gain antenna and is operating well with one

exception. The ranging transponder is inoperative (see Subsection III-B).

B. Helios-2 Operations

The Helios-2 spacecraft entered its first solar superior conjunction (sun-Earth-probe angle < 5 deg) on 4 May 1976, thereby completing its primary mission. Solar occultation (spacecraft behind the sun) occurred on 16 May. The sun-Earth-probe (SEP) angle will remain less than 5 deg until approximately 6 October 1976. This superior conjunction phase is of extreme interest to spacecraft experiments 11 and 12 (Celestial Mechanics and Faraday Rotation, respectively). Plans to gather special spacecraft telemetry and DSN performance data pertinent to these experiments have been initiated. The Helios radio science team, located at JPL, has been active in planning and coordinating special operational activities to assemble and analyze spacecraft data relative to these two experiments.

For the enhancement of certain spacecraft data, the high-power transmitter at Goldstone (DSS 14) was requested and authorized for specific dates during the superior conjunction.

Ranging data obtained by the Mu_2 ranging equipment during Helios-2 entrance into solar occultation clearly indicates the superiority of the Mu_2 over the Planetary Ranging Assembly (PRA) at small SEP angles. Due to the Helios-2 trajectory having small SEP angles until the late October 1976 second perihelion, it is highly desirable to maintain the Mu_2 system at DSS 14 until that time.

As reported in the last report (Ref. 1), the Helios-2 spacecraft had experienced TWT anomalies—"out of limit" helix current conditions—during the month of April 1976. After extensive testing by Messerschmitt-Bolkow-Blohm (MBB) and Watkins-Johnson engineers, the TWT final current limits were redefined. On April 29 at 1430 GMT, the Helios-2 TWT-2 was switched to the high-power mode and, after settling time, the TWT-2 helix and collector current values were within the newly defined limits and have since remained there.

The Helios-2 spacecraft continues to operate in a nominal manner, on high-power, high-gain antenna; it is spin stabilized at 60.53 r/min.

C. Spaceflight Tracking and Data Network (STDN) Cross-Support

The STDN-Madrid station supported project Helios from 15 January through 9 April, when the downlink signal level reached recording threshold. The STDN-

Goldstone station supported from 6 April until 5 May, when support was terminated by Project management. Evaluation of the STDN-Goldstone recorded data (after processing and playback from the DSN equipment at the Spacecraft Compatibility-Monitor Station (STDN (MIL-71)) showed an average loss of approximately 8-10 dB when compared to a DSN 26-meter station. This means that the spacecraft would have to operate at 1/8 the data rate achievable at a DSN station to obtain the same data quality from analog tapes recorded at a STDN station.

According to management guidelines established before the DSN-STDN cross-support was initiated, this performance was considered marginal.

The Helios project management terminated the STDN cross-support in the analog tape record-only mode for Helios on 5 May 1976. This decision was reached at a Helios Operations Status Review conducted at JPL on 4 and 5 May 1976. The overriding reason for this decision was an announcement that the German Telecommand Station at Weilheim would be modified in the fall of 1976 to include a telemetry data receiving capability. This station would be dedicated to Helios support. The additional telemetry coverage offered by a dedicated German station, coupled with the capability to store data aboard the spacecraft for subsequent dump during a later tracking period, makes the practicality of a "record-only mode" (with its attendant losses and built-in time lag) questionable. Project management decided, however, to continue engineering tests to evaluate the use of a microwave link between an STDN and a DSN station for real-time telemetry processing and commanding. A project decision on whether to request use of the Goldstone STDN-DSN real-time microwave link configuration to support Helios perihelion operation in October 1976 was deferred until later (September), pending results of the engineering evaluation.

D. DSN-STDN Engineering Test Results

Because the Goldstone intersite microwave link used to support Apollo has been removed, the first Helios Engineering tests were conducted at Spain between STDN-Madrid and Deep Space Station (DSS) 62. Meanwhile, efforts to restore the Goldstone STDN-DSN microwave link were started.

A real-time Telemetry Engineering test was successfully performed at Madrid on 21 April 1976. After establishing the microwave configuration and adjusting levels, a 32.768-kHz subcarrier modulated with simulated Helios data was sent from DSS 62 to STDN-Madrid to modulate their test transmitter. The receiver baseband signal was returned via

the microwave link and successfully processed at DSS 62 in their Telemetry and Command Data (TCD) handling equipment. This was followed on 22 April by a test that provided live Helios-1 spacecraft telemetry from STDN-Madrid via microwave for simultaneous processing and comparison with DSS 62 telemetry data. The signal-to-noise ratio (SNR) difference was a minus 8.3 dB for the STDN telemetry.

The success of the Madrid STDN-DSN real-time telemetry engineering test led to a similar test of command performance. On 27 May, the stations were configured so that the DSS 62 Command Modulator Assembly (CMA) would modulate the STDN-Madrid station's uplink carrier while the Helios downlink telemetry was received and processed by DSS 62 only. The Helios-1 spacecraft commands were generated, executed, and monitored from the German Space Operations Center (GSOC). Twenty-eight commands were successfully sent to the Helios-1 spacecraft via the STDN-Madrid transmitter.

By May 18, 1976, the Goldstone STDN-DSN combined coaxial line and microwave link had been established one-way (STDN-to-DSN). With the Madrid engineering test as a model, a real-time telemetry engineering test was performed on 3 June 1976. The Goldstone STDN, using a Block III receiver, received the Helios-1 telemetry subcarrier and forwarded this to the DSS 12 TCD. Simultaneously, DSS 12 tracked Helios-1. The STDN telemetry performance was now only 4.5 dB below the DSN, due to improvements in the STDN station configuration. Other Goldstone STDN-DSN real-time telemetry engineering tests are planned to provide more data points to evaluate the DSN-STDN real-time cross-support configuration.

Parallel studies are being made to expand the Goldstone Helios tests to include simultaneous telemetry and command capability.

E. Actual Tracking Coverage Versus Scheduled Coverage

This report covers tracking activities for a 56-day period from 12 April through 6 June 1976, for the Helios-1 and -2 spacecraft. Operations during this period include Helios-1 cruise and Helios-2 first perihelion and first solar occultation. Both spacecraft were tracked a total of 197 times for a total of 1542.4 hours. Because this time period included part of Helios-2 prime mission and critical mission phases (perihelion and solar occultation), total Helios coverage exceeded that of Pioneer by almost 400 hours. Helios-1 was tracked 96 times for a total of 730 hours. This represented a 3-percent increase in coverage

over the last report period. The average pass duration for Helios-1 was 7.6 hours compared to 5.6 hours last period. Helios-2 was tracked 101 times for a total of 812.1 hours with an average track time of 8 hours. Prime mission coverage requirements were met 100 percent. Helios-2 perihelion and occultation coverage was supported by the 64-meter stations at Canberra and Goldstone, accounting for approximately 65 percent of the total DSN Helios-2 support.

The Spaceflight Tracking and Data Network (STDN) provided 20 hours of Helios telemetry recording support this period before being terminated on 5 May 1976.

Helios-1 and -2 spacecraft, now in extended mission phase, have equal priority with Pioneers 10 and 11 spacecraft. With Viking planetary activities in the spotlight during the next few months, only limited DSN support is expected for Helios.

III. DSN System Performance

A. Command System

Owing to the Helios-2 prime mission (when the DSN provided 100 percent tracking coverage) coming to an end during mid-May, there has been a marked decrease in the number of commands radiated to the Helios spacecraft when compared to the last report period. A total of 7331 commands were processed for both Helios spacecraft. This represents a 30-percent decrease in command activity over the last report period. The cumulative command totals now stand at 36,593 for Helios-1 and 13,173 for Helios-2.

Two command system aborts were reported for April and three for May, 1976—three with Helios-1 and two with Helios-2. Three of the five aborts were associated with station transmitter failures. The other two were associated with command alarms that did not clear. Two of the aborts occurred at DSS 14, but for different reasons. This station has provided the majority of Helios-2 support since entering superior conjunction in early May. These raise the cumulative command system abort count to eleven for Helios-1 and four for Helios-2.

For the months of April and May, command system downtime dropped to 18 hours and 55 minutes, or an approximate 27-percent decrease over the last period. Only two outages exceeded one hour (the biggest being 2.5 hours). Although it does show a decrease over the last report period, command system downtime was still high when compared to earlier periods.

B. Tracking System

The Helios-1 spacecraft ranging transponder again failed to respond on 26 April 1976. This spacecraft anomaly, associated with the transponder Very Stable Oscillator (VSO) temperature, has occurred twice before (see Ref. 1). The last valid Helios spacecraft ranging data were received on 9 April 1976. This anomalous condition is expected to last until September, when the transponder VSO temperature will again come within operational limits.

With the Helios-2 spacecraft's first superior conjunction, renewed and intense interest on the part of the Helios radio science experimenters resulted in special measures to assure the quality of the ranging acquisitions. These special tests and procedures included "receiver ramping" for each DSS 14 pass during the weeks immediately before and after the first spacecraft occultation (16-17 May 1976). This was done to obtain quality ranging data at the lowest possible SEP angles. The results of these efforts were that valuable ranging data were obtained at a lower SEP angle than before—less than 0.9 deg.

C. Telemetry System

Helios-2 entered its first solar conjunction on DOY 125, May 4, 1976, (SEP angle < 5.1 deg) and will exit on DOY 280, 6 October 1976. This mission period holds special interest to experiments 11 and 12 and also to the DSN. The DSN's interest lies in the answers to two questions: (1) what is the increase in system noise temperature due to the small SEP angles, and how does it compare to past solar conjunctions? and (2) to what extent are the signal level (AGC) and signal-to-noise-ratio (SNR) affected by the small SEP angles, how well can this be predicted, and what radio frequency (RF) and SDA bandwidths are best for minimizing degradation? To provide answers to these questions, special data types are being collected. The first type of data consists of special system noise temperature chart recordings; the second type is the results of spectral broadening tests. A plan (Table 1) to gather and analyze these data types was instituted and shall continue throughout the solar conjunction period (4 May through 6 October 1976).

Based on analysis of similar data collected during Helios-1 and -2, inferior conjunction (Ref. 1) predictions of

the signal level and SNR were made through 1 July 1976. A preliminary "quick look" analysis of May data from Helios-2 superior conjunction shows signal level and SNR degradation very close to predicted values. One exception to this is 8 bit-per-second coded data from 64-meter stations. These data have been erratic. The cause, to date, is unknown but is under investigation. A report (quick-look) of May and June data collected on the Helios-2 spacecraft superior conjunction is expected in late July 1976, from the Network Analysis Group.

Updated Helios-2 spacecraft downlink parameters, recently received from the Helios project, have been factored into the telemetry predicts program Link Analysis Prediction Program (LAPP) resulting in values closer to actual measurements. Helios-1 telemetry predicts have yet to be corrected with updated parameters.

IV. Conclusions

The Helios-1 spacecraft has continued on its trajectory recording scientific data and reading-out these data on command. The Helios-2 spacecraft completed its prime mission in which it enjoyed 100-percent tracking coverage. This prime mission, although as successful as that of Helios-1, did have its TWT anomalies. With these problems now passed, the Helios-2 spacecraft is experiencing its first superior conjunction.

The "Record Only" STDN cross-support was terminated as of 5 May 1976; however, STDN-DSN engineering tests are being performed to determine the practicality of using an STDN-DSN microwave link to send Helios spacecraft data in real time to a DSN station for processing. The results of these tests will determine if the STDN cross-support for Helios is to be requested to support the October perihelion of Helios-2. It is anticipated that the testing will be completed by 1 July 1976.

Special operational and analysis support activities to support the Helios-2 superior conjunction mission phase are in progress and shall continue throughout. Results on some of the data analysis (DSN performance at low SEP angles) is expected within the next report period.

Acknowledgments

The authors wish to thank the following members of the Network Operations Analysis Group for their contribution of periodic Network Performance Reports:

Command:	R. Gillette, W. L. Tucker
Telemetry:	R. Allis, G. LeMasters, C. Lunde
Tracking:	A. L. Berman, R. S. Schlaifer, L. Bright

Reference

1. Goodwin, P. S., "Helios Mission Support," in *The Deep Space Network Progress Report 42-33*, pp. 26-30. Jet Propulsion Laboratory, Pasadena, California, July 15, 1976.

Table 1. Helios-2 superior conjunction overview

Event	DOY	Time ^a
Begin data collection	125	(First pass)
Expected first degradation	126	
Begin blackout (first)	135	(Variable)
Minimum SEP angle (1st minimum)	137	1500Z
End blackout (first)	141	(Variable)
Begin blackout (second)	185	(Variable)
Minimum SEP angle (2nd minimum)	192	2200Z
End blackout (second)	200	(Variable)
Begin blackout (third)	267	(Variable)
Minimum SEP angle (3rd minimum)	269	1400Z
End blackout (third)	271	(Variable)
Expected end of degradation	278	
End data collection	280	(Last pass)

^aTimes are variable, depending on coverage (64-meter, or 26-meter, or STDN coverage).

**ORIGINAL PAGE IS
OF POOR QUALITY**

Foldover Effects on Viterbi Decoding

J. K. Omura¹ and S. A. Butman
Communications Systems Research Section

Viterbi decoding of X-band Mariner Venus-Mercury 1973 (MVM'73) spacecraft data using both a hardware Viterbi decoder and a software Viterbi decoder resulted in a significant and previously unexplained difference in decoded bit error rates. This difference is explained by foldover effects which arose when the 6-bit recorded data were reduced to the required 3-bit decoder input data in the hardware Viterbi decoder.

I. The Problem

On January 15, 1974, X-band convolutionally coded telemetry data were transmitted from the MVM'73 spacecraft and recorded at the Goldstone 64-m station. The purpose of the experiment was to use an in-flight spacecraft and an operational Deep Space Station (DSS) to demonstrate that X-band high-data-rate convolutionally coded telemetry data can be reliably transmitted according to the predicted theoretical performance.

The signal transmitted by the MVM'73 spacecraft was a periodic sequence consisting of repetition of bits 1 1 1 0 1 0, which corresponds to a periodic sequence of data bits 1 0 0 convolutionally encoded by a constraint length $v = 7$, rate $r = 1/2$ encoder. A hardware Viterbi decoder was employed on the recorded data and the decoded bit error probabilities were computed over a range of decoded bit signal-to-noise ratio E_b/N_0 of approximately 3 dB to 5 dB. Later the same recorded data were decoded using a software decoder that performed

the same Viterbi decoder operations. The hardware decoder experimental results and the software decoder experimental results based on the same X-band convolutionally coded telemetry data are shown in Fig. 1.

At $E_b/N_0 = 4$ dB, which is about the middle value of the experimental signal-to-noise ratio range, we see that the Linkabit decoder experiment had 42 times more bit errors than the predicted theoretical performance while the software decoder bit error rates agreed closely with the predicted theoretical performance. The problem is then to explain the large difference between two decoder experiments where both are apparently performing the same operations on the same X-band data.

II. Coded Data Reduction

The coded bits transmitted by the MVM'73 spacecraft appeared as telemetry sidebands of the X-band carrier. Reception of the signals was accomplished using the Block IV receiver system, and the recorded data consisted of the SSA matched filter output quantized with a sign bit plus 5 magnitude bits.

¹Consultant, University of California at Los Angeles.

The hardware Viterbi decoder accepts only 3-bit quantized (8 levels) data as inputs. With proper quantization spacing, performance with this 3-bit quantization has been shown to be within 0.25 dB in signal-to-noise ratio of the performance achievable with infinite quantization (Ref. 1). This is often referred to as "soft decision" decoding and the coding channel is modeled as a discrete memoryless channel with two input symbols and 8 output symbols. With about 2 dB degradation Viterbi decoding can be done using only the sign bit or one-bit quantized data (Ref. 2). The resulting "hard decision" coding channel is called a binary symmetric channel.

In the experimental results of Fig. 1, both decoders used 3-bit quantized data as inputs. It was discovered that there was an apparently small difference in how the 6-bit recorded data were converted to 3-bit decoder input data for the two experiments. Let $x_1, x_2, x_3, x_4, x_5, x_6$ be the 6 bits of any recorded data sample, where x_1 is the sign bit and the remaining 5 bits are magnitude bits with x_2 being the most significant and x_6 being the least significant. To achieve a good 3-bit quantization spacing, the least significant bit required was x_4 . Hence x_5 and x_6 were not used. There remained the problem of reducing 4-bit data x_1, x_2, x_3, x_4 to 3 bits.

In the 4-bit data the bits x_1, x_2, x_3, x_4 correspond to one of 16 uniformly spaced amplitudes as follows:

x_1	x_2	x_3	x_4	Amplitude
1	0	0	0	-8
1	0	0	1	-7
1	0	1	0	-6
1	0	1	1	-5
1	1	0	0	-4
1	1	0	1	-3
1	1	1	0	-2
1	1	1	1	-1
0	0	0	0	1
0	0	0	1	2
0	0	1	0	3
0	0	1	1	4
0	1	0	0	5
0	1	0	1	6
0	1	1	0	7
0	1	1	1	8

The recorded 4-bit data distribution is shown in Fig. 2 where we separate the empirical distribution due to coded transmitted "one" bits and "zero" bits. There was a total of 1,752,001 samples used to obtain these distributions. This corresponds to signal-to-noise ratios from 3 to 5 dB. We did not obtain separate distributions for more limited ranges of signal-to-noise ratios.

In reducing the 4-bit data to 3-bit data the two experiments performed the following reductions:

Hardware decoder:

$$\begin{array}{cccc} \text{recorded 4-bit data} & & & \text{decoder input data} \\ x_1 & x_2 & x_3 & x_4 \end{array} \Rightarrow \begin{array}{ccc} x_1 & x_3 & x_4 \end{array}$$

Software decoder:

$$\begin{array}{cc} \text{recorded 4-bit data} & \text{decoder input data} \\ \text{if } x_1 = x_2 & \Rightarrow x_1 \ x_3 \ x_4 \\ \text{if } x_1 = 0, x_2 = 1 & \Rightarrow 0 \ 1 \ 1 \\ \text{if } x_1 = 1, x_2 = 0 & \Rightarrow 1 \ 0 \ 0 \end{array}$$

Here the decoder input data correspond to 8 uniformly spaced amplitudes as follows:

Decoder input bits	Amplitude
1 0 0	-4
1 0 1	-3
1 1 0	-2
1 1 1	-1
0 0 0	1
0 0 1	2
0 1 0	3
0 1 1	4

Note that the only difference in these two coded data reductions appears when $x_1 \neq x_2$. The fraction of data samples where this occurred was measured and found to be

$$Pr\{x_1 \neq x_2\} = 0.30678 \quad (1)$$

When $x_1 \neq x_2$, the hardware decoder reduction "folds over" the 4-bit data by converting large amplitudes of the 4-bit data to 3-bit data amplitudes as follows:

4-Bit Data Amplitude		3-Bit Data Amplitude
-8	⇒	-4
-7	⇒	-3
-6	⇒	-2
-5	⇒	-1
5	⇒	1
6	⇒	2
7	⇒	3
8	⇒	4

The resulting 3-bit hardware decoder input amplitude distributions are shown in Fig. 3. The software decoder reduction essentially truncates the large 4-bit data amplitudes so that amplitudes -8, -7, +6, and -5 of the 4-bit data are converted to amplitude -4 of the 3-bit data. Similarly, amplitudes 8, 7, 6, and 5 are converted to amplitude 4. These 3-bit software decoder input amplitude distributions are shown in Fig. 4.

III. Analysis

For any binary input channel which has output denoted y we can define probability distributions $P_+(y)$ and $P_-(y)$ corresponding to a "zero" channel input bit (+) and a "one" channel input bit (-) respectively. For any such channel and the $v = 7$, $r = 1/2$ convolutional code, the decoded bit error probability P_b is bounded by (Ref. 2)

$$P_b \leq \frac{\partial T(D, I)}{\partial I} \Big|_{I=1, D=D_0} = 36 D_0^{10} + 211 D_0^{12} + 1404 D_0^{14} + 11633 D_0^{16} + \text{higher powers of } D_0 \quad (2)$$

where

$$D_0 = \sum_y \sqrt{P_+(y)P_-(y)} \quad (3)$$

First without any quantization, when "zero" is sent over the white Gaussian noise channel the matched filter output is assumed to be a Gaussian random variable with mean $A = \sqrt{E_s} = \sqrt{E_b/2}$ and variance $\sigma^2 = N_0/2$. When "one" is sent the mean is $-A$. For this unquantized case we have

$$P_+(y) = \frac{1}{\sqrt{\pi N_0}} e^{-\frac{(y-A)^2}{N_0}}; \quad \text{all } y$$

$$P_-(y) = \frac{1}{\sqrt{\pi N_0}} e^{-\frac{(y+A)^2}{N_0}}; \quad \text{all } y \quad (4)$$

and

$$D_0 = e^{-\frac{A^2}{N_0}} = e^{-\frac{E_b}{2N_0}}. \quad (5)$$

For the 4-bit data distribution shown in Fig. 2 we obtained directly

$$D_0 = \sum_y \sqrt{P_+(y)P_-(y)} = 0.245176 \quad (6)$$

Using the bound² in (2) we have for this 4-bit data

$$P_b \leq 4.42 \times 10^{-5}. \quad (7)$$

Similarly, for the 3-bit data of the hardware decoder experiment given in Fig. 3, we have directly

$$D_0^* = 0.332164 \quad (8)$$

and the bound from (2)

$$P_b^* \leq 1.50 \times 10^{-3}. \quad (9)$$

Finally, with the software decoder experiment of Fig. 4,

$$D_0^{**} = 0.250502 \quad (10)$$

and

$$P_b^{**} \leq 5.61 \times 10^{-5}. \quad (11)$$

The bound given by (2) is known to be reasonably tight, and so we show the bounds in Fig. 1 as P_b , P_b^* , and P_b^{**} . Because of uncertainty as to the signal-to-noise ratio, E_b/N_0 , corresponding to the total distributions of Figs. 2, 3, and 4, we used the midvalue of 4 dB for the signal-to-noise ratio. It is clear that the large difference between the hardware decoder experiment and the software decoder experiment can be explained by the foldover effects observed in reducing the original 6-bit data to 3-bit data in the hardware decoder experiment. Finally, note that P_b^* appears to be slightly smaller than expected. This can be accounted for by the fact that higher power terms in

²We ignore terms of powers of D_0 greater than 17.

the bound in (2) contribute non-negligible amounts to P_b^* for $D_0^* = 0.332164$. We took only the terms to the 16th power of D_0^* in the above bound. Ignoring these higher order terms for $D_0 = 0.245176$ and $D_0 = 0.250502$ makes little difference in the bound on P_b and P_b^{**} , respectively.

IV. Discussion

The MVM'73 experiment included both X-band and S-band data. The S-band data also consisted of convolutionally coded bits represented by the same periodic sequence 1 1 1 0 1 0. For S-band, the signal-to-noise ratio was too low to show any significant coding gain. In reducing the original 6-bit data to 3-bit decoder input data, we find that for the S-band data

$$Pr\{x_1 \neq x_2\} = 0.13566 \quad (12)$$

This means that for S-band there was much less "fold-over" observed in the hardware Viterbi decoder input data. Indeed, if we were to observe some sections of the MVM'73 S-band data, we could easily conclude that

dropping x_2 , as was done in the hardware decoder data, would make little difference in decoder performance.

Finally, we note that in reducing 6-bit data of the form $x_1, x_2, x_3, x_4, x_5, x_6$ to 3 bits, an obvious suggestion is to take the 3 most significant bits x_1, x_2, x_3 . If this is done for the X-band data, we get the data distributions shown in Fig. 5 and the resulting parameter

$$D_0^{***} = 0.2644 \quad (13)$$

with bit error bound from (2) of

$$P_b^{***} \leq 1.03 \times 10^{-4}. \quad (14)$$

While this data reduction yields better decoder performance than the hardware data reduction which caused foldover effects, it is not as good as the software decoder data reduction. The Viterbi decoding performance seems to be sensitive to the probability distribution values for small amplitudes, and taking the 3 most significant bits for the decoder input data yields too coarse a division of the input amplitudes.

Acknowledgment

The authors thank J. C. Springett, W. J. Weber, and J. W. Layland of the Jet Propulsion Laboratory for their contributions to this work.

References

1. Heller, J. A., and Jacobs, I. M., "Viterbi Decoding for Satellite and Space Communication," *IEEE Trans. Commun. Technol.*, Vol. COM-19, pp. 835-848, Oct. 1971.
2. Viterbi, A. J., "Convolutional Codes and Their Performance to Communication Systems," *IEEE Trans. Commun. Technol.*, Vol. COM-19, pp. 751-772, Oct. 1971.

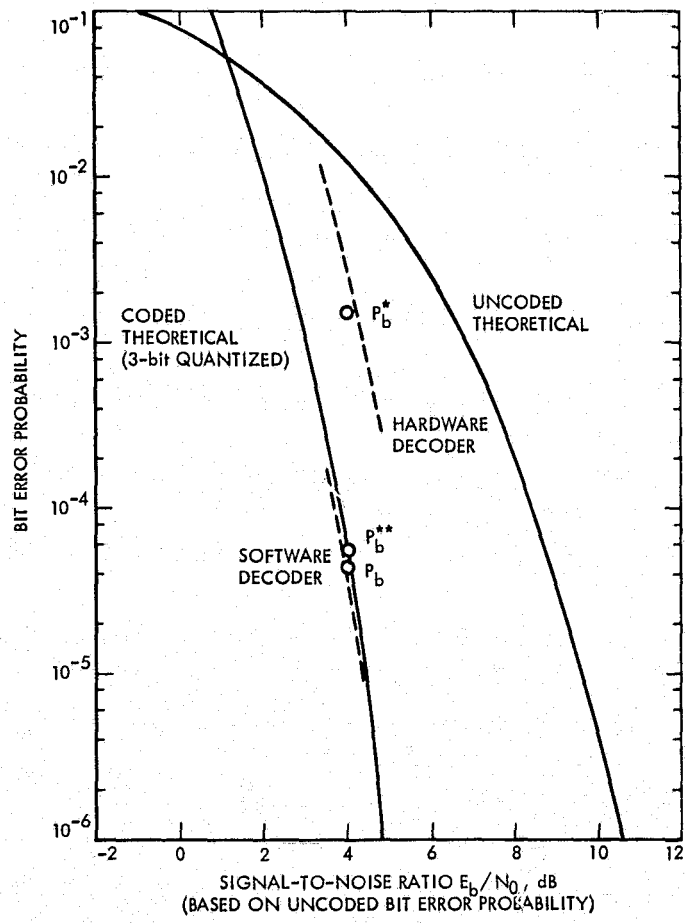


Fig. 1. X-band decoded bit error rates

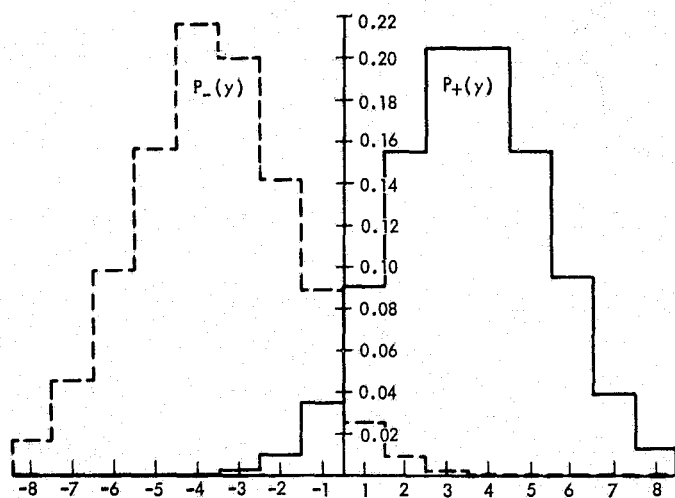


Fig. 2. 4-bit data distribution

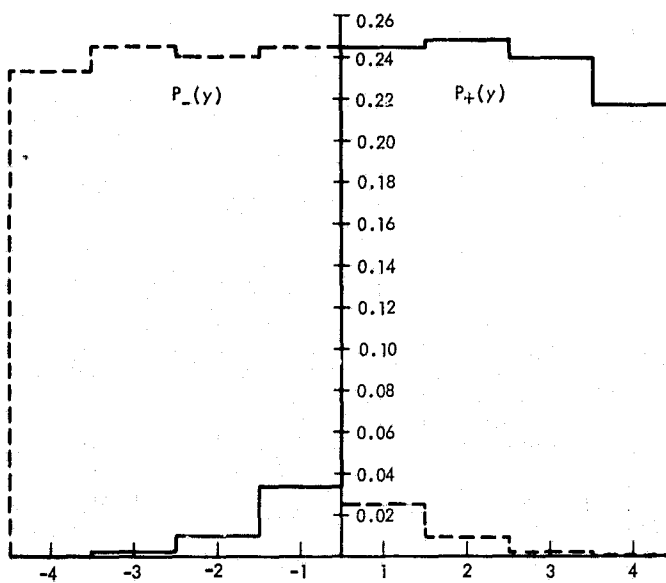


Fig. 3. 3-bit hardware decoder data

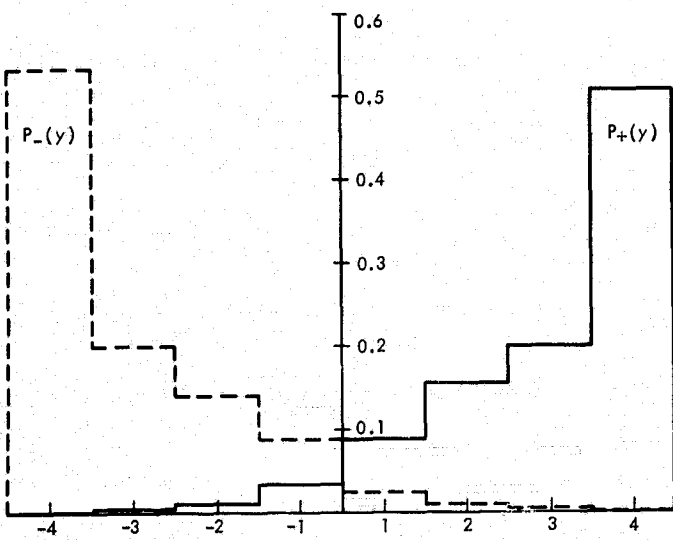


Fig. 4. 3-bit software decoder data

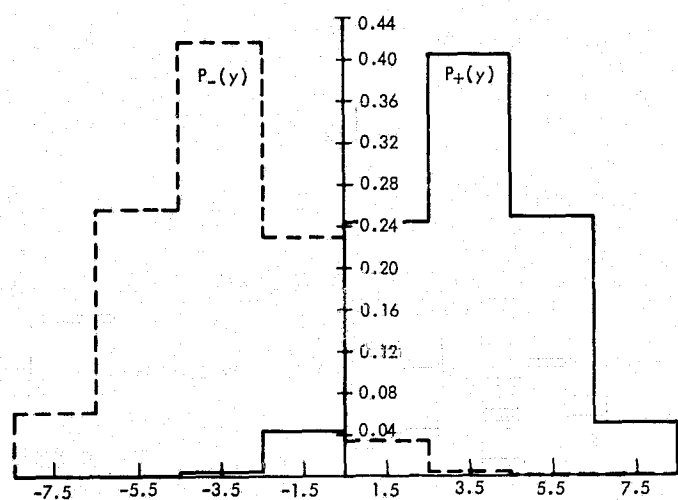


Fig. 5. 3 most significant bits

ORIGINAL PAGE IS
OF POOR QUALITY

N 76-29322

Computation of Spacecraft Signal Raypath Trajectories Relative to the Sun

A. R. Cannon and C. T. Stelzried
Communications Elements Research Section

An updated double-precision computer program has been developed to determine the trajectory of a spacecraft telemetry signal raypath relative to the sun. Using trajectory information available on DPTRAJ save tapes, the program efficiently and accurately computes the desired raypath trajectory and delivers the results in the form of plots, punched cards, and a tabular listing.

I. Introduction

When a spacecraft undergoes a superior conjunction with respect to some body (e.g., the sun or a planet), the signal carrier is affected. In order to predict the occurrence and magnitude of these effects, and to utilize the potential information they may provide, it is essential to determine the trajectory of the signal raypath with respect to the conjunction body. This trajectory information was formerly computed by the program CTS 41 (Ref. 1, pp. 16-19). However, since the program was originally written in 1968, the output of the DPTRAJ program has been expanded to provide data that can be used more efficiently and accurately than is done in CTS 41. Hence, an updated double-precision program, CTS 41B, has been developed.

While the program presented here is specifically designed for solar conjunctions, it could, with slight modi-

fication, be applied to planetary conjunctions as well. It has been shown theoretically (Ref. 1, p. 12) that the deviation of an S-band signal trajectory from the geometrical line of sight due to refractive effects in the solar corona is negligible, and experimental observations during previous solar conjunctions have verified that no large refractive effects occur. Hence, no attempt to compensate for refraction has been included, and it should be explicitly understood that CTS 41B refers to the geometrical line of sight rather than the actual signal raypath.

II. Input

The basic input data are obtained in the form of a save tape from the DPTRAJ program, which provides the most accurate possible trajectory and ephemeris information. A save tape is generated by initiating a DPTRAJ run in which the user specifies the data frequency and any

conjunction bodies that are desired. The geocentric and heliocentric blocks of data are automatically provided for every DPTRAJ run. For solar conjunctions, the only data required are the Earth-probe range and the Earth-sun range from the geocentric coordinate block and the coordinates of the probe in the heliocentric coordinate block, typically at one-day intervals.

A. Coordinates and Equations

The basic coordinate system to be used is the heliocentric system, defined as follows:

\hat{X} = direction from sun to Earth

\hat{Z} = normal to ecliptic, positive to north

Then the X-Y plane is the ecliptic plane, and the coordinates of Earth and the probe are

$$\text{Earth} = (X_E, 0, 0)$$

$$\text{probe} = (X_P, Y_P, Z_P)$$

where

$$X_E = \text{Earth-sun range}$$

$$(X_P, Y_P, Z_P) = \text{coordinates of probe in the heliocentric block}$$

The geometry is illustrated in Fig. 1. Point A (0, Y_A , Z_A) is the point of intersection of the line of sight with the Y-Z plane. In looking from Earth toward the sun, the apparent position of the spacecraft is given by the coordinates of point A. However, the point of closest approach of the signal raypath to the sun is point B (X_B , Y_B , Z_B), and the raypath offset from the sun is the distance $R = \sqrt{X_B^2 + Y_B^2 + Z_B^2}$ from the sun to point B. In most conjunction experiments, the sun-Earth-probe angle (SEP) will be so small that points A and B virtually coincide.

The coordinates of point A can be computed very simply from similar triangles. In the X-Y plane, we thus obtain

$$Y_A = Y_P \frac{X_E}{X_E - X_P}$$

while in the X-Z plane, we find

$$Z_A = Z_P \frac{X_E}{X_E - X_P}$$

The raypath offset R can also be obtained from similar triangles in the sun-Earth probe plane, where

$$R = \frac{X_E \sqrt{Y_P^2 + Z_P^2}}{R_P}$$

where R_P is the Earth-probe range and is given in the block of geocentric coordinates on the DPTRAJ save tape.

Other quantities of interest include the distance from Earth to the point of closest approach R_{EB} and the distance from the probe to the point of closest approach R_{BP} . These distances are

$$R_{EB} = X_E^2 - R^2$$

$$R_{BP} = R_P - R_{EB}$$

A complete listing of the program is provided in the Appendix.

The symbols used for variables in this description correspond to the binary-coded decimal (BCD) header record names on the DPTRAJ save tape as follows:

R_P ~ REARPR, geocentric block, record 12

X_E ~ REARSU, geocentric block, record 15

X_P ~ XSCSEL, heliocentric block, record 28

Y_P ~ YSCSEL, heliocentric block, record 29

Z_P ~ ZSCSEL, heliocentric block, record 30

B. Output

The values of Y_A , Z_A , R , R_{EB} , and R_{BP} as functions of time are listed in tabular form on the printout at the same frequency as the original DPTRAJ save tape data. In the solar version of the program, the apparent angle between the solar equatorial plane and the ecliptic plane, as seen from Earth, PHIEQ, is also tabulated as a function of time in order to facilitate correlations with standard observations of solar phenomena.

A plot of the coordinates (Y_A , Z_A) shows the trajectory of the line of sight relative to the sun. Figure 2 is an example for the superior conjunction of Mariner 10 in 1974. The trajectory points are plotted at one-day intervals and in units of solar radii. They may be identified by referring to the dates of the first and last points (i.e., day

number 146 to 174), which are listed to the lower left of the plot, or by referring to the tabular listing of (Y_A, Z_A) as functions of time. The program automatically supplies three such plots to provide a range of scale and resolution.

A plot of R as a function of time (Fig. 8) shows how the raypath offset varies through the conjunction. The values of Y_A , Z_A , and R as functions of time are also punched on cards.

Reference

1. Stelzried, C. T., *A Faraday Rotation Measurement of a 13-cm Signal in the Solar Corona*, Technical Report 32-1401, Jet Propulsion Laboratory, Pasadena, Calif., July 15, 1970.

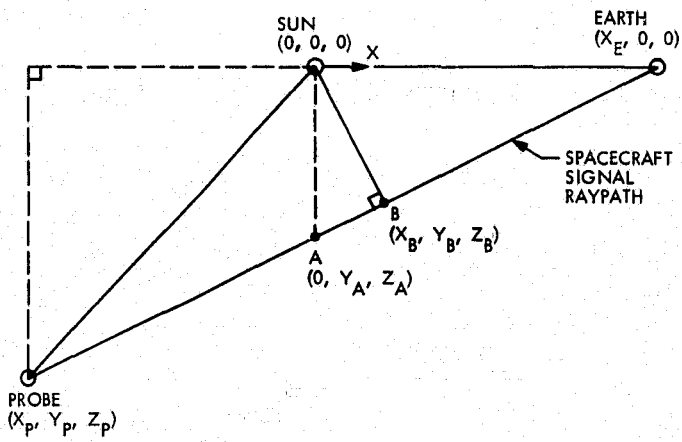


Fig. 1. Diagram of the sun-Earth-probe geometry showing the spacecraft signal raypath

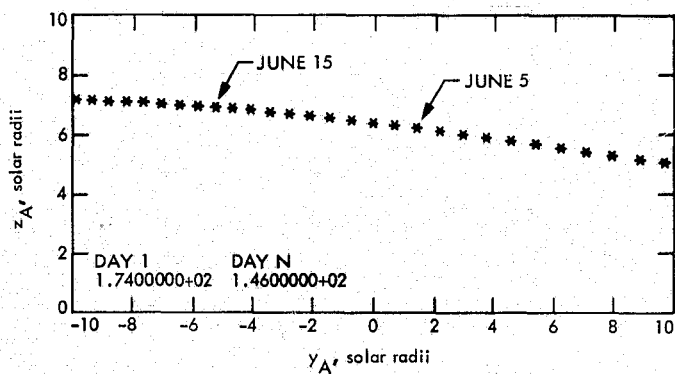


Fig. 2. Mariner 10 probe raypath trajectory shown with increments of one-day relative to a fixed sun-Earth line, 1974

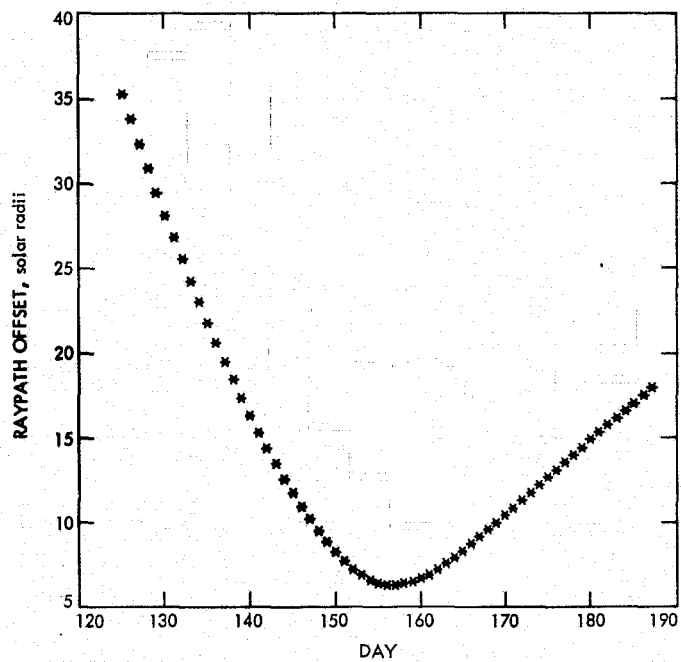


Fig. 3. Mariner 10 probe raypath offset vs 1974 day of year

Appendix

Spacecraft Signal Raypath Trajectory Computer Program, CTS 41B Listing

TJC*RA.CTS41B

```
1      INTEGER NDAY(366),IREC(750)
2      C*****START=STACTB,AB3=PICTS
3      REAL DDA(366)
4      DOUBLE PRECISION REC(375),X(366),Y(366),Z(366),
5      1RE(366),RS,P,A,R(366),RPR(366),REB(366),RBP(366),
6      1SEP(366),SPE(366),DSPE(366),RTD
7      EQUIVALENCE (IREC(1),REC(1))
8      DIMENSION TI(2),X1(366),Z1(366),R1(366),D(366),P(366)
9      DATA /RS/.6959806/TP1/6.2831853/PI/3.14159265/
10     DATA /RTD/.2957795131D0/
11     READ(5,4000)XXXX
12     4000 FORMAT(8E)
13     C*****XXXX IS A DUMMY AND NOT USED
14     READ(5,4005)NSTART,NFIN,NYEAR
15     4005 FORMAT()
16     READ(5,4000)XXXX
17     READ(5,4000)XXXX
18     READ(5,4000)XXXX
19     READ(5,4005)NH,NP,NT
20     READ(5,4010)TI
21     4010 FORMAT(2A6)
22     IF(NP.EQ.1)CALL PLOT
23     WRITE(6,1015)TI
24     1015 FORMAT(1H1,/,1X,'PROBE PATH (',2A6,1H))
25     IF(NT.NE.2)GO TO 3
26     WRITE(6,4015)
27     4015 FORMAT('NDAY',9X,'XSEL',9X,'YSEL',9X,'ZSEL',9X,'REARSU')
28
29     WRITE(6,4020)
30     4020 FORMAT(4X,4(13X,'KM'))
31     3 REWIND 4
32     READ(4)NWRDS
33     READ(4)NWRDS
34     MSAVE=0
35     M=0
36     5 READ(4,END=1010)NWRDS,(IREC(J),J=1,NWRDS)
37     M1=IREC(5)/10000000
38     M2=IREC(5)-M1*10000000
39     M3=M2/100000
40     M=M2-M3*100000
41     M=JD(M1,M3,M2)-JD(M1,1,1)+1
42     IF(M1.LT.NYEAR)GO TO 5
43     IF(M.LT.NSTART.AND.M.EQ.0)GO TO 5
44     IF(M.EQ.MSAVE)GO TO 5
45     MSAVE=M
46     N=N+1
47     NDAY(N)=M
48     DDA(N)=NDAY(1)+N-1
49     J1=JD(M1,3,6)
50     J2=JD(M1,9,8)
51     JJ=JD(M1,M3,M2)
52     IF(M.GE.66.AND.M.LE.251)P(N)=7.25*SIN(PI*(J1-JJ)/186.)
53     IF(M.LT.66.OR.M.GT.251)P(N)=7.25*SIN(PI*(JJ-J2)/179.)
54     X(N)=REC(28)
55     Y(N)=REC(29)
56     Z(N)=REC(30)
```

```

56      RPR (N)=REC (12)
57      RE (N)=REC (15)
58      IF (NT.EQ.2) WRITE (6,1005)MDAY(N),X(N),Y(N),Z(N),RE(N)
59      1005 FORMAT(I4,4D15.8)
60      IF (M.NE.MFIN) GO TO 5
61      1010 IF (NT.NE.2) GO TO 4030
62      WRITE (6,1015) TI
63      WRITE (6,1020)
64      1020 FORMAT('ODAY',9X,'REARPR',12X,'REB',12X,'RBP',10X,'PHIEQ')
65      WRITE (6,4025)
66      4025 FORMAT(4X,3(13X,'KM'),12X,'DEG')
67      4030 DO 10 I=1,M
68      R(I)=RE(I)*DSQRT(Y(I)**2+Z(I)**2)/RPR(I)
69      A=RE(I)/(RE(I)-X(I))
70      X(I)=Y(I)*A
71      X1(I)=X(I)/RS
72      Z(I)=Z(I)*A
73      Z1(I)=Z(I)/RS
74      R1(I)=R(I)/RS
75      D(I)=MDAY(I)
76      REB(I)=DSQRT(RE(I)**2-R(I)**2)
77      REP(I)=RPR(I)-REB(I)
78      SEP(I)=DASIN(R(I)/RE(I))*RTD
79      SPE(I)=DATAN(R(I)/RBP(I))*RTD
80      IF (I.GE.3) DSPE(I-1)=(SPE(I)-SPE(I-2))/2.00
81      IF (MH.EQ.1) PUNCH 4055,MDAY(I),X1(I),Z1(I),R1(I)
82      4055 FORMAT(I3,3F15.8)
83      10 IF (NT.EQ.2) WRITE (6,1005)MDAY(I),RPR(I),REB(I),RBP(I),P(I)
84      DSPE(1)=0
85      DSPE(M)=0
86      IF (NT.NE.2) GO TO 1023
87      WRITE (6,1015) TI
88      WRITE (6,4060)
89      4060 FORMAT('ODAY',12X,'SEP',12X,'SPE',11X,'DSPE')
90      WRITE (6,4065)
91      4065 FORMAT(4X,2(12X,'DEG'),8X,7HDEC-DAY)
92      DO 11 I=1,N
93      11 WRITE (6,1005)MDAY(I),SEP(I),SPE(I),DSPE(I)
94      1023 IF (NT.EQ.0) GO TO 25
95      WRITE (6,1015) TI
96      WRITE (6,1025)
97      1025 FORMAT('ODAY',12X,'YA',12X,'ZA',14X,'R')
98      WRITE (6,1027)
99      1027 FORMAT(4X,3(13X,'KM'))
100     DO 12 I=1,N
101     12 WRITE (6,1005)MDAY(I),X(I),Z(I),R(I)
102     WRITE (6,1015) TI
103     WRITE (6,1025)
104     WRITE (6,1029)
105     1029 FORMAT(4X,3(4X,'SOLAR RADI') )
106     DO 15 I=1,N
107     15 WRITE (6,1030)MDAY(I),X1(I),Z1(I),R1(I)
108     1030 FORMAT(I4,4E15.8)
109     25 IF (NP.NE.1) STOP
110     A3=TI(1)
111     A4=TI(2)
112     CALL EPLT(X1,Z1,M,A3,A4,D)
113     CALL EPLT(000A,R1,M)
114     STOP
115     END

```

N 76-29323

Telecommunications Division Fourth Harmonic Power Analyzer

C. Foster

R.F. Systems Development Section

This report describes the development of a microprocessor-based instrumentation system to be used in the measurement and analysis of fourth harmonic power generated by the DSN high-power transmitters.

I. Introduction

The requirements of the high-power harmonic analyzer, as well as its physical details, were covered in Ref. 1. The harmonic analyzer design in Ref. 2 describes the ability to predict the accuracy of measurements made on harmonic power, in a multimode waveguide, terminated in other than a matched load.

Initial evaluation of the harmonic analyzer, both in the field and in the laboratory, as well as a detailed description of a minicomputer data reduction system is described in Ref. 3. The success of the minicomputer design resulted in the initiation of a program to develop a self-contained portable microprocessor system, with a primary design goal of reducing required operator skill, increasing measurement accuracy, and reducing measurement and data reduction time by greater than fifty percent.

II. Implementation

A simplified block diagram (Fig. 1) shows the major components used in the development of the portable harmonic analyzer. The design of this instrument has been separated into two efforts, the design of the microprocessor controller, and the design of the RF sensor. The design goals of the microprocessor controller are to eliminate complex operator functions and to improve measurement accuracy. The design goals of the RF sensor are overall amplitude stability of less than 0.5 dB variation over the time required for measurement, a dynamic measurement range of -150 dBm to 30 dBm, and an accuracy of ± 2.5 dB.

The major effort during this period centered on development of the microprocessor instrument interface and the control software. The control software has been

developed using a structured design approach and the INTEL PLM language. The main program flow chart (Fig. 2) shows that the operator has three options. Responding with a letter P initiates the data input routine. This routine prompts the operator to designate starting port number, after which the power meter is configured for a measurement, and the operator is asked to signify when the probe is inserted into the proper port. Data are stored and the next port is identified for the operator. At the completion of data collection, the program notifies the operator that data collection is complete and waits for output command.

Responding with a letter R initiates report output routine. This routine uses data taken on input routine, and with stored voltage standing wave ratio (VSWR) Data, corrects measured power for each port. This information is then output to the thermal printer where each port is identified with its corrected power displayed. The report

is completed with each port power summed and total power printed out. Responding with a letter T initiates the total output routine. This routine, like the report routine, corrects the measured power of each port using stored constants (VSWR, probe gain/loss, frequency), sums all ports, and prints out only total power.

III. Conclusion

The Control Program and Interface bus have been successfully designed and demonstrated in the laboratory (Fig. 3). Operator functions have been reduced to a maximum of three: (1) reading prompt message, (2) inserting probe into proper port, and (3) operating switch signifying to microcontroller that operator task is complete. During the next reporting period the RF sensor design will be completed and the total system accuracy calibrated.

References

1. Smith, R. H., "Fourth Harmonic Analyzer," in *The Deep Space Network Progress Report 42-20*, pp. 121-123, Jet Propulsion Laboratory, Pasadena, Calif., April 15, 1974.
2. *Final Report: JPL Harmonic Analyzer Study Program*, Report No. 953443. Jet Propulsion Laboratory, Pasadena, Calif., October 1972. (JPL internal document.)
3. Grigsby, Y. L., "Automation of Data Gathering and Analysis for the Fourth-Harmonic Analyzer," in *The Deep Space Network Progress Report 42-26*, pp. 126-132, Jet Propulsion Laboratory, Pasadena, Calif., April 15, 1975.

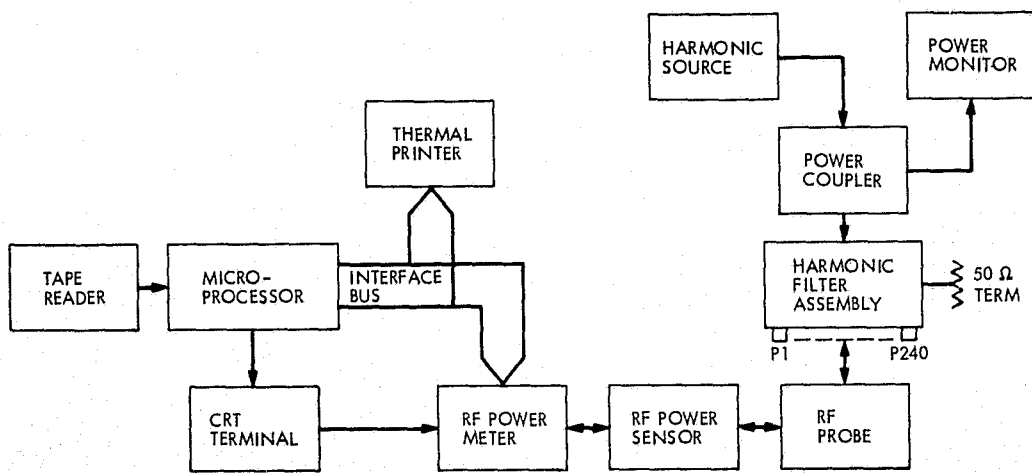


Fig. 1. Harmonic analyzer

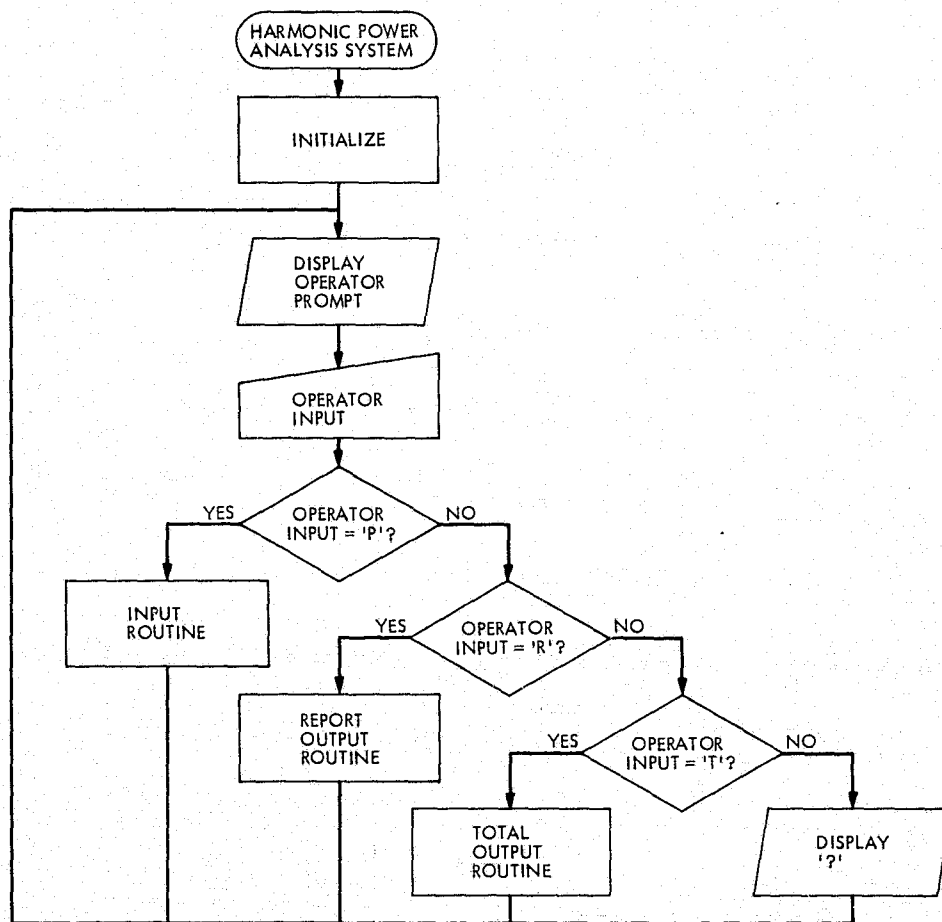


Fig. 2. Main program flow chart

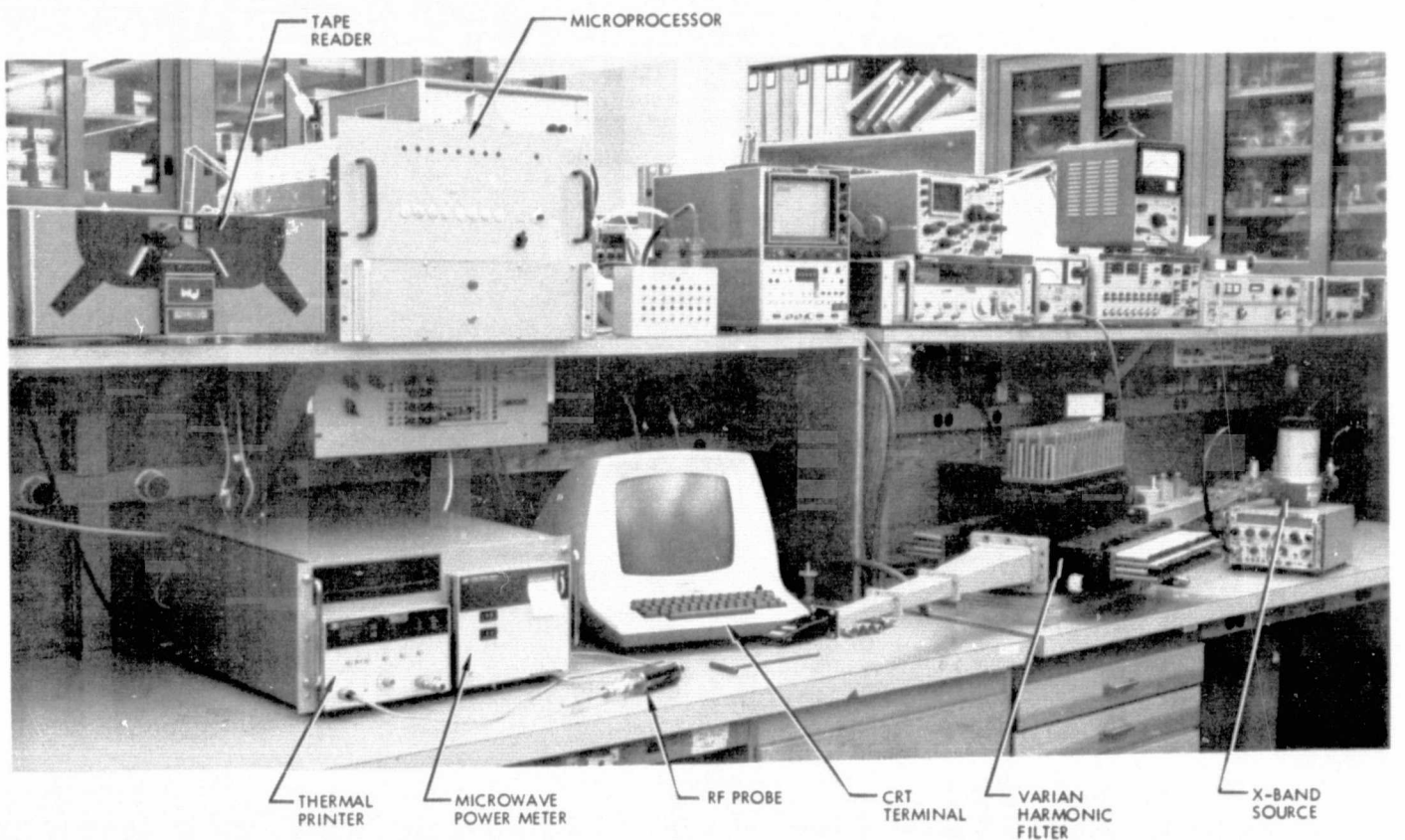


Fig. 3. High-power harmonic analyzer laboratory engineering model

N 76-29324

Decoding with Multipliers

L. D. Baumert, R. J. McEliece, and G. Solomon¹
Communications Systems Research Section

We present a general technique, called decoding with multipliers, that can be used to decode any linear code. The technique is applied to the (48,24) quadratic residue code and yields the first known practical decoding algorithm for this powerful code.

I. Introduction

It is widely believed that the next breakthrough in coding technology for a wideband Gaussian channel will come from *soft-decision decoding* of block codes (Ref. 1). Chase (Refs. 1 and 2) has devised an algorithm which allows reasonably efficient soft-decision decoding of any block code for which a hard-decision (i.e., binary) decoding algorithm is known, provided the block length is not too large. This motivates us to find good binary decoding algorithms for powerful short block codes. In this paper we shall describe a technique which is well-suited for this task; it is called *decoding with multipliers*.

In Section II, we define the notion of multiplier; in Section III, we give a general decoding algorithm; and in Section IV we devise a specific algorithm for decoding the powerful (48,24) quadratic residue code—a code whose performance on a Gaussian channel is likely to be very good.

¹Consultant from University of California at Los Angeles.

II. Information Sets and Multipliers

Consider a set of j coordinates of an (n, k) linear code C over $GF(q)$. Let X be the set of all distinct j -tuples which appear in these coordinates in at least one of the codewords of C . Linearity guarantees that

$$|X| = q^s$$

for some s , $0 \leq s \leq j$, and establishes a many ($=q^{k-s}$) to one mapping

$$\phi: C \rightarrow X$$

Clearly, given any codeword c the corresponding j -tuple is easily found. Conversely, given any j -tuple of X the q^{k-s} codewords which are its preimages under ϕ can be constructed by means of linear algebra.

Since C has q^k codewords, $|X| \leq q^k$ and so $s \leq k$, independent of j . When $k = s \leq j$, the j coordinates are said to constitute an *information set* for the code since any

codeword can be uniquely determined from its values at these j coordinates. All linear codes have information sets of size $j = k$.

We associate with any subset J of the numbers $1, \dots, n$ its incidence vector m , i.e.

$$m_i = \begin{cases} 1 & \text{if } i \in J \\ 0 & \text{otherwise} \end{cases}$$

for $1 \leq i \leq n$. We shall call such a vector a *multiplier*. For decoding purposes we shall usually be interested in multipliers which specify an information set of the code under consideration; they will be called *proper* multipliers.

III. Decoding with Multipliers

Let C be an (n, k) linear code over $GF(q)$, which is capable of correcting all patterns of e or fewer errors, i.e., one whose minimum distance d satisfies $d \geq 2e + 1$. Let $M = \{m_1, m_2, \dots, m_N\}$ be a collection of N multipliers for C with the property that for each e -tuple of codeword coordinates there is at least one $m_i \in M$ which is zero at each of these coordinates. Then we can use M to decode C as follows:

Given a received vector $y = (y_1, \dots, y_n)$ —we assume it is a codeword which has suffered $\leq e$ errors—for each $m \in M$ we form the vector $m \times y$ which is defined by

$$(m \times y)_i = \begin{cases} y_i & \text{if } m_i = 1 \\ 0 & \text{if } m_i = 0 \end{cases}$$

Let us temporarily assume the multipliers $m \in M$ are all proper. This means that the vector $m \times y$ can be uniquely extended to a codeword of C . If the vector y contains at most e errors, then by the property of M cited above, at least one of these codewords will be the one transmitted. Thus if we compare y to each of the N (not necessarily distinct) generated codewords, the one closest to y will be the one sent.

If some or all of the multipliers are improper, the decoding procedure is similar, except that in general it will be possible to extend the vectors $m \times y$ to codewords in several ways: if m is a multiplier with $k - s = i$ (we say m has *defect* i), this extension can be done in q^i ways. Thus if M contains N_i multipliers of defect i , then the decoding process will generate $N_0 + qN_1 + q^2N_2 + \dots$ codewords, each of which must be compared to the received vector y .

In the next section we will apply these general considerations to the $(48, 24)$ quadratic residue code.

IV. Multipliers for the $(48, 24)$ Quadratic Residue Code

The $(n, k) = (48, 24)$ quadratic residue code over $GF(2)$ has minimum distance 12 and so can be used to correct $e = 5$ errors. We would like to find a minimal set of multipliers for this code. Since all 5-tuples of coordinates from $1, \dots, 48$ must be covered by 0's in some multiplier, in order to minimize $|M|$ we want each multiplier to have as many 0's as possible. On the other hand, we would like the multipliers to be proper; this implies that each multiplier must have at least $k = 24$ nonzero entries. Let us assume then, for the time being, that each multiplier has 24 1's and 24 0's. Thus we have the combinatorial problem of covering all 5-tuples from $1, \dots, 48$ with 24-tuples in such a way as to use the least possible number of 24-tuples.

While the answer to the above problem is unknown, there is a general result, due to Schönheim (Ref. 3), which provides lower bounds for such questions. In this case, Schönheim tells us that we need at least 62 such 24-tuples. On the other hand, as we shall see, a covering which uses 63 sets is possible. So

$$63 \geq \min |M| \geq 62$$

In terms of decoding effort there is little to choose between 63 and 62 and since there is no guarantee that 62 is even possible, we would be quite content with $|M| = 63$.

A set M of 63 multipliers, whose zeros cover every set of 5 coordinates from $1, \dots, 48$, is given by the nonzero codewords of a binary $(48, 6)$ punctured Solomon-Stiffler (Ref. 4) code. Given any 5 coordinates, there are at most $2^5 = 32$ distinct 5-tuples appearing in these coordinates in the codewords and, by linearity, each 5-tuple which does occur appears equally often. Since this code has dimension $k = 6$ this means that, in particular, 00000 occurs at least twice, and so there is at least one nonzero codeword which has 0's in the desired 5 coordinates. So the nonzero codewords do cover the 0's properly. There are 60 codewords of weight 24 and 3 codewords of weight 32 in this collection. Furthermore, 8 1's can be removed from each of the words of weight 32 without sacrificing the property that they specify information sets for the $(48, 24)$ quadratic residue code. Unfortunately, however, in the representations of the Solomon-Stiffler code so far tested not

all the words of weight 24 yield proper multipliers for the quadratic residue code. In fact, for the best case yet found, of the 63 multipliers so obtained, 37 are proper, 24 have defect 1, and 2 have defect 2. Thus while $M = 63$ there could be as many as $37 + 2.24 + 4.2 = 93$ codewords to be compared with y in the decoding process. Since any of the $48!$ coordinate permutations of the Solomon-Stiffler code also has the desired 0's covering property, we conjecture that this bound of 93 can be reduced—but not, of course, below 62.

The complexity of the decoding process is at worst linear in the number of codewords to be compared with y , so 93 (vs 62) represents less than a factor of 2 in decoding time. Thus, if no better multiplier set is discovered, it would be feasible to decode the $(48,24)$ quadratic residue code using this set M .

For definiteness, this multiplier set and the parity check matrix for the $(48,24)$ quadratic residue code are given in the Appendix.

References

1. Baumert, L. D., and McEliece, R. J., "Performance of Some Block Codes on a Gaussian Channel," *Proc. 1975 International Telemetering Conf.*, Washington, D.C., pp. 189-195.
2. Chase, D., "A Class of Algorithms for Decoding Block Codes with Channel Measurement Information," *IEEE Trans. Inform. Th.*, IT-18, pp. 170-182, 1972.
3. Schönheim, J., "On Coverings," *Pacific J. Math.*, 14, pp. 1405-1411, 1964.
4. Solomon, G., and Stiffler, J. J., "Algebraically Punctured Cyclic Codes," *Inform. Contr.* 8, p. 170-179, 1965.

Appendix

The multiplier set discussed above consists of all the nonzero codewords of a particular representation of the

Solomon-Stiffler (48,6) code. Since this code is linear it suffices to list generators for the code. These are:

```

 $g_1 = 110100\ 011011\ 101111\ 111010\ 111000\ 101110\ 110101\ 101111$ 
 $g_2 = 101111\ 111110\ 011100\ 011111\ 101111\ 010011\ 001010\ 011101$ 
 $g_3 = 010110\ 001010\ 100100\ 000100\ 111111\ 111011\ 010101\ 010001$ 
 $g_4 = 010111\ 111000\ 001001\ 101101\ 101100\ 111000\ 000011\ 100110$ 
 $g_5 = 010101\ 001101\ 111001\ 010110\ 010101\ 001111\ 000010\ 000111$ 
 $g_6 = 000110\ 010010\ 111000\ 000111\ 100010\ 101101\ 111010\ 101011$ 

```

The (48,24) quadratic residue code is cyclic with an overall parity check adjoined. Thus its parity check

matrix is a cyclic 47×47 matrix with one extra row and column added:

N 76-29325

MODC2 Procedures for Assembly of MODCOMP-II Programs Using the Sigma 5 Assembler

J. W. Layland
Communications Systems Research Section

This article describes a set of programs which have been written to enable the METASYMBOL assembler of the Sigma 5 to assemble programs for an attached MODCOMP-II minicomputer. This program set is a follow-on to previously developed program sets which facilitated assemblies for the PDP-11 and SDS-930.

I. Introduction

The METASYMBOL assembler for the Sigma 5 is a very powerful macro-assembler which we have used in the past to build programs for the SDS 920/930's or for the PDP-11 minicomputer (Ref. 1). The flexibility of this assembler has more recently been used to build programs for the MODCOMP-II. In this way, the more powerful and familiar features of the Sigma assembler are made available for minicomputer software development without requiring a user to become familiar with the total software system of the minicomputer, which he may not need for his application. One potential pitfall here is that software developed with the Sigma host assembler cannot be readily maintained on the MODCOMP, or vice versa, due to lexical differences of the two assemblers. This potential problem is not deemed serious for our application, which will use MODCOMP without peripherals, which is to be direct-link connected to the Sigma 5.

The assembly package for the MODCOMP consists of two parts: a system procedure deck "MODC2," which allows METASYMBOL to assemble a source language similar to the MODCOMP's native assembler, and a secondary loader which reformats the Sigma 5 core-image load module into proper binary format for loading into the target minicomputer and punches it onto paper tape or cards. Figure 1 describes the operation flow for use of MODC2.

The procedure deck defines the valid operators to the Sigma 5 METASYMBOL assembler and determines what code will be generated for the valid source statements. METASYMBOL procedures are similar to macro definitions. The code produced from the source program under control of the procedures is reformatted by METASYMBOL into a Sigma relocatable object module (ROM) containing relocation information, external references and definitions, and generated code.

A number of read-only memories (ROMs) may then be linked together, and the external references and definitions resolved by the Sigma loader. Normally the loader gives the user the option of saving relocation information, creating a task-control block (TCB), and satisfying unresolved external references from the system library. These are SIGMA-oriented functions and should be disallowed during loading for MODCOMP-II programs by specifying the options (ABS), (NOTCB), and (NOSYSLIB) on the load control card. The Sigma loader also has the capability of relocating the program to any boundary which is a multiple of 800 (hex) bytes. It will automatically relocate to the background lower limit unless the BIAS option is specified on the load card; (BIAS, 0) will cause the first ROM to be not relocated. The Sigma loader structures its output into a file called a load module (LMN), which consists of the core image program and several records of control information. The Sigma 5 has write protection, so the core image is in several pieces, one for each protection type.

At present, we are using the secondary loader "SLOAD: DSN" developed for the PDP-11 (Ref. 1) to format and punch the developed program into portable form. The secondary loader reads a Sigma load module and writes the 00 protection-type core image data in the format which is loaded by the PDP-11 absolute loader. So that the program need not start on a multiple of 800 hex, the secondary loader skips all data until the first nonzero 16-bit word. Thus the first valid word in the MODCOMP program must be nonzero. A special one-card bootstrap loader has been written for the MODCOMP which accepts programs in the PDP-11 absolute binary format from the twin-coax intercomputer communication links (Ref. 2).

II. MODC2 Language Definitions

The source language is defined by the lexical analyzer and directives of the METASYMBOL assembler and by the procedure definitions of SYSTEM MODC2. The METASYMBOL reference manual (Ref. 3) contains a complete description of the structure imposed upon character strings, symbols, expressions, and statements that are to be processed by this assembler, and also describes the data definition facilities and conditional assembly features of this assembler.

Character strings in the Sigma 5 are intrinsically EBCDIC, while strings are represented internally as ASCII in the MODCOMP-II. Thus, the Sigma's text-string generating directives, while available to the MODCOMP

programmer, are relatively useless. A procedure "ANSCI" is provided which can convert short strings of one to four characters into ASCII character codes for use on the MODCOMP. An example of its use is given later.

Symbols may consist of 1-63 alphabetic characters, not containing embedded blanks. All characters in a symbol are significant. An extended alphabetic character set includes the characters \$, @, #, :, and _ (underscore). The special symbols \$, and \$\$ represent the values of the location counters and must be given an intrinsic two-byte resolution by the directive

```
ORG,2    x'sss'
```

which both establishes address resolution, and sets the starting address of the program to the hexadecimal value 'sss'.

Statements consist typically of four fields known as Label, Command, Address, and Comment. Statements are free-form, and each field is terminated by a blank, or end-of-line, although semirigid field definition is to be preferred for readability. The Label field is optional, and may be eliminated by beginning any statement with a blank. A statement is a comment-only if it begins with an asterisk. The Label, Command, or Address fields may consist of one or more subfields separated by commas. The first subfield of the command field must invoke a directive, a procedure from SYSTEM MODC2, or a user-defined procedure. Any subfield within the address field may be preceded by an asterisk. This feature is used within SYSTEM MODC2 to invoke indirect addressing where appropriate. Multiple label subfields are allowed, and may be used in a user-defined procedure to label different lines within a procedure which generates multiple code lines, although there is no use of this feature within SYSTEM MODC2.

The MODCOMP-II instruction set as described in the Computer Reference Manual (Ref. 4) is available, with the exception of the floating point arithmetic set. These can be added at a later date, along with procedures to define floating constants in the MODCOMP format. The instructions are grouped into eight distinct classes, distinguished by the instruction addressing mode, and the format of the executable instruction in memory.

Class 1 is the immediate mode instructions which have the format

```
CMD,R1    value
```

The instruction 'LDI' is an example from this class which, when executed, will place "value" into register R1. Value may be a number, a symbol, or an expression which is evaluated by the METASYMBOL assembler.

Class 2 is the register-to-register mode instructions which have the format

CMD,R1 R2

The instruction 'LDX' is an example from this class, which when executed, will place the contents of the memory cell whose address is in register R2 into register R1. This class also contains the bit-manipulating instructions and the register I-O instructions.

Class 3 is the memory-to-register instructions which have the format

CMD,R1 [*]LOCATION[,XR]

Brackets denote that their contents are optional. The asterisk, if present, invokes indirect addressing, and the ".XR", if present, invokes indexing by the contents of register XR. The instruction 'LDM' is an example from this class which, when executed, will place the value contained in the memory cell addressed by the instruction into the register R1. Determination of the effective address of instructions under the optional indexing and/or indirect addressing is specified in the Computer Reference Manual (Ref. 4).

Class 4 is the register-to-register test instructions with conditional branching. They have the format

CMD,R1 R2,B-LOC

These instructions execute as their class 2 counterparts except that a branch to B-LOC is performed if the instruction's test conditions are satisfied.

Class 5 is the memory-to-register test instructions with conditional branching. They have the format

CMD,R1 [*]LOC[,XR],B-LOC

These instructions execute as their class 3 counterparts except that a branch to B-LOC is performed if the test conditions are satisfied.

Class 6 is the register-to-register comparison instructions which have the format

CMD,R1 R2,B-LOC1,B-LOC2

Class 7 is the register-to-memory comparison instructions which have the format

CMD,R1 [*]LOC[,XR],B-LOC1,B-LOC2

The address structure of class 6 and 7 corresponds to that of class 2 and 3, respectively, with the addition of the conditional branch location words.

Class 8 is a varied collection of two-byte instructions with the format

CMD value

where "value" may be missing for some specific instructions.

A summary of MODCOMP-II instructions may be found in Appendix E of the Computer Reference Manual (Ref. 4).

III. The Secondary Loader

The secondary loader reformats Sigma 5 load modules into the format required by the minicomputer's absolute binary loader. Input to the secondary loader is through the M:EI DCB; output is through the M:PO DCB. The input load module must be on a disk file, and output is typically to paper tape, or to cards. The M:EI and M:PO DCBs must be assigned to the appropriate files or devices before execution of the secondary loader. The control information expected by the absolute loader at the beginning and end of each physical record is supplied by the secondary loader.

The present secondary loader was initially written for the PDP-11. Data punched by this loader are organized into 16-bit (two-byte) words, with the least significant byte first. The following three control words precede the data to be loaded: a word containing the value '01', a word containing the total byte count in the physical record, and a word containing the starting location for loading the data from the record. As noted above, a special bootstrap loader has been written to load data in this format into the MODCOMP memory from an inter-computer communications link. Should the need arise, a secondary loader which punches data compatible with the MODCOMP-II loaders could be developed.

The length of a core-image segment in a Sigma load module is a multiple of a Sigma double word (64 bits), so the last byte of a program created through MODC2 will load on a MODCOMP-II byte address which is 1 less than a multiple of 8. This means that several bytes of zeros may follow the actual program.

IV. Assembly Example

Figure 2 is an example of a job-step sequence for the assembly of a simple nonsense program for the MODCOMP-II. At least one instruction from each class is included to illustrate the addressing and listing structure which results. A listing line consists of the input source-line number, the (4-byte) word address at which the instruction begins, and (if nonzero) a byte-offset from that word boundary. This is followed by a hexadecimal copy of the generated instruction and a copy of the input source line. Some source lines may result in more than one line

of listing to accommodate the generated instruction(s), as for example, lines 16 or 37. The eight instruction classes are each indicated by a “*n” comment line preceding the appearance of that instruction class, as on line 9, which precedes the class 3 instruction LDM. Data are defined as 2-byte units by “DATA,2” as on line 38. Generation of ASCII Text is illustrated on lines 41 and 42.

The job-control-language shown produces a paper tape copy of the program. Cards would be produced if the explicit ASSIGNment of M:PO were deleted, and the default assignment used instead.

The SYSTEM MODC2 has been used successfully to generate programs totalling many hundreds of lines of code for the MODCOMP-II. These programs have been loaded into the MODCOMP via the direct link and successfully executed. While the SYSTEM MODC2 cannot be guaranteed to be correct, it at present contains no known problems.

References

1. Layland, J. W., Klimasauskas, C. C., and Erickson, D. E., “An Introduction to Minicomputer Software Support,” “The X930 Program Set for Sigma 5 Assembly,” and “The SAPDP Program Set for Sigma 5 Assembly,” *The DSN Progress Report*, Technical Report 32-1526, Vol. VII, pp. 84-96, Jet Propulsion Laboratory, Pasadena, Calif., Feb. 15, 1972.
2. Lushbaugh, W. A., “A Driver/Receiver Unit for an Intercomputer Communications Link,” *The DSN Progress Report*, Technical Report 32-1526, Vol. XV, pp. 109-115, Jet Propulsion Laboratory, Pasadena, Calif., June 15, 1973.
3. “Xerox Data Systems Sigma 5-9 METASYMBOL Reference Manual,” Publication 90-09-52F, Xerox Data Systems, Sept. 1972.
4. “MODCOMP-II Computer Reference Manual,” 210-102000-000, Modular Computer Systems, May 1974.

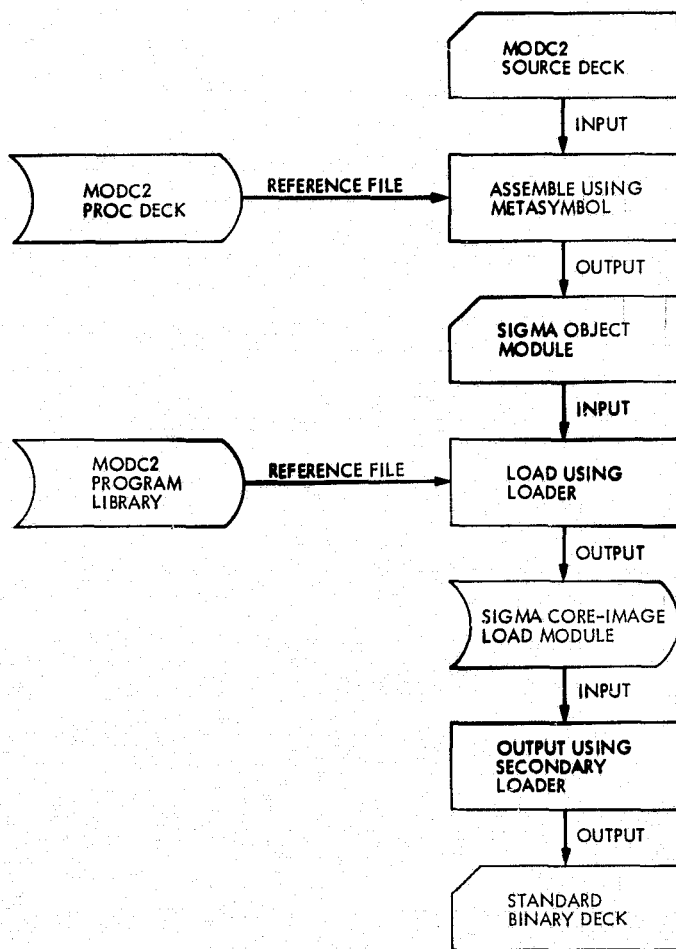


Fig. 1. Operational flowchart for the MODC2 program package

ORIGINAL PAGE IS
OF POOR QUALITY

14105 JUN 17, 1976 ID=0006=FOO
 JOB M0DC2,LYL
 ASSIGN M:00,(FILE,TESTB)
 METASYM SI,L0,B0,AC(LYL)

HOU 14105 JUN 17, 1976

1 THIS IS A COMMENT
 2 REG#2 X'140'
 3 SET START LOCATION
 4 SYSTEM M0DC2
 5 BEGIN
 6 01 000A0 ED200162 N *1 BEGIN LDI,2 TABLE
 7 01 000A0 01 000A0 *2 LDX,3 2
 8 01 000A1 FD32 A *3 LDM,4 *TABLE
 9 01 000A1 2 E5480162 N LDM,5 TABLE,3
 10 01 000A2 2 E5530162 N *4 TRRB,6 5,JUMP1
 11 01 000A3 2 7D65014A N HLT
 12 01 000A4 2 0000 A *5 JUMP1 ADMB,4 VALUE,JUMP2
 13 01 000A5 C4400161 N 0152 ADMB,4 BNE,2,JUMP2
 14 01 000A6 2 C4420001 N 0152 ADD (REG#4) TO VALUE, BRANCH IF
 15 01 000A8 E7000150 N BRU EQU1
 16 01 000A9 DF320157 N *6 JUMP2 CRXB,3 2,EQUAL,LESS;THAN ADD (REG#4) TO (REG#2)+BNE, BRANCH IF
 17 01 000AA 2 E7000160 N 0160
 18 01 000AB 2 87FB0162 N *7 EQUAL CBMB,15 *TABLE,3,EQU1,LESS;THAN
 19 01 000AD 2 E7000160 N BRU GREATER;THAN
 20 01 000AE 2 6600 A *8 EQU1 NOP
 21 01 000AF 2601 A SIA 1
 22 01 000AF 2 0000 A HLT
 23 01 000B0 015D0160 SIMULATE PARITY TRAP
 24 01 000B0 2 E7000160 N AND HALT PROCESSING
 25 01 000B0 0000 A * LESS;THAN EQU HA(*)
 26 01 000B0 0000 A GREATER;THAN EQU HA(*)
 27 01 000B0 0000 A HLT
 28 *
 29 *
 30 *
 31 *
 32 *

HOU 14105 JUN 17, 1976

33 PZE COM,16 0
 34 00000001 BNE EQU 1
 35 *
 36 01 000B0 2 0000 A VALUE PZE
 37 01 000B1 000A A TABLE DATA,2 10, TABLE,BEGIN,0
 01 000B1 2 0162 N
 01 000B2 0140 N
 01 000B2 2 0000 A
 38 01 000B3 001 A DATA,2 10
 39 01 000B3 00C1 A C'A!' TEN EBCDIC A'S
 01 000B4 00C1 A
 01 000B4 2 00C1 A
 01 000B5 00C1 A
 01 000B5 2 00C1 A
 01 000B6 00C1 A
 01 000B6 2 00C1 A
 01 000B7 00C1 A
 01 000B7 2 00C1 A
 40 *
 41 01 000B8 41 A ANSCI,4 'ABCD'
 01 000B8 1 42 A AND SOME ANSCII TEXT
 01 000B8 2 43 A
 01 000B8 3 44 A
 42 01 000B9 5A A ANSCI,1 '21'
 43 DEF TABLE
 44 END BEGIN

CONTROL SECTION SUMMARY: 01 000B9 1 PT 0

Fig. 2. Example assembly

HOU 14:05 JUN 17, '76 3
 * SYMBOL VALUES
 ANSI:CTI/LIST EQUAL/01 000AB EQUAL/01 000AE GREATER; THAN/01 00080
 I1/00000001 I2/00000001 J/00000000 JUMP1/01 000A5
 JUMP2/01 000A9 J1/00000029 LESS; THAN/01 00090 LQ/ LIST
 ONE/00000001 VALUE/01 000B0
 * EXTERNAL DEFINITIONS
 BEGIN/01 000AD
 * NO PRIMARY REFERENCES
 * NO SECONDARY REFERENCES
 * NO UNDEFINED SYMBOLS
 * ERROR SEVERITY LEVEL: 0
 * NO ERROR LINES

!LOAD (BIAS,0),(N8SYSLIB),(N8TCB),(ABS),(MAP),(EF,(TESTB)),(LMN,TESTL)

* * ALLOCATION SUMMARY * *

PROTECTION	LOCATION	PAGES
DATA (00)		1
PROCEDURE (01)	200	1
UDEF	A0 0 BEGIN	
UDEF	B1 0 TABLE	
CSEL	0	
BA	DATA	
200	SIZE	
16	PROCEDURE	
	SIZE	

!ASSIGN M1EI,(FILE,TESTL)
 !ASSIGN M1PO,(DEVICE,PPA01)
 !RUN (LMN,SLOAD,DSN)

!FIN

Fig. 2. (contd)

ORIGINAL PAGE IS
 (E) POOR QUALITY.

N 76-29326

Biplex Pipelined FFT

R. F. Emerson
Communications Systems Research Section

A method of implementing a pipelined fast Fourier transform (FFT) that makes full use of the elements that comprise it is presented. For a given bandwidth and spectral resolution this approach requires 25 percent less memory, and needs only half the logic speed required for the conventional implementation. Since the spectrum is broken into two parts, two analog-to-digital converters, and attendant mixer-filters, are needed. These two input elements need only operate at half the speed of the one they replace.

I. Introduction

The Biplex pipelined fast Fourier transform (FFT) is an improved hardware implementation of the pipelined FFT processor. After a brief discussion of the FFT algorithm and illustrations of some possible implementations, the Biplex approach will be presented. For a given bandwidth and spectral resolution, the Biplex FFT uses 75 percent of the memory, and logic of half the speed, needed for a conventional implementation. In addition, it saves one stage of complex arithmetic processing—the butterfly (*bf*). This gain is not free. Since the spectrum is split, an additional mixer-filter-converter module is required. Again, however, these elements need operate at only half the speed of those that they replace.

Briefly, the FFT is a method of rapidly computing the digital Fourier transform (Ref. 1). The bandwidth and resolution of the transform are determined by the sam-

pling rate and the number of points used to calculate the transform.

II. Implementation Background

The minimum amount of hardware to implement an FFT can be described by an in-place algorithm, see Fig. 1 (Ref. 1, p. 574). This approach requires storage for N complex points (N is the number of points used to compute the spectrum and must be a power of 2). In Fig. 1 these are represented as dots (•). While four sets of eight are shown, these are the same eight cells with different contents as processing progresses from left to right. At level 0 (zero), the eight complex samples are stored into the locations 0 through 7. At level 3 ($\log_2(N)$ in general) the frequency points are available, indexed in bit-reversed order, and illustrated by the F_i 's in the figure. In this figure there are two directions that represent increasing

time: from top to bottom and from left to right. All points must be processed at level n before processing is started at level $n + 1$. Because of this, only one bf processor is required for the entire transformer. A bf processor performs a complex multiplication and two complex additions. These are implemented with four real multipliers and six real adders. Figure 2 shows, in increasing detail, the bf processor. In the first representation (a), A , B , C , and D are complex numbers, with A and B as inputs to the bf , and C and D as the outputs. The arrow with the letter I near it represents a complex multiplication by the I^{th} coefficient, W^I ($W^I = \text{cis}(2\pi I/N)$). Figure 2b shows this processor in more conventional block diagram form. The arithmetic units of Fig. 2b operate on complex numbers but are implemented by the combination of real arithmetic units of Fig. 2c. Here a complex number, A , is broken into its real A_r , and imaginary, A_i , parts. These are processed separately to produce the outputs.

Returning to Fig. 1 and scanning the storage cells to the left of the diagram, we see that only $N/2$ points need be stored before processing is started since the first bf operation is performed on samples zero and 4 (0 and $N/2$ in general). Only half of the resultants, $N/4$, need be stored at level 1 before processing can begin. Each resultant is, however, two values and therefore two sections of $N/4$ memory are required. For each level from this point on, the storage requirement is one-half the previous stage. By this process of distributing the memory and by adding a bf processor at each level, a pipelined processor can be constructed (Fig. 3). The switches between stages operate at increasing speeds ($T/2$, $T/4$, \dots), and are used to route the resultants through the memories at the proper times. Each switch has two positions—straight through or crossed. The pipeline processor requires storage for $1.5N$ complex points and $\log_2(N)$ bf 's and switches. Both bf 's and memory are used only half the time and operate at the input sampling rate. The next section will discuss several ways of improving this utilization.

III. Improvements Toward Full Utilization

Several approaches have been developed to improve the use of the elements in the pipelined processor.

The memory can be used all of the time by recirculating half the bf resultants in the present stage memory (through switching), before transferring them to the next stage (see Fig. 4). This has the further advantage of requiring only N complex storage locations rather than

$1.5N$. The bf 's in this approach still operate only half the time and must be capable of processing at the sampling rate.

Another approach permits the use of the bf 's all the time and at half the input sampling rate (see Fig. 5). This was derived by observing that two input points are required before processing and that two values result from each operation. Unfortunately, this method needs an additional input buffer of $1.5N$ complex storage cells. The total memory required for this method is, therefore, $3N$. It further requires that these input buffers operate at two different clocking rates.

The new approach presented in this report, Bplex (Fig. 6), takes advantage of the idle time of the processor in Fig. 3 by sampling a different signal when it would have been idle. The pipeline processor is switched between two sets of analog-to-digital converters, each sampling a separate signal. These are represented as complex mixers, CM1 and CM2. This approach can be used to process two independent signals or, by splitting a single signal into two adjacent channels, process one signal at the same resolution with lower speed logic and less memory. The values at various points in this interleaved operation are shown in Table 1. The letter heading of each column refers to a point labeled in Fig. 6. The value a_{ij} is the j^{th} sample of the i^{th} spectrum of the signal from CM1. β_{ij} refers to the signal from CM2. X_{ij} , Y_{ij} , and Z_{ij} are the results of the bf operations on the signal α and R_{ij} , S_{ij} , and T_{ij} are the results of processing signal β . Previous and subsequent spectra would fill the table, but were deleted for clarity. The entries of the table clearly show that each spectrum, while interleaved, is kept separate in time. Each appears at the output as a separate block of data. The decommutation rate is $T/2$.

IV. Benefits and Costs of the Bplex FFT

The benefits of the Bplex FFT arise out of reduced memory size and processor speed. For the same bandwidth and resolution only 75 percent of the memory is required when compared to the in-place algorithm. To illustrate, if a 40-MHz bandwidth signal is to be transformed with a resolution of about 300-Hz it would require 2^{17} or 131,072 complex storage locations using the in-place algorithm. The same requirements can be met using $1\frac{1}{2} \times 2^{16}$ locations with the Bplex processor. (20-MHz bandwidth at ≈ 300 Hz resolution takes 2^{16} locations in-place or $1\frac{1}{2} \times 2^{16}$ pipelined). This saving in memory is accompanied by the saving of one bf processor.

The reduced sampling bandwidth of the Biplex technique reduces the memory and processor speed requirements by the same amount. For the example, the Biplex processor uses logic elements with delays of from 30 to 40 ns rather than the 15 to 20 ns of the more conventional processor.

These benefits are not gained without some cost. Since the full bandwidth is split in two, two analog-to-digital converter elements (complex mixers) are required. These

elements, however, operate at half the speed and, therefore, may be easier and less costly to implement.

V. Conclusions

The use of the Biplex FFT significantly reduces equipment costs when operating near the state-of-the-art speeds. It may also make pipeline techniques applicable and desirable at lower speeds where previously the in-place algorithm was considered most economical.

Reference

1. Rabiner, L. R., and Gold, B., *Theory and Application of Digital Signal Processing*, p. 573ff, Prentice-Hall, Inc., Englewood Cliffs, New Jersey, 1975.

Table 1. Intermediate contents of Biplex FFT

A	B	C	D	E	F	G	H	I	J	K	L	M	N	O
α_{30}														
α_{31}														
α_{32}														
α_{33}														
β_{30}	α_{34}	α_{30}	X_{30}	X_{34}	X_{30}									
β_{31}	α_{35}	α_{31}	X_{31}	X_{35}	X_{31}									
β_{32}	α_{36}	α_{32}	X_{32}	X_{36}	X_{34}	X_{32}	X_{30}	Y_{30}	Y_{32}	Y_{30}				
β_{33}	α_{37}	α_{33}	X_{33}	X_{37}	X_{35}	X_{33}	X_{31}	Y_{31}	Y_{33}	Y_{32}	Y_{31}	Y_{30}	Z_{30}	Z_{31}
β_{34}	β_{31}	R_{30}	R_{34}	R_{30}	X_{36}	X_{34}	Y_{34}	Y_{36}	Y_{34}	Y_{33}	Y_{32}	Z_{32}	Z_{33}	
β_{35}	β_{32}	R_{31}	R_{35}	R_{31}	X_{37}	X_{35}	Y_{35}	Y_{37}	Y_{36}	Y_{35}	Y_{34}	Z_{34}	Z_{35}	
β_{36}	β_{33}	R_{32}	R_{36}	R_{34}	R_{32}	R_{30}	S_{30}	S_{32}	S_{30}	Y_{37}	Y_{36}	Z_{36}	Z_{30}	
β_{37}	β_{34}	R_{33}	R_{37}	R_{35}	R_{33}	R_{31}	S_{31}	S_{33}	S_{32}	S_{31}	S_{30}	T_{30}	T_{31}	
						R_{36}	R_{34}	S_{34}	S_{36}	S_{34}	S_{33}	S_{32}	T_{32}	T_{33}
						R_{37}	R_{35}	S_{35}	S_{37}	S_{36}	S_{35}	S_{34}	T_{34}	T_{36}
										S_{37}	S_{36}	T_{36}	T_{37}	

ORIGINAL PAGE IS
OF POOR QUALITY

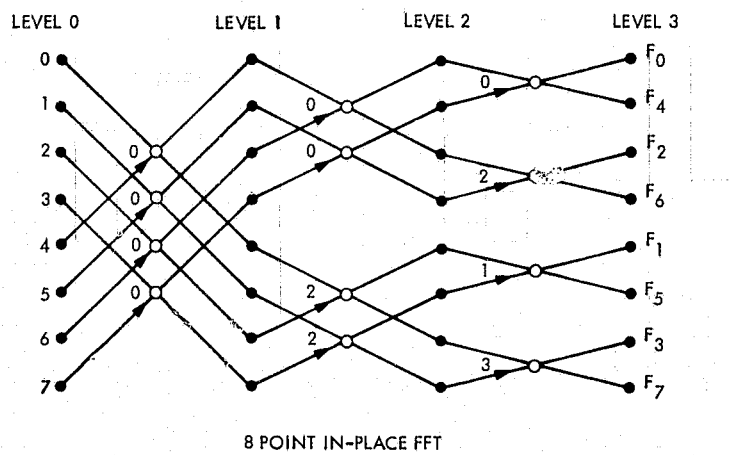


Fig. 1. Schematic of in-place FFT

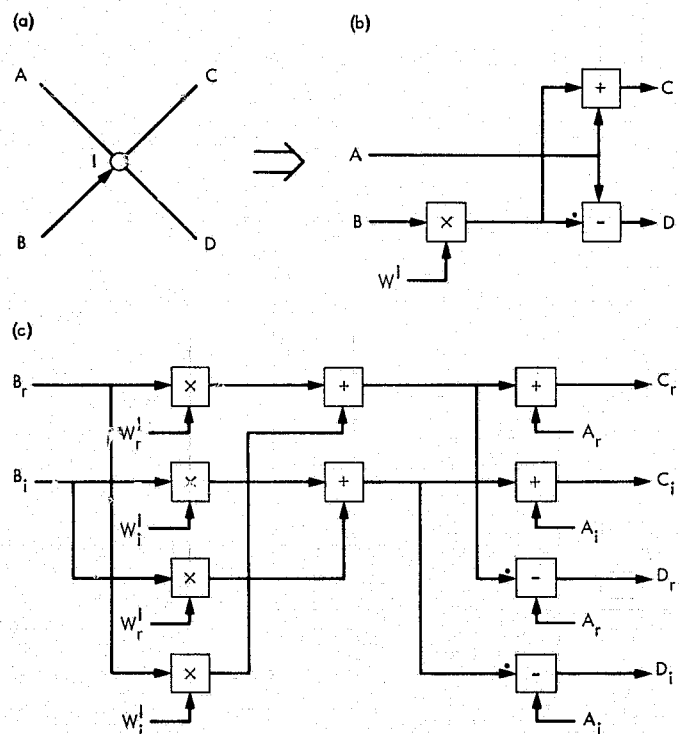


Fig. 2. Butterfly processor and expansion

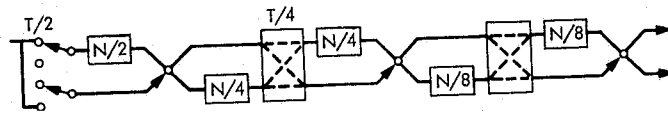


Fig. 3. Pipelined FFT processor

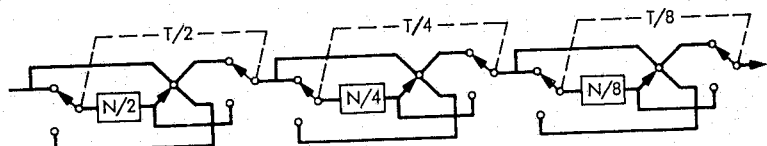


Fig. 4. Memory conservative pipelined FFT

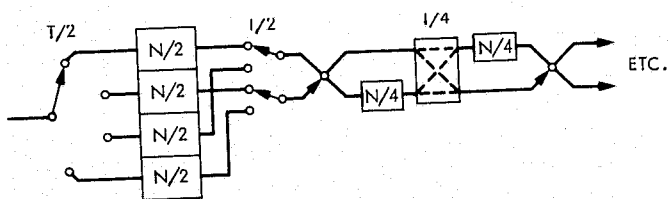


Fig. 5. Half-rate butterfly pipelined FFT

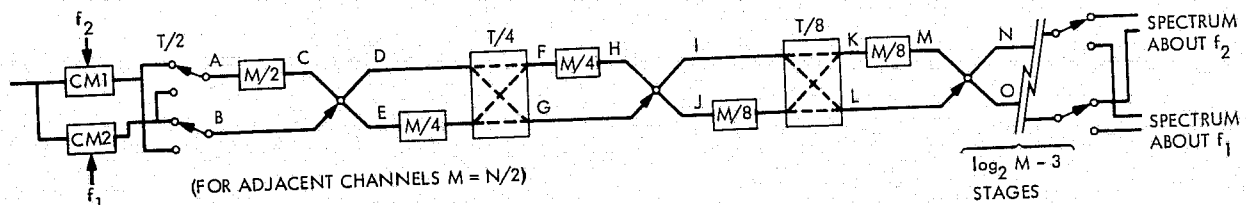


Fig. 6. Biplex FFT

ORIGINAL PAGE IS
OF POOR QUALITY

N 76-29327

Viking Telecommunication Effects of GEOS Satellite Interference Based on Testing at the Madrid Deep Space Station

F. V. Stuhr

Spacecraft Telecommunications Systems Section

S. S. Kent

RF Systems Development Section

J. L. Galvez, B. G. Luaces, G. R. Pasero, and J. M. Urech
Madrid Deep Space Station

In support of the ongoing NASA-European Space Agency (ESA) effort to understand and control possible interference between missions, testing was conducted at the Madrid Deep Space Station from July 1975 to February 1976 to characterize the effect on Viking 1975 telecommunication link performance of Geodetic Earth-Orbiting Satellite (GEOS) downlink signals. The prime use of the data was to develop a capability to predict GEOS interference effects for evaluation of Viking 1975 mission impacts and possible temporary GEOS shutdown. Also, the data would serve as a basis for assessment of the GEOS impact on missions other than Viking as well as for more general interference applications. Performances of the reference receiver, telemetry, and planetary ranging were measured in the presence of various types of GEOS-related interference, including an unmodulated GEOS carrier and simulation of the actual spectrum by an ESA-supplied GEOS suitcase model. This article describes the testing performed at the Madrid Deep Space Station and the potential GEOS interference impacts on the Viking Extended Mission.

I. Introduction

The European Space Agency (ESA) Geodetic Earth-Orbiting Satellite (GEOS) geosynchronous satellite presents a significant interference potential for all NASA

deep space missions since the downlink carrier frequency is in the deep space allocation band at channel 26.2 (2299.5 MHz). The Viking channels are 9 and 20 for the Orbiters and 13 for the Landers. A total GEOS power of -90 dBm is expected on-axis at the 64-meter stations.

The potential GEOS interference impacts of -90 dBm on-axis levels are severe since the reference receiver and the telemetry are likely to be knocked out of lock. This will occur for a spacecraft operating at any channel across most of the deep space band when the desired signals are at or near threshold. In particular, the farthest Viking channel 9 would be affected. GEOS spectrum components as much as 90 dB down from the total GEOS power are of interest for -90 dBm on-axis levels. Such levels are difficult to measure and control so that their presence must be assumed at the worst-case frequency location. The question is how far off the DSN antenna axis must GEOS be geometrically in order not to cause a problem. The answer for Viking appears to be at least 3 degrees. This should preclude any noticeable degradation for normally expected Viking levels with worst-case frequency alignment of the interfering spectrum.

While the immediacy of the interference problem has been alleviated somewhat by the GEOS launch postponement from August 1976 to April 1977, its potential impact remains for the Viking Extended Mission, Mariner Jupiter-Saturn 1977 and Pioneer Venus 1978. The DSN Network Control Center will be responsible for the operating interface with ESA relative to interference and will work in accordance with established detailed procedures and priorities. The tests described herein are in support of the ongoing NASA-ESA effort to understand and control interference.

II. Test Objective

The test objective was to characterize the effect of GEOS interference on Viking Orbiter (VO) and Viking Lander (VL) telecommunication link performance. Use of the test results was planned for:

- (1) Evaluating Viking mission impact and possible GEOS shutdown.
- (2) Evaluating GEOS impacts on missions other than Viking.
- (3) Miscellaneous potential interference applications.

III. Test Approach

An investigative approach was emphasized such that subsets of tests could be performed as required to understand unpredicted degradation mechanisms and to characterize their effects.

- (1) The saturation characteristics of each system element and its performance impact were investigated as a function of signal level and frequency offset.
- (2) A significant unpredicted mechanism was identified during strong signal testing and was independently investigated. Sidebands were found to be generated within the station telemetry and ranging channels due to multiplication of an interfering component by the channel demodulation reference square wave.

IV. Tests Performed

The performance of each downlink function for selected VO and VL modes was measured in the presence of various types of GEOS-related interference at strong and weak signals and with various frequency offset conditions. Table 1 summarizes the tests performed.

A. Types of Interference

Four types of interference were used:

- (1) Unmodulated GEOS carrier (CW).
- (2) Worst-case line spectrum at GEOS frequencies.
- (3) Spectrum simulating typical GEOS condition.
- (4) Spectrum of GEOS suitcase model supplied by ESA.

Most of the tests were performed with CW since this type signal is most effective for investigative results. In particular, the total power effects could be separated from other interference, and telemetry and ranging channel multiplication harmonics could be more easily isolated and their effects evaluated. Also CW data could be more readily extrapolated for GEOS effects on missions other than Viking as well as for more general interference applications. The worst-case line spectrum testing bounded the potential effects on Viking, since line spectrum effects are expected to be the most severe. Use of a simulated GEOS spectrum provided a preliminary look at probable GEOS effects and also provided a look at the effects of a more nearly continuous type of spectrum. Use of the GEOS suitcase model verified that the actual GEOS spectrum will typically produce results predicted based on analysis and tests.

B. Parameters Varied

Strong interfering signals were used primarily to determine saturation effects and the maximum GEOS

level was -85 dBm. Interfering GEOS signals as low as -140 dBm were tested with Viking signals ranging from the maximum predicted orbital design values to specified thresholds.

All of the Viking frequency channels (9, 13, 16, and 20) were tested with at least CW, and the worst-case channel 20 was used most extensively. The nominal GEOS frequency was set for 2299.5 MHz. The GEOS frequency was adjusted to place multiplication harmonics at various offsets from the Viking channel frequency.

Viking telemetry modes tested included uncoded low rate at 33-1/3 b/s (for low rate only and with high rate on) and coded high rate at 500 b/s, 1 kb/s and 8 kb/s.

C. Performance Parameters Measured

The carrier, telemetry and ranging performance were each measured.

- (1) Carrier performance included suppression in the receiver, phase jitter and the maximum interference level at which the receiver could acquire a Viking signal of a given level.
- (2) Telemetry performance included saturation levels in the telemetry string, drop-lock conditions, and ST_B/N_0 degradation. Bit and word error rates were also measured. However, error rate results agreed well with ST_B/N_0 and only ST_B/N_0 was reported for brevity.
- (3) Ranging performance consisted of P_R/N_0 degradation. DRVID standard deviation was also measured. However, DRVID results agreed well with P_R/N_0 and only P_R/N_0 was reported for brevity.

In addition to measuring performance of various telecom links, the simulated GEOS spectrums were examined to assure they were as predicted and to search for significant spurious signals.

V. Prediction Models

Models were developed in some cases to compare with observed test results and can be used to predict effects in flight.

A. Receiver Carrier Suppression

A model was generated for Viking carrier suppression in the RF receiver assuming a soft limiter for each saturating module:

$$\alpha = \frac{1 + P_V/P_L + P_N/P_L}{1 + P_V/P_L + P_N/P_L + P_I/P_L}$$

where

α = suppression factor

P_V = Viking power

P_N = noise power

P_I = GEOS interfering power

P_L = limit level power

For P_L and P_I much greater than P_V or P_N , this simplifies to

$$\alpha \approx \frac{1}{1 + P_I/P_L}$$

The S-band mixer and 50 MHz intermediate frequency (IF) amplifier and mixer are the most significant modules, since saturation in other modules occurs at substantially higher levels. The power levels for the S-band mixer are referenced at the maser input and P_L is -79 dBm (based on measured data). For the 50-MHz IF, the closed loop automatic gain control (AGC) increases the gain to compensate for suppression of the Viking signal. This also increases the GEOS "linear" output and consequently the suppression such that a cumulative effect occurs. At equilibrium, the Viking output level is -81 dBm (by loop design), while the "linear" GEOS output has increased by the amount Viking has been suppressed. For the 50-MHz IF suppression factor, powers are referenced to the module output, P_L is -10 dBm (based on measured data) and P_I is the "linear" GEOS output. The total receiver suppression is the sum of the values for the S-band mixer and 50-MHz IF modules. Frequency separation considerations are excluded from the above equations and can be accounted for by reducing the interference level according to bandwidth losses.

B. Interfering Sidebands Generated Within Receiver

Interfering sidebands are generated within the receiving station telemetry and ranging channels due to multiplication of an incoming interfering component by the channel demodulation reference square wave. In the case of telemetry, this occurs in the Subcarrier Demodulator Assembly (SDA) quad generator, where the reference is a square wave at the subcarrier frequency. In the case of ranging, this occurs in the 10-MHz IF amplifier and phase switch, where the reference is a square wave at the clock frequency of about 516 kHz (for postacquisition tracking). The odd multiplication harmonic nearest the

channel 10-MHz center frequency is the closest odd integer to $\Delta f/f_{REF}$ and is nominally at a frequency offset of

$$\Delta f_N = \Delta f - Nf_{REF}$$

where

N = number of multiplication harmonic nearest the desired signal center frequency

Δf_N = frequency offset of nearest harmonic from the desired signal frequency

Δf = nominal frequency separation between interference and the desired signal.

f_{REF} = frequency of channel reference square wave

The level of a given multiplication harmonic produced by an interfering signal line component is determined from

$$P_N = P_I \left(\frac{2}{N\Pi} \right)^2$$

where

P_N = power in the n th multiplication harmonic

P_I = power in the interfering signal line component

Frequency separation considerations are excluded from the equation for P_N and can be accounted for by reducing the interference level according to bandwidth losses.

C. Condition for Telemetry SDA Drop-Lock

The telemetry channel SDA will be knocked out of lock when the interfering sideband is approximately equal in power to the desired telemetry data, with a frequency offset from the desired signal of half the data symbol rate. The level of an interfering signal line component which can produce such a multiplication harmonic is

$$P_I = P_D \left(\frac{N\Pi}{2} \right)^2$$

where

P_D = desired signal telemetry data power

D. Condition for Interfering Signal Spectral Density = N_0

When the interfering signal spectral density is nearly continuous and is approximately equal to the receive

noise spectral density in a given channel, degradation of approximately 3 dB will occur. Assuming the interfering signal spectrum to be uniform across a given bandwidth, the level of the interfering signal data power which can produce multiplication harmonic spectral density equal to the receive noise spectral density in the channel of interest is

$$P_{ID} = kT_{sys}B \left(\frac{N\Pi}{2} \right)^2$$

where

P_{ID} = interfering signal data power

k = Boltzmann's constant

T_{sys} = receiving system noise temperature

B = bandwidth in region of interfering spectrum whose multiplication harmonic is near the frequency of the desired signal over which power is uniform.

VI. Carrier Tracking Test Results

Carrier tracking performance was evaluated based on the measurement of carrier suppression in the receiver and the effects on receiver acquisition and coherent doppler jitter. The higher levels required for acquisition and the increased doppler jitter in the presence of interference are each the result of suppression. While data discussed below were measured using a CW signal, results for other GEOS spectrums were in agreement on a total power basis. That is, since the GEOS spectrum is narrow as compared to the receiver bandpass and the frequency between GEOS and the Viking channels, total GEOS power is the important parameter for receiver saturation effects.

A. Carrier Suppression

Figure 1 shows the Viking carrier suppression in dB measured by AGC for the worst-case channel 20 as a function of CW interference level at the GEOS frequency. The predicted suppression using the model of paragraph VA is shown for comparison.

B. Acquisition Levels

Table 2 summarizes the maximum CW interference levels at which the Viking carrier could be acquired with the Viking frequency at a static value equal to the receiver rest frequency for channels 9, 13, 16 and 20.

C. Doppler Phase Jitter

Figure 2 shows doppler phase jitter as a function of CW interference level for the worst-case channel 20.

VII. Telemetry Test Results

Levels were measured at which telemetry string saturation occurred, but the saturation effects were found to be secondary to the degradation by multiplication harmonics. Telemetry ST_B/N_0 degradation and the level at which drop-lock occurred were measured for various interference conditions resulting from harmonics generated by SDA reference multiplication of the GEOS input. Line spectrum multiplication harmonic effects were found to be the most severe. Multiplication harmonic energy from near-continuous interfering spectrums has a significant effect only as the level approaches that of the inherent receiver noise. Since the line spectrum effects are most severe, the CW case provides an excellent bounding measure of degradation effects and results can be easily extrapolated to other cases. In particular, the results for the GEOS carrier with modulating spectrums are in agreement with the CW case on a carrier power basis. That is, the modulated carrier is the strongest component producing harmonics from multiplication and its effect dominates over modulating components. Further, any case where line interference is involved will differ from the CW only by the level of the interfering line.

A. Telemetry Saturation

The 10-MHz SDA is the first stage to saturate and does so for a level of interfering GEOS power within the telemetry channel bandwidth of -95 dBm, referenced at the traveling-wave maser (TWM) input.

B. Telemetry Drop-Lock Due to Multiplication Harmonics

Table 3 summarizes the levels of CW interference for drop-lock of Viking telemetry at an ST_B/N_0 of 8 dB with the GEOS frequency adjusted for the nearest multiplication harmonic offset at half the telemetry symbol rate from the Viking operating frequency. With the interfering harmonic slightly offset from the Viking operating frequency, interfering levels for drop-lock were about 2 dB weaker than for half the symbol rate. With the harmonic near the edge of the band, drop-lock levels were about 16 dB stronger than for half the symbol rate. It is noted that for interference exactly at the Viking operating frequency, the effect is less severe than with a slight offset. Drop-lock occurs at a level about 6 dB stronger with no

offset than with a slight offset. Based on the results of Table 3, the differences in severity of interference effects relative to channel 20 are about 9 dB for channel 16, 17 dB for channel 13 (with orbiter subcarriers), and 26 dB for channel 9.

While the above results are for a CW signal, results for other GEOS spectrums were in agreement on a carrier power basis, since the modulated carrier dominates over the modulating components.

C. Telemetry ST_B/N_0 Degradation by Multiplication Harmonics

Telemetry ST_B/N_0 degradation data presented below are limited to:

- (1) Multiplication harmonic interference.
- (2) Worst-case Viking channel 20.
- (3) Interfering spectrum cases of CW and the GEOS suitcase model.

The CW interference is the worst case since lines produce the most severe degradation and the power is confined to a single line. The suitcase model is the expected case and includes both lines (sidebands of the high-rate telemetry subcarrier at 190.5 kHz) and near-continuous portions (modulating data energy).

Figures 3, 4, and 5 show three Viking telemetry modes: cruise at 33-1/3 b/s (uncoded low rate only), coded high rate at 1 kb/s and coded high rate at 8 kb/s, respectively. Each is with an unmodulated GEOS carrier (CW) adjusted in frequency for the nearest multiplication harmonic at various offsets from channel 20. The following observations are made:

- (1) While the most severe ST_B/N_0 degradation occurs for the CW line at a slight offset from channel 20, an offset of half the Viking symbol rate is only slightly less severe.
- (2) Degradation with the CW line exactly on channel 20 is much less severe than a slight offset.
- (3) Degradation is least severe for 33-1/3 b/s and coded 1 kb/s with the CW line near the telemetry band edge. The severity is reduced by about 13 dB relative to the worst-case slight offset.
- (4) For symbol rates greater than 5000 per second, the bandwidth of 500 kHz is sufficiently wide that an odd multiplication harmonic will always fall within the bandwidth. This is because the odd harmonics

from multiplication with the Viking subcarrier are spaced at 480 kHz, or twice the subcarrier frequency of 240 kHz. This is important since the use of ground frequency tuning can minimize but cannot remove the interference.

(5) When two harmonics fall in the telemetry bandwidth simultaneously, increased degradation over the case of a lesser frequency offset is produced. This is illustrated in Fig. 5 for the 8-kb/s case, where the maximum offset of 240 kHz produced a more severe effect than 200 kHz.

Figure 6 shows the Viking coded high-rate telemetry at 1 kb/s with the GEOS suitcase model spectrum. The GEOS frequency was adjusted to place the multiplication harmonic interference at a frequency offset of half the symbol rate from channel 20. The three cases shown are for the multiplication harmonic interference produced by the modulated GEOS carrier, the first GEOS telemetry subcarrier sideband, and the strongest portion of the GEOS telemetry data spectrum. The following observations are made:

- (1) The modulated GEOS carrier produces the most severe degradation due to its line structure and relative strength. It is less severe than the CW case of Fig. 4 by the amount of modulation suppression (approximately 5.5 dB).
- (2) The first GEOS telemetry subcarrier sideband produces degradation less severe than the modulated carrier by about the difference in levels of the spectral lines (about 12 dB).
- (3) The strongest portion of the GEOS telemetry data spectrum produces only slightly less degradation than the subcarrier sideband. While the maximum data spectrum level is slightly greater than the subcarrier sideband, line structure is less pronounced than is the subcarrier sideband. The effect of a more continuous spectrum is similar to that of increased noise and is less severe than for a well-defined line.
- (4) Some portion of the GEOS spectrum will always produce multiplication harmonics in the Viking telemetry bandwidth for any channel, regardless of the relative frequency alignment or the Viking telemetry bandwidth. This is important since the use of ground tuning can only minimize the effect. The minimum effect should occur with on-channel location of the multiplication harmonics from the GEOS data spectrum in the region of 143 kHz from the GEOS carrier (halfway between the subcarrier

and the maximum data level). It was verified by measurement using a simulated GEOS spectrum for the coded 1-kb/s case that this portion of the data spectrum was about 5 dB less severe than the strongest portion.

(5) With frequency alignment for multiplication harmonics of the 143-kHz data spectrum region, the 50-kHz telemetry bandwidth for 1 kb/s tends to preclude harmonics from either the subcarrier (at 190.5 kHz) or the strongest portion of the data spectrum (at about 95 kHz). However, for symbol rates greater than 5000 per second the 500-kHz telemetry bandwidth will allow harmonics of the carrier, subcarrier, and data spectrum simultaneously. While no data were measured for the 500-kHz bandwidth using the GEOS data spectrum, degradation can be bounded by the interference levels for the CW case and as much as 18 dB stronger. For example, with coded 8 kb/s on channel 20, the modulated GEOS spectrum will produce drop-lock for a total GEOS power of no less than about -117 dBm (CW case) and no greater than about -99 dBm. The 18-dB difference assumes that the strongest level required is that of a modulated carrier near the band edge. The measured data in Fig. 5 show that the ninth CW harmonic at a 200-kHz offset is about 13 dB less severe than for the worst-case slight offset. To this, 5-dB modulation suppression must be added. The 1-kb/s data of Fig. 6 also tend to confirm this, since the strongest level for the least of the major interfering spectrum components is about 12 dB less than for the modulated carrier.

VIII. Ranging Test Results

For interfering signals outside the narrow channel bandwidth, ranging signal suppression due to overall receiver saturation is the dominant effect and is the same as for the carrier. For signals within the ranging channel bandwidth, additional degradation occurs due to ranging module saturation and the appearance of interference as noise at the ranging detector. Investigative tests show the low-pass (LP) dc amplifier to be the first ranging channel saturation component. The two most significant bandwidths are the ± 225 Hz of the crystal filter (about 10 MHz) and the <1 Hz of the LP dc amplifier. Figure 7 shows the Viking channel 20 ranging P_R/N_0 degradation as a function of CW interference level for various frequency offsets from the Viking operating value. The data were obtained for a downlink carrier of -152 dBm (mini-

mum level at maximum range) and a P_r/N_0 of +12 dB (in the absence of interference). The interfering sideband was the nearest harmonic (5th) produced by multiplication of the interfering carrier by a 516-kHz reference square wave. This is not an expected Viking condition since the potential GEOS/Viking frequency separation will not allow a GEOS carrier multiplication harmonic so near any Viking channel. The nominal separation between any Viking channel and the GEOS frequency places the nearest odd ranging clock harmonic at an offset from the Viking channel greater than the combined uncertainties of the Viking and GEOS operating frequencies and the DSN receiver offset from the channel 20 center frequency to account for doppler. Since the DSN transmitter frequency is offset to account for the Earth-Mars uplink doppler, the DSN receiver will be offset only by the amount of the downlink Earth-Mars doppler. The nominal offsets of the nearest odd ranging clock harmonics are 300 kHz for channels 9 and 20 and 227 kHz for channel 13. The downlink Earth-Mars doppler will not exceed 125 kHz, and the combined frequency uncertainties will not exceed 90 kHz. While interference is highly unlikely for Viking in the postacquisition mode (516-kHz clock only), it is the most meaningful mode to test and is useful for extrapolation to other cases. Observations of data with the 516-kHz clock 5th harmonic at various frequency offsets from the Viking channel 20 are made as follows:

- (1) Figure 7 shows that the worst-case degradation is for the interfering multiplication harmonic aligned with the Viking channel 20. Here the effect as increased noise in the detection bandwidth dominates.
- (2) For increasing frequency offset (1.2 to 33.6 Hz in Fig. 7), the LP dc amplifier bandpass characteristic will increasingly attenuate the interfering harmonic and reduce its effect as increased noise until the noise and suppression effects are constant relative to each other.
- (3) After frequency offsets for which the relative noise and suppression effects are essentially constant (33.6 Hz in Fig. 7), added offset will merely attenuate both effects equally by the amount of the crystal filter insertion loss. The attenuation for an offset slightly beyond the ± 225 -Hz bandwidth (500 Hz in Fig. 7) becomes a nearly constant 20 dB.
- (4) For offsets significantly beyond the ± 225 -Hz crystal filter bandwidth, levels of interference required to produce LP dc amplifier saturation and increased detector noise will first cause receiver saturation.

That is, outside the ranging channel bandwidth, receiver saturation will be the predominant interference effect.

IX. GEOS Spectrum Examination

The spectrum of the GEOS suitcase model was examined to assure that it was as predicted and to search for any spurious signals. The regions within channels 9, 13 and 20 were obtained carefully for the unmodulated carrier as well as the modulated case with a total GEOS power of -85 dBm. The worst-case line spectrum was examined as well, but only in the region of channel 20. In all cases the spectrum was essentially as predicted and no spurious signals were found. However, signals were found which were not GEOS output components but were intermodulation products of well-defined spectral lines generated within the saturated receiver 50-MHz IF amplifier and mixer. This was confirmed when the signals disappeared with the addition of a ± 1 -MHz filter at the 50-MHz IF module input. These signals had levels as strong as -155 dBm in channel 20. Acquisition of these signals required a special operating procedure due to the saturation condition. By using manual gain control (MGC) at an appropriate level some suppression could be avoided.

X. Potential Mission Impacts

The expected GEOS level along a 64-m antenna bore-sight is -90 dBm. At this level the protection normally afforded by frequency separation is significantly reduced. This is because satellite signals far removed from the satellite carrier are of concern even if they are as much as 90 dB weaker than the carrier. Such signals cannot be effectively controlled or even accurately measured and must be assumed to occur. More importantly, as the tests reported herein show, a satellite carrier near the deep space band can cause interference even at relatively weak levels due to generation of harmonics from multiplication by data channel demodulation square wave references.

A. Viking Extended Mission

A summary of the planned GEOS orbit geometry for the April 1977 launch has been supplied to NASA by ESA. These data are presently under evaluation to determine the times of potential GEOS interference to the Viking Extended Mission, if any. Table 4 is a summary of the worst-case potential effects for each Viking telecommunication link should GEOS cross the main beam of a DSN antenna which is tracking Viking.

It can be seen that the worst-case frequency alignment will knock the high-rate telemetry links out of lock for any Viking channel with the 64-m on-axis GEOS level of -90 dBm. Further, regardless of frequency alignment, high-rate drop-lock on channel 20 will occur for a total GEOS power level of -99 dBm or lower. Hence, GEOS shutdown appears to be necessary when GEOS is located near the 64-m boresight look direction for Viking. An angle of 3 deg off boresight should produce a total GEOS level of about -140 dBm (for $P_c/P_r = -0.5$ dB), which would place the ninth GEOS carrier multiplication harmonic about 22 dB below the Viking data power on channel 20. Measured data indicate that this relative level of interference, even for the worst-case frequency alignment, would produce negligible telemetry ST_r/N_0 degra-

dation (<0.1 dB). This is in agreement with an analysis by M. A. Koerner (Ref. 1). It should be noted that potential degradation to the ranging channel during acquisitions remains even for the -140 dBm GEOS level. However, for the expected Viking P_r/N_0 of about 20 dB such degradation depends on a frequency alignment to within 5 or 10 Hz. Such a condition is highly unlikely.

B. Other Missions

As shown by Viking testing, any channel in the deep space band can be degraded by a satellite downlink near the band having sufficient power. Hence, all NASA deep space missions are potentially susceptible to impacts from GEOS as well as other satellites, present or future.

Reference

1. Koerner, M. A., *Effect of Interference on a Binary Communication Channel Using Known Signals*, Technical Report 32-1281, Jet Propulsion Laboratory, Pasadena, Calif., Dec. 1, 1968.

Table 1. Summary of tests conducted to determine Viking susceptibility to GEOS interference

Measured performance		GEOS interference						Viking signals			
		Spectrum			Interfering component	Offset ^a of interference from Viking frequency	Level, dBm	Channel	Data rate, b/s	Level	
Function	Parameter	CW	Line	Simulated							
Carrier	Signal suppression	X	X	X	X	Total power	GEOS @ Ch 26.2	-85 to -105	20,16, 13 and 9	N/A	-140 to -165 dBm
	Acquisition while saturated	X		X	Same	Same	Meas	Same	N/A	Same	
	Jitter	X	X		Same	Same	Same	20	N/A		-155 to -165 dBm
	False lock		X		X	Intermods within saturated receiver	Random	-85	20,18 and 9	N/A	N/A
Telemetry	Level at which saturation occurred	X			Power in telemetry BW	GEOS @ Ch 26.2	-95	20	8k		-145 dBm
	Drop-lock and ST_B/N_0 degradation	X			Harmonic ^b of CW	0 to edge of telemetry channel BW	-105 to -135	20	33-1/3, 1k and 8k	5 and 8 dB	
		X	X	X	Harmonic ^b of modulated GEOS carrier	Half Viking data symbol rate	Same	20	33-1/3 and 1k	$ST_B/N_0 = 8 \text{ dB}$	
		X	X	X	Harmonic ^b of strongest line	Same	Same	Same	Same	Same	
Ranging	P_R/N_0 degradation	X			Harmonic ^b of continuous spectrum between carrier and first line	Same	Same	Same	Same	Same	
					Harmonic ^c of CW	0 to 500 Hz ^d	-95 to -165	20	$T_{INT} = 1 \text{ min}$	$P_R/N_0 = 12 \text{ dB}$	

^aGEOS adjusted where required from its nominal value of 2299.5 MHz.

^bHarmonics are those generated due to multiplication of given signal by the telemetry subcarrier demodulation reference.

^cHarmonics are those generated due to multiplication of CW by the ranging clock demodulation reference.

^dLow-pass (LP) dc amplifier BW $< 1 \text{ Hz}$ and crystal filter BW $= \pm 225 \text{ Hz}$ in 10-MHz stage.

Table 2. Maximum GEOS signal level for Viking receiver acquisition (dBm)

Viking channel	Viking signal level					
	-140	-145	-150	-155	-160	-165
20	-85 ^a	-85 ^a	-89	-91	-97	-102
16	-85 ^a	-85 ^a	-87	-93	-97	-103
13	-85 ^a	-85 ^a	-85 ^a	-89	-95	-101
9	-85 ^a	-85 ^a	-85 ^a	-85 ^a	-85 ^a	-91

^aNo stronger signal level was checked.

Table 3. Predicted and measured CW power for Viking telemetry drop-lock at an $ST_B/N_0 = 8$ dB with the interfering harmonic offset at half the data symbol rate

RF channel	Viking signal				CW interference		
	Mode	Telemetry	b/s	Coding	Multiplication harmonic number	Total power, dBm	Measured
20	High rate	8k	8k	Block	9	-114.5	-115
			1k	Block	9	-123.5	-124
		33-1/3 ^a	33-1/3	None	95	-118.0	-115
16	Cruise	33-1/3	33-1/3	None	95	-118.0	-118
			8k	Block	15	-103.5	-106
13	High rate	8k ^b	8k ^b	Block	21	-102.0	-98
			500	Block	67	-104.0	-101
9	High rate	8k	8k	Block	27	-90.8	-89

^aLow rate channel on 24-kHz subcarrier in the high-rate mode with coded 1 kbps simultaneously on a 240-kHz subcarrier.

^bThis case is for orbiter telemetry data rate and subcarrier to compare relative channel separation effects. The lander on channel 13 will in practice transmit a maximum of 500 b/s on a 72-kHz subcarrier.

ORIGINAL PAGE IS
POOR QUALITY

Table 4. Summary of worst-case potential Viking interference effects due to GEOS based on test data

Function	Parameter	Interference condition ^a	Mode	Viking degradation ^b		
				20	13	9
Carrier	Signal suppression	Saturation	All	-0.7 dB	-0.2 dB	-0.1 dB
	Interference level for acquisition	Saturation	All	None ^c	None ^c	None ^c
	Increased jitter	Saturation	All	<1 deg	None	None
Telemetry	Total interference power for drop-lock ^d	GEOS carrier multiplication harmonic at slight offset from Viking frequency ^e	33-1/3 (LRT only)	-103	-92	-78
			33-1/3 (HRT)	-117	-98	-91
			500	N/A	-103	N/A
			8k	-117	N/A	-91

^aGEOS carrier modulated by low speed data only with $P_c/P_T = -0.5$ dB; $P_c/P_T = -5.5$ dB when high speed data on. Carrier frequency near 2299.5 MHz and maximum total power = -90 dBm.

^bWith expected total Viking power of -140 dBm for VO and -147 dBm for VL, each at maximum range.

^cNo degradation since the carrier could be acquired even under the worst-case saturating level of -90 dBm.

^d1 dB of ST_B/N_0 degradation occurs for interference levels about 5 dB weaker than for drop-lock.

^eDrop-lock occurs at stronger signal by about 2 dB for a frequency offset of half the data symbol rate and by about 12 dB at edge of telemetry BW. Drop-lock occurs for stronger signal by about 6 dB for interference exactly at the Viking frequency.

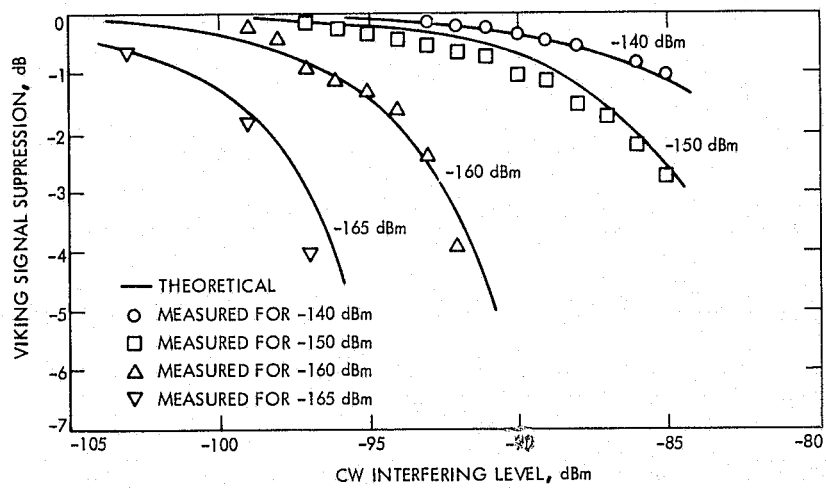


Fig. 1. Theoretical and measured reference receiver signal suppression on channel 20 vs CW interfering level for various Viking carrier levels

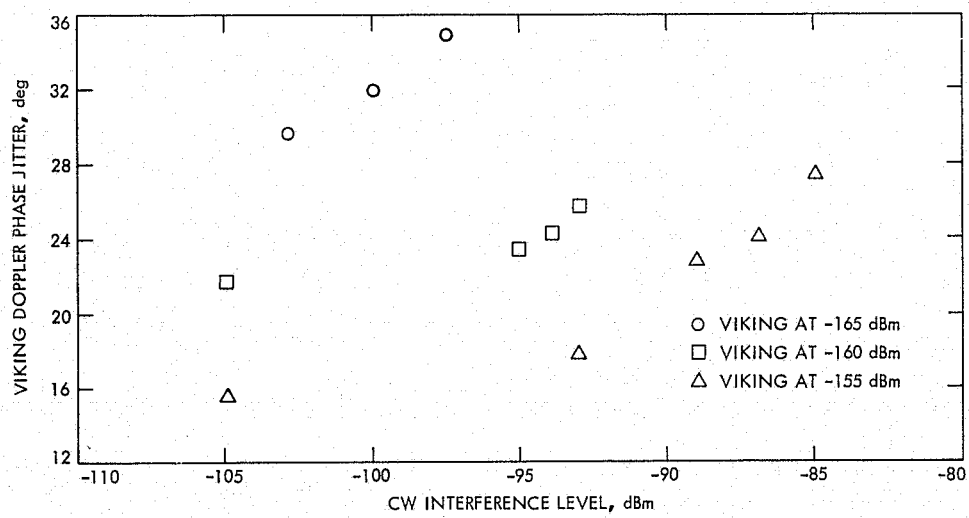


Fig. 2. Measured doppler phase jitter on channel 20 vs GEOS level for various Viking carrier levels

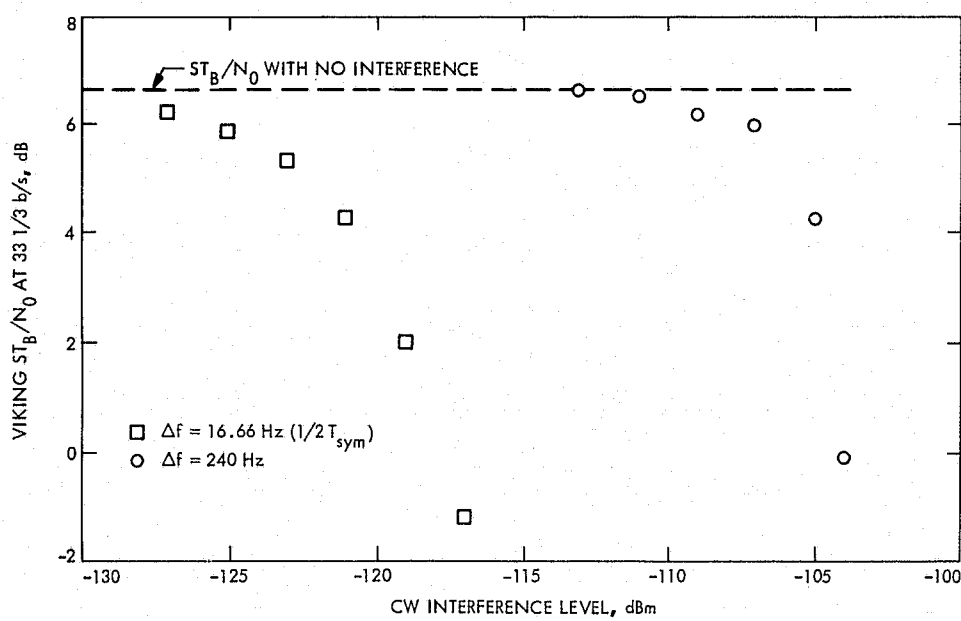


Fig. 3. Measured cruise mode 33-1/3 b/s telemetry ST_B/N_0 degradation on channel 20 vs CW interfering level for various frequency offsets

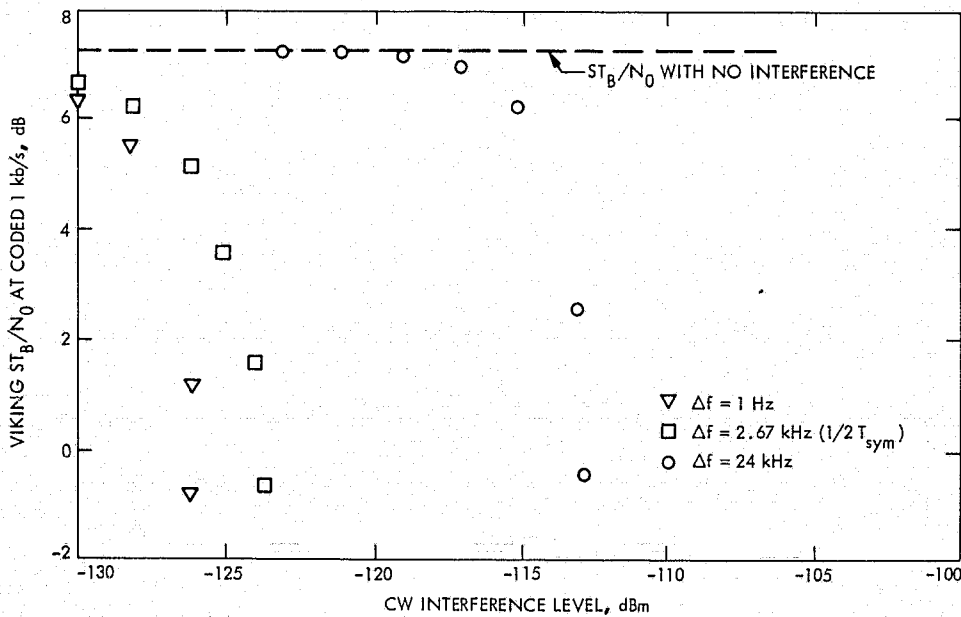


Fig. 4. Measured coded 1-kb/s telemetry ST_B/N_0 degradation on channel 20 vs CW interfering level for various frequency offsets

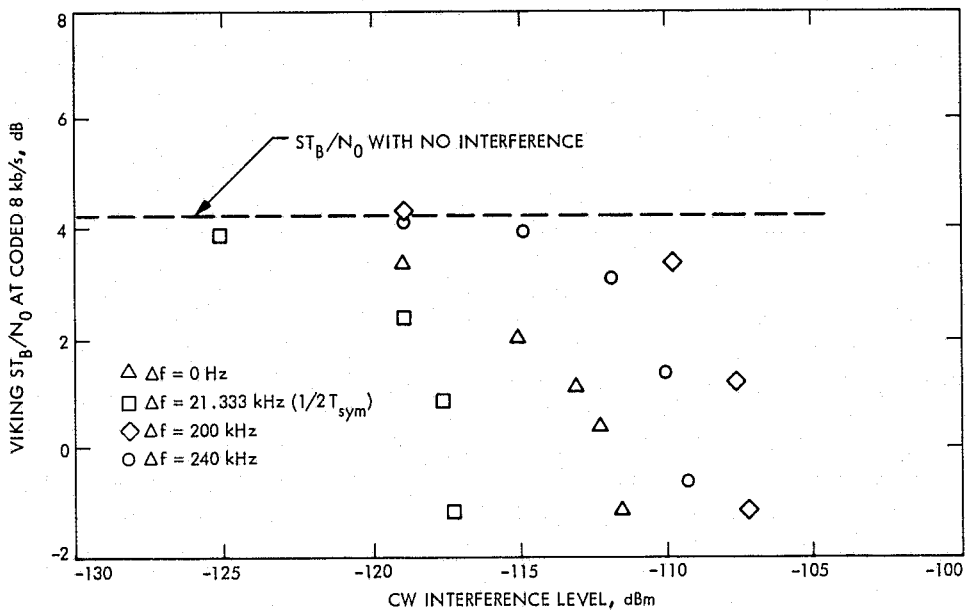


Fig. 5. Measured coded 8-kb/s telemetry ST_B/N_0 degradation on channel 20 vs CW interfering level for various frequency offsets

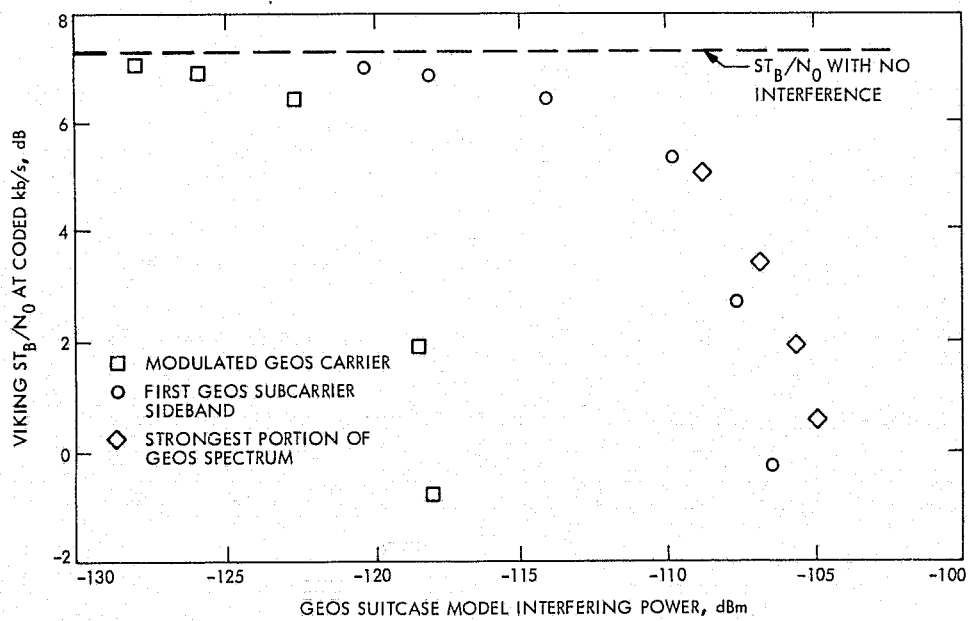


Fig. 6. Measured coded 1-kb/s telemetry ST_B/N_0 degradation on channel 20 vs GEOS suitcase model interfering power for various portions of the interfering spectrum to produce harmonics at offset of half the Viking symbol rate (2.67 kHz)

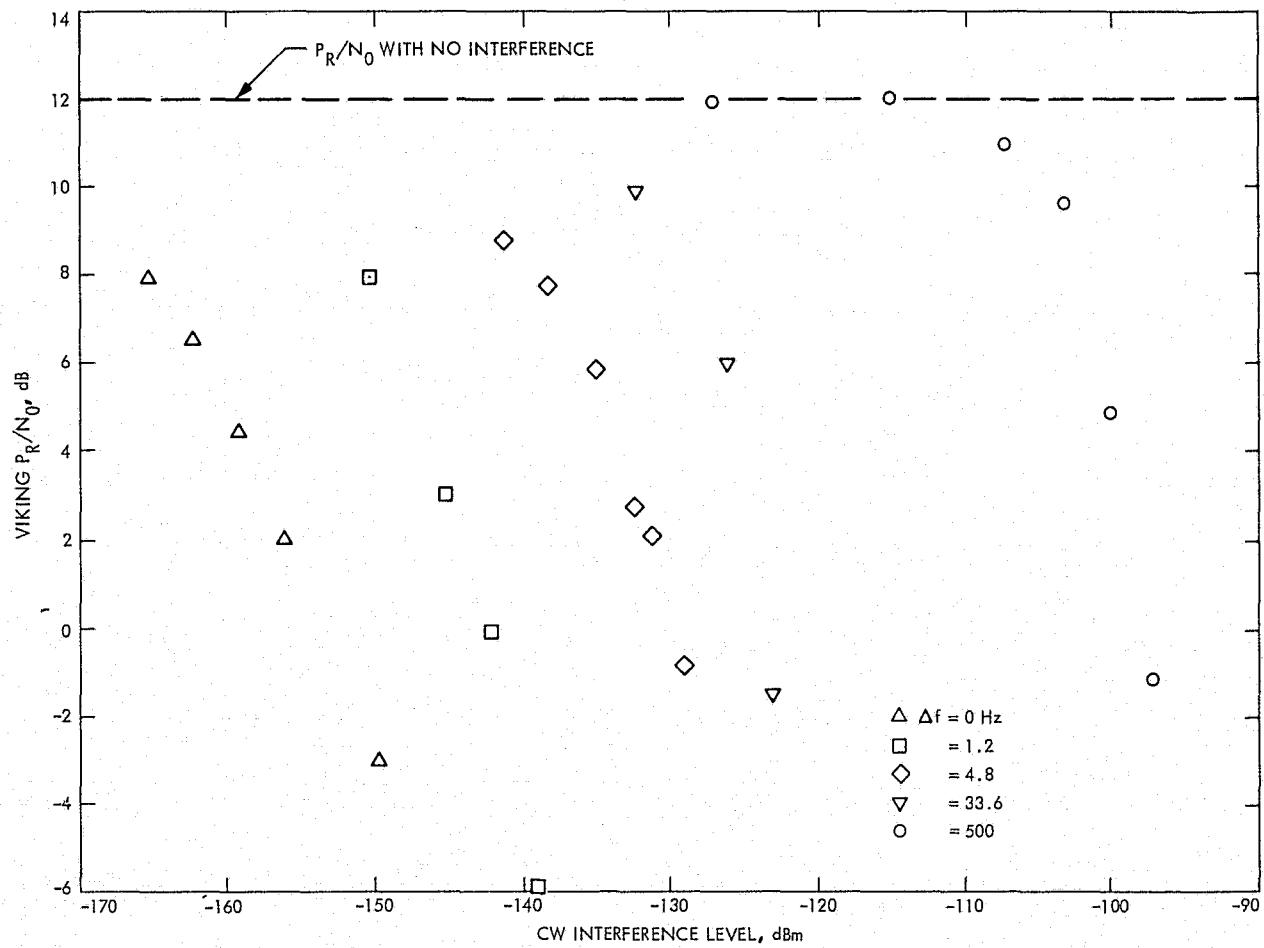


Fig. 7. Measured ranging P_r/N_0 degradation on channel 20 vs CW interfering level for various frequency offsets

N 76-29328

DSN Standard Interface Adapter and Buffer Assembly Used in the Mark III Data System

T. Anderson
DSN Data Systems Development Section

This article describes the DSN Standard Interface Adapter and Buffer Assembly (referred to as the "900/SIA") used to effect interface compatibility between the Xerox Data Systems 920 computer (XDS 920) and the Mark III Data System (MDS) processors. It sets forth the requirements based on the differences between the two systems. Described are the operational characteristics and general design strategy as well as certain efficient implementation techniques used. From a software standpoint, the transfer protocol is discussed to a level of detail sufficient for its operation.

I. Mark III Data System Requirements

The Mark III Data System (MDS) retains the Digital Instrumentation Subsystem (DIS) 920, which is then required to communicate with the MDS Modular Computer Systems (MODCOMP) processors through the Star Switch Controllers (SSCs). Because of the gross incompatibilities between the 920 and the DSN Standard Interface, an interface adapter and buffer is required. The incompatibilities exist in the areas of:

- (1) Speed of operation.
- (2) Data format.
- (3) Interface protocol.
- (4) Electrical signals.

The 920 cycle time is $8 \mu s$, requiring an average of 5 to 6 cycle times per word transfer (i.e., 40 to $48 \mu s$), while the Standard Interface transfer rate may be as high as 500 kHz (i.e., $2 \mu s$ per word transfer), depending on cable length. The 920-word format is 24 bits per word, while the word format of the MDS processors is 16 bits per word and the Standard Interface word format is 8 bits per word.

The 920 I/O register mode interface control is based on outbound requests in the form of EOM (energize output medium) code words and inbound single line "interrupt" responses.

The 920 then operates on a pulse technology where the event of a pulse must be stored in the adapter as must

the sequence of succession of events. The Standard Interface consists of an outbound "request to transmit" signal, an inbound "response," i.e., ready to receive signal, and an outbound "data available" or "data ready" signal. The 920 control signals are short-duration pulses (8 V), one for the beginning and one for the end of an operation, while the Standard Interface signals are "levels" (5 V) which prevail during an operation, the beginning of the level signaling the beginning of the operation and the end of the level the end of the operation. Control signal memories for the Standard Interface need then not be furnished in the interface adapter.

The 920 and the Standard Interface parameters of concern to the adapter are described in the following sections.

II. Standard Interface, General Description

The MDS consists of a large number of processors and peripherals, many from different manufacturers and with gross interface incompatibilities. Each device has been made to conform to the Standard Interface. The Standard Interface uses an 8-bit parallel (byte) transfer and the transfer control signals are simple. They consist of a unidirectional "request to transmit" signal, one in each direction, a "response" and a "ready" signal, both bidirectional. Electrically these signals are 5-V signal levels, where +5 V is the idle level and GND is the active level.

III. 900/SIA Adapter Buffer Requirements

Systems analysis has concluded that transmission between the DIS 920 and an MDS processor over a single register would create too large an overhead time for the MDS processor, which would then be inefficiently used. A data memory or buffer is therefore included in the adapter. The capacity of this buffer is equal to a high speed data block, or approximately 1200 bits. The buffer, which is a rate and format buffer, can be functionally visualized as a shift-register with the first data in being the first data out.

Systems analysis considerations further suggest the use of two identical buffers, one in each direction. If an MDS processor were to request to transmit to the adapter buffer while the buffer was being filled by the 920, either the partial block from the 920 would have to be discarded or the processor would have to reconfigure its I/O and be faced with an additional overhead. The amount of hardware required for switching of data and control, for a

single buffer to be able to operate in either direction, is considerably larger than an additional buffer without such switching.

The operation of such a buffer is as follows: When transmitting from the DIS 920 to the MDS processor, data are metered out from the 920, through its register I/O POT (parallel output) connections, to the adapter buffer until a full data block has been assembled in the buffer. At that instant, the adapter requests to transmit this data block to the MDS processor at a high rate through the SSC. When the buffer has been fully unloaded it is again available to be loaded and the sequence is repeated.

When transmitting from an MDS processor to the 920, the sequence is essentially reversed. The processor requests to transmit a complete data block at high speed to the adapter buffer.

IV. 900/SIA/Design Parameters, Summary

The design parameters for the 920/SIA are summarized as follows (for reference see Fig. 1):

- (1) Two identical channels are provided, one each on directly interchangeable subassemblies.
- (2) For each channel, four distinctly identifiable interfaces exist.
- (3) Two of the four interfaces, to and from the SSC through the SIA, share one port.
- (4) One set of PIN/POT connections is shared between the two channels.
- (5) The POT connections are common to both channels.
- (6) The PIN connections are collector OR-controlled between the channels.
- (7) The adapter operates at maximum speed commensurate with the access times of the buffers.
- (8) Because of the timing specifications between Input Data, Address and Load Pulse for the buffers, each 920 EOM involved in buffer control is divided into phases.
- (9) The interrupts to the 920 are time buffered to comply with the 920 8- μ s requirement.

A. Word Formats

The 920 word format is 24 parallel bits while the MDS processor word format is 16 bits. The Standard Interface

to which the MDS processors conform operates on 8-bit bytes. The assembly and disassembly of half a processor word into a third of the 920 word would be both cumbersome and time consuming, especially in handling parity and check sum. Systems analysis has concluded, based on a tradeoff between idle core capacity and increased speed of operation, to limit the 920 word length to 16 bits, commensurate with the MDS processor word length and with two standard interface 8-bit bytes.

B. Buffer Control

For each channel there are two buffers: Buffer A from the 920 to the SIA and Buffer B from the SIA to the 920. Because of the required word assembly and disassembly between the 920 16-bit word and the SIA 8-bit byte, each buffer is divided into two branches of 8 bits each: A_1 , A_2 , B_1 , B_2 . For reference, see Fig. 2. This configuration has been used during checkout and test.

C. Block Length Control

The block length control is implemented by using one additional buffer track for flags or markers. A single flag bit on a unique track indicates the end of a data block. At the time the end flag is inserted the content is available to be read out. End of readout is signaled by the end-of-block flag appearing at the output. The buffers are implemented using a Random Access Memory (RAM), and the beginning of a data block is synonymous with reset of the address register. The end of a data block is a single flag bit inserted at the address of the last byte. For readout, the address register is reset and sequenced in the same manner as during loading, until the flag bit is detected signaling unload complete.

D. Buffer Control Summary

Both the A and the B buffers are configured as 16-bit-wide buffers. Buffer A is 160 words long, Buffer B 80 words. Buffer A loads two identical 16-bit words with data change for every other address change. The address changes for each load pulse. The alternating control is applied to the OE (Output Enable). The end-of-block flag is loaded into the control buffer at the address of the last byte plus one. Buffer A unload is accomplished by resetting its address register and augmenting it by the data strobe pulse until the end-of-block flag is encountered at the control buffer output. Buffer A_1 and A_2 outputs are paralleled, and their OEs are alternately asserted. Since the buffer output circuit is a tristate circuit, the parallel connection and alternating OEs will produce the desired

8-bit-byte data stream to the SIA, with no auxiliary data switching logic required.

Buffer B operates in a similar manner. During the load operation the inbound 8-bit-byte data are connected in parallel to the input of both branches, B_1 and B_2 . The address changes for every other load pulse. During the unload operation, both branches B_1 and B_2 are unloaded simultaneously, thus forming the assembled 16-bit words.

V. Control of the Four Interfaces

There are four different major interfaces:

- (1) The 920 to Adapter Interface, Buffer A Load.
- (2) The Adapter to SIA Interface, Buffer A Unload.
- (3) The SIA to Adapter Interface, Buffer B Load.
- (4) The Adapter to 920 Interface, Buffer B Unload.

For reference see Fig. 3.

The terminology and timing control in general are the same for all four interfaces listed above. For reasons discussed elsewhere, the interface strategy as well as terminology is influenced by the MDS processor interface rather than by the 920 and is as follows.

A computer (920) or device (adapter) that has data to be transmitted initiates the operation by asserting an outbound request-to-transmit line. To this request the recipient responds by asserting an outbound response line (RSP) indicating a ready-to-receive condition. As the sender receives an inbound RSP it asserts an outbound RDY line, indicating that the data he wishes to send are on the data lines and stable. The recipient can then use this information on the inbound RDY line to generate a data strobe by which to strobe-in the incoming data into a receiving register or buffer. Upon receipt of the data the recipient signals the sender that the data have been successfully received. This is accomplished by releasing his outbound RSP line. As the sender detects the release of the inbound RSP, he releases his outbound RDY line as it is no longer required.

The SIA operates with level control as described above. Its inbound and outbound request lines are unidirectional while the RSP, RDY lines are bidirectional. The 920 operates on pulses in the form of outbound EOM pulses and inbound interrupt pulses. If one were to send a request-to-transmit pulse over an interrupt line to the 920, it may not, however, be prepared to receive unless preceded by an EOM message stating that this condition is also true.

In listing the sequences for each interface, attempts were made to keep them as uniform as possible. Secondly, each sequence is repetitive and requires no single unique directive such as initialization, buffer clear, or reset. Figure 4 shows the timing sequence for data transfer.

Additional stipulations pertain to the recognition of a single transition on a line, to noise filtering and synchronization, and to insertion of delays between the signals for easier recognition. Examples of such stipulations with a bearing on the implementation of the control circuits follow.

In order to combat noise and to synchronize the data transfer interface timing control signals to the internal clock of a recipient device, a signal transition is, in general, recognized only upon the second consecutive sample of the internal clock that the signal remains in its new state, and then only if the signal remained in its previous state for the same length of time. This specification is valid for transitions in either direction. Stated differently, a single noise pulse of either polarity of a duration less than 2 clock periods occurring at any time shall have no effect on the true operation.

VI. 920 EOM/Interrupt Summary

Between the four interfaces listed there are five EOMs and four interrupts used for each channel. They are listed in Table 1. The EOMs are decoded on the channel sub-assemblies. The interrupts are returned to the 920 through separate coax lines, four for each channel.

For a quick-look summary, Figs. 5 and 6 depict the four interfaces through arrow-and-number-labeled EOMs and interrupts.

VII. 920 I/O Register Interface and Data Transfer Protocol

The interface considered here is the parallel input-output operation through the computer's C-register, which is the method used for general communication. The 920/adapter interface operates in an open-loop configuration, relying on EOM requests and return interrupt responses. Parallel input-output operations, where a data transfer is involved, consist of two instructions, an EOM (energize output medium) instruction followed by either a POT (parallel output) or a PIN (parallel input) instruction.

VIII. Design Verification and Operational Acceptance Testing

A bench tester for the 900/SIA was designed and built at JPL for design verification and for bench checkout of manufactured units. It consists of a 900/SIA chassis with a separate built-in EOM sequencer which is controlled by the adapter interrupts. It serves as a test jig for the IC boards, there being two identical boards for each adapter. This tester could, with nominal effort, be updated to become another adapter.

The operational system test is a software test using a MODCOMP built-in 920 emulator and a special wrap-around test box or a Star Switch Controller from Buffer A channel 1 output to Buffer B channel 2 input. The hardware configuration is shown in Fig. 7.

IX. Design and Development Milestones

The detail design of the 900/SIA was a sole JPL effort during a three-week period. This included completion of detail logic and timing diagrams, as well as descriptive text. A detail design review and transfer of the design to contractor engineering personnel has been concluded. No engineering breadboard or prototype was built. Checkout of the contractor manufacturing prototype (first article) was a sole contractor effort concluded in a two-week period. Cursory system checkout using the Telemetry Processor Assembly (TPA) Mod Comp Emulator at CTA 21 was a combined contractor/JPL effort concluded during one week.

Final system checkout, which included the contractor-produced test software, was successfully concluded during a two-week period in April 1976. This was a combined effort between JPL hardware and contractor software personnel. During the above overall period, a JPL engineering prototype unit was being built and tested at JPL in parallel with the contractor-built unit.

X. Documentation

The original logic design diagrams provided the source information for the automatically produced sectionalized manufacturing drawings and associated wire lists. While the original diagrams are best suited to convey a functional understanding, the sectionalized drawings and associated wire lists are best suited for local troubleshooting.

The following is a list of the documents mentioned above:

- (1) 920/adapter interface timing control circuitry.
- (2) Buffer A data flow circuits.
- (3) Buffer B data flow circuits.
- (4) Adapter/SIA interface timing control (hand-shake) circuitry.

(5) Detail timing chart for Buffer A load/unload operation.

(6) Detail timing chart for Buffer B load/unload operation.

(7) Design verification sequencer, logic diagram.

Additional descriptive material relating to system circuitry is currently being prepared.

Table 1. List of 920/SIA adapter EOMs and interrupts

Sequence	EOM/interrupt	Description
1	EOM 1	920 Request to transmit to adapter Buffer A
1	EOM 2	920 to adapter Buffer A data transfer EOM 2/POT loop
1	EOM 3	920 to adapter Buffer A end-of-data block
4	EOM 4	920 ready to accept "request to transmit" from adapter Buffer B
4	EOM 5	Adapter Buffer B to the 920, data transfer EOM 5/PIN loop
1	Interrupt 1	Adapter response to 920, EOM 1, adapter ready to accept data EOM 2 from the 920
2	Interrupt 2	SSA time-out, data block transferred over interface 2 not complete, adapter to the 920, repeat sequence 2
4	Interrupt 3	Adapter Buffer B response to EOM 4 request to transmit
4	Interrupt 4	Adapter Buffer B empty, transmission complete

ORIGINAL PAGE IS
OF POOR QUALITY

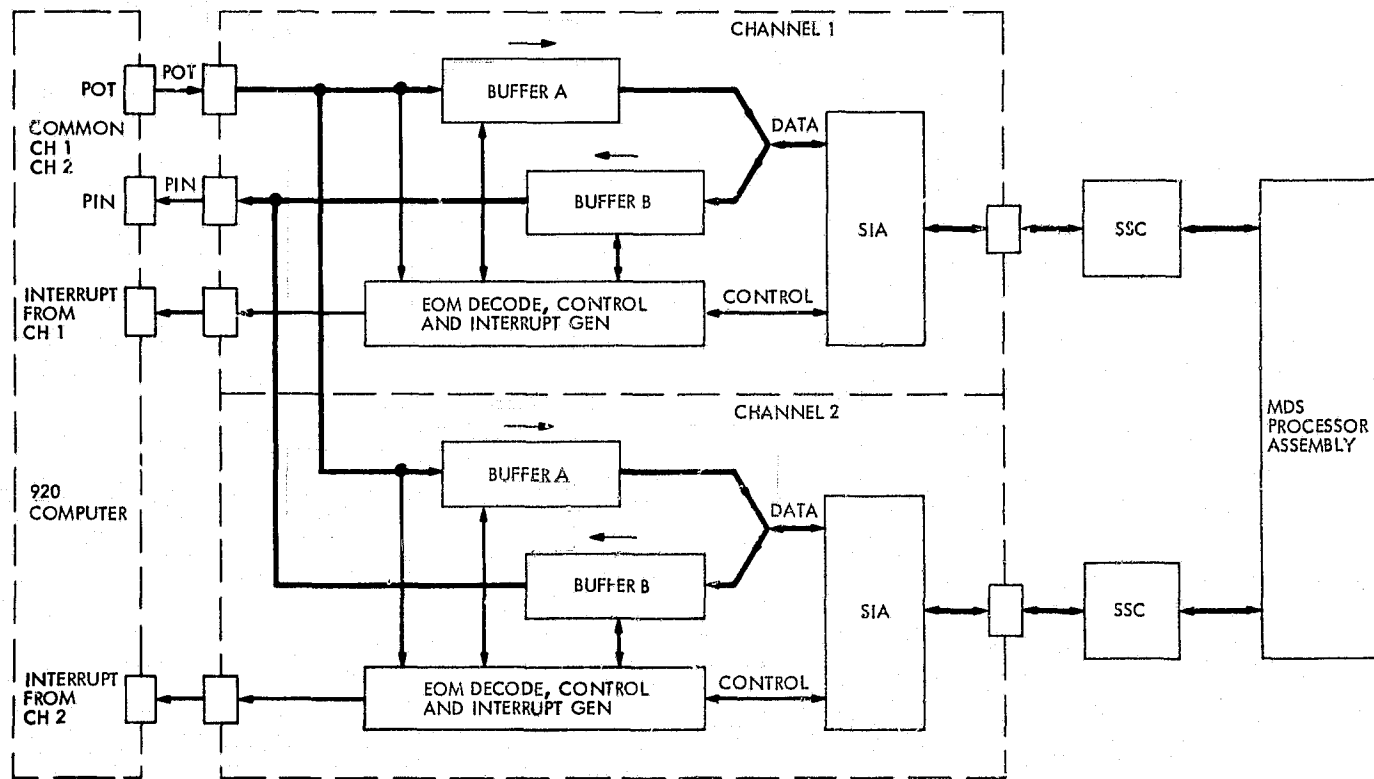


Fig. 1. 920/SIA Adapter and Buffer Assembly block diagram shown in subsystem configuration

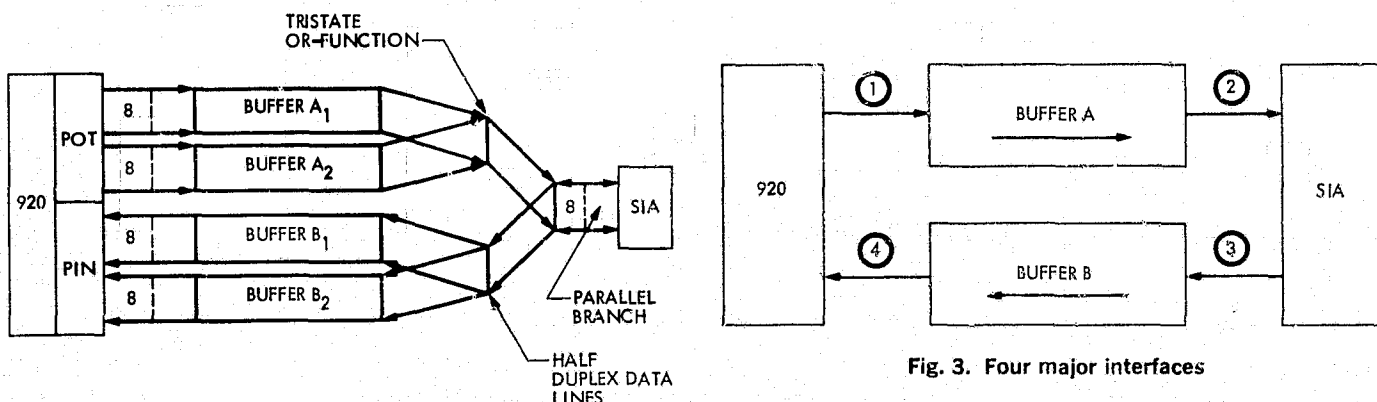


Fig. 2. Block diagram showing data buffer branches A_1, A_2, B_1, B_2 with no external data switching required

ORIGINAL PAGE IS
OF POOR QUALITY

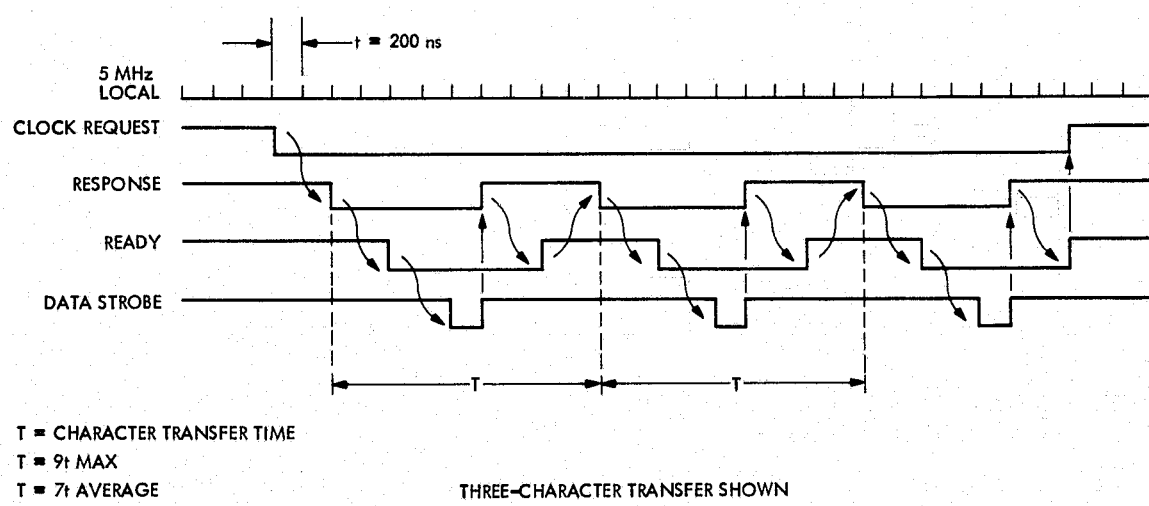


Fig. 4. Timing chart for the standard interface timing control lines

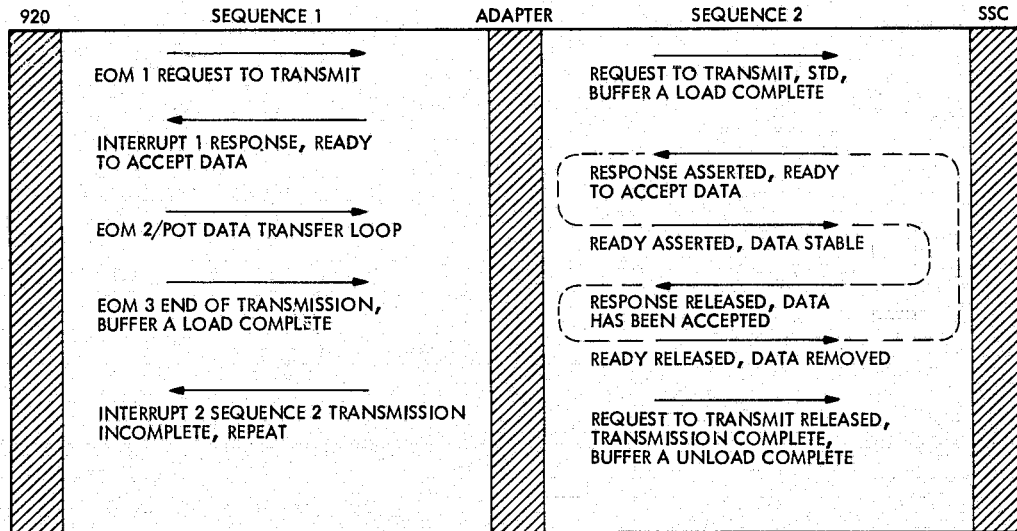


Fig. 5. Summary of interface sequences 1 and 2

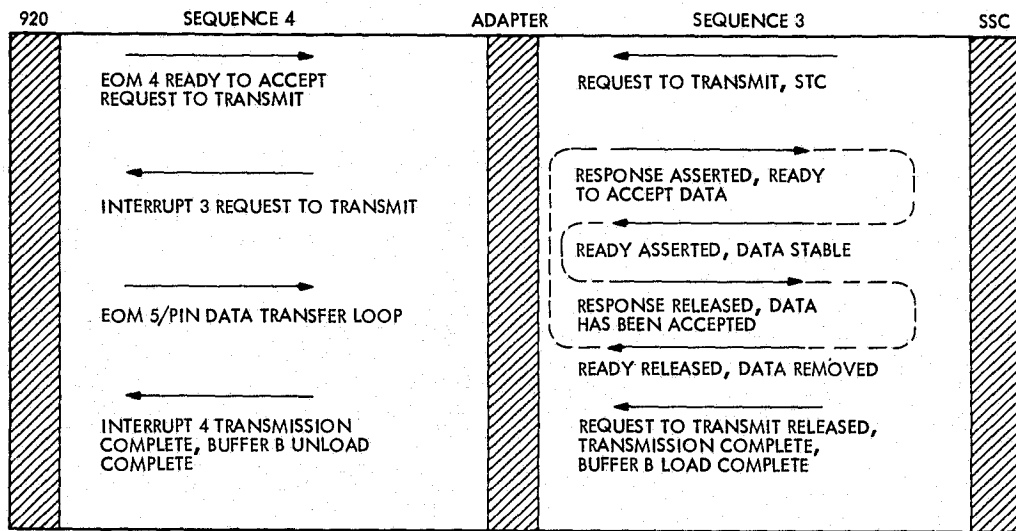


Fig. 6. Summary of interface sequences 3 and 4

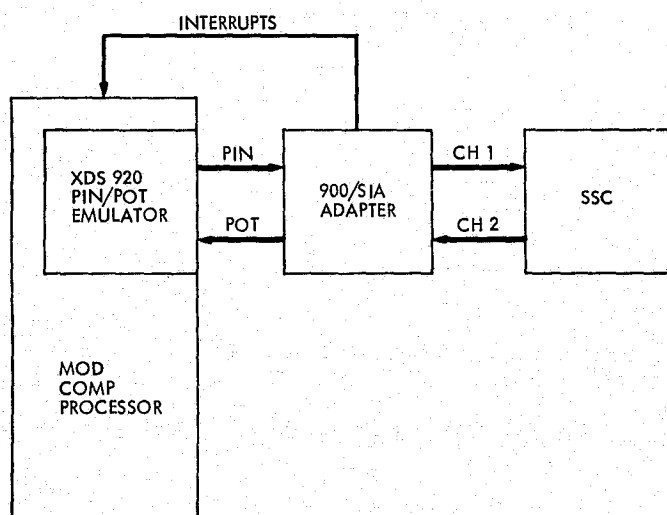


Fig. 7. Hardware configuration for 900/SIA software testing

ORIGINAL PAGE IS
OF POOR QUALITY

N 76-29329

A New Sequential Decoder for the DSN Telemetry Subsystem

J. H. Wilcher

DSN Data Systems Development Section

A new sequential decoder has been implemented in the DSS Telemetry Subsystem for the DSN MARK III Data System Implementation. This decoder performs the same decoding function as the Data Decoder Assembly performs in the Telemetry and Command Data Handling Subsystem. However, the new decoder is much faster, allowing potentially high data rates in the future.

I. Introduction

The DSS Telemetry Subsystem (DTM) being implemented as a part of the DSN MARK III Data System (MDS) Implementation Project must be capable of performing the same functions which are presently performed by the Telemetry and Command Data Handling Subsystem (TCD). Among these functions is sequential decoding. Sequential decoding is presently being performed by the Data Decoder Assembly (DDA) in conjunction with the Telemetry and Command Processor (TCP).

Early in the design phase of the MDS Implementation Project a decision was made to explore the possibility of implementing the sequential decoder function directly in the Telemetry Processor Assembly (TPA), which replaces the TCP, thereby doing away with the DDA as well.

A contract was issued with Modular Computer Systems, Ft. Lauderdale, Florida, to design and fabricate, to JPL

specification, a prototype sequential decoder which would interface directly with the TPA, a Modular Computer Systems (MODCOMP) II-25 minicomputer.

This article presents a description of the implementation of this sequential decoder and the performance obtained from this decoder.

II. Decoder Implementation

The specification for the new sequential decoder required that the decoder be implemented using the Fano-Algorithm, the same algorithm which was used in implementing the sequential decoder function in the DDA. This was made a requirement since the algorithm is well understood within the DSN and that the probability of a successful implementation was greater with a well known algorithm versus a new, untried algorithm.

The specification also called for the consideration of failure diagnostic capabilities in the implementation of the

decoder. This feature would also prove to be beneficial in the testing of the decoder implementation.

A. Sequential Decoder Interface

The sequential decoder was implemented as a single-plane microcoded, read-only memory processor interfaced to the TPA and MODCOMP II-25 via Modular Bus Control (MBC) and Port 0 of the 4-port memory (see Fig. 1). This method of implementation allows the decoder to be initiated by the central processing unit's (CPU's) execution of any of the decoder's custom macroinstruction and then the CPU is released to run in parallel with the decoder.

The decoder accesses memory through the highest priority port (Port 0), of the 4-port memory controller to obtain parameter values and the received data symbols to decode. Access to all the required tables is also via the 4-port memory controller. One module (16 kwords) of the 64 kwords of memory is reserved for the sequential decode function. The received data buffers, tables, encoder parameters, etc. are contained in specific locations of this module. This feature allows the decoder to operate relatively independent of the CPU and the external Direct Memory Processor (DMP). The decoder competes with the CPU for access time to this dedicated module only when it is necessary for the CPU to perform housekeeping tasks such as formatting data for transmission, etc. The decoder competes with the external DMP when the DMP must input a new frame of received data symbols. Therefore, the decoder is not placing demands for time on the CPU or DMP when they are accessing other modules of memory and other tasks may be carried on in the CPU independent of the sequential decoder.

B. Sequential Decode Macroinstructions

The following macroinstructions are used in the normal operation of the sequential decoder:

1. Compute Tail Correlation (CTC). This instruction makes use of the so-called "quick look" property, of the class of convolutional codes currently being used, to compute the likelihood that a given position in the received data stream is the end or tail of a frame of coded data. Repeated execution of this instruction at all possible positions in the input symbol stream is sufficient to find frame synchronization with arbitrarily high confidence.

2. Sequential Decode (SEQD). This instruction implements the sequential decoding algorithm. It is necessary that there exist a properly formatted data buffer containing the received symbols and tail sequence

associated with one spacecraft data frame. It is also necessary that the processor's general registers be loaded with all the parameters required by the instruction such as the location of metric tables, the impulse response, and the tail length. The execution time of this instruction is a variable depending upon the frame size and the details of the noisy received data. The instruction is terminated only by successfully decoding the frame or by the execution of a terminate instruction.

3. Terminate Sequential Decode (TSD). This instruction is used to terminate the sequential decode instruction when a frame of coded data has not been decoded in the allowable time limit as determined by the input data rate and the data buffer management scheme. The execution of this instruction will result in the controlled termination of the sequential decode instruction with the 'Erased Frame' bit of the sequential decoder status word set.

C. Sequential Decode Diagnostic Macroinstructions

The following macroinstruction when used with appropriate diagnostic software can be, and has been, very beneficial in ascertaining the condition of the sequential decoder, either as a troubleshooting aid in a maintenance depot to detect a failed part, or as an aid in analyzing the operation of the decoder:

1. Load Sequential Decoder (LSD). This diagnostic macroinstruction will cause the contents of CPU Register 1 to be read into each of the sequential decoder registers.

2. Dump Sequential Decoder (DSD). This diagnostic macro will dump the contents of the sequential decoder registers to a specific part of memory.

3. Step Sequential Decoder (SSD). Execution of this diagnostic MACRO is identical to SEQD except that the decoder will halt and interrupt the CPU after each step in the decoder algorithm.

Using the aforementioned diagnostic macroinstruction it is then possible to perform a complete checkout and failure analysis of the decoder by repeatedly loading the sequential decoder with a known pattern (LSD), stepping the sequential decoder (SSD), dumping the decoder (DSD), and comparing the results against known values. The "known" pattern could be a specific frame of coded data, therefore allowing the observation of the decoding process on a step-by-step basis. This feature could be useful for analyzing subtle failures in the decoder or for analyzing the data from a spacecraft for coder failures, for instance.

III. Performance

The performance of the sequential decoder was ascertained by comparing the results of the new decoder against known results. To accomplish this, frames of data were decoded by the DDA and these frames were retained as the "known". The same frames were then decoded by the new sequential decoder and the results compared on a bit-for-bit basis. If the new decoder was implemented to the same algorithm, the results of the decoding should match completely bit-for-bit and step-for-step. The only difference would be in the time to decode, which is a function of the method of implementing the decoder algorithm, not the algorithm. Approximately one-thousand frames of convolutionally coded data, of various frame lengths, bit rates, and signal-to-noise ratios, were processed by the new decoder and the results compared against the "known" results. The results matched in all cases.

One further parameter was measured while decoding the test frames with the new decoder. This was the decoder speed.

The time to decode a frame of data was recorded along with the data. Also recorded was the number of computations needed to decode the frame, a computation being defined as either a forward step or a backward step in the decoder. A figure of merit for a sequential decoder universally used is the computational rate (R_{comp}). In order to determine the R_{comp} for the new decoder, the time to decode and the number of computations were recorded and averaged over many hundreds of frames resulting in an average time per computation of $10.5 \mu\text{sec}$. This translates into an R_{comp} of 95.2×10^3 computations per second. This compares with an average computation rate for the DDA of 22×10^3 computation per second, a factor of 4.3 improvement.

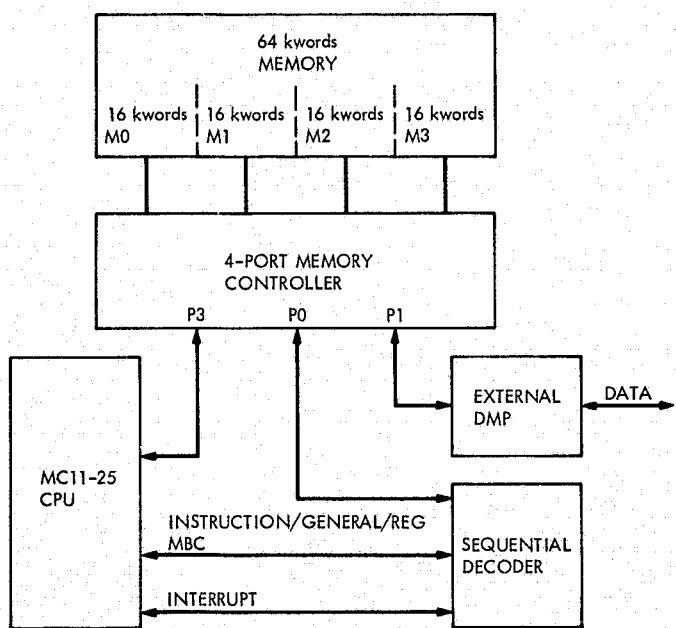


Fig. 1. The sequential decoder interface

ORIGINAL PAGE IS
OF POOR QUALITY

N 76-29330

Antenna Pointing Subsystem Conscan Implementation

R. Tappan

DSN Data Systems Development Section

The software of the computer that drives the tracking antennas in the DSN has been modified to improve the pointing accuracy for tracking operations at X-band frequencies. The change implemented an improved model for atmospheric refraction correction and added a software tracking option that corrects any remaining pointing errors. The software tracking option that was added measures the actual pointing error and corrects the antenna position accordingly. This option will be discussed.

The computer program that drives the 26-meter and the 64-meter antennas in the DSN has been updated to improve its performance. The improvement was obtained by revising the model used for atmospheric refraction correction, changing the method used to compute the ephemeris, and adding an option to use the computer as part of a closed loop tracking system.

The 26- and 64-meter parabolic antennas used in the DSN are driven in two axes by hydraulic servo systems that may be operated either manually or under computer control.

The computer program has three modes of operation that may be used to track a target.

The star track mode accepts inputs of right ascension and declination, and tracks the target at a sidereal rate.

The planetary mode requires three inputs of right ascension and declination. A quadratic equation is fitted to the three points and evaluated to determine the ephemeris.

The tape drive mode reads sets of time-tagged coordinates from paper tape. A quadratic equation is least squares fitted to four points and the program tracks between points 2 and 3.

Each of these modes has an option of using a method of conical scanning (conscan) as part of a closed-loop tracking system to improve the accuracy with which the antenna tracks the target. The option requires the addition of an analog to digital (A-D) converter to the hardware. The converters have been installed in the 64-meter stations to assist in X-band tracking operations.

Conscan adds corrections to the antenna position that maximize the received signal level. The corrections added are small, but they are important for operations at X-band frequencies where the narrow beam width causes the received signal to be reduced by one decibel for a pointing error of 0.011 degree.

Conscan imposes a circular scan pattern on the path of an antenna that is tracking a target. The circular scan pattern is generated by adding a sinusoidal signal to the servo error signal of the hour angle (HA) axis, and a consinusoidal signal to the declination (DEC) axis. The period and radius of the scan pattern are entered by the operator prior to the start of the conscan operation.

$$HA = R * \text{SIN}(\text{SCNANG})$$

$$DEC = R * \text{COS}(\text{SCNANG})$$

where R is the radius of the scan in degrees, and $SCNANG$ is the scan angle.

If the radio-frequency (RF) boresight of the receiving system is not pointing directly at the target, the scan will produce a small sinusoidal variation in the received signal power as the antenna sweeps toward the signal source and back again. The rate of the sinusoid is the scan period. The phase with respect to the scan rotation is determined by the direction of the pointing error, and the amplitude is proportional to the angular deviation from the source. The amplitude proportionality constant, the gain, is also an operator input. The received signal is monitored by an A-D converter that can be switched to sample either the automatic gain control (AGC) voltage of the receiver for tracking the coherent signal from the spacecraft, or the

voltage of a radiometer for tracking noncoherent (noise) sources.

The pointing error that exists for each axis is recovered from the A-D converter samples by correlating them with the scan drive of the axis, suitably offset in phase to account for the mechanical and electrical delays in the receiving system.

$$HA \text{ correlation} = SIG * \text{SIN}(\text{SCNANG} - LPS)$$

$$DEC \text{ correlation} = SIG * \text{COS}(\text{SCNANG} - LPS)$$

where SIG is the A-D converter sample, $SCNANG$ is the scan angle associated with the A-D converter sample, and LPS is the phase delay in the receiving system.

The correlations are summed for one complete scan period and scaled to become the angular corrections that are required to move the RF boresight back to the target.

The gain is selected to cause a fraction of the required correction to be made at the end of each scan period to minimize positioning errors due to noise on the A-D converter samples. The radius is selected to cause an acceptable signal loss when the pointing error has been reduced to zero. Typically, for X-band operations, a radius of 0.011 degree would be selected for the initial scan, causing a signal loss of one decibel. The radius would then be changed to 0.004 degree (the 0.1-dB point) after several scans had reduced the pointing error. The period selected is one that corrects the pointing angle as frequently as is necessary and avoids synchronization with a periodically fluctuating signal from the target, as might occur when tracking spin stabilized spacecraft. Normally used periods range from 60 to 120 seconds.

N 76-29331

High Performance Flat Plate Solar Collector

F. L. Lansing and R. Reynolds
DSN Engineering Section

This article presents briefly the potential use of porous construction to achieve efficient heat removal from a power producing solid and its new application to solar air heaters. Analytical solutions are given for the temperature distribution within a gas-cooled porous flat plate having its surface exposed to the sun's energy. The extracted thermal energy is calculated for two different types of plate transparency. The results of the analysis show the great improvement in performance obtained with porous flat plate collectors as compared with analogous nonporous types.

I. Introduction

It is technically possible to use solar-heated air to provide energy for almost any application that uses solar-heated liquids. However, it is foreseen that the most likely areas of use will be for the heating or cooling of buildings and in industrial processes such as the drying of agricultural crops and timber.

In general, solar air heaters possess the same adverse cost-temperature relationship as solar water heaters. However, they appear to cost less than water heaters because:

- (1) The corrosion problems which can become serious in solar water heaters are virtually nonexistent with air heaters. This allows the use of cheaper constructional materials for reducing the cost of the collector and its accessories.

- (2) The leakage of air from the ducts or the heater connection does not present a serious problem. A hermetic system is not essential as when using water as the working fluid. This presents another potential cost reduction in installation and maintenance.
- (3) Solar air heaters are lighter in weight and less complex than solar water heaters. This again reduces the inherently high cost of "add on" systems if solar collectors are integrated into a building structure.

On the other hand, solar air heaters have relatively high fan power requirements and without careful design the duct costs can also be high. Also, storage of energy with a solar air heating system presents problems different from storage with solar water heating where the actual heat transfer fluid can generally be used as the storage medium. The storage material to be chosen should be of

low cost, high thermal capacitance, and be able to exchange heat with the air with small heat transfer surface area.

Though it can be concluded that there exists an economic potential for using air as the working medium in solar collectors, the state of the art remains a technical achievement awaiting commercial exploitation. A solar air heater that provides effective heating and combines high power density with compactness of heat exchange surface is exemplified by the porous flat plate solar collector, which is the main subject of this article.

Porous materials have become increasingly attractive for application in high temperature heat exchangers. The present new application of porous heat transfer in a plate subjected to solar radiation is exceptionally effective in both heating the working fluid and improving the absorptive characteristics of the plate. The high effectiveness of the heat exchange mechanism is mainly due to the intimate contact in the interstices between the gas particles and the porous plate, as will be explained in the next sections.

II. Collector Description

The high performance flat plate solar collector utilizes air as the heat transfer fluid and is shown schematically in Figs. 1, 2, and 3. It is composed mainly of a metallic matrix whose mesh size and porosity depend on the required performance and acts as the absorber plate in a conventional flat plate solar collector. The porosity of the matrix surface behaves as a large set of cavity radiators (black bodies) whose absorptivity greatly exceeds that of a regular solid surface. One or two sheets of glass are mounted on top of the matrix, allowing a space for the air flow passage. The space between the glazings, if more than one sheet is used, may be evacuated to reduce the thermal convection and conduction losses. Also, the matrix surface can be coated by a "selective" material to reduce the outward long wave radiation losses. It should be pointed out that the use of vacuum and selective coating are not the main points behind the high performance obtained in the present work but rather the new heat exchange mechanism in a porous material. The comparison will always be made between two identical collectors, one with a porous plate, and the other without. The cold air flows through the matrix plate and exchanges heat with its thermally stratified layers. The heat exchange mechanism may take either one of the three patterns shown in Figs. 1, 2, and 3, depending on the direction of air flow with respect to the matrix thermal stratification.

To show, in a simple manner, the important features of the novel porous plate solar collector, the one-dimensional flow pattern illustrated in Fig. 1 is found to be the best candidate pattern for the present work comparison. The flow pattern in Fig. 2 is subject to reversing flow effects due to hot air buoyancy and it possesses a complex flow regime. Also, the flow pattern in Fig. 3 is excluded from the present discussion since it needs a more complicated, two-dimensional study.

III. Basic Assumptions and Analysis

The basic assumptions that are used in the steady state thermal analysis can be listed as follows:

- (1) Thermal, physical, and transport properties of the matrix plate and the fluid (air) are constant with temperature and uniform over the entire collector area.
- (2) Heat conduction and fluid flow are one dimensional in a direction perpendicular to the bounding surfaces of the matrix.
- (3) Temperatures of the fluid and the matrix pores are equal at any position within the plate. This assumption may not be very accurate for matrix heat exchangers (regenerators) with large fluid flow rates. However, this idealization in the mathematical model is still considered essential in most of the analytical studies of transpiration-cooled matrices as described in Refs. 1-5.
- (4) Heat losses to the ambient air by convection and radiation are only from the top surface of the matrix plate facing the solar radiation. No allowance is made for the bottom surface losses.

Based on these idealizations, a segment of the collector matrix of thickness dy and at a depth y from the top surface facing the sun is analyzed as shown in Fig. 4.

The steady state temperature distribution is determined by solving the heat balance equation of the collector segment, which is written as: The sum of the net rates of heat conduction, increase of fluid energy content, and internal heat absorption is equal to the rate of energy storage, i.e.,

$$K_e \frac{d^2T}{dy^2} + G_f C_f \frac{dT}{dy} + Q_{in}(y) = 0 \quad (1)$$

Equation (1) is the system differential equation and is solved for the following two extreme cases:

Case 1: an opaque surface matrix with total absorption of the sun's energy at the top surface. This is a case of close packed meshes whose internal heat absorption, Q_{in} , is treated as a surface property.

Case 2: a diathermanous matrix (semitransparent to radiation) with successive absorption of the solar energy within the matrix depth. This is a case of loose packed semitransparent matrix with relatively large mesh size whose internal heat absorption, Q_{in} , is treated as a bulk property.

The temperature profile in each of the above cases is analyzed as follows:

Case 1: An Opaque Matrix Surface: for total absorption of solar irradiancy at the surface ($y = 0$), then

$$Q_{in}(y) = 0 \quad \text{for } y > 0 \quad (2)$$

and Eq. (1) is reduced to

$$K_e \frac{d^2T}{dy^2} + G_f C_f \frac{dT}{dy} = 0 \quad (3)$$

with its general solution given by

$$T = A_1 + B_1 \exp\left(-\frac{G_f C_f y}{K_e}\right) \quad \text{for } 0 \leq y \leq L \quad (4)$$

where A_1 and B_1 are arbitrary constants to be determined from the boundary conditions. Equation (4) is only applicable to matrix (or fluid) temperatures within the range $0 \leq y \leq L$.

The boundary conditions of case 1 are set as follows:

- (1) At the fluid entry section ($y = L$), the rise in fluid energy is equal to the rate of heat conduction from the matrix surface.
- (2) At the fluid exit section ($y = 0$), the first law of thermodynamics necessitates that the net absorbed solar energy (the absorbed solar energy minus the heat losses to the environment) equals the rise in fluid energy from its entry up to the exit section.

The temperature distribution within the plate is thus given by the exponential form:

$$T = T_{in} + \left[\frac{a_p \tau_g q - U_e (T_{in} - T_a)}{G_f C_f + U_e} \right] \exp\left(-\frac{G_f C_f y}{K_e}\right) \quad (5)$$

and is sketched in Fig. 5. The temperature distribution is dependent on the conductivity K_e and the thickness L . However, the fluid temperature rise across the collector is independent of K_e and L and is given by:

$$[T(0) - T_{in}] = \left[\frac{a_p \tau_g q - U_e (T_{in} - T_a)}{(G_f C_f + U_e)} \right] \quad (6)$$

The useful heat gain Q_u per unit area is then expressed as

$$Q_u = G_f C_f [T(0) - T_{in}] = [a_p \tau_g q - U_e (T_{in} - T_a)] \left(\frac{G_f C_f}{G_f C_f + U_e} \right) \quad (7)$$

Case 2: A Diathermanous Matrix (Semitransparent to Radiation): in this case, the matrix absorbs incident solar radiation not only at the top surface but at successive depths also. The internal heat absorbed per unit volume, $Q_{in}(y)$, is derived using Beer's Law for diathermanous materials and is given by

$$Q_{in}(y) = a \tau_g q \exp(-ay) \quad (8)$$

where a is the extinction coefficient of the plate. The system differential equation, Eq. (1), is reduced to

$$K_e \frac{d^2T}{dy^2} + G_f C_f \frac{dT}{dy} + a \tau_g q \exp(-ay) = 0 \quad (9)$$

whose general solution is given by:

$$T = A_2 + B_2 \exp\left(-\frac{G_f C_f y}{K_e}\right) + \frac{q \tau_g \exp(-ay)}{(G_f C_f - K_e a)} \quad (10)$$

where A_2 and B_2 are arbitrary constants to be determined from the boundary conditions. Equation (10) is only applicable to matrix (or fluid) temperatures within the range $0 \leq y \leq L$.

The boundary conditions for case 2 are set as follows:

- (1) At the fluid entry section ($y = L$), the rise in fluid energy is equal to the rate of heat conduction from the matrix surface plus the leaving unabsorbed radiation.
- (2) At the fluid exit section ($y = 0$), the first law of thermodynamics necessitates that the net absorbed solar energy (the absorbed solar energy minus the

heat losses to the environment) equals the rise in fluid energy from its entry up to the exit section.

The temperature distribution within the diathermanous matrix is thus given by

$$T = T_{in} \left[\frac{q \tau_g (1 - \exp(-aL)) - U_e (T_{in} - T_a)}{(U_e + G_f C_f)} \right] \times \exp \left(\frac{-G_f C_f y}{K_e} \right) + \frac{q \tau_g \left[\exp(-ay) - \exp \left(\frac{-G_f C_f y}{K_e} \right) \right]}{(G_f C_f - K_e a)} \quad (11)$$

and is sketched in Fig. (6). The maximum fluid temperature rise is written as

$$[T(0) - T_{in}] = \left[\frac{q \tau_g (1 - \exp(-aL)) - U_e (T_{in} - T_a)}{(U_e + G_f C_f)} \right] \quad (12)$$

which is independent of the conductivity K_e of the matrix. The useful heat gain Q_u can be derived using Eq. (12) as

$$Q_u = G_f C_f [T(0) - T_{in}] = [\tau_g q (1 - \exp(-aL)) - U_e (T_{in} - T_a)] \left(\frac{G_f C_f}{G_f C_f + U_e} \right) \quad (13)$$

which is similar to that obtained in Eq. (7) except that the plate absorptivity (α_p) is now replaced by its equivalent form $(1 - \exp(-al))$.

The temperature profile within the porous structure is plotted for the above two cases as shown in Figs. 5 and 6, and at some selected values for G_f , C_f , K_e , L , q , a , and τ_g . For an opaque surface, the temperature decreases monotonically from the absorber surface as shown in Fig. 5.

In the diathermanous matrix, the temperature experiences a maximum value at some point inside the matrix due to the successive absorption of the sun's energy and the energy transported away by the fluid. It is desirable, from the thermal stresses view point, to have a uniform matrix plate temperature distribution. To satisfy this criteria the operating conditions should result in a higher value for the wall temperature $T(L)$ at the fluid entry

section. The latter is promoted by using a high thermal conductivity, K_e , a small plate thickness, L , and a small air mass flux, G_f .

IV. Comparison With a Nonporous (Solid) Flat Plate Collector

The conventional, solid flat plate solar collector that uses air as the working medium is sketched in Fig. 7. The absorber plate is provided with side fins to enhance the heat conductance rate to the air blowing underneath it. The useful heat gain expression is presented in detail in several literature sources (Ref. 6, for example) and is rewritten for reference as

$$Q_u = \left\{ \alpha_p \tau_g q - U_e (T_{in} - T_a) \right\} \times \frac{G_f C_f}{U_e} \left\{ 1 - \exp \left(- \frac{U_e U_{pf}}{G_f C_f (U_e + U_{pf})} \right) \right\} \quad (14)$$

where U_{pf} is the conductance coefficient between the plate and the adjacent working fluid (air). The rest of the parameters bear the same meaning as used before.

The present analysis of the high performance solar collector that uses a porous flat plate with a working fluid flowing through the interstices, yields an analogous expression for its useful heat gain, and it is given in Eqs. 7 and 13 as

$$Q_u = \left\{ \alpha_p \tau_g q - U_e (T_{in} - T_a) \right\} \frac{G_f C_f}{(G_f C_f + U_e)} \quad (15)$$

It can be concluded that for the same optical properties (α_p , τ_g), solar radiation intensity, q , and the loss coefficient from the plate surface to the environment U_e , the performance of a porous collector depends exclusively on the product of the fluid mass flux times its specific heat ($G_f C_f$), while that of the solid type depends on the conductance coefficient U_{pf} as well as the product $G_f C_f$. Table 1 presents the results of a numeric comparison between the two types and is constructed from the following assumed operating conditions:

$$\text{Solar radiation intensity } q = 678 \text{ kcal/h-m}^2 \quad (250 \text{ BTU/h-ft}^2)$$

$$\text{Ambient air temperature } T_a = 10^\circ\text{C} (50^\circ\text{F})$$

$$\text{Inlet air temperature } T_{in} = 23.89^\circ\text{C} (75^\circ\text{F})$$

Matrix plate absorptivity $\alpha_p = 0.9$ (this corresponds to an extinction coefficient of 0.906 cm^{-1} (27.63 ft^{-1}) for 2.54-cm (1-in.) thickness diathermanous material)

Matrix plate emissivity $\epsilon_p = 0.9$

Glass cover transmissivity $\tau_g = 0.9$

Loss coefficient between plate surface and environment
 $U_e = 5.86 \text{ kcal/h-m}^2 \text{ }^\circ\text{C}$ ($1.2 \text{ BTU/h-ft}^2 \text{ }^\circ\text{F}$)

Air Specific heat $C_f = 0.24 \text{ kcal/kg }^\circ\text{C}$ ($0.24 \text{ BTU/lb }^\circ\text{F}$)

Matrix porosity $p = 0.8$

the solid plate to air conductance coefficient U_{pf} is given by the approximate formula

$$U_{pf} \approx 4.883 (1.0 + 0.248 V) \text{ kcal/h-m}^2 \text{ }^\circ\text{C}$$

where V is the air velocity in km/h.

The above operating conditions were abstracted from the experimental results of flat plate solar collectors to yield a practical evaluation of the present comparison. The efficiency results are plotted as shown in Fig. 8.

It is evident from Fig. 8 that a much higher performance can be obtained with a porous flat plate collector relative to the analogous solid type. This is due to the fact that the heat transfer mechanism between the matrix plate and the air in the interstices is far more effective in making their temperatures equal. This means that the porous flat plate heat exchanger is in effect working with

an extremely larger value of the plate to fluid conductance U_{pf} , relative to the nonporous type. Their performance can be identical only at the "no flow" condition, and both of them yield

$$\lim_{C_f \rightarrow 0} [T(0) - T_{in}] = \{\alpha_p \tau_g q - U_e (T_{in} - T_a)\} \frac{1}{U_e} \quad (16)$$

which is the highest temperature difference that could be attained by any of them.

The above calculations do not consider other factors such as the variation of the loss coefficient U_e and plate to fluid conductance U_{pf} with operating temperatures, and the potential improvement of optical absorptivity brought by a black body type absorbing surface for the porous material. The efficiency value obtained from the present high performance collector still leads with a sizable margin at all operating conditions. As an example, for a high efficiency collector application, Table 1 indicates that with an air mass flux of 4880 kg/h-m^2 (1000 lb/h-ft^2), which corresponds to an air velocity of approximately 4 km/h (2.5 mi/h), the efficiency improvement is 59 percent over a conventional solid type, however, the temperature gain is very little. On the other hand, for a higher temperature application where the air is heated by 16°C (29°F), the corresponding mass flux is approximately 98 kg/h-m^2 (20 lb/h-ft^2), and an improvement in efficiency over a conventional type of 84 percent could be obtained. Preliminary evaluation of this high performance solar collector indicates that it is capable of working with liquid phase heat exchange fluids as well as gases. Future work will address the application of this configuration of collector to liquid and boiling type heat exchange fluids.

Definition of Symbols

a	extinction coefficient	U_e	"effective" heat loss coefficient between matrix and ambient
C_f	fluid specific heat	U_{pf}	solid plate to fluid conductance coefficient
G_f	fluid mass flux (Flow rate per unit area)	V	velocity
K_e	"effective" matrix conductivity	y	distance measured from the top surface facing the sun
L	matrix plate thickness	α_p	plate absorptivity
p	porosity (pore volume/total volume)	τ_g	glass cover transmissivity
q	solar radiation intensity	ϵ_p	plate emissivity
Q_{in}	internal heat generation per unit volume		
T	temperature		

References

1. Burch, D. M., and Peavy, B. A., "Transient Temperature Distribution in Heat-Generating-Transpiration Cooled Tubes and Plates," *Journal of Heat Transfer, ASME Trans. Series C*, Vol. 97, Aug. 1975.
2. Rohsensow, W. M., and Hartnett, J. P., *Handbook of Heat Transfer*. McGraw Hill Book Co., N.Y., 1973, Ch. 3.
3. Schneider, P. J., "Temperatures and Thermal Stresses in Transpiration-Cooled Power Producing Plates and Tubes," *Jet Propulsion*, Vol. 27, Aug. 1957, pp. 882-889.
4. Schneider, P. J., "Numerical Method for Porous Heat Sources," *Journal of Applied Physics*, Vol. 24, No. 3, March 1953, pp. 271-274.
5. Green, L., "Gas Cooling of a Porous Heat Source," *Journal of Applied Mechanics, TRANS ASME*, Vol. 19, No. 2, 1952, pp. 173-178.
6. Whillier, A., "Design Factors Influencing Solar Collector Performance," in *Low Temperature Engineering Application of Solar Energy*, ASHRAE Publications, 1967, Ch. III, pp. 27-40.

Table 1. Comparison between a porous and a nonporous flat plate solar air heater

G_f , kg/h-m ² (lb/h-ft ²)	Useful temperature rise ($T(0) - T_{in}$), °C (°F)		Thermal efficiency, %		Improvement in efficiency, %
	Porous	Nonporous (solid)	Porous	Nonporous	
0	79.86 (143.75)	79.86 (143.75)	0.00	0.00	0
24.4 (5)	39.93 (71.88)	29.23 (52.62)	34.50	25.26	37
48.8 (10)	26.62 (47.92)	16.31 (29.36)	46.00	28.19	63
97.6 (20)	15.97 (28.75)	8.66 (15.60)	55.20	29.95	84
244 (50)	7.26 (13.07)	3.64 (6.55)	62.73	31.46	99
488 (100)	3.80 (6.84)	1.89 (3.40)	65.71	32.61	102
976 (200)	1.95 (3.51)	0.99 (1.78)	67.32	34.28	96
2440 (500)	0.79 (1.42)	0.44 (0.80)	68.32	38.23	79
4880 (1000)	0.39 (0.71)	0.25 (0.45)	68.66	43.06	59

ORIGINAL PAGE IS
OF POOR QUALITY

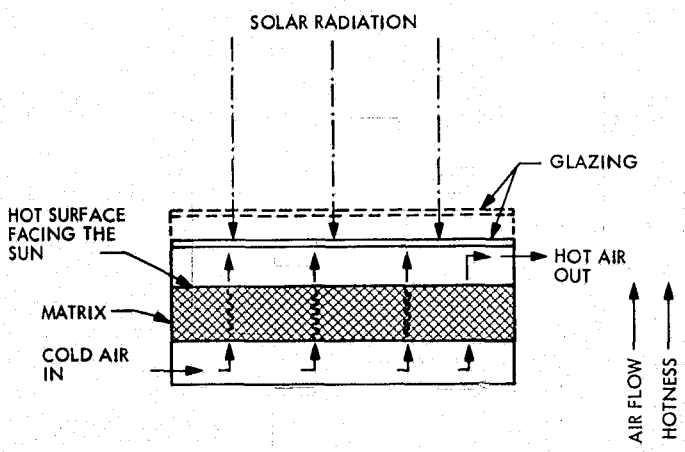


Fig. 1. Upward flow of cold air towards the direction of hotter layers of the matrix

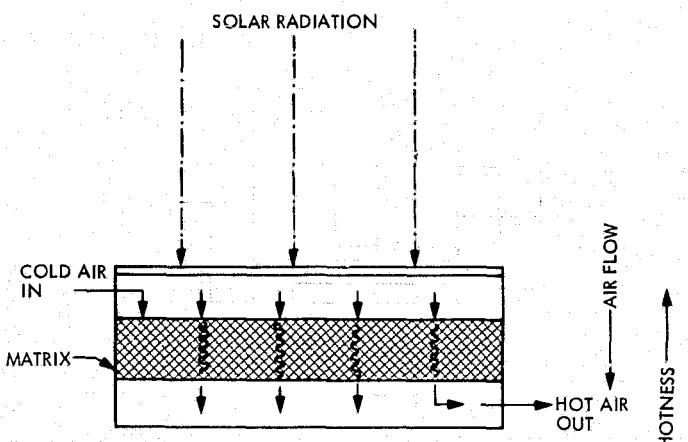


Fig. 2. Downward flow of cold air against the direction of hotter layers of the matrix

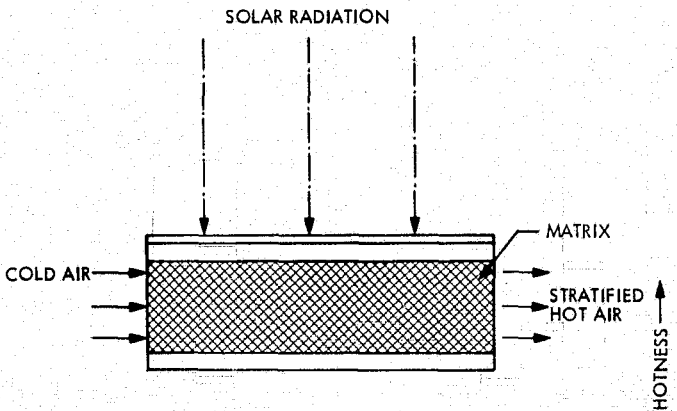


Fig. 3. Lateral flow of cold air across the direction of hotter layers of the matrix

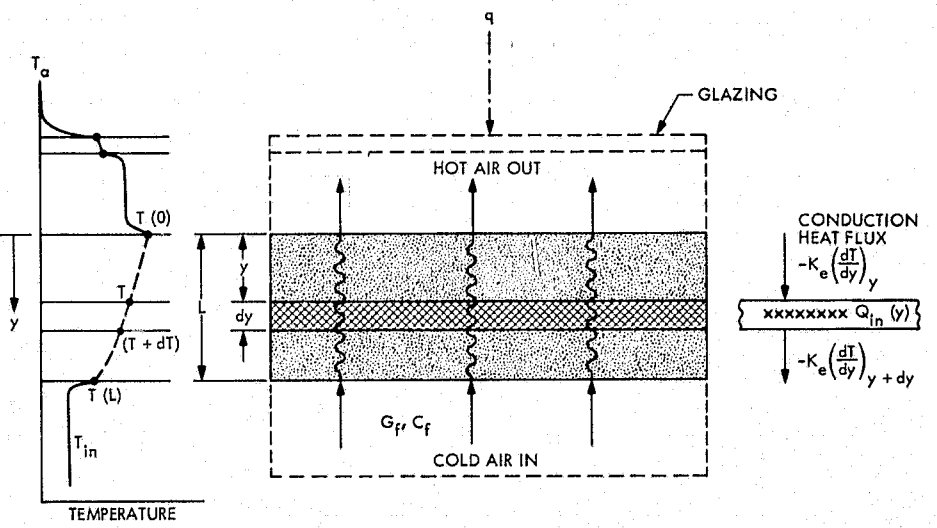


Fig. 4. Heat balance of an element of matrix plate

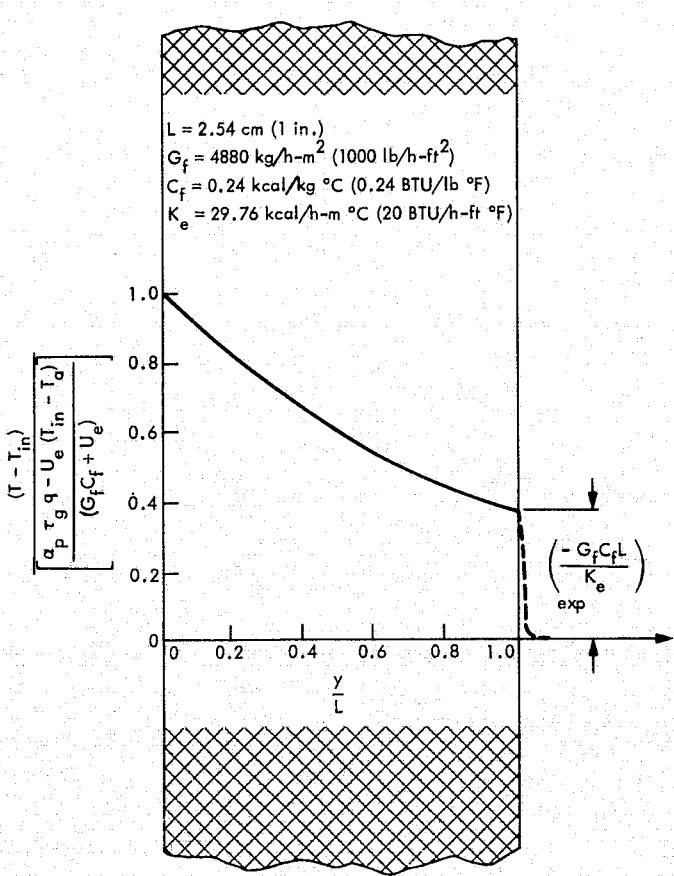


Fig. 5. Matrix and fluid temperature profile for an opaque matrix surface

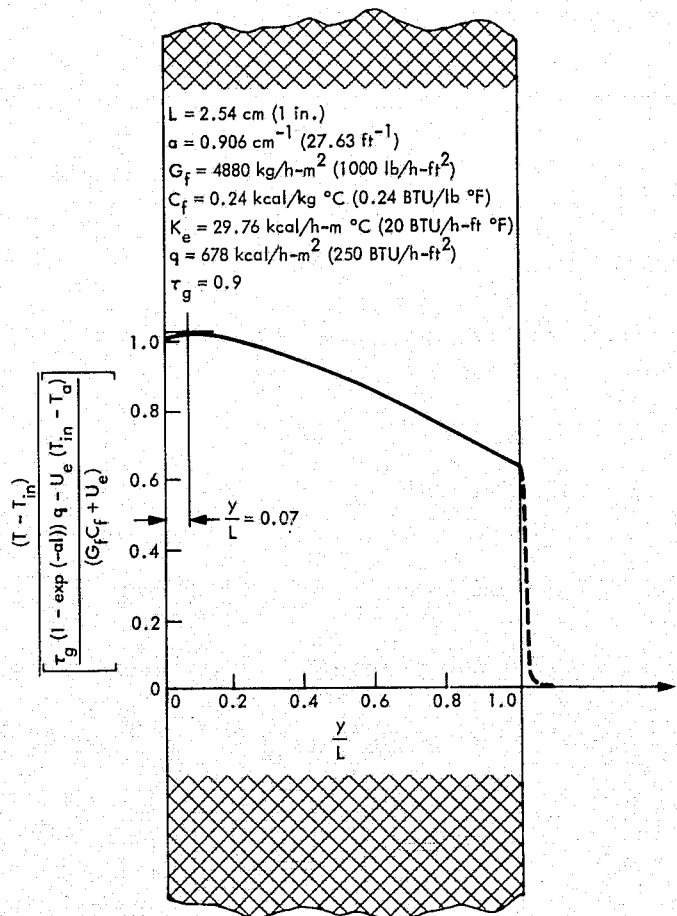


Fig. 6. Matrix and fluid temperature profile for a diathermanous matrix

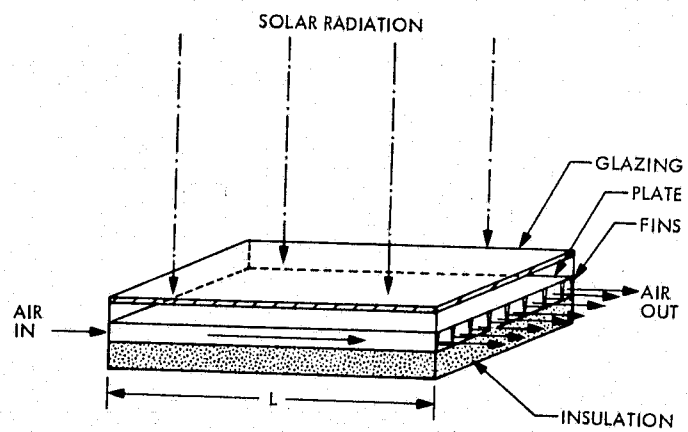


Fig. 7. Nonporous, flat plate solar air heater

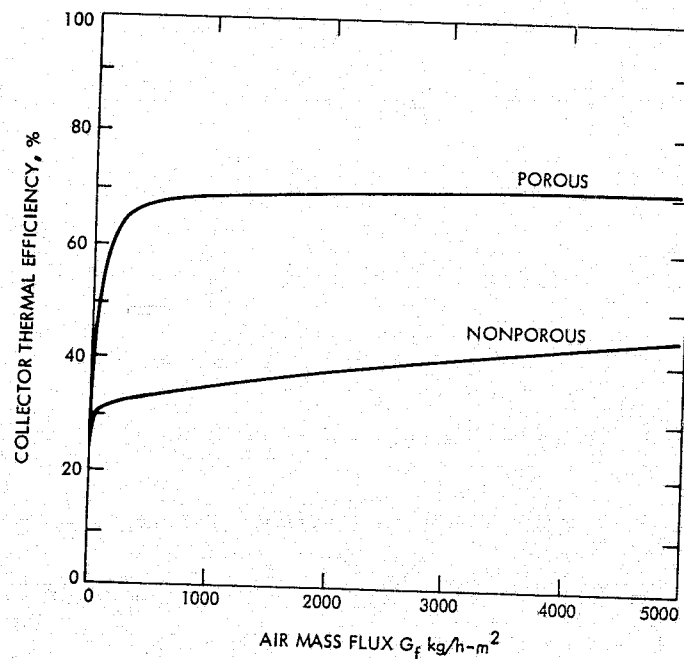


Fig. 8. Results of the numerical example to compare the thermal efficiency between a porous and nonporous collector

ORIGINAL PAGE IS
OF POOR QUALITY

N 76-29332

An MBASIC Application Program for Relational Inquiries on a Database

R. M. Smith
DSN Facility Operations Office

An MBASIC application program is described that allows a user to specify and perform a sequence of relational operations on a database.

I. Introduction

A previous article (Ref. 1) dealt with the recent implementation of a relational database in MBASIC, and focused upon the realization of the use of the five relational operations (Refs. 2 and 3).

This article describes an MBASIC application program that allows a user to specify and use a sequence of relational operations on a relational database for the purpose of making an inquiry or for the purpose of transferring data to a new file.

II. Relational Structure

In the relational model of data, data are organized into arrays (called relations) with fields (called domains), so that each record entry (called a tuple) is a set of attributes

describing the characteristics of a real world entity. For instance the assignment of test equipment might be represented by the following notation:

'ASSIGNMENT' (CON, OWNER, LOCATION, OPSTAT, REC DATE)

where:

CON = control number

OWNER = facility responsible for the equipment

LOCATION = facility where equipment is presently located

OPSTAT = operational status

REC DATE = date received at the indicated location

In the same manner, the failure of an item of test equipment might be represented:

'FAILURE' (CON,DATE,TIME,DOWN#,FACILITY)

where:

DATE and TIME = date and time of the failure occurrence

DOWN# = a unique event number for the failure occurrence

FACILITY = the operational facility at which the failure occurred

Finally, the status of a subsystem (containing test equipment) might be represented:

'SSDOWN' (DOWN#,SSMA,UNIT,REFDES,DATE, TIME)

where:

SSMA = subsystem-major assembly number

UNIT = equipment rack unit number where the failure occurred

REFDES = reference designator (a coordinate position within a subsystem unit) where the failure occurred.

DATE and TIME = date and time that the subsystem became inoperative

Other relations may be constructed to describe other relationships but these three will be used as illustrations in this paper.

III. Relational Operations

There are five operations specified in the relational model and explained in Refs. 1, 2, and 3:

(1) Join

(2) Restriction

(3) Division

(4) Projection

(5) Permutation

Specific notation is used as a convenient way of expressing relational operations. The notation is simple and allows the annotation of a database access strategy and can be converted easily to MBASIC code or used with the application program discussed in this article.

Typical notation is as follows:

(1) Restriction

'RELATION' | DOMAIN1 = selected data value

stated: restrict 'RELATION' on DOMAIN1 equal to selected data value

meaning: select from 'RELATION' all tuples where the data value in DOMAIN is equal to the selected data value.

(2) Join

'RELATION1' (DOMAIN1) 'RELATION2'

stated: join 'RELATION1' with 'RELATION2' over DOMAIN1

meaning: compare tuples in 'RELATION1' with tuples in 'RELATION2' and, where the data value in DOMAIN1 is the same in both tuples, produce a resultant tuple that contains the domains of both tuples.

(3) Projection

π 'RELATION3' (DOMAIN1, DOMAIN2, . . . DOMAINn)

stated: project 'RELATION3'

meaning: create 'RELATION3' containing DOMAIN1, DOMAIN2, . . . DOMAINn

(4) Permutation

Permutation is a function of the projection operation where the resultant domain order is changed from the original order:

π 'RELATION4' (DOMAIN2, DOMAIN6, . . . DOMAINn)

(5) Division

Division is a special case of restriction and projection in this implementation and will not be dealt with separately.

IV. Description of the Application Program

'INQUIRY' is a generalized program allowing a user to use the relational operations singly or in a selected sequence to manipulate the domains of one or more relations in a database. The program is data independent; that is, it does not need to be rewritten or altered if the database is reorganized. This feature is realized by the use of a directory relation that contains a description of the database. The program derives the current data description from the directory relation. When 'INQUIRY' is used to create a new relation, the directory relation is automatically updated to contain the new description. When a "temporary" relation is created the program will delete the directory update at the request of the user.

'INQUIRY' accepts relational operations in the following formats from an operator:

(1) Restriction

RELATION1, DOMAIN1, =, data value¹

(2) Join

RELATION1, DOMAIN1, RELATION2

(3) Projection

RELATION1, QD, RELATION3, DOMAIN2, . . . , DOMAINn

where RELATION1 and RELATION2 are existing relations; QD is the quantity of domains to be projected; RELATION3 is a new relation to be created (may be the terminal); DOMAIN1 is an existing domain; DOMAIN2 through DOMAINn are the domains to be contained in the new relation.

Compare these formats with the standard notation formats in Section III of the article.

The relational operations may be used in the following combinations in 'INQUIRY':

(1) Restriction

(2) Projection

(3) Join

(4) Restriction, join

- (5) Restriction, projection
- (6) Restriction, join, projection
- (7) Join, projection
- (8) Join, restriction
- (9) Join, restriction, projection

Projection: may be to:

- (1) Terminal ("TERM")
- (2) Permanent relation (NAME)
- (3) Temporary relation (*NAME)

Figure 1 is a functional flowchart of the program and illustrates the possible combinations graphically.

V. Applications

'INQUIRY' may be used as a general purpose access program or as a design tool in planning the strategy of a single purpose program.

Figure 4 illustrates a session at a terminal using 'INQUIRY' to extract data from the relation called 'ASSIGNMENT' (Fig. 5). The process depicted in Fig. 4 is a restriction followed by a projection, the same process that is depicted in Fig. 2. Figure 6 illustrates a session at a terminal using 'INQUIRY' to manipulate data from two relations and to display a resultant data list at the terminal. The process depicted in Fig. 6 is a join followed by a projection, the same process that is depicted in Fig. 3. This sort of activity is representative of the general purpose aspect of the program.

To use 'INQUIRY' as a tool to design a single purpose program the user would "construct" using 'INQUIRY', a sequence of relational operations in a manner similar to that depicted in Fig. 6. If the resultant content and domain order were as desired then the user would convert the relational statements to MBASIC code using additional code as necessary for column headings, spacing, titling, etc.

Figures 2 and 3 depict, respectively, the restriction and join operations first in standard relational notation then in typical flowchart configuration and finally in MBASIC code. The applications described in this article require the use of relations that are in, at least, first normal form (Ref. 3). 'ASSIGNMENT' (Fig. 5), which is used in some of the examples in this article, is in third normal form (Ref. 3).

¹In the restriction operation, "=", ">", or "<" may be used.

References

1. Smith, R. M., "A Relational Data Base Implemented Using MBASIC," in *The Deep Space Network Progress Report 42-30*, pp. 291-305, Jet Propulsion Laboratory, Pasadena, Calif., Dec. 15, 1975.
2. Codd, E. F., "A Relational Model of Data for Large Shared Data Banks," *Communications of ACM*, Vol. 13, No. 6, June 1970.
3. Date, C. J., *An Introduction to Database Systems*, Addison-Wesley Publishing Co., Inc., Reading, Mass., 1975.

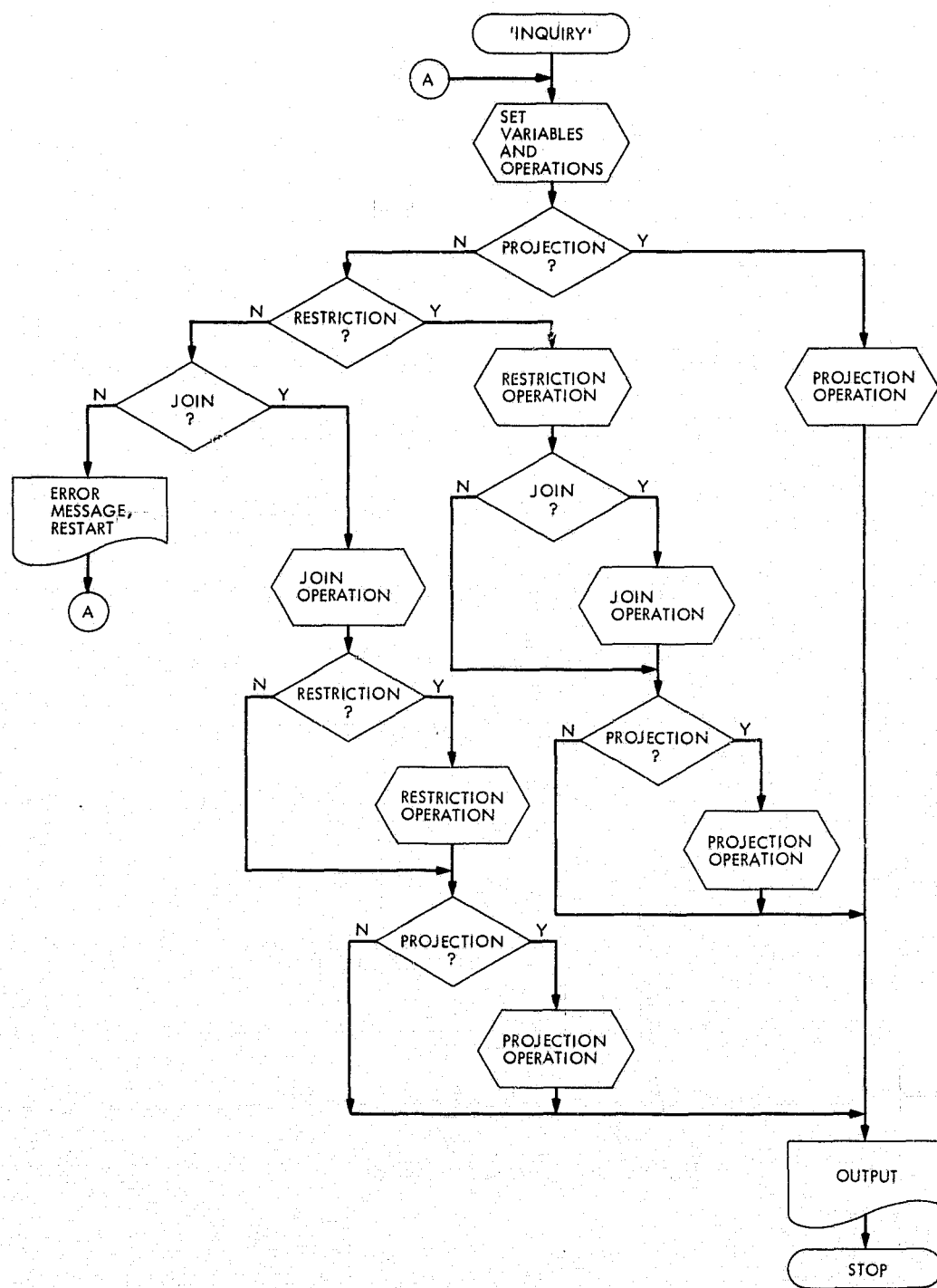
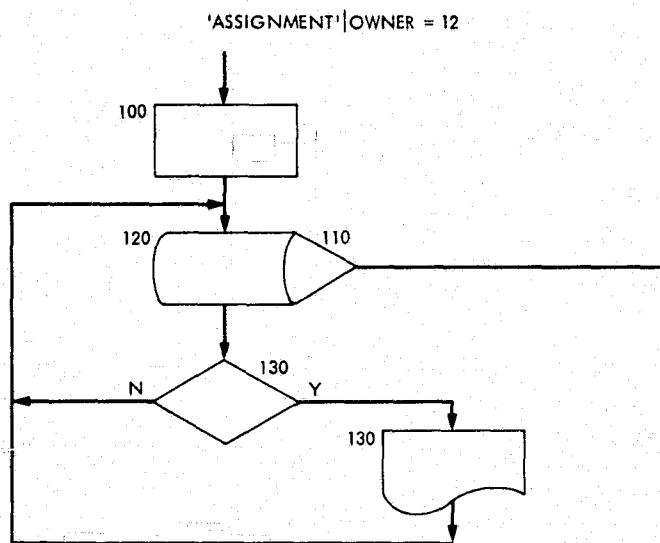


Fig. 1. Functional flowchart for 'INQUIRY'



```

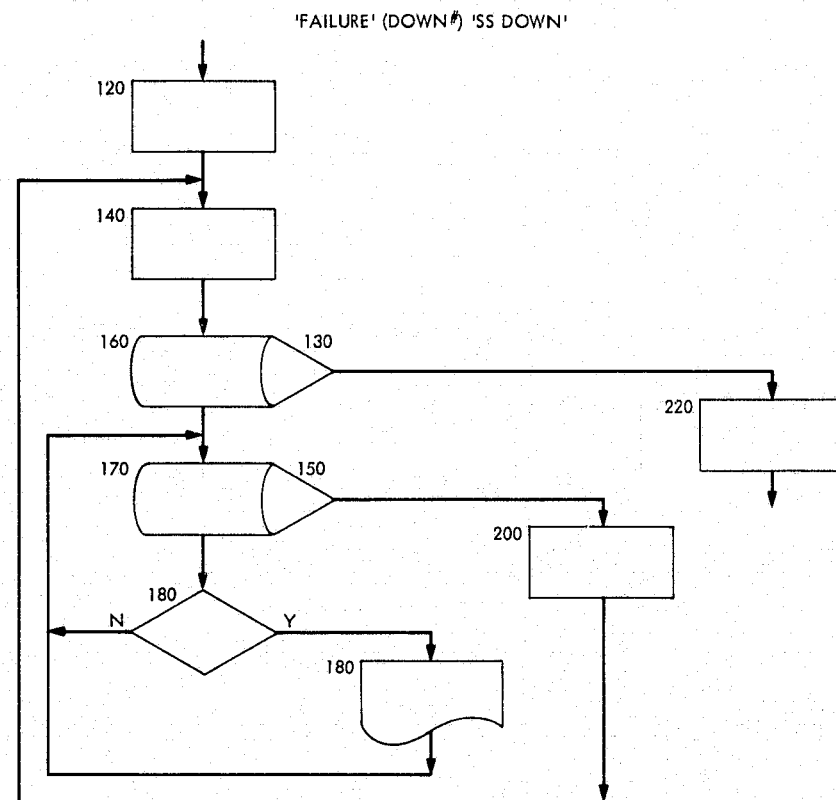
100 OPEN 'ASSIGNMENT',INPUT,1
110 AT ENDFILE(1) GO TO 150

120 INPUT FROM 1:C$(1),D$(1),L$(1),D$(1),FD$(1)
130 IF D$(1)='12' THEN PRINT C$(1);L$(1);D$(1)
140 GO TO 120

150 CLOSE 1
  
```

Fig. 2. The restriction operation

ORIGINAL PAGE IS
OF POOR QUALITY



```

120 OPEN 'FAILURE',INPUT,1
130 AT ENDFILE(1) GO TO 220

140 OPEN 'SSDOWN',INPUT,2
150 AT ENDFILE(2) GO TO 200
160 INPUT FROM 1:OC$(1),UD1$(1),TD$(1),DN1$(1),L$(1)
170 INPUT FROM 2:DN2$(1),SS$(1),UM$(1),REF$(1),UD2$(1),TD2$(1)
180 IF DN1$(1)=DN2$(1) THEN PRINT L$(1);SS$(1);UD1$(1);DN1$(1)
190 GO TO 170
200 CLOSE 2
210 GO TO 140
220 CLOSE 1,2
  
```

Fig. 3. The join operation

```

>RUN
?R
?ASSIGNMENT,OWNER += 12
JOINT N
PROJECTION? Y
?3,TERM,CON,LOCATION,OPSTAT
BB5C11 12 DL
CR6B12 1Y US
♦♦♦END

```

Fig. 4. Using 'INQUIRY' to plan the restriction strategy of Fig. 2

```

COPY 'ASSIGNMENT' TO TERMINAL
AR3A12,1Y,1Y,DL,010675
RB6C21,1X,1X,DL,170273
CD3B15,1X,1X,SP,1E1072
BB5C12,14,14,DL,091274
AX3B09,11,1Y,EP,190176
DA4C12,1X,1X,DL,071071
BB5C11,12,12,DL,091274
AR7D15,1Y,1X,US,250276
BB5C13,11,11,SP,091274
CC7C0E,1X,1X,US,151172
CM5B13,1Y,1Y,DL,151071
CR6B12,12,1Y,US,110376
>

```

Fig. 5. A listing of data contained in the relation 'ASSIGNMENT'

```

RUN
?J
?RMS♦EQPT.FAILURE,DOWN#,RMS♦EQPT.ESDOWN
RESTRICTION ?H
PROJECTION ?Y
?4,TERM,FACILITY,SSMA,DATE,DOWN#
12 3606 100376 3775

DO *FILES NEED TO BE DELETED? N
♦♦♦END
>

```

Fig. 6. Using 'INQUIRY' to plan the join strategy of Fig. 3

ORIGINAL PAGE IS
OF POOR QUALITY

N 76-29333

Maximum Likelihood Convolutional Decoding (MCD) Performance Due to System Losses

L. Webster
Network Operations Section

A model for predicting the computational performance of a maximum likelihood convolutional decoder (MCD) operating in a noisy carrier reference environment is described. This model is used to develop a subroutine that will be utilized by the Telemetry Analysis Program (TAP) to compute the MCD bit error rate. When this computational model is averaged over noisy reference phase errors using a high-rate interpolation scheme, the results are found to agree quite favorably with experimental measurements.

I. Introduction

The maximum likelihood or Viterbi decoding algorithm was discovered and analyzed by Viterbi (Ref. 1) in 1967. Maximum likelihood convolutional decoding (MCD) using the Viterbi decoding algorithm is presently being implemented in the Deep Space Network (DSN).

In order to develop specifications and criteria for executing system performance tests, it was necessary to develop a program to provide a prediction of the MCD's performance. This program is to be integrated into the Telemetry Analysis Program (TAP).

Using curve fitting techniques on data produced by the baseband characteristic performance curve (Fig. 1) the model predicts MCD performance under noisy carrier reference conditions.

II. Discussion of MCD Performance Prediction Model (One-Way Radio Loss)

In developing the MCD performance prediction model, we begin with the baseband performance characteristic curve for maximum likelihood convolutional decoding of a $K = 7$, rate 1/2 convolutional code with $Q = 3$ (Ref. 2). In general, the characteristic curves here mentioned represent the best baseband estimate of the MJS'77 code performance under ideal (i.e., laboratory) conditions. As such, the characteristics represent an upper bound on telemetry system performance. However, owing to the fact that there is no exact analytical expression for the performance characteristic, we have to use measured baseband performance data and, noting the fact that these data, as well as the simulation results of the MCD (Ref. 3, Section 4), define a relationship between P_e and

E_b/N_0 , numerically approximate an expression for the MCD performance characteristics. Written formally,

$$P_e = f\left(\frac{E_b}{N_0}\right) \quad (1)$$

for a given code, receiver quantization, and Viterbi decoder, where P_e denotes the probability of bit error and E_b/N_0 is the ratio of signal energy per bit to noise spectral density.

An inaccurate carrier phase reference at the demodulator will degrade system performance (see Fig. 2). In particular, a constant error ϕ in the demodulator phase will cause the signal component of the matched filter output to be suppressed by the factor $\cos \phi$ (Ref. 3, Section 5).

$$r_i = I \sqrt{\frac{2E_s}{N_0}} \cos \phi + n_i \quad (2)$$

Since the carrier phase is being tracked in the presence of noise, the phase error ϕ will vary with time. When the data rate is large compared to the carrier loop bandwidth, the carrier phase error ϕ does not vary significantly during perhaps 20–30 information bit times. Therefore, the phase error is assumed to be constant over the length of almost any decoder error. This being the case, the bit error probability for a constant phase error ϕ can be written as

$$P_e(\phi) = f\left(\frac{E_b}{N_0} \cos^2 \phi\right) \quad (3)$$

from (1) and (2), making use of the fact that the received signal energy is degraded by $\cos^2 \phi$.

Let $\phi(t)$ be the phase error in the receiver phase locked loop (PLL). The phase error $\phi(t)$ is an ergodic random process whose probability density function (for a second order PLL) may be written as

$$P(\phi) = \frac{\exp(\alpha \cos \phi)}{2\pi I_0(\alpha)}, \quad \alpha \gg 1 \quad (4)$$

where α is the signal-to-noise ratio in the carrier phase tracking loop, and $I_0(\cdot)$ is the zeroth order modified Bessel function. See Ref. 4, pages 90 and 198, for derivation of $p(\phi)$. In Ref. 4, it is shown that for large α

$$I_0(\alpha) \sim \frac{\exp(\alpha)}{(2\pi\alpha)^{1/2}} \quad (5)$$

Therefore, we can write for the probability density function (PDF) of ϕ :

$$P(\phi) \sim \left(\frac{\alpha}{2\pi}\right)^{1/2} \exp(\alpha \cos \phi - \alpha) \quad (6)$$

If we let $P(E)$ denote the resulting probability of bit error when considering the performance of the MCD when the carrier phase is being tracked in the presence of noise (imperfect carrier phase reference), where ϕ is a random variable with PDF $p(\phi)$, Eq. (6),

$$P(E) = \int_{-\pi}^{\pi} P(\phi) P_e(\phi) d\phi \quad (7)$$

Since $p(\phi)$ is known as a function of loop SNR, the joint density $P(E, \phi)$ is also known as a function of loop SNR and the dependence on ϕ can be integrated out, hence Eq. (7). However, since $P_e(\phi)$ does not have an exact analytical expression, we must use the Viterbi decoder measured performance data and obtain a model representing the functional relationship expressed in Eq. (3).

Recognizing the fact that the bit error rate curve (Fig. 1) is a semi-log plot; we can use the relationship used in Ref. 5,

$$Y = A \exp(BX) \quad (8)$$

to model $P_e(\phi)$.

The model is

$$P_e(\phi) = A \exp(BX) \quad (9)$$

where $X = E_b/N_0$ and A and B are constants (Ref. 6). The constants A and B were determined using the TYMSHARE program CURFIT (see Appendix for a discussion of the curve fitting).

$$A = 85.7501$$

$$B = -5.7230$$

Since E_b/N_0 is degraded by the factor $\cos^2 \phi$ for imperfectly coherent performance,

$$P_e(\phi) = A \exp\left(B\left(\frac{E_b}{N_0}\right) \cos^2 \phi\right) \quad (10)$$

Substituting Eqs. (6) and (10) into Eq. (7), we get

$$P(E) = \int_{-\pi}^{\pi} \left(\frac{\alpha}{2\pi}\right)^{1/2} \exp(\alpha \cos \phi - \alpha) A \exp\left(B\left(\frac{E_b}{N_0}\right) \cos^2 \phi\right) d\phi \quad (11)$$

Now, by performing the algebra on Eq. (11) we get the following:

$$P(E) = \left(\frac{2\alpha}{\pi}\right)^{1/2} A \int_0^{\pi} \exp\left[B\left(\frac{E_b}{N_0}\right) \cos^2 \phi - \alpha(1 - \cos \phi)\right] d\phi \quad (12)$$

Equation (12) has been integrated numerically using a modified Romberg quadrature subroutine. The tabulated results are found in Table 1 with the plot of the MCD performance predicting curves with the carrier phase tracking loop SNR α as a parameter (Fig. 2). Figure 3 shows the error rate performance requirement.

III. Comparison of Predicted and Experimental MCD Performance

The real test of a model is its ability to predict performance under real system operation conditions. In order to make a valid comparison, MCD performance data taken from NASA's Deep Space Network tracking stations must be compared with the model. Due to the fact that, at present, stations throughout the Network have barely begun to install and test the MCD, only a small amount of data are available with which to compare the model. In this paper, the model will be compared to data received from the Compatibility Test Area (CTA 21) and DSS 62 (Madrid, Spain).

The data from DSS 62 show in Fig. 4 (see Fig. 5 of Ref. 7, page 27) the behavior of the bit errors as a function of modulation indices. From this graph one can establish the optimum point of performance by choosing (for each P_t/N_0) that carrier suppression yielding the lowest error rate. As can be seen from Fig. 4, there exists a minimum degradation point at approximately 70 ± 1 deg modulation index.

In the $\Delta E_b/N_0$ column of Table 1 it is shown that the MCD performance prediction model compares very well to the actual MCD performance at DSS 62 and DSS 63 (Spain) for modulation indices of 69-71 deg. At a mod index of 70 ± 1 deg the model predicts to within 0.2 dB of the actual MCD performance on the average.

Table 2 shows the range of data taken at DSS 62/63. Column 1 of this table shows that the carrier phase tracking loop SNR ranges from 18.0 to 22.1 dB. By taking an average of the $\Delta E_b/N_0$ column, it is shown that the MCD

prediction model predicts to within 0.25 dB of the actual MCD performance over this entire range of data.

Figures 5 and 6 show how well the MCD model compares with the tests performed at CTA 21. A more detailed comparison will be performed when more data are available from CTA 21.

IV. Telemetry Analysis Program (TAP) and the MCD Subroutine

The Network Operations System Support Group maintains a telemetry system analysis program that must be updated to include the MCD performance prediction subroutine. The performance prediction model will be incorporated in the Telemetry Analysis Program (TAP) as a subroutine. The conversational TAP has the capability of analyzing both block-coded and uncoded data for the Viking mission and uncoded data for the Pioneer and Helios missions. Block III as well as Block IV configurations are available. For a given receiver subcarrier demodulator assembly (SDA) and symbol synchronizer assembly (SSA) configuration (Blk III or Blk IV bandwidth settings), bit rate, modulation index, and ST_s/N_0 , the program outputs telemetry performances in the form of receiver, SDA and SSA degradation. Following the adding of the MCD subroutine, the TAP will then provide a predicted performance degradation of signal due to carrier phase jitter and tracking loop SNR. It will also provide overall telemetry degradation as related to the addition of the MCD.

The items in Fig. 7 labeled "new" are essentially the changes necessary to implement the Telemetry Analysis Program processing steps to include the MCD update (see Fig. 8).

V. Conclusions

We have seen that the model of the maximum likelihood convolutional decoder (MCD) works quite well in predicting the performance of the on-station MCD. Table 1 shows that at an optimum mod index of 71 deg the $\Delta E_b/N_0$ (dB) between the performance prediction model and the actual data taken from DSS 62/63 (Spain) is approximately 0.17 dB average. Further comparisons will be made when we receive data from the other network stations.

References

1. Viterbi, A. J., "Error Bounds for Convolutional Codes and an Asymptotically Optimum Decoding Algorithm," *IEEE Trans. Inform. Th.*, Vol. IT-18, Apr. 1976, pp. 260-269.
2. "Telemetry Performance Characteristics for MJS-77 TPAP Program," IOM 3396-75-093, Jet Propulsion Laboratory, Pasadena, Calif., June 16, 1975 (an internal document).
3. Heller, J. A., and Jacobs, I. M., "Viterbi Decoding for Satellite and Space Communication," *IEEE Trans. Comm. Tech.*, COM-19, No. 5, Oct. 1971.
4. Viterbi, A. J., *Principles of Coherent Communication*, McGraw-Hill, New York, N. Y., 1966, p. 90.
5. Richards, J. W., *Interpretation of Technical Data*, D. Van Nostrand, New York, N. Y., 1967, p. 44.
6. Webster, L., "Viterbi Decoder Performance Degradation Due to Imperfect Carrier Phase Reference," IOM 421E-75-377, Jet Propulsion Laboratory, Pasadena, Calif., Sept. 15, 1975 (an internal document).
7. Urech, J. M., and Delgado, L., "Final Report on the DSN Performance for Convolutional Codes with a Viterbi Decoder," JPL Systems Engineering Section/DSS 62/63, Madrid, Spain, Jan. 1976 (an internal document).

Table 1. Comparison of the MCD performance data from DSS 62/63 and the MCD performance prediction model for optimum mod index selected from Fig. 4

Mod index	Carrier phase tracking loop SNR, dB	Bit error rate	Energy per bit to noise spectral density ratio (Spain)	Energy per bit to noise spectral density ratio (prediction model)	$\Delta E_b/N_0$, dB
70	14.62	0.204×10^{-4}	4.43	4.58	0.15
	14.72	0.250×10^{-4}	4.25	4.55	0.30
	15.18	0.448×10^{-5}	4.66	5.00	0.34
71	14.24	0.536×10^{-4}	4.53	4.45	-0.08
	14.33	0.388×10^{-4}	4.38	4.51	0.18
	14.37	0.340×10^{-4}	4.23	4.50	0.27
	14.77	0.547×10^{-5}	4.86	5.07	0.21
69	15.00	0.119×10^{-4}	4.28	4.70	0.42
	15.09	0.800×10^{-5}	4.89	4.81	0.42
	15.14	0.845×10^{-4}	3.985	4.30	0.30
	15.57	0.855×10^{-5}	4.71	5.00	0.29

Table 2. Comparison of the MCD performance data from DSS 62/63 and the MCD performance prediction model

Carrier phase tracking loop SNR, dB	Bit error rate	Energy per bit to noise spectral density ratio (Spain)	Energy per bit to noise spectral density ratio (model)	$\Delta E_b/N_0$, dB
13.0	0.686×10^{-4}	4.40	5.1	0.7
13.5	0.202×10^{-4}	4.86	5.31	0.45
14.0	0.471×10^{-4}	4.39	4.55	0.16
14.4	0.633×10^{-5}	4.87	5.1	0.23
15.00	0.119×10^{-4}	4.28	4.7	0.42
15.57	0.355×10^{-5}	4.71	5.00	0.29
17.08	0.655×10^{-5}	4.51	4.6	0.09
19.79	0.413×10^{-3}	3.31	3.81	0.0
20.50	0.792×10^{-4}	3.83	3.85	0.02
22.10	0.887×10^{-5}	4.61	4.48	-0.13

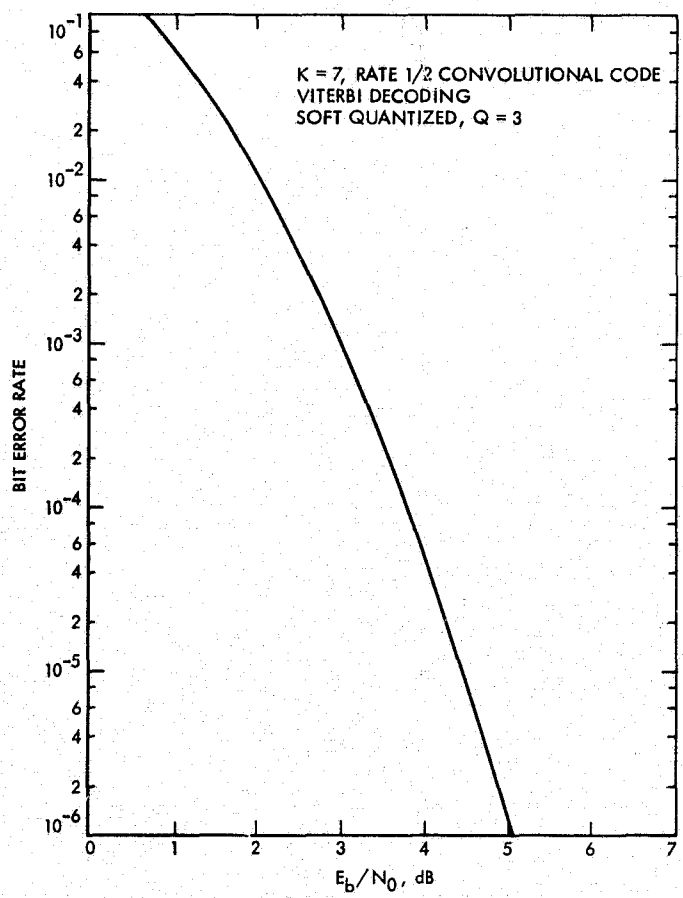


Fig. 1. Baseband performance characteristic

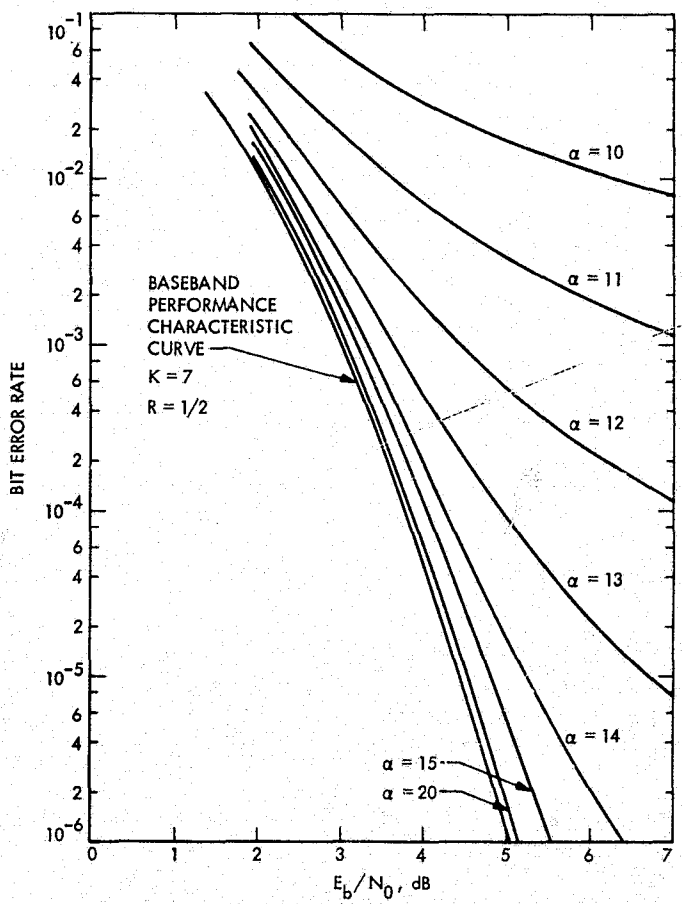


Fig. 2. MCD model output

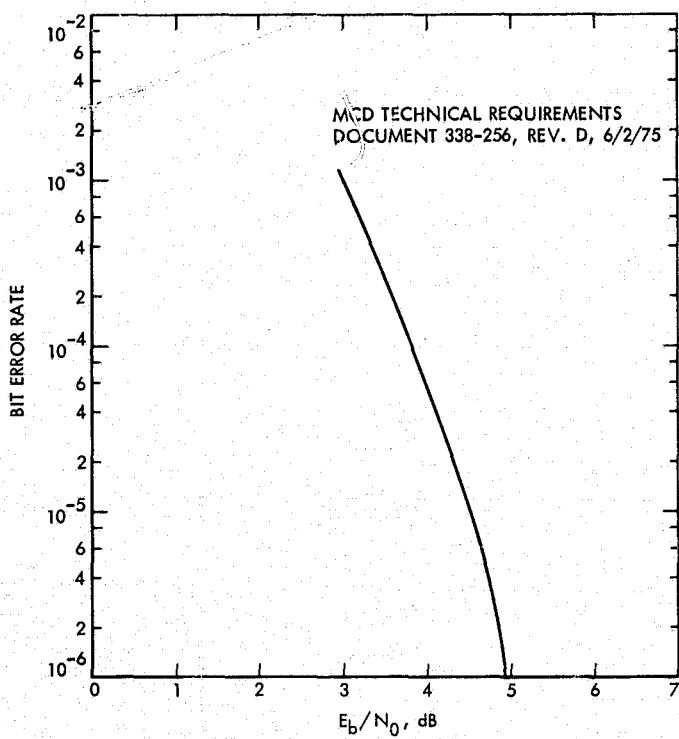


Fig. 3. Error rate performance requirement

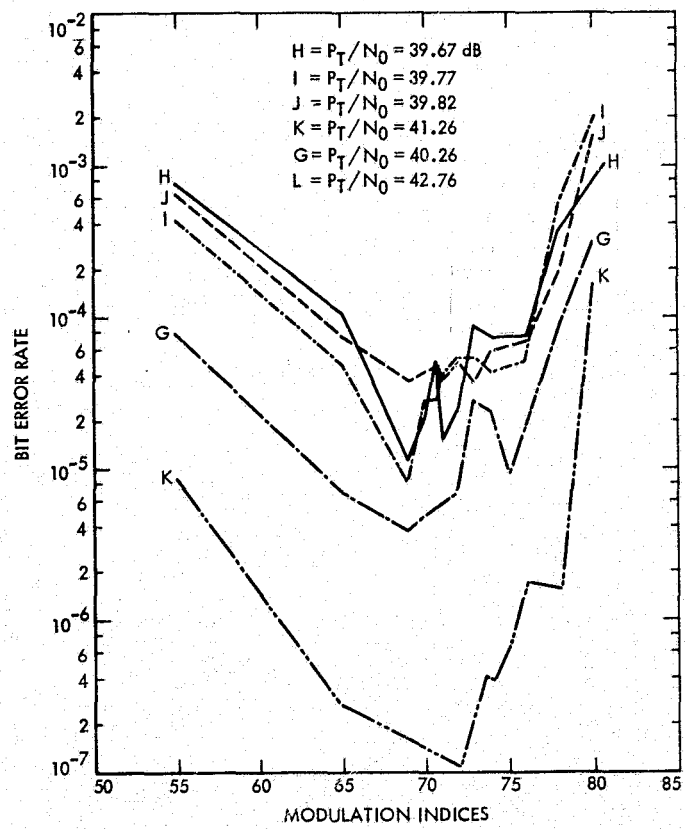


Fig. 4. BER vs modulation indices

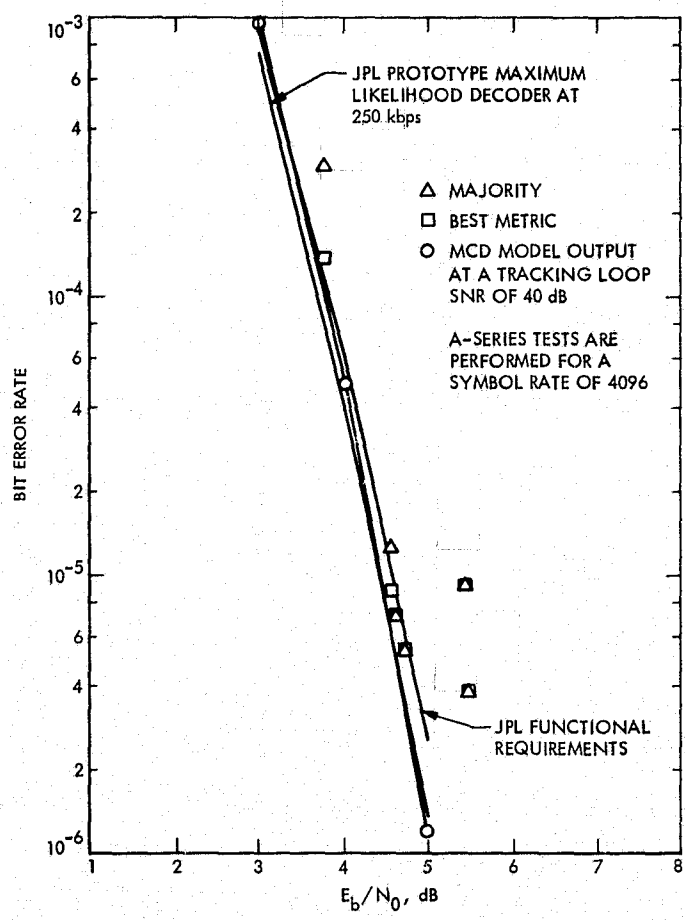


Fig. 5. E_b/N_0 vs bit error probability, A-series test

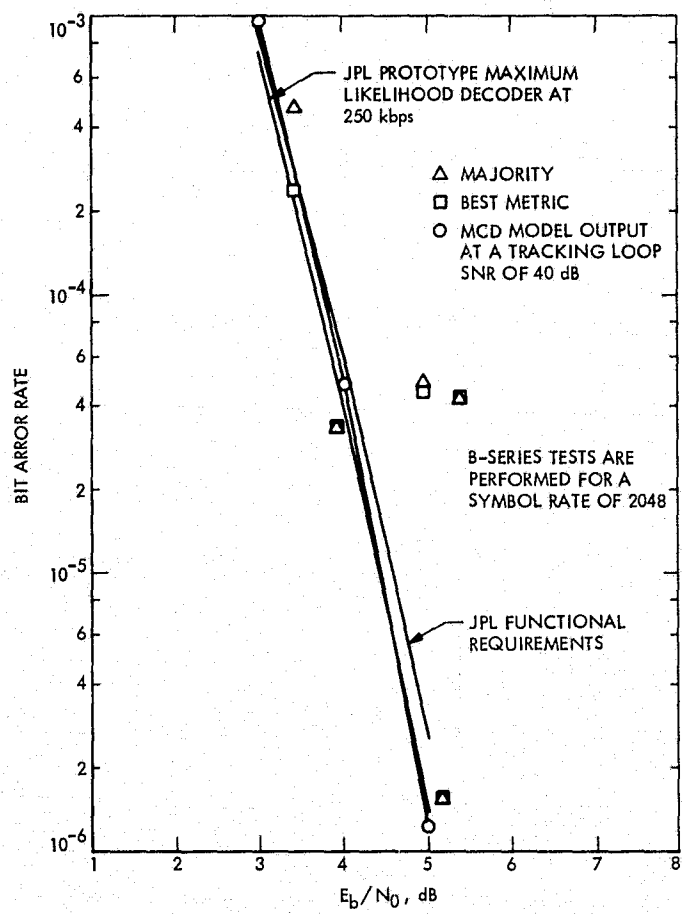


Fig. 6. E_b/N_0 vs bit error probability, B-series test

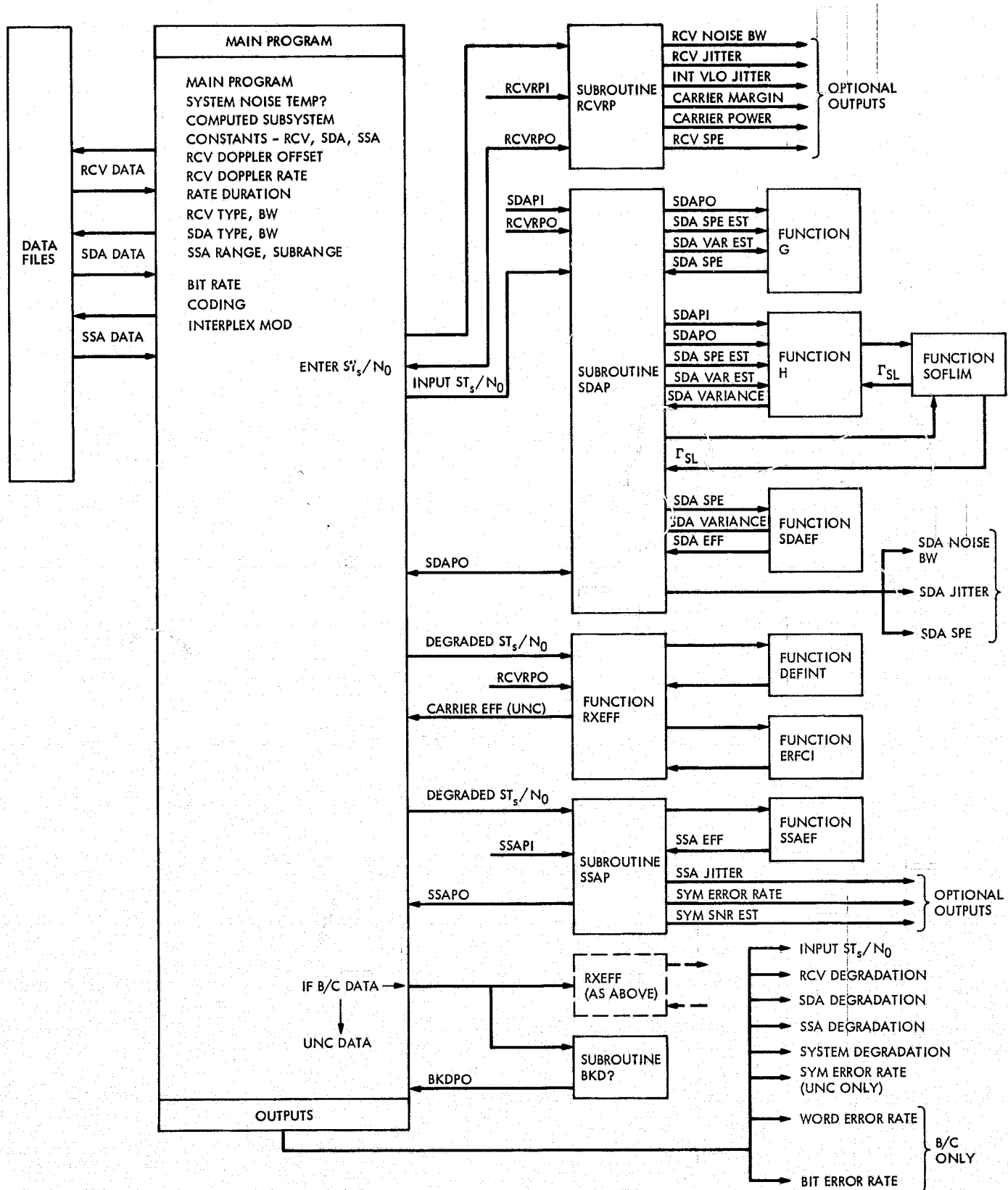


Fig. 7. Telemetry Analysis Program processing steps

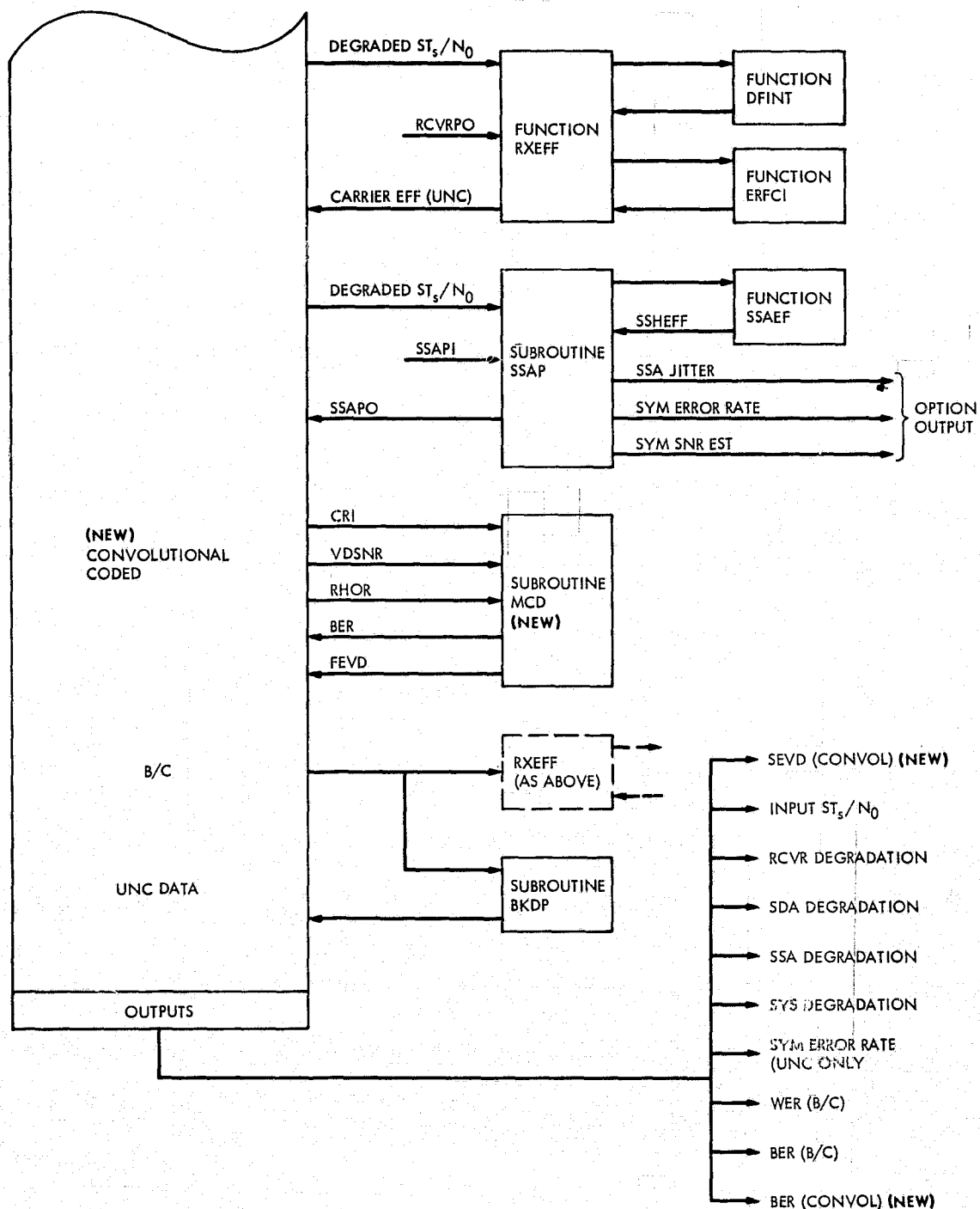


Fig. 8. Telemetry Analysis Program processing steps, MCD update

ORIGINAL PAGE IS
OF POOR QUALITY

Appendix

CURFIT is a linear regression program for data with two variables, X and Y . It accepts as many as 200 observations on two variables. The program CURFIT determines which of the following curves can best approximate a set of input points described by X and Y coordinates.

(a) $Y = a + bx$

(b) $Y = ae^{bx}$

(c) $Y = ax^b$

(d) $Y = a + \frac{b}{x}$

(e) $Y = \frac{1}{a + bx}$

(f) $Y = \frac{x}{ax + b}$

Equation (b) best approximated the input points described by E_b/N_0 vs bit error rates (BER) taken from the baseband characteristic curve of Fig. 1.

Recognizing the fact that for convolutional coding with phase-coherent demodulation and Viterbi decoding, exact analytical expressions for bit error rate P_e vs E_b/N_0 are not attainable, we would like to establish the suitability of the empirical function:

$$Y = ae^{bx} \quad (A-1)$$

that has been determined by CURFIT as yielding the best approximation for BER vs E_b/N_0 .

One method of determining the suitability of the empirical function is that of finite differences. This method relies principally on the hypothesis that, for a given function, differences of the function $Y = ae^{bx}$ are constant for successive equal increments of some known function of X .

For

$$P(E) = Ae^{bx} \quad (A-2)$$

where A and B are constants and $X = E_b/N_0$, suppose that ΔX is a small constant incremental change in X and

$\Delta P(E)$ is the corresponding change in $P(E)$. Then, corresponding to an increased change from X to $(X + \Delta X)$,

$$P(E) + \Delta P(E) = AC^{B(X+\Delta X)} \quad (A-3)$$

must also hold true if this is a suitable empirical function.

If we subtract from $[P(E) + \Delta P(E)]$ the value $P(E)$ we get the following:

$$\begin{aligned} [P(E) + \Delta P(E)] - P(E) &= Ae^{B(X+\Delta X)} - Ae^{BX} \\ \Delta P(E) &= Ae^{BX}e^{B\Delta X} - Ae^{BX} \\ \Delta P(E) &= Ae^{BX}(e^{B\Delta X} - 1) \end{aligned} \quad (A-4)$$

Taking the natural logarithm of both sides

$$\ln \Delta P(E) = \ln A + \ln e^{BX} + \ln (e^{B\Delta X} - 1) \quad (A-5)$$

But ΔX is constant by supposition, and therefore $\ln (e^{B\Delta X} - 1)$ is a constant, independent of X (but not ΔX); hence, we can rewrite $\ln \Delta P(E)$ in the following way;

$$\ln \Delta P(E) = A^1 + BX \quad (A-6)$$

where $\ln e^{BX} = BX$, and $A^1 = \ln A + \ln (e^{B\Delta X} - 1)$.

Let us take an incremental change in $\ln \Delta P(E)$ denoted as follows:

$$\ln \Delta P(E) + \Delta [\ln \Delta P(E)] \quad (A-7)$$

and subtract this new identity (Eq. A-6); we get

$$\begin{aligned} (\ln \Delta P(E) + \Delta [\ln \Delta P(E)] - [\ln \Delta P(E)]) &= [A^1 + B(X + \Delta X)] \\ &\quad - [(A^1 + BX)] \end{aligned} \quad (A-8)$$

Hence

$$\Delta [\ln \Delta P(E)] = B\Delta X \quad (A-9)$$

Thus, for this type of relationship, the differences of the logarithm of the first differences will be constant. As an added advantage, Eq. (A-9) can be used in the determination of the coefficient B by averaging or using a mean-square average of the factors $\Delta [\ln \Delta P(E)]$.

N 76-29334

DSN Research and Technology Support

E. B. Jackson
R. F. Systems Development Section

The activities of the Venus Station (DSS 13) and the Microwave Test Facility (MTF) during the period April 19 through June 13, 1976, are discussed and progress noted.

Continuing reliability testing and computer program refinement of the remote controlled, unattended automated pulsar observing station is noted, along with routine observations of 17 pulsars. Radar observations of a geostationary satellite are reported, along with the routine automatic testing of the stability of the DSS 13 maser-receiving system. Additional testing of thermal characteristics of semi-flexible coaxial cables is reported, along with phase stabilization measurements thereon.

Routine support of the planetary radio astronomy experiment, with 43.25 hours of observations of Jupiter and various radio calibration sources, is reported, along with 18.75 hours of differential VLBI observations in conjunction with Australia, DSS 43.

Modifications of the clock synchronization winterization system are reported, along with a discussion of the activities of the DSN High-Power Transmitter Maintenance Facility. A detailed scanning of the orbital region in which geostationary satellites are found is reported as part of the DSN radio frequency interference analysis task.

The activities of the Development Support Group, in operating the Venus Station (DSS 13) and the Microwave Test Facility (MTF) during the period April 19 through June 13, 1976, are discussed and project support and progress discussed below.

I. Station Automation

In support of RTOP 70 "Network Monitor, Control, & Operations Technology," DSS 13 will be the demonstra-

tion station with which remotely operated, unattended operation is demonstrated.

Including automated tracking, 37.25 hours of station support were provided. Automated tracking, directed from a control computer at JPL, was performed for 23.75 hours, during which data were collected from pulsars 0031-07, 0329+54, 0525+21, 0736-40 and 0823+26. After initial program loading and checkout, no on-site operator intervention was made. The target to be tracked, and other appropriate inputs, were provided from the control com-

puter at JPL to the DSS 13 on-site master computer (an SDS-930 digital computer), and antenna movement, receiver frequency selection, and data collection were performed automatically under the direction of the three on-site computers. These three computers include an SDS-910 for data sampling timing, another SDS-910 for 26-m antenna movement, and the SDS-930 computer for control and data processing. Katherine Moyd, of the Communications Elements Research Section, assisted by station personnel, has been performing this testing.

II. Pulsar Observations

In support of the radio science experiment "Pulsar Rotation Constancy" NASA Office of Space Sciences (OSS-188-41-51-09), DSS 13 provided 62.75 hours of observations during which the emissions from the pulsars tabulated in Table 1 were recorded. These data, recorded at 2388 MHz, left circular polarization (LCP), are used to determine precise pulse-to-pulse spacing, changes in this spacing, pulse shape, and pulse power content of the signals emitted by these pulsars.

III. Radar Observations, Satellite

With Goldstone Mars, DSS 14 transmitting and DSS 13 receiving, reflected signal radar observations are being made of a geostationary satellite. Using the DSS 14 64-m antenna and 400-kW S-band transmitter, the satellite is illuminated at a nominal frequency of 2388 MHz. Reception of the reflected signals is accomplished on alternate round-trip light times (RTLT) at DSS 13, using a programmed oscillator controlled receiver and a 26-m antenna. Two stations are necessary because the RTLT is so short (approximately 242 ms) that waveguide switching on a single antenna is impractical. The transmitting station switches frequency approximately 2 MHz every RTLT and the receiving station receives the reflected signal every other RTLT. These observations were conducted for 9 hours.

IV. Maser-Receiver-NAR Reliability-Stability Testing

Reliability and stability testing of the DSS 13 total receiving system is conducted during nonmanned station periods. The 26-m antenna is prepositioned to a fixed azimuth and elevation, and the Noise-Adding Radiometer (NAR) data collection system automatically records total receiving system temperature as the antenna beam is

swept across the sky by the rotation of Earth. During this reporting period, the antenna was positioned at 360 deg azimuth and progressively positioned from 50.7 to 49.9 deg elevation and 450 hours of testing were automatically performed. This testing is done at 2295 MHz, using right circular polarization (RCP) on the 26-m antenna.

V. Receiver Phase Stability Testing

Continuing with an investigation into the phase stability characteristics of coaxial cables (Ref. 1), temperature rise measurements are being conducted on two cable bundles subjected to solar heating. Two bundles of four each semi-flexible coaxial cables, jacketed, were made up and placed on wooden supports atop the cable tray. A thermocouple was inserted underneath the jacketing, in thermal contact with the outer aluminum conductor. One cable bundle was painted white prior to bundling; the other was left in the natural black state. A third thermocouple was used to record ambient air temperature. Care was taken to ensure that no direct solar heating of the thermocouples took place.

It was anticipated that the white cable bundle would experience less solar heating, but quantitative data were desired. During the periods of maximum temperature, the black cable bundle outer conductor temperature rose 7-10°C above ambient air, while the white cable bundle rose only 1-2°C above ambient. Inasmuch as these cable bundles are approximately 1 m long, their thermal time constant is relatively short, and conductor temperature is easily affected by winds. The changes in conductor temperature of the black bundle were much more rapid and more frequent than those in the white bundle, which remained relatively constant, apparently unaffected by winds. Tests will be conducted on much longer samples to learn more about thermal time constants of cable lengths representative of operational conditions in the DSN.

As expected, the white cable bundle performed better thermally than did the black cable bundle. The black cable bundle was then installed into white plastic rectangular conduit, with 8-mm diameter "break out" spaces spaced 19 mm apart. These spaces, on two sides of the conduit, provided free air circulation. While enclosed in white conduit, the black cable bundle stabilized at approximately the same temperature above ambient as did the white jacketed cables, and exhibited approximately the same thermal behavior. Since this type of conduit, trade named "Panduit," has a removable cover, installation into this conduit of coaxial cables that are already

installed into cable trays would be relatively easy. Wherever critical phase stability conditions are encountered for cables subjected to solar heating, installation into "Panduit" or similar conduit would limit maximum temperatures and smooth temperature changes, thus minimizing changes in electrical length. Several days of recordings taken during this testing under varying weather conditions (intermittent clouds, over-cast, windy, sunny, etc.) are available, and testing is continuing.

Two proposed techniques for stabilizing coaxial cable electrical lengths are undergoing testing at DSS 13 on 610-m lengths of 12.7-mm diameter, jacketed, Spir-O-Line. Both techniques use approximately 100 MHz as the test frequency and monitor phase changes at that frequency. In one approach, changes in phase are used to modulate internal cable pressurization, using pressures up to 4.2 kg/cm² as required.

In the other approach, changes in the phase of the test signal are used to introduce compensating phase changes with a phase shifter so as to maintain a constant electrical length.

Although both approaches worked well in laboratory tests on short cable lengths, performance on these 610-m cable lengths under field conditions is poor. Investigation is continuing.

VI. Microwave Power Transmission

It is planned to test samples of the microwave oven magnetrons produced by three of the major manufacturers. Testing is aimed toward determining the feasibility of using phase locked microwave oven magnetrons as an inexpensive source of microwave power for testing adaptive phased arrays.

VII. Planetary Radio Astronomy

In support of the radio science experiment "Planetary Radio Astronomy" (OSS 196-41-73-01), DSS 13 measures and records the radiation received, at 2295 MHz, from the planet Jupiter and various radio calibration sources. These measurements are made using the 26-m antenna, the S-band receiving system, and the NAR. During this period, 43.25 hours of observations were made, during which the received radiation from Jupiter and the radio calibration sources tabulated in Table 2 were measured and recorded.

VIII. Differential VLBI

The advanced Systems experiment "Differential Very Long Baseline Interferometry" (OTDA 310-10-60-56) is designed to develop the capability of navigating interplanetary vehicles relative to "fixed" extragalactic radio objects. Primary to this task is the development of a catalogue of suitable extragalactic objects to be used as guides. In support of this catalogue development, DSS 13, in cooperation with DSS 43, provided 32 hours of support during this period. During these hours, 18.75 hours of actual observing, during which 95 sources were measured, was accomplished. Difficulties at DSS 43 prevented more actual observing from being accomplished.

IX. Clock Synchronization System

Difficulties at the receiving stations prevented satisfactory reception of some scheduled transmissions, but 10 transmissions, for 9.5 hours, were made, with 5 each being made to Australia DSS 42-43 and Spain DSS 62-63. A X12 multiplier failed in the 100-kW transmitter exciter, but the spare was installed and the system was restored to service.

The winterization system, which prevents the transmitter cooling water system from freezing, was modified during this period to reduce energy consumption. Previously, thermostatic controls turned the pumps on and off as a function of air temperature alone. When the air dropped to the set point temperature of 8°C (47°F), the pumps would come on and remain on until the air temperature rose above the set point temperature plus thermostat hysteresis. Often the air temperature would drop to the set point temperature, and remain there for hours without reaching freezing point, resulting in long term operation of the pumps and resulting heating of the water. The control system modification now turns on the pumps when both the air and water temperature fall to 10°C (50°F). The pumps will remain on until the water is heated to 27°C (80°F) or the air temperature rises to 10°C (50°F) plus thermostat hysteresis, whichever comes first. Restarting of the pumps will then occur only if both air and water temperature again fall to 10°C (50°F).

X. Deep Space Network High-Power Transmitter Maintenance Facility (DSN HPTMF)

The DSN HPTMF, located at DSS 13 and the MTF, continued to support the 10, 20, and 100-kW transmitters used in the DSN. Special testing of a 450-kW klystron to be loaned to Arecibo Radio Observatory was also accomplished.

At the request of the Cognizant Operations Engineer (COE) and the Cognizant Subsystem Manager (CSM), special priority testing of klystrons was accomplished in preparation for the critical phases of the Viking and Helios missions. Four klystrons, 10-kW, Model 4KM50SI (SNs H4-71, J4-45, K4-19, and L5-10) were tested for use as replacement klystrons as needed. Only two klystrons, SNs K4-19 and L5-10, met specifications, and are available for utilization as necessary. Also, similar testing of a 20-kW klystron, Model 5K70SG, SN IO-15, was accomplished, it met all DSN criteria, and is likewise available for use as needed.

A 100-kW klystron, Model X-3060, SN A6-17R2, returned from DSS 63 as defective, was tested at the Viking Lander frequency of 2112.96 MHz to ascertain whether the previously observed output power instability at the low end of the 2110-2120 MHz band would allow utilization at 2113 MHz if necessary. During a two-hour test period, the RF output power remained at the initial value of $101 \text{ kW} \pm 3\%$ without readjustment of any parameters, and it was concluded that, at this single frequency, this klystron is usable as a DSN spare, if necessary.

Klystron Model X-3060, SN A6-17R2, was also used at 2115 MHz to provide high-power (100-kW) testing of harmonic filters designed to reduce the fourth harmonic of the 100-kW S-band transmitters installed within the DSN. Three filters, Model F430FA1, SNs 02, 03, and 04 were tested at 100 kW for periods in excess of three hours each, with no anomalies of any kind. These filters were shipped to the COE for Engineering Change Order (ECO)

implementation into DSS 43 and DSS 63, with one filter held as a Network spare.

Arecibo Radio Observatory, which is conducting S-band radar observations of Mars in support of the Viking mission, suffered a 450-kW klystron failure. At the request of the Viking Project Office, two 450-kW klystrons were tested (Model X-3070, SNs K1-01 and D7-55R2), and one (D7-55R2) was chosen for loan to Arecibo. Final testing at 400 kW was accomplished using the magnet in which this klystron would be operated at Arecibo, and with Mr. Tom Dickinson, of Arecibo, as an observer. The tested klystron, along with the Arecibo magnet and special water hoses, was airlifted to Arecibo for use as needed. Klystron K1-01 was reinstalled into the 400-kW transmitter on the DSS 13 26-m antenna.

XI. DSN Radio Frequency Interference Analysis

In support of this program, the 26-m antenna at DSS 13 was used, along with the station receiver and special detection equipment, to search for interfering signals in the 2290-2300 MHz band. In particular, the band was examined for interference emanating from geostationary satellites.

Scanning in both frequency and antenna position at a rate consistent with a desired detection probability, the zero declination ± 1 deg region was searched for interfering signals. During 59.25 hours of observations, no positively identified interfering signals were found. The detection system used had a noise "floor" of -154.7 dBm .

Reference

1. Jackson, E. B., "DSN Research and Technology Support," in *The Deep Space Network Progress Report 42-33*. Jet Propulsion Laboratory, Pasadena, Calif., June 15, 1976.

**Table 1. Pulsars observed at DSS 13,
April 19 through June 13, 1976**

0031-07	0823+26	1933+16
0329+54	0833-45	2021+51
0355+54	1133+16	2045-16
0525+21	1237+25	2111+46
0628-28	1911-04	2218+47
0736-40	1929+10	

**Table 2. Radio calibration sources observed at DSS 13,
April 19 through June 13, 1976**

3C17	3C188	OJ 287
3C48	3C218	PKS 0237-23
3C84	3C309.1	PKS 2134-00
3C123	3C418	VRO 4222
	3C454.3	

**ORIGINAL PAGE IS
OF POOR QUALITY**

N 76-29335

Use of "Load and Go" Countdowns by the DSN Deep Space Stations

J. T. Hatch
Network Operations Section

The Level-4 Prepass Readiness Test (PRT) (the "load and go" countdown) provides an effective and low risk method of improving Network productivity. A carefully controlled trial period preceded the full-scale application of the Level-4 PRT to Pioneer, Helios and Viking cruise tracking operations. Use of this "load and go" concept to count down a station brings about a substantial increase in the proportion of total station hours devoted to spacecraft tracking.

I. Introduction

Time is scheduled at a Deep Space Station (DSS) prior to direct support of spacecraft tracking operations so as to prepare the station to meet all requirements of a forthcoming pass. These prepass preparations are termed Prepass Readiness Tests (PRTs) and consist of establishing and testing the specified configuration. Levels of support are used to define the extent to which equipment and systems are to be tested to support the scheduled activities. The four basic levels of support are summarized in Table 1 in terms of capabilities provided and the amount of time needed to perform a PRT for the level of support required.

Increasing the number of station hours devoted to actual tracking operations enhances the productivity of the Network. Since reducing the amount of time required for PRTs has the effect of increasing the total hours available for tracking, use of the Level-4 PRT offers a sub-

stantial potential for improving Network productivity. The flight projects benefit from any increase in the amount of tracking support they receive.

II. Characteristics

From the standpoint of Network productivity, the most significant characteristic of the "load and go" countdown is the short length of time required to complete it. Other characteristics that differ from those of the longer countdowns are described below.

A. Calibration Data

No equipment calibrations are performed. Rather, use is made of the latest previous calibration data available.

B. Software

Telemetry and Command Processor (TCP), Antenna Pointing Subsystem (APS) and Digital Instrumentation

Subsystem (DIS) software programs are not exercised as required for the other levels of support. After configuring the equipment, the programs are merely loaded into the computers and initialized to commence running at the beginning of the pass. However, prior to acquisition, two test commands are sent from the TCP to a dummy load to validate the on-site command system interface.

C. Data Validation

No telemetry, command, tracking, or monitor data transfer tests are run between the station and the Network Operations Control Center (NOCC). Instead, the first 30 minutes of each pass are used for this purpose and to validate the data. The data obtained during this period are provided to the Project.

D. Discrepancy Reports

Deep Space Network Discrepancy Reports (DRs) are handled differently in those cases where equipment calibrations are out of limits, equipment failures and procedural errors occur during the first 30 min of a pass, and the acquisition of signal (AOS) from a spacecraft is not accomplished on time. On these types of problems, DRs are closed out on the basis of having resulted from a load and go countdown, with its attendant and recognized slightly higher risk. Throughout the Pioneer-Helios trial period that is described in this article, DRs were waived on problems encountered during the 30-min period immediately following the scheduled AOS time.

III. Implementation

Level-4 PRTs were implemented on a Network-wide basis in two phases. The first phase involved Pioneer and Helios projects. It was preceded by a successfully completed two-week trial period (November 10-23, 1975), following which the countdowns were scheduled routinely, as negotiated by the Network Operations Representative (NOR) for each Project. The second phase trial period was successfully conducted for the Viking Project between January 5 and January 18, 1976, and routine scheduling of the countdowns for cruise phase support, as negotiated with the Project by the Viking NOR, was commenced on January 19, 1976.

A. Pioneer/Helios Trial Period

As depicted by Table 2, 52 load and go countdowns (27 for Pioneer and 25 for Helios) were accomplished during the period. An analysis of DSS performance during this period was made to determine if any significant

conclusions could be drawn from the statistics relative to ability of the stations to complete the countdowns on time, problems encountered, and the incidence of DRs initiated during the trial period as compared to the preceding four-week period. The following significant facts emerged from the analysis of DSS performance with respect to countdown completion times and ability to achieve AOS on time (Table 3):

- (1) Ten of the 54 total AOSs were achieved exactly on time.
- (2) Of the remaining trial tracks, early AOSs outnumbered the late ones, making possible the realization of some 26 min additional tracking time.

During the trial period, six problems were encountered that affected support and on which DRs would have been initiated under normal circumstances. Two of these involved equipment malfunctions and four were related to procedural or operator problems. The problems resulted in late AOSs. However, DRs were waived for this period, as mentioned above. Analysis of figures presented in Table 4 reveals the following:

- (1) The number of DRs initiated during the trial period is consistent with the number initiated in each of the preceding two-week periods.
- (2) Assuming DRs had been initiated on the six problems mentioned above, the total number (21) for the trial period then would have been the same as that for the October 13-26 period and not too far out of line with the number (18) for the period October 27-November 9.

Both Projects were well satisfied with the DSS performance during the trial period. However, it was also recognized that, with Viking being allocated the most support and using higher level (longer) countdowns than Pioneer and Helios, it was necessary to adopt the load and go concept for Viking in order for Pioneer and Helios Projects to receive any appreciable increase in tracking hours. Because the Pioneer/Helios view periods preceded and overlapped Viking's, Pioneer and Helios tracks could be extended by the amount of time "saved" by the shorter Viking countdowns (Fig. 1).

B. Viking Trial Period

Success with the Pioneer-Helios Level-4 PRT trial period facilitated obtaining agreement to conduct a similar program for Viking during the period January 5-18, 1976. A slight increase in the occurrence of DRs was noted; the increase was attributed to the fact that a policy

had been initiated on January 1 requiring that DRs be initiated on all problems. However, the incidence of DRs soon returned to the same level as existed before the advent of a load and go countdown. The Viking trial period was considered a success, and scheduling of the Level-4 PRT was implemented immediately for all routine Viking cruise passes.

C. Communication Circuit Activation

Philosophy regarding communication circuit activation requirements evolved through the following different concepts, commencing with the Pioneer-Helios trial period:

- (1) Initially, the circuit activation times remained unchanged, and circuits were available for use one hour before AOS. This presented problems for those stations that were not staffed continually, and particularly when a load and go countdown was scheduled to commence at the very beginning of the arrival of a new shift (following a station closed period). In this situation, the circuits were scheduled to be activated 30 min before the station was to be staffed, which disrupted accomplishment of the normal DSN Ground Communications Facility (GCF) and NASA Communications (NASCOM) line checkout procedures.
- (2) A Level-4 PRT concept for communications circuit activation was implemented on January 1, 1976. In this mode of operation the GCF/NASCOM line checkout procedures were waived and the circuits turned over to the DSS and Network Operations Control Team (NOCT) for use immediately upon activation (30 min prior to AOS).
- (3) On April 6, 1976, the waiver on use of GCF/NASCOM procedures was withdrawn and the requirement to perform the necessary line checks on a compressed schedule was instituted, with circuits being turned over to the DSS and NOCT for use at AOS minus 15 min. This remains the current mode of operation; but problems have been caused for the DSSs and NOCT when extended line checkout activities have made the circuits unavailable until AOS time or even later.

Experience has shown that the load and go concept for circuit activation resulted in fewer problems for the DSSs and NOCT. Therefore, a return to that mode of operation is anticipated in the near future, on the assumption that it will be acceptable to both GCF and NASCOM management.

IV. Productivity Assessment

A study was conducted to determine the amount of additional tracking time that was made available to the Flight Projects through use of the Level-4 PRT during the period November 23, 1975–May 10, 1976. Table 5 provides a breakdown, by Flight Project, of the number of standard and short countdowns utilized, plus the amount of tracking time associated with each type of countdown. Since a Level-4 PRT makes available an additional 1.5 hours of tracking time, it is calculated (1276 passes \times 1.5 hours) that 1914 additional tracking hours actually were realized. For the load and go passes only, this represents a 22% increase in tracking time; the increase for all passes ("load and go" and "standard" countdowns combined) is a substantial 17%.

V. Conclusion

The Level-4 PRT was used by the DSN stations in support of approximately 75% of all spacecraft tracking passes during the period November 23, 1975–June 1, 1976. A new computer-aided countdown (CAC), which was developed by Madrid Complex personnel, has been implemented for Viking planetary operations. Although longer than a Level-4 PRT, the CAC is considerably shorter (2 to 5 hours) than the Level-1 PRT that otherwise would have to be used for the critical Viking support. Use of the Level-4 PRT for Pioneer and Helios continues, and a return to more extensive use of the load and go countdown for all Flight Projects is anticipated on November 15, 1976, when the Viking prime mission ends. Since all three Flight Projects then will be in an extended mission mode, it seems reasonable to assume that the additional tracking time resulting from use of the Level-4 PRT will exceed the 17% increase that already has been realized over a period of several months duration.

Table 1. PRT levels of support

PRT		Type of requirement	Capability provided
Level	Hours ^a		
1	8.0	Critical redundant support	Highest possible degree of reliability and accuracy in system calibrations including on-line redundant system
2	5.0	Critical nonredundant support	Same as Level-1 except redundant systems are on 10-min standby and tested to Level-3 requirements
3	2.0	Normal support	Lower data quality tolerances than for Levels 1 and 2 but exceeding those of Level-4. Redundant equipment on 30-min standby and tested to Level-4 requirements
4	0.5	Minimum (load and go) support	Satisfies basic requirement for housekeeping data from cruising spacecraft, with telemetry predicted SNR greater than 3dB. First data point understood to be unimportant

^aAdditional time (as much as 1 hr) may be required when items such as polarizers, high-power transmitters, and ranging calibrations are required.

Table 2. Pioneer/Helios level-4 PRT trial period (Nov. 10-23, 1975)

DSS	Planned		Accomplished	
	Pioneer	Helios	Pioneer	Helios
11	4	4	4	4
12	0	0	1	1
14		1		1
42	4	8	4	8
43	7	1	7	1
44	2		2	
61		10		10
62				
63	9		9	
	26	24	27	25
Totals		50		52

Table 3. DSS AOS record for Pioneer/Helios level-4 PRT trial period

AOS	Number of times		Time, min	
	Pioneer	Helios	Average	Total
Early	14	10	6.5	156
Late	7	11	7.2	130
Additional tracking time realized				26

Table 4. DR comparisons

Period	Number of DR'S		
	Pioneer	Helios	Total
Oct. 13-26	14	7	21
Oct. 27-Nov. 9	10	3	13
Nov. 10-23 ^a	9	6	15

^aLoad and go countdown trial period.

Table 5. DSS countdown and tracking time comparisons (Nov. 23, 1975-May 10, 1976)

Project	Standard countdowns		Load and go countdowns	
	Number	Tracking hours	Number	Tracking hours
Pioneer	126	810.2	411	2107.2
Helios	119	649.7	451	2927.8
Viking	156	1475.7	414	3479.2
Totals	401	2935.6	1276	8514.2

ORIGINAL PAGE IS
OF POOR QUALITY

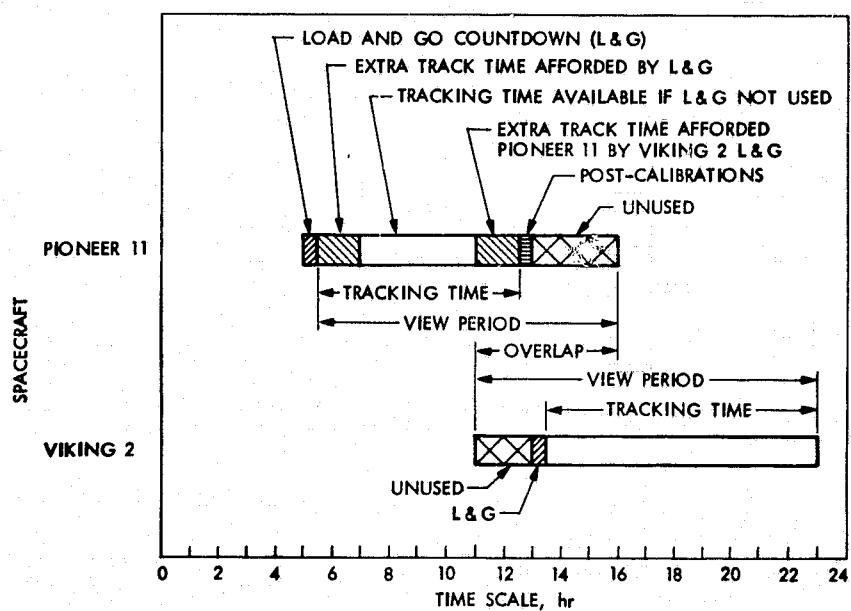


Fig. 1. Example of additional Pioneer 11 tracking time afforded by Level-4 PRT (load and go)

N 76-29336

Aspects of Job Scheduling

K. Phillips
DSN Facility Operations Office

A mathematical model for job scheduling in a specified context is presented. The model uses both linear programming and combinatorial methods. While designed with a view toward optimization of scheduling of facility and plant operations at the Deep Space Communications Complex (DSCC) at Goldstone, the context is sufficiently general to be widely applicable. The general scheduling problem including options for scheduling objectives is discussed and fundamental parameters identified. Mathematical algorithms for partitioning problems germane to scheduling are presented. A more detailed description of algorithms and of operational aspects of the model is planned for a later report.

I. Introduction

The efficiency and productivity of a service or production facility can be affected by the way in which the jobs performed by the facility are scheduled. As a part of the move to increase operational efficiency in the DSN, it was decided to study the effect of scheduling on the facility and plant function at the Deep Space Communications Complex at Goldstone and to partially automate the scheduling of maintenance. This report is a preliminary description of some of these efforts.

In general terms the object of mathematical scheduling is to identify measures of performance on the jobs done by a facility and to schedule the jobs to maximize the performance. Measures of performance are stated in such terms as maximal efficiency, minimal work inventory

(backlog), and minimal lateness. The performance is measured by a function. The mathematical model of the problem then takes the form of maximizing or minimizing this performance function subject to the constraints of the problem. The constraints take many forms, of which a few are: one man cannot do two jobs at once; some jobs have higher priorities than others; the jobs are not all available to be worked on at all times; the jobs have different skill levels. The constraints in most real problems define a large and combinatorially complex set. This is the case for the model presented here. The model presented minimizes work inventory and flow time and maximizes gross efficiency. With additional analysis it can also yield schedules for maximal average efficiency, minimal maximal tardiness, or minimal average tardiness. Precise definitions appear in Section III.

Most of the results and discussion are presented in a general context, after an initial brief description of the immediate problem at Goldstone in Section II. The ideas have wide applicability. In Section III the general scheduling problem is discussed. A model for "flow-time scheduling" is presented in Section IV. Section V treats partitioning algorithms important for scheduling. In Section VI the Goldstone problem is again discussed.

II. The Maintenance Operation at Goldstone

Facility maintenance is accomplished by seven shops: electrical, carpenter, etc. Each of these shops performs jobs in three categories, as follows:

- (1) *Preventive maintenance*, consisting of periodic servicing and checking of equipment.
- (2) *Corrective maintenance*, consisting of minor repairs and modifications.
- (3) *Special jobs*, consisting of original construction or installation, and generally more complex than (2).

The information for scheduling function (1) is known well in advance, but functions (2) and (3) occur rather randomly and have varying priorities. Function (1), and possibly some portions of functions (2) and (3), have top priority in that the tasks must be done during the month called for by specifications. The users generally compete for services in categories (2) and (3). In this context possible scheduling objectives are:

- (1) Keep all users as happy as possible by minimizing either the average or the maximum time the users must wait for completion of jobs.
- (2) Operate the shop efficiently by minimizing job backlog.
- (3) An intelligent balance between (1) and (2).

As explained in Section III, (1) and (2) are not generally compatible.

In Sections III through V we discuss aspects of general scheduling with only occasional mention of Goldstone. In Section VI we return to the context described here to give a more complete discussion of the options at Goldstone. An overall description of the proposed automation of the Deep Space Network Facility Operations appears in Ref. 7.

III. Scheduling Problems

There is a large literature on scheduling and assignment problems, Refs. 1, 2, 5, and 6 form a sample and contain between them a large current list of references. Many difficult mathematical and computational problems arise in considering optimal scheduling. For this report a particular setting is chosen—general enough for several applications—to discuss some of these problems.

A. A Context

Suppose that a service or manufacturing facility has n jobs to do in a time interval $[0, q]$ and that there are m processors (women, men, or machines) to do the jobs. Label the jobs $\{J_i\}_{i=1}^n$. Assume that the processors all have the same capability and that a certain fixed number z_i of them work simultaneously on job J_i until it is finished, but that this number can vary with the job. Associated with the job J_i is its *processing time* p_i , the number of man hours required to complete the job. The actual time the job J_i is being worked on is thus $y_i = p_i/z_i$. If h is the total number of man hours available in the interval $[0, q]$, then we assume that

$$\sum_{i=1}^n p_i \leq h,$$

so that the jobs can in fact be done. It is assumed that p_i and z_i are schedule-independent; scheduling does not affect the time it takes to do a job or the number of processors needed. Each job J_i also comes with a *due date* d_i and is ready to be worked on at a *ready time* r_i in $[0, q]$. Thus p , z , d , r , and y are vectors or n -tuples; e.g., $d = (d_i)_{i=1}^n$. Other vectors associated with the jobs are defined below.

B. Utility

Utilization of the facility is measured by the n -tuple

$$u = (u_i)_{i=1}^n$$

where

$$u_i = p_i/h \quad (\text{utilization on } J_i)$$

Also let

$$U = \frac{1}{h} \sum_{i=1}^n p_i \quad (\text{total utilization})$$

$$Au = \frac{1}{n} U \quad (\text{average utilization})$$

These factors simply measure what portion of the capability of the facility is being used. They are schedule-independent.

C. Schedule-Dependent Variables

Listed below are several schedule-dependent variables associated with the jobs J_i :

starting times: s_i

completion times: c_i

flow times: $f_i = c_i - r_i$
(time J_i is in the shop)

late times: $\ell_i = c_i - d_i$

tardy times: $t_i = \max(0, \ell_i)$

waiting times: $w_i = s_i - r_i$

These definitions are illustrated on the time axis in Fig. 1.

For example, suppose that there are three jobs, J_1, J_2, J_3 , only one processor ($m = 1$), and that $q = 5$. Suppose that the schedule-independent vectors are

$r = (0, 1, 1)$ ready times (i.e., $r_1 = 0, r_2 = 1, r_3 = 1$)

$p = (1, 1, 3)$ processing times

$d = (1, 5, 5)$ due dates

The vectors z and y are necessarily given by

$z = (1, 1, 1)$ only one processor

$y = p = (1, 1, 3)$ (work times)

If the jobs are done in order J_1, J_2, J_3 with no lag between the jobs, then

$$s = (0, 1, 2)$$

$$c = (1, 1 + 1, 2 + 3) = (1, 2, 5)$$

$$f = c - r = (1, 1, 4)$$

$$\ell = c - d = (0, -3, 0)$$

$$t = \max(0, \ell) = (0, 0, 0)$$

$$w = s - r = (0, 0, 1)$$

Notice in particular that flow time f_i is the time that the job J_i is in the shop. It is generally larger than the actual

work time y_i and in fact will be the same only if the ready time r_i is equal to the completion time of the preceding job in the schedule. Such is the case for J_1 and J_2 in this schedule, but not for J_3 . The total flow time for this schedule is $f_1 + f_2 + f_3 = 6$, while the total processing time is $p_1 + p_2 + p_3 = 5$.

D. Efficiency

We define the efficiency vector $e = (e_i)_{i=1}^n$ of the schedule by

$$e_i = \frac{y_i}{f_i} = \frac{p_i}{z_i f_i} \quad (1)$$

Thus e_i is the ratio of work time to flow time. The average efficiency is

$$Ae = \frac{1}{n} \sum_{i=1}^n e_i \quad (2)$$

Another measure of efficiency is *gross efficiency*, defined by

$$G = \left(\sum_{i=1}^n y_i \right) / \left(\sum_{i=1}^n f_i \right) \quad (3)$$

In general, $Ae \neq G$ (of course).

E. Scheduling Objectives

If the jobs have no priorities (e.g., no bigger profit or penalty is associated with some jobs than with others) then objectives available for scheduling are:

- (1) Minimize the average of f, ℓ, w , or t .
- (2) Minimize the maximum of f, ℓ, w , or t .
- (3) Maximize the average efficiency Ae .
- (4) Maximize the minimum of e .
- (5) Maximize gross efficiency G .

In this report we emphasize minimizing average flow time Af , discussed in Subsection III-F. Before beginning, note that the problem is combinatorially much too large to solve on a computer by direct computation of all possible schedules, even for fairly small n . For example if $m = 1$ and $r_i = 0$ for all i then there are $n!$ schedules; recall that

$$10! = 3,628,800$$

$$20! \cong 2,432,900,000,000,000,000$$

$$50! \cong 3 \times 10^{64}$$

If the jobs have priorities, weights can be given to the coordinates of the vectors, and weighted averages and maximums can then be considered. Weighting factors are not considered in this report. There are in fact priorities for the jobs at Goldstone. In the model described in Section VI, these priorities are handled by categorizing then optimizing within categories. Weighted vectors will be developed as another alternative.

F. Flow Time

Minimizing total flow time

$$\sum f \left(= \sum_{i=1}^n f_i \right)$$

or average flow time

$$Af = \frac{1}{n} \sum_{i=1}^n f_i$$

also achieves each of points (1)–(3) below. The letter A is used for average, so that for a vector v , Av denotes the average of the components of v .

- (1) Maximizes gross efficiency G .
- (2) Minimizes average waiting time Aw and average lateness Al .
- (3) Minimizes average backlog (or work inventory).

Assertion (1) is apparent from the definition of gross efficiency. To see (2) observe that

$$\sum_{i=1}^n w_i = \sum_{i=1}^n f_i - \sum_{i=1}^n y_i \quad (4)$$

$$\sum_{i=1}^n l_i = \sum_{i=1}^n f_i + \sum_{i=1}^n (r_i - d_i) \quad (5)$$

and that y_i, r_i, d_i are all schedule-independent. Assertion (3) is not quite so trivial, although it is intuitively clear that the faster the work moves through the shop the smaller the outstanding workload. Letting $N(t)$ denote the work inventory at time t (the number of jobs ready to be processed or in processing), the critical formula is

$$\int_0^q N(t) dt = \sum_{i=1}^n f_i \quad (6)$$

A proof of Eq. (6) is given in Appendix A. The formula proves assertion (3), for the left side of Eq. (6) is q times the average backlog.

Another way to state Eq. (6) is

$$AN = \frac{1}{q} \sum_{i=1}^n f_i = \frac{n}{q} Af \quad (7)$$

The last expression is (arrival rate) • (average flow time). Equality (7) appears in Ref. 2, but with the unneeded hypothesis that the original c_i are ordered.

G. Minimizing Flow Time

The problem of minimizing total flow time $\sum f$ in all but the simplest cases appears to be unsolved in that no generally effective algorithms exist. A discussion appears in Ref. 2, where much of the exposition is devoted to the problem.

The simplest case is that in which all jobs have the same starting time ($r_i = 0$) and there is one processor ($m = 1$). Then a schedule is simply a permutation of the n jobs. Suppose that the jobs are done in the order of the indices. The flow time of J_1 is simply its processing time p_1 . Job J_2 is started on the completion of J_1 , so its starting is $s_2 = p_1$ and its flow time is

$$f_2 = c_2 - r_2 = s_2 + p_2 - 0 = p_1 + p_2$$

Job J_3 is started at time $p_1 + p_2$ and so

$$f_3 = p_1 + p_2 + p_3$$

The flow time of the job J_i (i.e., time required to complete J_i from the time it was first available) is

$$f_i = \sum_{j=1}^i p_j \quad (8)$$

and total flow time is given by

$$\sum_{i=1}^n f_i = \sum_{i=1}^n \sum_{j=1}^i p_j = \sum_{i=1}^n (n - i + 1)p_i \quad (9)$$

For the fixed set of numbers $\{p_i : 1 \leq i \leq n\}$ the number on the right in Eq. (9) is minimal for the permutation in which the p_i are ordered by increasing magnitude (See Appendix B). Hence the optimal flow time schedule in this case is that in which the jobs are done according to increasing processing times. This is called an LPT schedule, for "least processing time" first. In more complicated scheduling problems, the "LPT principle" can be applied to portions of the schedule after other requirements have been met.

In Section IV a mathematical model for achieving minimal flow time for the problem stated in Subsection III-A is presented.

H. Tardiness and Flow Time

It seems clear that tardiness is a more important measure of performance than lateness, as defined above. There is no advantage as far as due dates are concerned in having the jobs finished early, that is in having $l_i < 0$. Unfortunately it is not true that minimum flow time also gives minimum average tardiness. The equality corresponding to Eq. (5) is

$$\sum_{i=1}^n t_i = \sum_{i=1}^n \max(0, c_i - d_i) = \sum_{i \in I} f_i + \sum_{i \in I} (r_i - d_i) \quad (10)$$

where I is the set of indices defined by $I = \{i : c_i - d_i > 0\}$. The set I is dependent on the schedule so there is no reason to expect that the right side of Eq. (10) is minimal with

$$\sum_{i=1}^n f_i$$

To see explicitly that minimal $\sum t_i$ and minimal $\sum f_i$ may require different schedules, consider the simple case where $m = 1$, $n = 2$. Assume that the ready times $r_1 = r_2 = 0$. In schedule $J_1 J_2$ the start time vector is $s = (0, p_1)$ and the completion vector is $c = (p_1, p_1 + p_2)$. It is always assumed that $d_i > r_i + y_i$, so in this case

$$t_1 = \max(0, p_1 - d_1) = 0$$

and

$$t_2 = \max(0, p_1 + p_2 - d_2) = p_1 + p_2 - d_2$$

the last equality holding if $d_2 \leq p_1 + p_2$. The same analysis applies to the schedule $J_2 J_1$ with the roles of 1 and 2 exchanged. Total flow time and total tardiness are thus given in the table below.

Schedule	$\sum f$	$\sum t$
$J_1 J_2$	$2p_1 + p_2$	$p_1 + p_2 - d_2$
$J_2 J_1$	$2p_2 + p_1$	$p_1 + p_2 - d_1$

If $p_1 < p_2$ and $d_1 > d_2$ then the first schedule minimizes total flow time but the second schedule minimizes total tardiness.

In the context of this report (the problem of Subsection III-A) the major tradeoff is between due date satisfaction in terms of either average of minimal maximal tardiness and minimal average flow time.

I. Remarks on Flow Time and Outstanding Work

In discussing backlog in Subsection III-F, we called backlog the number of jobs outstanding. Another measure of remaining workload is processing time remaining, say $P(t)$ at time t . If it is assumed that all processors work continuously and no new work arrives, then it is clear that $P(t)$ is independent of schedule and in fact is linearly decreasing with slope -1 . However, if we assume gaps in the work interval, then the graph of $P(t)$ will be a decreasing function with intervals of constancy or of smaller slopes.

To illustrate, suppose that $n = 5$ and $m = 1$ and that the gaps are constant. Then the area under the graph of P is minimal if the *longest* jobs are done first (see Fig. 2). Hence under these assumptions minimizing average $P(t)$ is antithetical to minimizing average $N(t)$. In some cases minimizing AP might be more realistic; "get the big jobs out of the way first." Such an optimization procedure could be further developed.

IV. Model for Flow Time Scheduling

A. Formulation

The context and notation are as in Subsection III-A; the goal is to achieve minimum flow time. That is, the goal is to find starting times for the jobs that make the corresponding flow time minimal. Clearly there are constraints on the starting times. For example, if there are two processors and ten jobs then an obvious constraint is that not all ten jobs can be started at $t = 0$. The constraints will yield certain allowable n -tuples $s = (s_i)_{i=1}^n$ as starting times for the jobs J_i . In geometric language, there is a certain allowable subset A of n -dimensional real space in which the vector s of starting times can lie. Among all these possible starting times in A the object is to choose one which makes the total flow time for the jobs minimal. The set A is a rather unwieldy collection of corners of an n -dimensional right parallelepiped. It is first described below for the general case and then its geometric properties are developed by considering simpler cases.

To begin, observe that total flow time can be expressed

$$\sum_{i=1}^n f_i = \sum_{i=1}^n (s_i + y_i - r_i) = \sum_{i=1}^n s_i + \sum_{i=1}^n (y_i - r_i) \quad (11)$$

Since y_i and r_i are schedule-independent, the problem of minimizing total flow time is the same as the problem of minimizing

$$\sum s_i \quad (= \sum_{i=1}^n s_i)$$

The analysis that follows emphasizes s .

The ready-time and finish-time constraints are simple enough and are expressed by

$$r_i \leq s_i, \quad s_i + y_i \leq q \quad (12)$$

Thus the allowable set A must lie in the set C of n -dimensional space R^n defined by

$$C = \{s : r_i \leq s_i \leq q - y_i\} \quad (13)$$

The set C is an n -dimensional right parallelepiped. The processor constraint that at most m processors can be in use at any time is a little trickier. It may be phrased in terms of subsets of R^n defined by n -tuples $\delta = (\delta_i)_{i=1}^n$ in which each δ_i is 0 or 1. Let T denote the set of all such δ and define a subset of T by

$$\Delta = \left\{ \delta \in T : \sum_{i=1}^n \delta_i z_i > m \right\} \quad (14)$$

For $\delta \in \Delta$, the set of jobs J_i for which $\delta_i = 1$ cannot occur simultaneously; i.e., the number of processors required for this combination of jobs J_i exceeds the total number of processors available. The condition that the jobs *do* occur simultaneously is that there is some time t at which all jobs J_i for i in the set $I(\delta) = \{i : \delta_i = 1\}$ are being processed; i.e., t is in $(s_i, s_i + y_i)$ for each i in $I(\delta)$. In set notation, the subset of R^n defined by

$$E(\delta) = \left\{ s \in R^n : \bigcap_{\delta_j=1} (s_j, s_j + y_j) \neq \emptyset \right\} \quad (15)$$

is thus excluded as possible starting times, for each δ in Δ . Hence the set

$$E = \bigcup_{\delta \in \Delta} E(\delta) \quad (16)$$

is excluded. The starting times must therefore be in the complement E' in R^n of E . The allowable set A is thus

given by

$$A = E' \cap C \quad (17)$$

where C is defined by Eq. (13). Hence the flow time problem may be formulated as follows.

Flow time problem: find the minimum value of $\sum s_i$ for $s \in A$.

The set A is discussed in more detail in Subsections IV-D and IV-E, after simpler cases have been described in Subsections IV-B and IV-C.

The set A can also be written

$$A = \bigcap_{\delta \in \Delta} A(\delta) \quad (18)$$

where

$$A(\delta) = E(\delta)' \cap C \quad (19)$$

In many cases the intersection defining A can actually be taken over a smaller set than Δ : for, if $A(\delta) \subset A(\sigma)$ then $A(\sigma)$ need not be included in the intersection.

B. Illustrative Example

Suppose there are two jobs for scheduling and one processor, i.e., $n = 2$, $m = 1$. Suppose that $r_1 = 0$, $r_2 > 0$. The set C is

$$C = \{s : s_1 \leq q - p_1, r_2 \leq s_2 \leq q - p_2\} \quad (20)$$

a rectangle. The only δ in Δ is $\delta = (1, 1)$; i.e., both jobs cannot be processed at once. The excluded set $E = E(\delta)$ is

$$E = \{s = (s_1, s_2) : (s_1, s_1 + p_1) \cap (s_2, s_2 + p_2) \neq \emptyset\}$$

from which it follows that

$$E' = \{s : s_1 + p_1 \leq s_2 \text{ or } s_2 + p_2 \leq s_1\} \quad (21)$$

Hence the allowable set A is given by

$$\begin{aligned} A &= (C \cap \{s : s_1 + p_1 \leq s_2\}) \cup (C \cap \{s : s_2 + p_2 \leq s_1\}) \\ &= [C \cap A_1] \cup [C \cap A_2] \end{aligned} \quad (22)$$

Simply stated, the requirement that the starting time vector $s = (s_1, s_2)$ be in E' given in Eq. (21) means that either J_2 must start after J_1 is finished, or J_1 must start after J_2 is finished. In Fig. 3, C has boundary indicated by short cross lines and $C \cap A_1$ and $C \cap A_2$ are indicated by shading. The graph of $\sum s$ is a plane inclined at 45 deg to

the $s_1 - s_2$ plane and lying above the first quadrant. The minimum of Σs for $s \in A$ occurs at one of the nodes (or extreme points) of the set A , namely the one for which $s_1 + s_2$ is minimal. If lines of slope -1 are drawn through the nodes, then the line that lies closest to the origin gives the node for minimal Σs because $s_1 + s_2$ is constant on these lines. In Fig. 3 these lines are sketched with dots and labeled.

In the case sketched, minimal Σs occurs at $N_1 = (0, r_2)$ with value $\Sigma s = r_2$. The flow time value is

$$f(0, r_2) = r_2 + (p_1 - r_1) + (p_2 - r_2) = p_1 + p_2$$

hardly unexpected for this simple case.

The set A has two components in this case. Clearly one need not check all nodes, but only one node in each component, the one closest to the origin; N_1 and N_3 in Fig. 3.

If $r_2 < p_1$, then N_1 does not appear and the choice is between N_2 and N_3 . In this case $N_2 = (0, p_1)$. What is required for N_3 to give the minimum? Since

$$\Sigma s(N_2) = p_1 \text{ and } \Sigma s(N_3) = 2r_2 + p_2$$

the inequality

$$2r_2 + p_2 < p_1 \quad (23)$$

is required. Descriptively speaking, if Eq. (23) holds, it pays to wait and do the short job first even if the long job is available and the short one is not, provided that the long job is sufficiently long. A case in which this occurs is: $r_1 = 0, r_2 = 5, p_1 = 17, p_2 = 2$. See Fig. 4.

C. The One Processor Case

If $m = 1$, then $z_i = 1$ for all i . The set Δ is all n -tuples of zeros and ones that contain at least two ones. Suppose δ contains exactly two ones, say $\delta_i = \delta_j = 1$ and $\delta_k = 0$ if $k \neq i, j$. Then

$$E(\delta) = \{s : (s_i, s_i + p_i) \cap (s_j, s_j + p_j) \neq \emptyset\}$$

and

$$E'(\delta) = \{s : s_i + p_i \leq s_j \text{ or } s_j + p_j \leq s_i\} \quad (24)$$

The set $E'(\delta)$ is like E' in Eq. (21). In fact the projection of $E'(\delta)$ in the $s_i - s_j$ plane is precisely as analyzed in Subsection IV-B ($n = 2$). Every set $E(\sigma)$ for $\sigma \in \Delta$ contains

some $E(\delta)$ in which δ has exactly two ones. It follows that the set A can be expressed

$$A = C \cap \left[\bigcap_{i \neq j} (\{s : s_i + p_i \leq s_j\} \cup \{s : s_j + p_j \leq s_i\}) \right] \quad (25)$$

where the second intersection is to be taken over all pairs (i, j) with $i \neq j$. The projection of A in each $s_i - s_j$ plane has precisely the geometry described in Subsection IV-B. The set A is thus the union of certain corners of an n -dimensional right parallelepiped. The restriction on each pair of coordinates "chops off" a corner at 45 deg.

Another description of A follows. Let Ω be the set of δ s with exactly two ones. One can think of each set $E(\delta)$ for $\delta \in \Omega$ as the infinite cylinder over the infinite rectangle in the $s_i - s_j$ plane defined by

$$R_{ij} = \{s : s_i < s_j + p_j \text{ and } s_j < s_i + p_i\} \quad (26)$$

The set R_{ij} is inclined 45 deg to the s_i and s_j axes. The excluded set

$$E = \bigcup_{\delta \in \Omega} E(\delta)$$

is the union of these cylinders and the allowable set A is the intersection of C with the complement of E .

D. General Case; z_i and m Arbitrary

Each set $E(\delta)$ for $\delta \in \Delta$ can be analyzed by considering pairs of coordinates. For a given δ and each pair (i, j) for which $\delta_i = \delta_j = 1$, let

$$R_{ij} = \{s : (s_i, s_i + y_i) \cap (s_j, s_j + y_j) \neq \emptyset\}$$

just as described above. Then

$$E(\delta) = \bigcap_P R_{ij} \quad (P = \{(i, j) : \delta_i = \delta_j = 1\}) \quad (27)$$

To see that Eq. (27) holds suppose first that $s \in E(\delta)$. Then clearly $(s_i, s_i + y_i) \cap (s_j, s_j + y_j) \neq \emptyset$ for each pair $(i, j) \in P$. Hence $s \in \bigcap_P R_{ij}$ and $E(\delta) \subseteq \bigcap_P R_{ij}$ holds. To prove the reverse inclusion, suppose $s \in \bigcap_P R_{ij}$. Let s_k be the largest coordinate of s . Then $s_k \in [s_i, s_i + y_i]$ for all i having $\delta_i = 1$ because $s \in R_{ki}$ for all i . Hence

$$s_k \in \bigcap_{\delta_i=1} [s_i, s_i + y_i]$$

and so $s \in E(\delta)$.

Each $\delta \in \Delta$ thus gives rise to an excluded set which is an intersection of rectangular cylinders above the coordinate planes. The excluded set within the set C is then the union over $\delta \in \Delta$ of all these $E(\delta)$. This is the "heart" of the parallelepiped C and the allowable set A is pieces of the corners. The set T of all δ can be ordered by " $\delta \leq \sigma$ if $\delta_i = 1 \Rightarrow \sigma_i = 1$." The intersection defining A can be taken over the set Δ_1 of least elements in Δ .

E. Summary and Algorithm Outline

A procedural outline for finding minimal Σs , and hence minimal flow time $\Sigma f(s)$ follows.

- (1) Determine a minimal set Δ_1 of δ s for which

$$\sum_{i=1}^n \delta_i z_i > m$$

The set Δ over which the intersection is taken can be replaced by Δ_1 . This is a combinatorial partitioning problem and will be discussed in more detail in Section V.

- (2) Determine the set C . This is a simple matter; C is defined by $2n$ inequalities, hence by $2n$ numbers.
- (3) Identify the nodes of the components of the set A and determine those which minimize Σs . Use a modification of the simplex method to determine feasible nodes and minimum. While A is not convex its complement in C is the set $E = C \cap [\cup_{\delta \in \Delta} E(\delta)]$, which is a union of convex sets. However E does not have all the extreme points of the complement of A , as a glance at Fig. 2 clearly demonstrates; N_1 is an extreme point of A but not of E .

V. Remarks on Partitioning

As indicated in Section IV, partitioning algorithms are important for scheduling. Given positive integers $\{z_i : 1 \leq i \leq n\}$ and a number m , the problem is to find all subsets J of $\{1, 2, \dots, n\}$ for which

$$\sum_j z_j = m$$

The problem is equivalent to finding all n -tuples δ of zeros and ones for which

$$\sum_{i=1}^n \delta_i z_i = m$$

Bounds for the number of such partitions can be obtained using combinatorial methods appearing in Refs. 3 and 4.

To the author's knowledge there is no known probabilistically optimal algorithm for obtaining all partitions. The state of the art appears to be contained in the papers Refs. 5 and 6, where statistical comparisons are made for various algorithms. In two steps, Subsections V-A and V-B, we describe the best of Ref. 5.

A. Obtaining All Sums

We use the notation $\{0, 1\}^n$ for the set of n -tuples of zeros and ones. In this algorithm the sum

$$S(\delta) = \sum_{i=1}^n \delta_i z_i$$

is calculated for every $\delta \in \{0, 1\}^n$ and the δ are coded. For $0 \leq r \leq n$ define sets of ordered pairs A_r recursively by

$$A_0 = \{(0, 0)\}$$

$$A_r = A_{r-1} \cup \{A_{r-1} + (z_r, 2^{r-1})\}$$

All sums using z_1, \dots, z_r appear as first coordinates in A_r . Since the correspondence

$$\delta \leftrightarrow \sum_{i=1}^r \delta_i 2^{i-1}$$

is 1-1 between $\{0, 1\}^r$ and $\{0, 1, 2, \dots, 2^{r-1}\}$ the second coordinate of an element of A_r contains a unique description of the δ used to obtain the first coordinate. The set A_n is thus

$$A_n = \{(S(\delta), \delta) : \delta \in \{0, 1\}^n\}$$

where the second coordinate is "coded" as above.

If only certain sums are wanted, then in the recursive step from A_{r-1} to A_r all sums that cannot possibly yield the desired sums are eliminated. This elimination is optimized by ordering the z_i . The sum is then decoded to give δ for the desired sums.

B. An Improvement

For the problem of obtaining all partitions of m for a given m an improvement in computing time is achieved by first splitting the z_i into two sets, applying Subsection V-A procedures to each of these, then combining the resulting sums. The analysis appears in Ref. (5). Combinatorial complexities prevent additional improvement by further splitting.

VI. Models for Maintenance Scheduling at Goldstone

Some of the jobs in categories (2) and (3) of Section II have high priority; essentially they must be done when they arise. A subset of these can be anticipated; that is, their ready times r_i are known, while the others occur at random. Using scheduling interval $[0, q]$ equal to a month, in the notation of Section III the jobs fall into categories C_1 , C_2 , C_3 , and C_4 defined by

C_1 : preventive maintenance; $r_i = 0, d_i = q$

C_2 : high priority; r_i known but variable, $d_i = r_i + y_i$
"must" be done at $t = r_i$

C_3 : variable r_i and d_i ; no other priorities

C_4 : random; unknown prior to scheduling, but must be done as they arise.

There is an additional problem among the C_1 jobs in that the individual jobs are so numerous that they cannot reasonably be handled directly. They are first categorized by building and site and then consolidated by a partitioning algorithm like that in Subsection V-A.

A first step in any scheduling routine leaves time for the expected C_4 jobs. A weekly modification routine can then

be applied to adjust for the C_4 jobs that occurred. Given this context, three options for scheduling are listed below.

Option 1: 1. Schedule the C_2 jobs.

2. Apply the flow time model described in Sections IV and V to all remaining jobs.

3. Make weekly modifications.

Option 2: 1. Schedule the C_2 jobs.

2. Apply the flow time model to the C_1 jobs and as time allows to the C_3 jobs for the first three weeks only.

3. At beginning of fourth week apply the flowtime model to all jobs remaining as result of interruption by C_4 jobs.

Option 3: 1. Schedule the C_2 jobs.

2. Apply a "Due-Date" algorithm instead of a "Flow-Time" algorithm to the entire month.

Computer programs for these options are being written. The options will be tried experimentally on data available for scheduling and compared using the ideas presented in Section III.

References

1. Ashour, S., *Sequencing Theory*, Springer, 1972.
2. Conway, Maxwell, and Miller, *Theory of Scheduling*, Addison-Wesley, 1967.
3. Dilworth, R. P., "A Decomposition Theorem for Partially Ordered Sets," *Ann. Math.* Vol. 2, No. 51, pp. 161-166, 1950.
4. Hall, Marshall, Jr., *Combinatorial Theory*, Blaisdell, 1967.
5. Horowitz, Ellis and Sahni, Sartaj, "Computing Partitions With Applications to the Knapsack Problem," *Jour. of the Assoc. for Computing Machinery*, Vol. 21, No. 2, pp. 277-292, April 1974.
6. Horowitz, Ellis and Sahni, Sartaj, "Algorithms for Scheduling Independent Tasks," *Jour. of the Assoc. for Computing Machinery*, Vol. 23, No. 1, January 1976.
7. Maiocco, F. R., and Hume, J. P., "Computerizing Goldstone Facility Maintenance Data for Management Decisions," in *The Deep Space Network Progress Report 42-32*. Jet Propulsion Laboratory, Pasadena, California, April 15, 1976.

Appendix A

Proof of Equation (6)

Lemma. With definitions as in Section III, the equality

$$\int_0^q N(t) dt = \sum_{i=1}^n f_i \quad (\text{A-1})$$

holds.

Proof. Assume that the jobs are numbered so that

$$0 = r_1 \leq r_2 \leq \cdots \leq r_n < q$$

Let $r_{n+1} = q$. Let $\{c'_i : 1 \leq i \leq n\}$ be a relabeling of $\{c_i\}_{i=1}^n$ which puts them in order; thus $0 < c'_1 \leq c'_2 \leq \cdots \leq c'_n = q$.

The number $N(t)$ is the number of jobs with $r_i \leq t$ and $c_i > t$. The equality $N(t) = R(t) - S(t)$ holds where

$$R(t) = \text{number of } \{r_i : r_i \leq t\}$$

$$S(t) = \text{number of } \{c_i : c_i \leq t\}$$

The integrals of R and S are given by

$$\int_0^q R(t) dt = \sum_{i=1}^n \int_{r_i}^{r_{i+1}} R(t) dt$$

$$\begin{aligned} &= \sum_{i=1}^n i(r_{i+1} - r_i) \\ &= nq - \sum_{i=2}^n r_i \end{aligned}$$

and

$$\begin{aligned} \int_0^q S(t) dt &= \sum_{i=2}^n \int_{c'_{i-1}}^{c'_i} S(t) dt \\ &= \sum_{i=2}^n (i-1)(c'_i - c'_{i-1}) \\ &= (n-1)q - \sum_{i=1}^{n-1} c'_i \end{aligned}$$

(recall that $r_1 = 0$). Hence

$$\begin{aligned} \int_0^q N(t) dt &= nq - (n-1)q + \sum_{i=1}^{n-1} c'_i - \sum_{i=2}^n r_i \\ &= \sum_{i=1}^n c'_i - \sum_{i=1}^n r_i = \sum_{i=1}^n f_i \end{aligned}$$

which proves Eq. (A-1).

Appendix B

A Minimal Sum

Lemma. Let $\{p_i\}_{i=1}^n$ be positive numbers. For a permutation ν of $\{1, \dots, n\}$, let

$$S(\nu) = \sum_{i=1}^n (n-i+1) p_{\nu(i)} \quad (B-1)$$

Then $S(\nu)$ is minimal for all permutations if

$$p_{\nu(1)} \leq p_{\nu(2)} \leq \dots \leq p_{\nu(n)} \quad (B-2)$$

Proof. Clearly $S(\nu)$ is minimal if and only if

$$E(\nu) = \sum_{i=1}^n i p_{\nu(i)}$$

is maximal. If μ is such that $E(\mu)$ is maximal but Eq. (B-2) does not hold then

$$p_{\mu(i)} > p_{\mu(j)} \quad \text{and} \quad i < j \quad (B-3)$$

holds for some i and j . However the inequality

$$ip_{\mu(i)} + jp_{\mu(j)} < ip_{\mu(j)} + jp_{\mu(i)}$$

holds by Eq. (B-3) and shows that $E(\nu) > E(\mu)$ if ν is obtained from μ by interchanging i and j . Thus $E(\mu)$ cannot be maximal if Eq. (B-2) does not hold for μ .

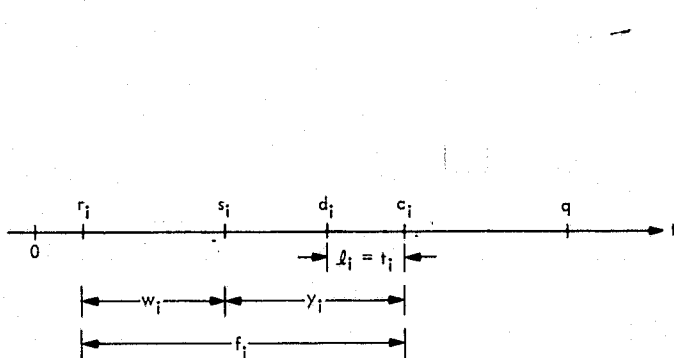
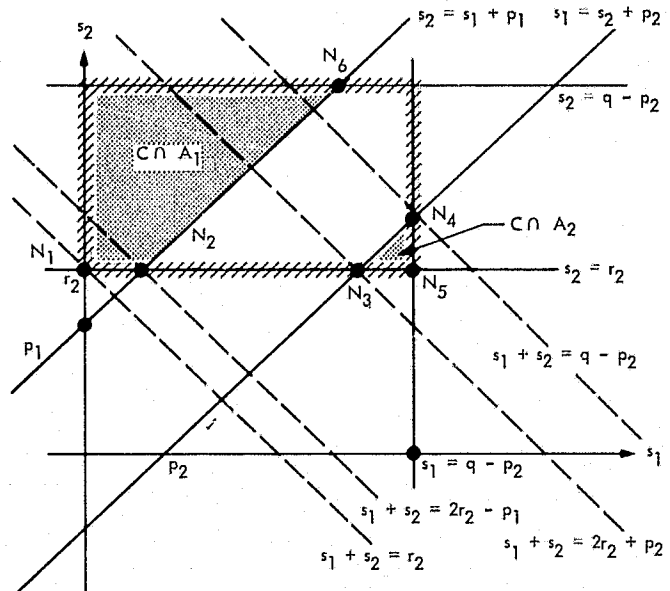


Fig. 1. Illustration of scheduling parameters



NODES OF A:
 $N_1 = (0, r_2)$
 $N_2 = (r_2 - p_1, r_2)$
 $N_3 = (r_2 + p_2, r_2)$
 $N_4 = (q - p_2, q - 2p_2)$

Fig. 3. Allowable set of starting times

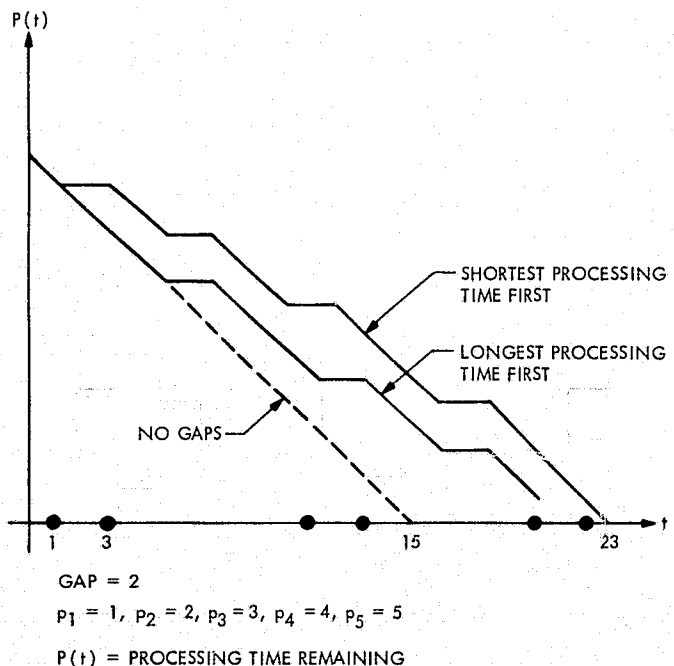


Fig. 2. Outstanding processing time with gaps

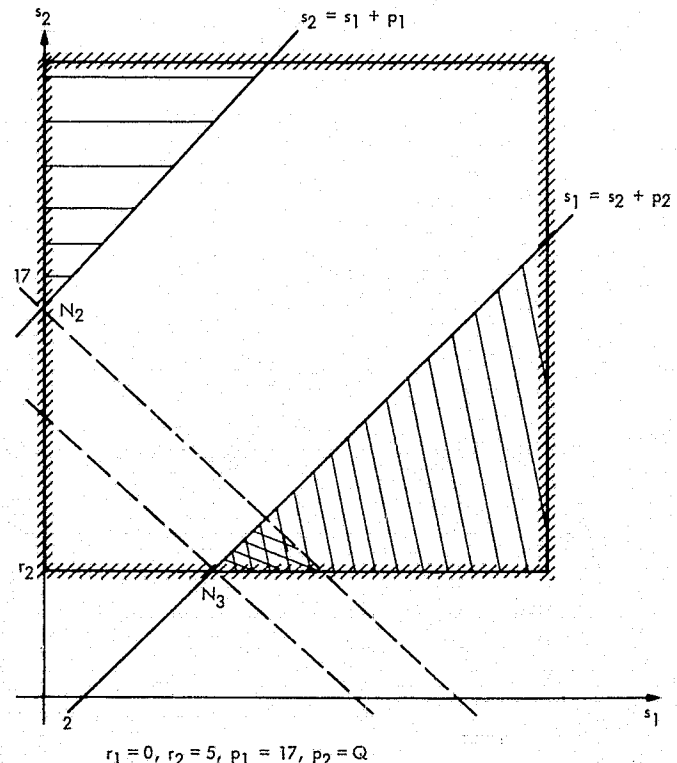


Fig. 4. Allowable starting times ($p_1 \gg p_2$)

N 76-29337

Dynamic Modeling for Evaluation of Solar Collector Performance

C. L. Hamilton
TDA Planning Office

A dynamic model program designed to aid in the understanding of solar collector behavior over the full range of operating conditions has been constructed and tested in the evaluation of a conceptual collector design.

I. Introduction

Dynamic modeling is being developed to provide a tool for systematic analysis of performance characteristics in energy systems where time-dependent behavior is important. It is intended that the technique be applicable to many levels of detail in analysis, from rough examination of system behavior in response to general specifications on subsystem performances to very detailed analysis of the effect exerted on a component's transient and integrated performance by its various characteristics. References 1 and 2 have discussed modeling of solar energy systems in terms of gross subsystem specifications. This paper reports work on simulating the performance of solar collectors by themselves, to allow more detailed understanding of one important system component. Construction of a model and its embodiment in a computer program were carried out using now standard procedures. The program was used to estimate the behavior to be expected from a conceptual collector design and then to check its variance with collector orientation.

II. Construction of Model and Program

The collector performance model is strictly analogous to the one embodied in program SUN (Ref. 1), except that it represents only one physical component. Therefore the program COLTEST, in which it is embodied, carries a single computational module. That computational module contains the same interfaces with environment and other components as the Solar Collector Module in SUN does (Fig. 1). Collector performance is determined by the intensity and angle of solar radiation, by ambient temperature, and by the temperature of fluid entering it from storage or a conversion device. Energy output from the collector is described by the rate of heat extraction from it and the temperature at which that heat is removed.

This particular program (named COLTEST for *Collector Test*) was intended to aid in understanding what happens to the energy gathered by a collector throughout a day's operation. For that reason it was set up to accept

exogenous inputs and record output at closely spaced intervals, simulating performance for a period of one day. Several derived values were produced, tabulating the fate of incoming radiation under the various modes of operation encountered; these are combined in the performance curve shown in Fig. 2. The analysis was done assuming the same collector operating strategy as employed in the system test analyses using programs SUN (Ref. 1) and SENSMOD2 (Ref. 2)—namely that the heat transfer fluid in the collector would be kept static until it had attained a minimum temperature. Once that minimum temperature was reached, the fluid flow rate would be regulated to keep the outlet temperature within a range of 10–15°C above the minimum. At the end of the day, when the temperature out of the collector dropped below the turn-on level, flow was again stopped.

At the end of each fifteen minutes of simulated operation, several rates were output. These were expressed as the averages experienced over that period (all in kW/m^2 of collector surface) and consisted of the radiation rate incident on the collector's front face, the radiation rate reaching and absorbed by the absorber surface, the rate at which absorbed energy is retained as sensible heat bringing the collector up to operating temperature, the heat loss rate, and the rate at which energy at or above the minimum operating temperature is extracted by the collector fluid. Cumulative variables recording the amount of energy funneled into each of the above categories (in kWh/m^2) were also printed, allowing estimation of integrated daily collector performance.

Measured values of solar radiation, recorded as intensity incident on a horizontal surface at Deep Space Station 13, Goldstone Space Communications Complex, on June 2, 1975, provided the basis for input files to drive the model. The sun's declination and transit time for that date were used to generate files containing values for angle of incidence of sunlight on the face of collectors facing south and tilted at various angles from horizontal. These entries were recorded at fifteen minute intervals, from 00:00 to 24:45 PST; a value of 90 deg was entered for all times in which the sun was not shining on the collector face. With the angles of incidence, files containing intensities on the front surfaces of appropriately tilted collectors, varying every fifteen minutes, were calculated from the horizontal measurements. In addition to the radiation intensity and angle-of-incidence files, a third input file was compiled from fifteen-minute readings of ambient temperature at the same location on the same day. All measurements used here were made under a program that has been conducted at Goldstone Space Communications Complex (GSCC)

since June 1974, dedicated to collecting an archive of solar data calibrated to the international standard (Ref. 3).

Because COLTEST was intended to fulfill a specific purpose (tracing aspects of collector performance one day at a time) and would never contain more than one computational module, its structure could be somewhat simpler than that of the more general programs embodying system models for which a wider range of manipulation is desired. Figures 4 and 5 are the flow charts describing the program. As in program SUN, collector behavior is simulated, in DH CALC, using a variable integration interval to achieve computational stability without requiring excessive iterations through the program's calculation loop. The variable-step-size loop is imbedded in a more slowly varying loop with step size $DT = 1/4$ hr, synchronized with the interval at which new exogenous inputs are supplied. The slower loop is where the fifteen-minute average rates are computed for output and where the corresponding cumulative variables are updated. As in all of the dynamic model programs, substitution of one component for another involves replacement of limited and discrete subprogram segments. An entirely different collector characterization can be submitted for analysis by substituting subprograms COLCALC (block 1.4.3), COLCC (1.4.4), and COLUPD (1.4.5), along with appropriate initialization statements.

III. Test of the Program

COLTEST was first exercised in estimating performance characteristics for a conceptual collector design that arose while the Goldstone Energy Project was looking into solar-fired power-on-demand systems. The system under consideration required delivery of heat at 300°C or above, and was estimated to return fluid to the collector with a 50°C temperature drop. The hypothetical collector was to have a concentration ratio of 2, involving a single glass cover with 94 percent transmissivity to normal radiation. A selectively coated absorber tube of thin copper was postulated; the coating was specified to have 90 percent absorptivity and 5 percent emissivity. The collector fluid was air, and the minimum operating temperature to be maintained was 300°C. It was specified that heat loss from the collector would be predominantly radiative, and amount to about 360 W/m^2 at an absorber temperature of 350°C. Note that this collector description is in terms of specifications on a hypothetical piece of hardware, and the function of the dynamic model here is to translate these specifications into a measure of collector performance and to reveal the sensitivity of that performance to those specifications.

The program was run for this conceptual collector design at two tilt angles. Results from the two runs are summarized in Figs. 2 and 3. Plotted as a function of time are the fifteen-minute average rates listed above. The outer envelope represents solar radiation incident on the collector's front face, while the line below that shows the rate at which energy reaches and is absorbed by the absorber surface. The difference in the areas under the two curves represents the percentage of daily total insolation that is uncollectable owing to the optical properties of the cover material. A small slice of the absorbed energy was sacrificed in the morning hours to satisfy the assumed requirement for relatively constant output temperature that is marked Energy Lost in Warmup on the figures; its very small size reflects the low thermal capacitance inherent in a thin copper tube using air as a heat transfer fluid. Along the bottom of each figure is a band reflecting heat loss. This is a combination of radiative and conductive loss and is consistent with a well-insulated collector with the specified absorber coating properties. Subtraction of the total losses from energy absorbed gives the area in the middle of the figure,

measuring the daily total useful energy extracted. For the collector tilted at 48.5 deg, integrated collector efficiency for that day would have been 46 percent. Changing collector angle to 20 deg, which is more favorable for summer collection, increases integrated efficiency to 57 percent. In both these cases the collector functioned with an average absorber temperature very close to 325°C during the whole period of useful energy delivery. Sensitivity analyses were not carried further, owing to a shift in project emphasis.

IV. Summary

Program COLTEST was developed for the purpose of carrying out specific performance studies on solar collectors. It was used to some extent for predicting behavior based on preliminary specifications of a hypothetical collector. More recently a commercially available collector, characterized by a general and detailed heat transfer analysis, has been examined using COLTEST. A separate report on that work is forthcoming.

References

1. Hamilton, C. L., "A Dynamic Model for Analysis of Solar Energy Systems," in *The Deep Space Network Progress Report 42-27*, pp. 41-51. Jet Propulsion Laboratory, Pasadena, California, June 15, 1975.
2. Hamilton, C. L., "An Experiment in Dynamic Modeling for a Complete Solar-Powered Energy System," in *The Deep Space Network Progress Report 42-31*, pp. 137-143. Jet Propulsion Laboratory, Pasadena, California, February 15, 1976.
3. Reid, M. S., Gardner, R. A., and Parham, O. B., "The Goldstone Solar Energy Instrumentation Project: Description, Instrumentation and Preliminary Results," in *The Deep Space Network Progress Report 42-26*, pp. 133-144. Jet Propulsion Laboratory, Pasadena, California, April 15, 1975.

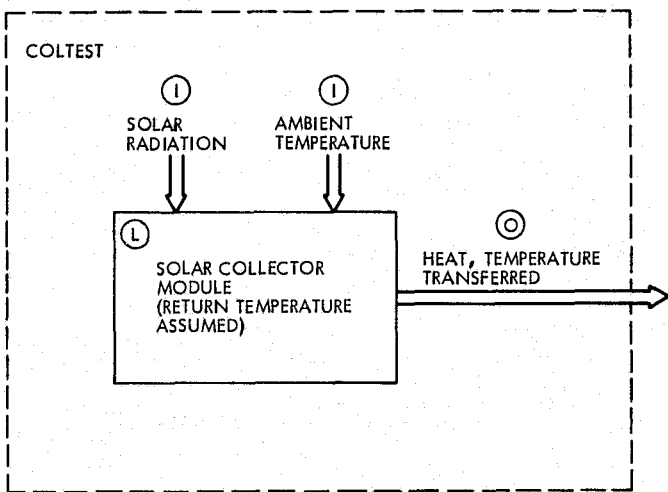


Fig. 1. Computational module and data interfaces

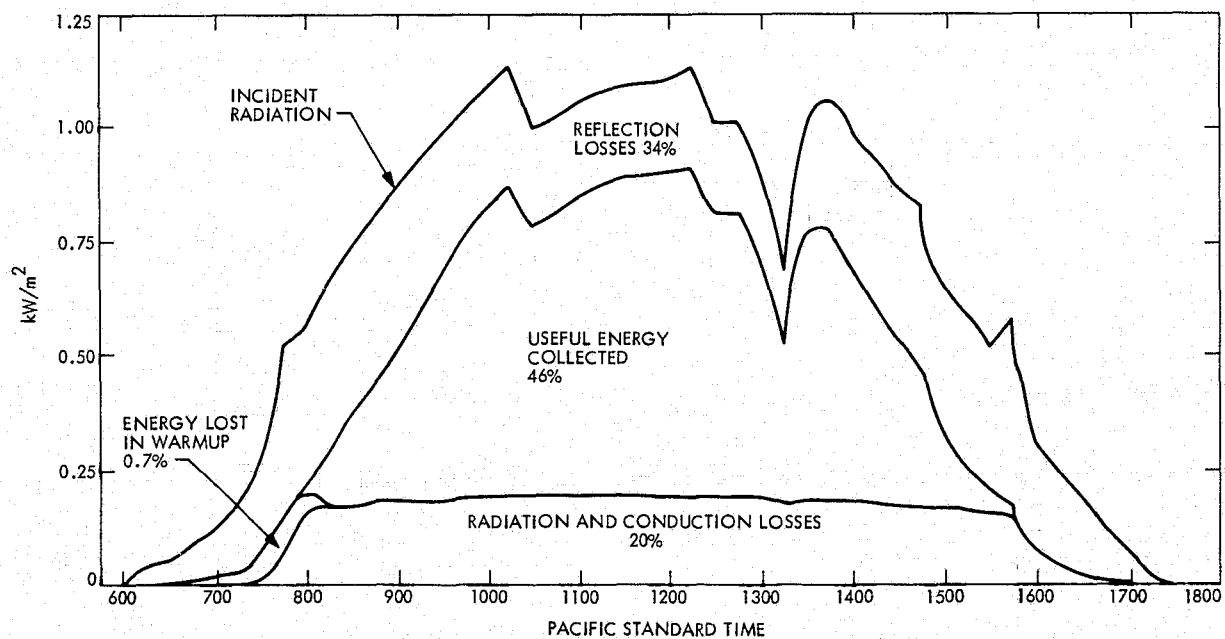


Fig. 2. Performance of collector tilted at 48.5 deg from horizontal

ORIGINAL PAGE IS
OF POOR QUALITY

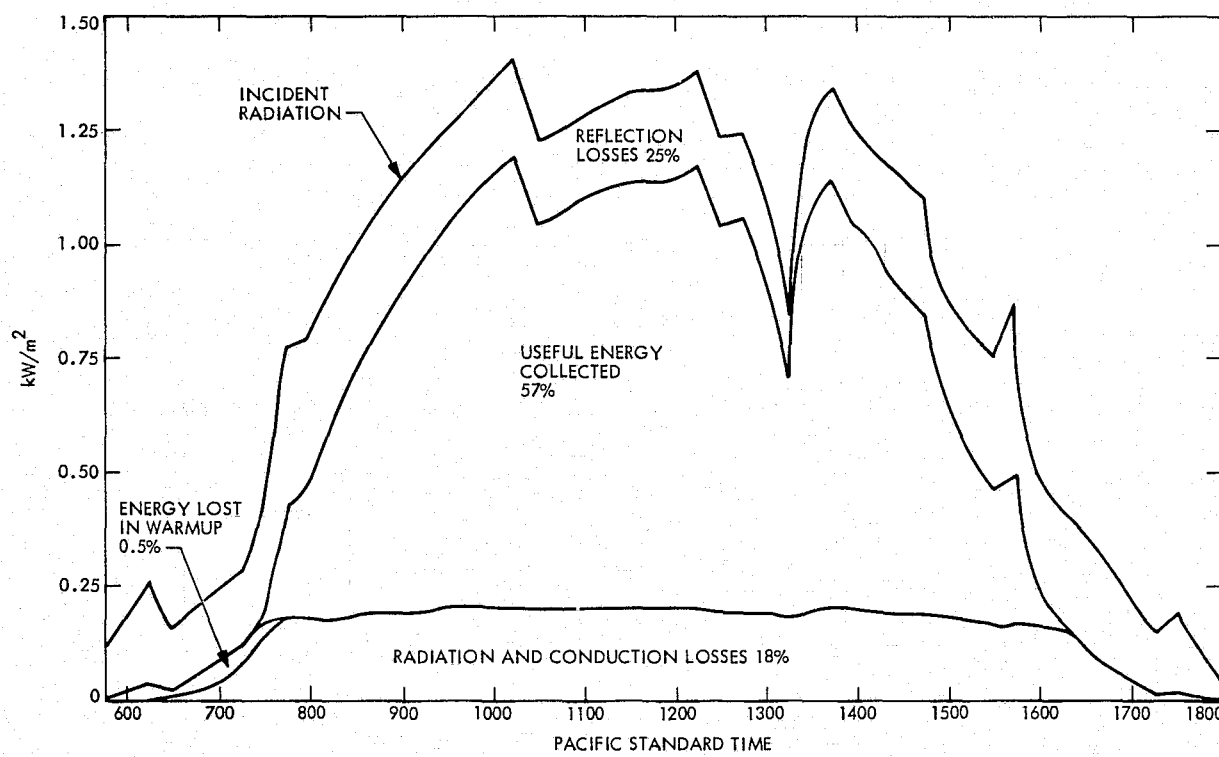


Fig. 3. Performance of collector tilted at 20 deg from horizontal

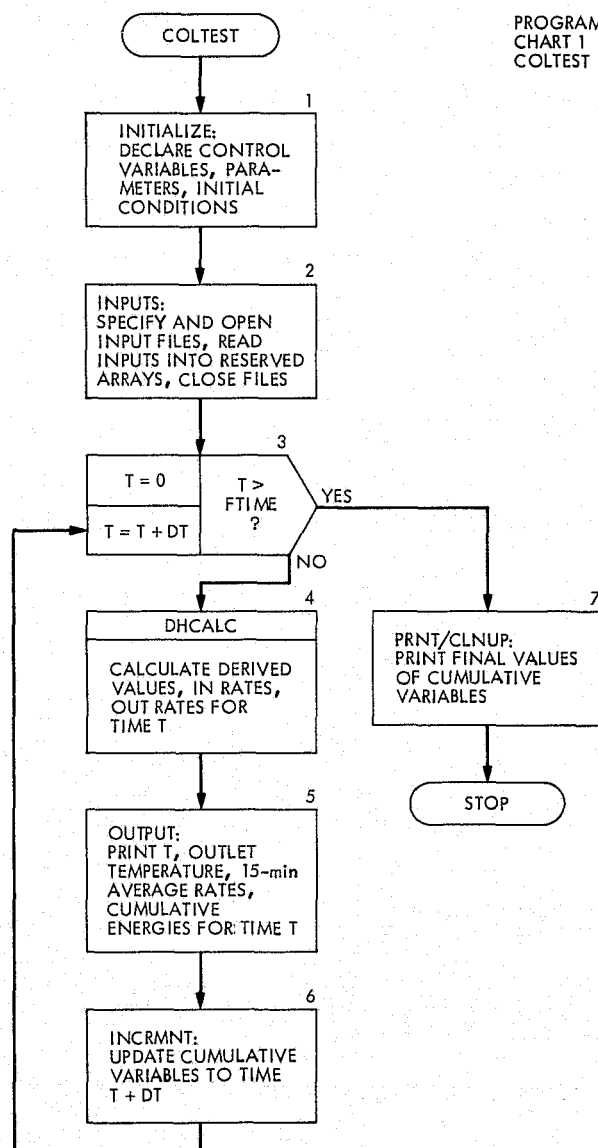


Fig. 4. Level 1 structure, Program COLTEST

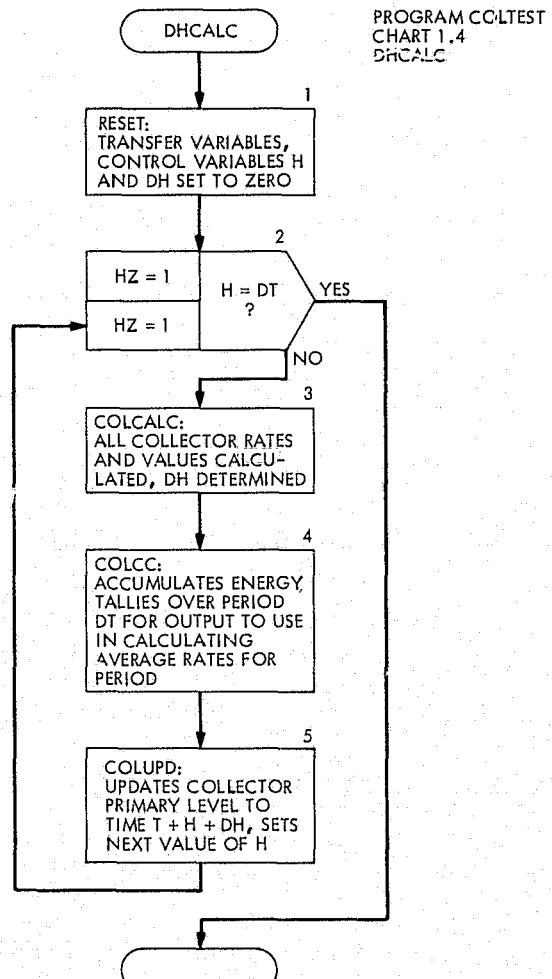


Fig. 5. Level 2 structure, Program COLTEST

ORIGINAL PAGE IS
OF POOR QUALITY

N 76-29338

Toward a Mathematical Model of Solar Radiation for Engineering Analysis of Solar Energy Systems

C. L. Hamilton
TDA Planning Office

M. S. Reid
Communications Elements Research Section

This report presents some first thoughts on mathematical models of solar radiation suitable for use in engineering analysis of solar energy systems. Included is a discussion of the currently most-used insolation model and what improvements might be made in it to better suit it for use in designing energy systems. An approach to constructing an upgraded model is sketched.

I. Introduction

After many years of study and experimentation on the subject, and in the face of continuing uncertainty over supply and price of conventional energy sources, serious consideration is now being given to the question of utilizing solar-powered energy systems on a relatively large scale. A necessary precursor to construction of well-designed, efficient, and economically viable solar energy systems is engineering analysis not only of the systems themselves but also of the solar radiation that will drive them. This report presents some first thoughts on mathematical models of insolation characteristics suitable for use in analysis of solar energy systems. Included is a discussion of the currently most-used insolation model and what improvements might be made in it to better suit it for use in designing solar energy systems. An approach to constructing an upgraded model is sketched.

II. Where an Insolation Model Fits

Before construction of any energy system is undertaken, there must be reasonable assurance that it will meet the demand it was planned to satisfy, and that it will do so with a low enough life-cycle cost to make the project economically attractive. System performance models can be used first to judge design alternatives against each other and against criteria for performance and cost and then to alter the design of the most promising systems to improve performance and/or lower costs. The function of an insolation model can be better understood by looking at some of the essential features of a solar energy system model.

Solar-powered systems can cover a range of applications, from space and water heating in a single structure to central station generation of electricity, and can vary

widely in complexity. A generalized solar-thermal system will be made up of solar collectors, possibly some sort of storage subsystem, and a subsystem to convert thermal energy to the desired form. Depending on the application, each of the subsystems might be quite simple or very complex; for illustrative purposes it will be sufficient to think in terms of the general groups. In a gross sense, the energy output of a solar-powered system is determined over a given time period by the amount of solar radiation collected by the system and the overall system efficiency. The efficiency with which the system operates depends in turn on characteristics of the included subsystems and the parameters on which their individual performances will depend.

Of the solar energy hitting a collector, a fraction, depending on the sun's position relative to the collector surface and the collector's own geometry and optical properties, fails to get to the absorbing surface. A portion of the absorbed energy is lost via heat leaks and reradiation; the amount is determined by collector properties and the temperature at which it operates along with other factors like ambient temperature and perhaps wind speed. The remaining energy is transferred from the collector as sensible heat in a fluid at a temperature depending on fluid characteristics, the temperature of fluid entering the collector, and the collector temperature. The temperature of fluid entering the collector depends on how much heat is removed from it by other subsystems, such as that devoted to energy conversion. The amount of heat required by the conversion subsystem is governed by the load it is to satisfy, by its own internal properties, by the temperature of the heat supplied to it, and by the temperature of the sink to which it rejects heat (if it must). The characteristics of the storage subsystem exert an effect on both collector and conversion components. All of these influences are reflected in a system model that is made up of an interrelated set of mathematical models representing the performance of each component. Because each piece depends strongly on factors that vary significantly with time, the resulting model should reflect the important dynamics. Inaccuracies associated with the various component models will propagate and compound during analysis of the system, of course. This means that each of them must represent the performance of the associated subsystem with greater accuracy than is required of the whole system model.

Given that a system model can be developed that will allow calculation of system output as a function of insolation and other weather parameters, where are we then? A viable energy system, solar or otherwise, must be

capable of supplying the output expected of it over the course of its useful lifetime. Conventional systems can be designed with the appropriate capacity and then provided with the amount of fuel necessary to do their job. Fuel for a solar-powered system, sunlight, is completely outside the control of man. Design of a solar energy system—the relative sizing and performance specifications of components—must be done then on the basis not only of its intended output but also on the basis of the energy input that can be expected during its lifetime. The question arises—how does one supply appropriate values for the prime driving function, solar radiation, to allow an estimate to be made of system performance over the span of 10 to 15 future years? That performance analysis must be accurate enough to permit design of a system that meets output criteria and cost criteria in a situation where compensation for even moderate uncertainty by oversizing components can be prohibitively costly.

Experimental measurements of solar radiation intensity could be used to drive a system model. Such measurements are scarce, limited to a few locations, and more often than not of questionable accuracy. Only rarely, in fact, have the needed aspects of incident radiation been measured. Empirical data suffer from a more fundamental deficiency, however. Using radiation measurements as input for a well-conceived system analysis may give a good estimate of how the system would have performed during the time the data were taken, but that estimate would only be good for the period in which the measurements were recorded. To arrive at the desired system performance it would be necessary, in addition, to simulate the system's behavior over that whole period, a procedure that could be unnecessarily costly and time-consuming.

What is needed is a representation of insolation characteristics that depicts those aspects of both its long-term and short-term behavior on which system performance depends, expressed in terms of a one-year description. That one-year description may never match insolation behavior for a particular measured year, but would be extrapolatable to match closely all important aspects of insolation integrated over a long time. The representation would, in short, be the output of a mathematical model describing solar radiation. Such a model, along with a suitable data base, would allow average or representative future behavior to be predicted, along with estimates of the frequency and magnitude of deviations from that average. As noted above, the accuracy of the outputs from this model must be greater than the accuracy required of the outputs of the composite system model.

III. The ASHRAE Model

An insolation model currently enjoying wide use is that developed by the American Society of Heating, Refrigeration and Air-Conditioning Engineers (ASHRAE). It was not created for the purpose of analyzing performance in solar-powered energy systems. Rather, its intended application was in estimating heat load on buildings for the purpose of specifying heating-cooling systems for installation there. The form of the ASHRAE model was dictated by its purpose—this is the case with all mathematical models. In general, the effect of insolation on cooling system requirements is felt on clear sunny days; they specify the conditions with which a cooling system must cope. Only clear days are modeled by the ASHRAE equations.

Some discussion of what happens to sunlight on its way to Earth's surface will aid in dissecting the ASHRAE model. Energy emitted by a point on the sun arrives at the edge of our atmosphere in parallel rays. Its intensity at that point depends on Earth's distance from the sun, and varies slightly with time of year. As the solar radiation passes through the atmosphere, its direct normal intensity (intensity on the plane perpendicular to the ray bundle's direction) is attenuated. Some of the energy is absorbed by molecules of atmospheric constituents and some is figuratively knocked out of the bundle of parallel rays by molecular and particulate scattering. The degree of attenuation from these effects is a function of the distance the radiation has to traverse in the atmosphere, and the concentration of absorbing and scattering species contained there. The ASHRAE model uses the following equation to mimic these influences under clear day conditions:

$$I_{DN} = N A e^{-B/\sin\beta} \quad (1)$$

I_{DN} is the direct normal intensity of radiation at Earth's surface. N is a clearness number that varies up or down slightly from a value of 1, depending on geographical location and season, and reflects the inevitable variation in clarity of what is considered to be a clear day. The parameter A is classified as apparent radiation at atmosphere's edge; it has a different value for each month and includes the combined influence of the sun's distance from Earth and some atmospheric attenuation. The value of B , the atmospheric extinction coefficient, also varies monthly, reflecting the concentration of absorbing and scattering species. Sets of values for both A and B were determined by empirical curve fitting. That is, they were the values that, when inserted into Eq. (1), produced values of I_{DN}

that best matched data actually measured over a long period at a site with a defined clearness number of 1. Finally, $1/\sin\beta$ (where β is the sun's elevation angle) approximates the distance that the parallel bundle of rays travels in the atmosphere, which varies with time of day and time of year.

A unit area of surface at ground level will receive direct radiation, I_D at a rate corresponding to the direct normal intensity modified by the cosine of α , the angle between the direction of incoming rays and the direction perpendicular to the surface.

$$I_D = I_{DN} \cos \alpha \quad (2)$$

In addition to the energy arriving in a direct line from the sun, the surface in question will receive radiation from two other sources. Some of the scattered rays will, after bouncing about in the atmosphere, reach ground level and the receiving surface, coming from all directions. Light that has been reflected from the surroundings will also be picked up. These two effects are treated in the terms

$$I_{DS} = C I_{DN} F_{SS} \quad (3)$$

and

$$I_{DG} = r I_g F_{SG} \quad (4)$$

where I_{DS} is intensity of diffuse radiation coming from the sky, C is an empirically determined factor showing monthly variation, and F_{SS} is a geometrical factor relating to the amount of sky in a position to radiate to the surface. I_{DG} represents radiation reflected onto the surface from the ground around it; I_g is the total radiation intensity falling on the ground (determined as for any surface); r is ground reflectance, and F_{SG} is another geometrical factor. Analogous terms dealing with reflection from other surfaces might be required if the surroundings warranted. To sum up, the total radiation intensity received by a surface near ground level, according to the ASHRAE model, is expressed as

$$I_T = I_{DN} \cos \alpha + C I_{DN} F_{SS} + r I_g F_{SG} \quad (5)$$

When the quantities included are properly evaluated, this model provides good approximations for total radiation intensity as a function of time during clear weather. This is one aspect of several needed for accurate analysis of solar system performance.

IV. Interaction of Solar Radiation and Collectors

There are many ways of collecting solar energy. As far as their dependence on the characteristics of insolation is concerned, they may be classified in terms of the degree of concentration they involve. While solar energy is intrinsically of high quality, it arrives at Earth's surface widely distributed and must be reconcentrated to be put to useful work. Flat plate collectors use large areas of absorbing material to intercept the radiation as it falls unaltered on the collecting surface. The resulting energy is removed as heat by a fluid circulating over the surface. A flat plate collector can use all the radiation that hits it, but at high operating temperatures heat losses from the large area of hot surface limit its efficiency. Collector designs that concentrate the radiation before it strikes the absorbing surface seek to reduce these heat losses by cutting down on the surface area of hot material, allowing higher efficiency. In effect, the concentrating collectors focus the light on a small absorbing area, from which heat is removed by a circulating fluid. Concentration ratio is a measure of the area over which radiation is captured relative to the area on which it is focused; the higher the concentration ratio the more precise focusing is required.

Only direct radiation is useful to a concentrating collector. Diffuse radiation cannot be focused. The ASHRAE model allows estimation of direct radiation on clear days, where it comprises a large fraction of the total incident light. Energy systems must also work on days that are not entirely clear. Then the proportion of diffuse radiation is much larger, and concentrating collectors will experience their own degradation of output. In comparing systems, one must decide whether large areas of possibly less expensive nonfocusing collectors, with high heat losses but capable of using all the components of incident light, are more or less effective than perhaps smaller arrays of more expensive focusing collectors that will attain high temperatures more efficiently but can't use all the light. This comparison cannot be made without knowing the availability of both direct and diffuse radiation as a function of time for all kinds of days.

The ASHRAE equations embody a semi-empirical, deterministic model. By dealing exclusively with one kind of day, a type that is practically eventless except for the rise and fall of the sun, they can be successfully applied. A requirement for dealing with all days demands a model with probabilistic components as well as deterministic ones. An ideal model will reflect the occurrence and density of clouds and haze, and will mimic their effects on

both direct and indirect radiation. For general application to all collectors, another phenomenon must be considered. That is the circumsolar radiation. This is caused mainly by scattering of the sun's rays by Earth's atmosphere, and possibly also by refraction to a smaller extent, and is always present. On clear days, the effect is small and is limited to a narrow angular diameter about the sun's disk. On hazy days the turbidity of the atmosphere increases the circumsolar radiation at the expense of the direct component. It also increases the angular extent of circumsolar radiation, which then merges with the diffuse radiation. The result is that concentrating collectors cannot focus the sun's disk sharply. Loss from atmospheric defocusing of the sun's image becomes more severe as concentration ratio increases. Neither this effect nor the frequency and nature of unclarity can be modeled deterministically at this time. Random variables must be employed to estimate their influence.

Since the ASHRAE model performs well in predicting radiation on clear days, it forms a sensible starting point for first attempts at constructing a generalized model. We will concentrate on the terms described by Eqs. (1) and (3), regarding the clear-day expressions for direct and diffuse radiation as being a baseline condition that is modified by the random effect of the weather. Modifications would occur via the insertion of a pair of random variables (call them M and m), one in each equation.

$$I_{DN} = MNAe^{-B/s \sin \beta} \quad (6)$$

$$I_{ns} = mCI_{DN}F_{ss} \quad (7)$$

Any terms for reflected radiation (Eq. 4) that might be required to model a situation will automatically be modified, since they would be derived from modified estimates of total radiation on the reflecting surface. On a clear day, both M and m would carry values of 1, and the original ASHRAE equations would stand. As "unclearness" increases, the value of M would vary on a short time scale —say, hourly. An additional variable could be inserted into Eq. (6) to model the circumsolar radiation, giving in the end

$$I_D = DMNAe^{-B/s \sin \beta} \quad (8)$$

An estimate of how the variable D might depend on concentration ratio has been made, but must be verified. Equations (6) and (8) form a solar radiation model that should be much more suitable than either experimental measurements or the ASHRAE model for supporting engi-

neering analysis of solar energy systems. The improved model will be more representative of solar behavior than a set of measurements, and will deal somehow with all the aspects of radiation that are important to a collector.

The question arises—where do values of M , m , and D come from? Their basis is a series of simultaneous measurements made as accurately as possible in one location over as long a period of time as practicable. The parameters collected would include total insolation intensity and direct radiation as measured by a set of devices with a number of different concentration ratios. Data would be taken at small time intervals, on the order of a few minutes. Diffuse radiation intensity could be derived by differencing measurements of total intensity and direct radiation determined without concentration. These data and Eqs. (6) and (8) would be used to calculate simultaneous values for the three random variables. From the calculated values, a joint probability density function for M and m would be determined, as well as a functional relationship between D and concentration ratio. The derived probability density functions are used, while model calculations are being carried out, to generate values of the random variables which will lead to a time series of calculated intensities with the same statistical properties as the original measurements.

For probability density functions to give the most representative results, they should be based on a very large

number of measurements. It is often the case that their form can be determined from a more limited set of data, after which they can be upgraded by small adjustments in the parameters in which they are expressed as more and more data become available. Modification of the density functions for application to another location may be possible, using a limited number of insolation measurements at the new site and correlation with other weather data that might be more abundant. Verification of such a transfer, and establishment of the conditions under which it would be valid, would require careful measurements for comparison with predicted values.

A program for gathering meteorological and solar data using absolute calibration standards has been underway at the Goldstone Space Communications Complex since June 1974 (Refs. 1 and 2). These measurements provide an archive of solar data calibrated to the international standard. In addition, they provide a data base that has allowed a start on development of a solar model such as the one sketched, which will be the subject of a forthcoming publication. It must be kept in mind, however, that the approach to an accurate insolation model described in these paragraphs is only a beginning. This probabilistic model is still very much simplified, and future effort might profitably be spent investigating those factors, now determined empirically, to more precisely identify and separate their deterministic and probabilistic components.

References

1. Reid, M. S., Gardner, R. A., and Parham, O. B., "The Goldstone Solar Energy Instrumentation Project: Description, Instrumentation and Preliminary Results," in *The Deep Space Network Progress Report 42-26*, pp. 133-144, Jet Propulsion Laboratory, Pasadena, Calif., April 15, 1975.
2. Reid, M. S., and Gardner, R. A., "A Versatile Data Acquisition System for Goldstone," in *The Deep Space Network Progress Report 42-30*, pp. 132-143, Jet Propulsion Laboratory, Pasadena, Calif., Dec. 15, 1975.